



# Annual Report 2014

MLZ is a cooperation between:

Bayerisches Staatsministerium für  
Bildung und Kultus, Wissenschaft und Kunst



SPONSORED BY THE



Federal Ministry  
of Education  
and Research

### **The Heinz Maier-Leibnitz Zentrum (MLZ):**

The Heinz Maier-Leibnitz Zentrum is a leading centre for cutting-edge research with neutrons and positrons. Operating as a user facility, the MLZ offers a unique suite of high-performance neutron scattering instruments. This cooperation involves the Technische Universität München, the Forschungszentrum Jülich and the Helmholtz-Zentrum Geesthacht. The MLZ is funded by the German Federal Ministry of Education and Research, together with the Bavarian State Ministry of Education, Science and the Arts and the partners of the cooperation.

### **The Forschungs-Neutronenquelle Heinz-Maier-Leibnitz (FRM II):**

The Forschungs-Neutronenquelle Heinz-Maier-Leibnitz provides neutron beams for the scientific experiments at the MLZ. The FRM II is operated by the Technische Universität München and is funded by the Bavarian State Ministry of Education, Science and the Arts.

**Joint Annual Report 2014**  
**of the MLZ and FRM II**

## Directors' Report

Celebrating milestones and meeting new challenges .....	9
The year in pictures .....	10
Workshops, Conferences and Schools .....	16

## Instrumental Upgrades & Services

Instrumental Upgrades .....	20
Beyond the instruments – laboratories and service groups.....	34

## Scientific Highlights

### Quantum Phenomena

Nematic spin correlations in the tetragonal state of uniaxial strained $\text{BaFe}_{2-x}\text{Ni}_x\text{As}_2$ .....	48
Real space description of excitations in $\text{SrCu}_2(\text{BO}_3)_2$ and spectral line shape at low temperatures .....	50
Nano phase separation responsible for hour-glass spectra in $\text{La}_{2-x}\text{Sr}_x\text{CoO}_4$ .....	52
Triplet superconducting correlations in oxide heterostructures with noncollinear magnetization .....	54
Competing ferromagnetic and antiferromagnetic interactions in the 2D spiral magnet $\text{Sr}_3\text{Fe}_2\text{O}_7$ ...	56
Exchange-bias-like coupling in a ferrimagnetic Fe/Tb multilayer with planar domain walls.....	58
Critical spin-flip scattering at the helimagnetic transition of MnSi.....	60

### Soft Matter

Studying the interactions between liposomes and silica nanoparticles using SANS, NSE and DLS .....	62
Internal nanosecond dynamics in the intrinsically disordered myelin basic protein .....	64
From molecular dehydration to excess volumes of demixing thermo-responsive polymer solutions .....	66
Polyethylene glycol polymer layers – studies from tethered lipid bilayers to protein-cell interactions .....	68
Structural insights into nanoparticles containing Gadolinium complexes as potential theranostics .....	70
Quasielastic neutron scattering insight into the molecular dynamics of all-polymer nano-composites .....	72
Highly asymmetric genetically encoded amphiphiles .....	74
Free volume in new and used high free volume thin film composite membranes .....	76

## Structure Research

Neutron cryo-crystallography sheds light on heme peroxidases reaction pathway.....	78
Structure solution of a new ordered mixed imide-amide compound for hydrogen storage .....	80
On the complex H-bonding network in paravauxite, $\text{Fe}^{2+}\text{Al}_2(\text{PO}_4)_2(\text{OH})_2 \cdot 8 \text{H}_2\text{O}$ .....	82
CN-mayenite $\text{Ca}_{12}\text{Al}_{14}\text{O}_{32}(\text{CN})_2$ – a new kind of solid anion conductor with a mobile molecular anion .....	84
Low-temperature properties of single-crystal $\text{CrB}_2$ .....	86
The mechanism of multiferroicity in melilite defined by Spherical Neutron Polarimetry .....	88

## Materials Science

Lithium plating investigated by in situ neutron diffraction .....	90
Local structure and lithium mobility in intercalated $\text{Li}_3\text{Al}_x\text{Ti}_{2-x}(\text{PO}_4)_3$ NASICON type materials .....	92
Variant redistribution in a Ni-Mn-Ga shape memory alloy during thermo-mechanical treatment ..	94
Studies of early stage precipitation in a tungsten-rich nickel-base superalloy using SAXS and SANS .....	96
Mapping the structure of a glass through its voids .....	98
Thin film annealing and alloying of a Au/Cu two-layer system studied with a positron beam .....	100

## Neutron Methods

Neutron spin echo spectroscopy under 17 T magnetic field at RESEDA.....	102
Neutron reflectometry on samples with curved geometry .....	104
PGAA-Actinide: a series of experiments for actinide nuclear data improvement .....	106
Versatile module for experiments with focussing neutron guides.....	108

## Reactor & Industry

Ten years of reactor operation – A reason to celebrate, but also to work even harder .....	112
Progress in UMo fuel development .....	114
Future Mo-99 irradiation facility .....	116

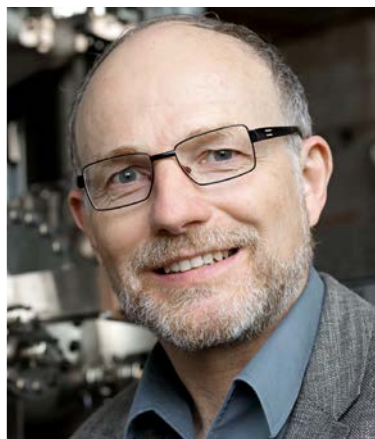
## Facts & Figures

Blogging, improving, travelling – The User Office 2014 .....	120
From science to media: the public relations office.....	122
Organisation .....	124
Staff .....	126
Budget .....	128
Publications & Theses .....	129
Committees .....	130
Partner institutions.....	136
Imprint.....	140

View of the hoisted flags of the MLZ and its cooperation partners as well as that of the FRM II at the front of the FRM II.



# Directors' Report



## Celebrating milestones and meeting new challenges

On 12<sup>th</sup> March 2014, we celebrated the 10<sup>th</sup> anniversary of FRM II's first criticality: Time to say "thank you" to all those from the realms of politics and science, and the public at large, who supported the construction of this most modern of continuous neutron sources. Special thanks are, of course, due to the operating team who, for 10 years, ensured a reliable supply of neutrons for science, industry and medicine. Former Ministers, who all lent their enthusiastic support to this project, were present at the celebration: Hans Zehetmair, Otto Schily, Wolfgang Heubisch and Edmund Stoiber.

After 10 years of operation, the FRM II underwent a planned and lengthy major maintenance break, beginning on 9<sup>th</sup> February 2014. In addition to the extensive decennial tests, a wide range of check-ups was carried out, e.g. the overhaul of the shutdown rods and reconstruction of the cooling tower cells. Having passed all the extensive mandatory in-service inspections without any objections on the part of the regulatory body, the FRM II began the 35<sup>th</sup> operating cycle right on-time on 21<sup>st</sup> August.

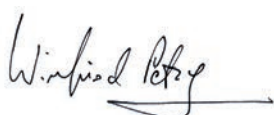
In May, the MLZ passed its first scientific evaluation by an international committee with flying colours. The committee was unanimously impressed by the written report prepared for this review, the discussions, the ongoing projects at all levels, and the high level of third party funding obtained over the last years. The panel acknowledged the important role of the young MLZ as a large scale facility combining an in-house research programme and a firm commitment to education in a strong network of universities, research centres, and industrial partners. Combining the enthusiasm of young researchers from universities with the technological and methodological expertise of research centres makes innovative instrumentation possible and is one of the recipes for the success of the MLZ.

The MLZ with its diverse applications in research, industry and medicine not only attracts users from all over the world, but also a great number of highly motivated staff. At the present time, some 400 people are employed on site and we expect this number

to grow even further over the next years. To overcome the current shortage of office and laboratory space, new container buildings were installed and office and laboratories rented from the neighbouring Max-Planck-Institute. This will be an interim solution until the new buildings on the premises of FRM II are erected. These two new four-storey buildings to be built by the TUM and Forschungszentrum Jülich will provide about 190 work places as well as a large workshop for the reactor division and numerous laboratories. The preparatory work began in August with the building of an underground duct for service pipes, as well as the demolition of two old laboratory and office buildings dating from the early days of the "Atomic Egg". Completion of construction of these two new buildings is foreseen for the end of 2018.

The year was eventful with a total of 118.5 days of operation. In the coming year, we look forward to 10 years of user operation and also to further structural alteration work with a maintenance break of approximately three months. The planned exchange of the plug SR5 is another step towards the "neutron connection" to the Guide Hall East and thus paves the way for further increase in scientific usage through additional instrumentation. This includes facilities for nuclear and fundamental physics (MEPHISTO and EDM), the high intensity powder diffractometer POWTEX, the polarized thermal time-of-flight spectrometer TOPAS, the six anvil press SAPHIR and the relocated three axes spin echo spectrometer TRISP. These additional instruments provide the basis for exciting experiments and new discoveries at one of the foremost neutron sources in the world.

At this point, we would like to take the opportunity to thank our outgoing colleague, Dieter Richter, for his long standing support for the German and European community of neutron scientists, his personal involvement in launching MLZ and his commitment and engagement as Scientific Director representing the Helmholtz centres at the MLZ. We wish him all the very best for the future. His successor as of 1<sup>st</sup> January 2015 will be Thomas Brückel, Head of the Institute for Scattering Methods of JCNS at the Forschungszentrum Jülich.



Winfried Petry



Thomas Brückel



Klaus Seebach



Anton Kastenmüller

# The year in pictures



**January 23<sup>rd</sup>**

15 students and their teacher (r.) from the Carl-Orff-Gymnasium in Unterschleissheim successfully completed their scientific seminar (W-seminar) with a helping hand from several scientists at the MLZ.

**January 30<sup>th</sup>**

In preparation for the 10<sup>th</sup> anniversary of the FRM II, students from the Werner-Heisenberg Gymnasium in Garching paint their „version of neutrons“.



**February 18<sup>th</sup>**

The Committee Research with Neutrons holds its annual meeting in Garching.

**March 12<sup>th</sup>**

The FRM II celebrates the 10<sup>th</sup> anniversary of the first criticality with (from left to right): Hannelore Gabor, mayor of Garching, Karl Eugen Huthmacher from the Federal Ministry for Science and Education, Johanna Rumschötel, District Administrator for München, Hans Zehetmair, former Minister for Science in Bavaria, Wolfgang Herrmann, President of the Technische Universität München, Ludwig Spaenle, State Minister for Education and Science, Anton Kastenmüller, Technical Director of the FRM II, Winfried Petry, Scientific Director MLZ, FRM II, Wolfgang Heubisch, former Minister for Science and the Arts in Bavaria.



**March 25<sup>th</sup>**

The Bavarian EliteAcademy, which supports gifted and motivated students from all Bavaria's universities on their way to becoming responsible leaders of the future, visits the MLZ with about 20 of their students.

**April 10<sup>th</sup>**

Christian Barth (middle), Director General of the Bavarian State Ministry for the Environment and Consumer Protection, tours the FRM II with his staff.



# The year in pictures



**February 9<sup>th</sup> to August 21<sup>st</sup>**

Staff from reactor operation in special suits during the decennial maintenance break undertaking their many check-ups and inspections. The FRM II began the 35<sup>th</sup> operating cycle right on-time on 21<sup>st</sup> August.

**April 30<sup>th</sup>**

Yuntao Liu (middle), Director of the Neutron Scattering Laboratory at the China Institute of Atomic Energy, presenting a gift to his host, Winfried Petry (right).



**May 19<sup>th</sup>/20<sup>th</sup>**

The MLZ is evaluated for its first three years of scientific cooperation by an international committee. Robert Georgii explains the achievements at the instrument MIRA to (from left to right): Reinhard Schwikowski (MLZ), Paul Langan (ORNL), Jürgen Neuhaus (MLZ) and Andrew Harrison (Diamond Light Source Ltd).

**May 28<sup>th</sup>**

Alumni and staff together with their families celebrate the 10<sup>th</sup> anniversary at the annual FRM II summer party.



**July 23<sup>rd</sup>**

Wolfgang Marquardt, Chairman of the Board of Directors of Forschungszentrum Jülich (2<sup>nd</sup> from left), and Dirk Schlotmann, Permanent Deputy Managing Director (right) visit the MLZ under the guidance of Dieter Richter, head of JCNS (2<sup>nd</sup> from right) and Alexander Ioffe, head at JCNS-MLZ (left).

**July 18<sup>th</sup>**

Members of the French Alternative Energies and Atomic Energy Commission (CEA) and Technische Universität München meet at MLZ to discuss common future projects.



# The year in pictures



**September 9<sup>th</sup>**

The excavators arrive to tear down old laboratories from the early days of the „atomic egg“ to make way for a new laboratory, workshop, and office buildings.

**September 9<sup>th</sup>**

Four apprentices finish their training at the FRM II and have all found jobs: Simon König, Stefan Rainow, Florian Jaumann and Katharina Bulla (from left to right).

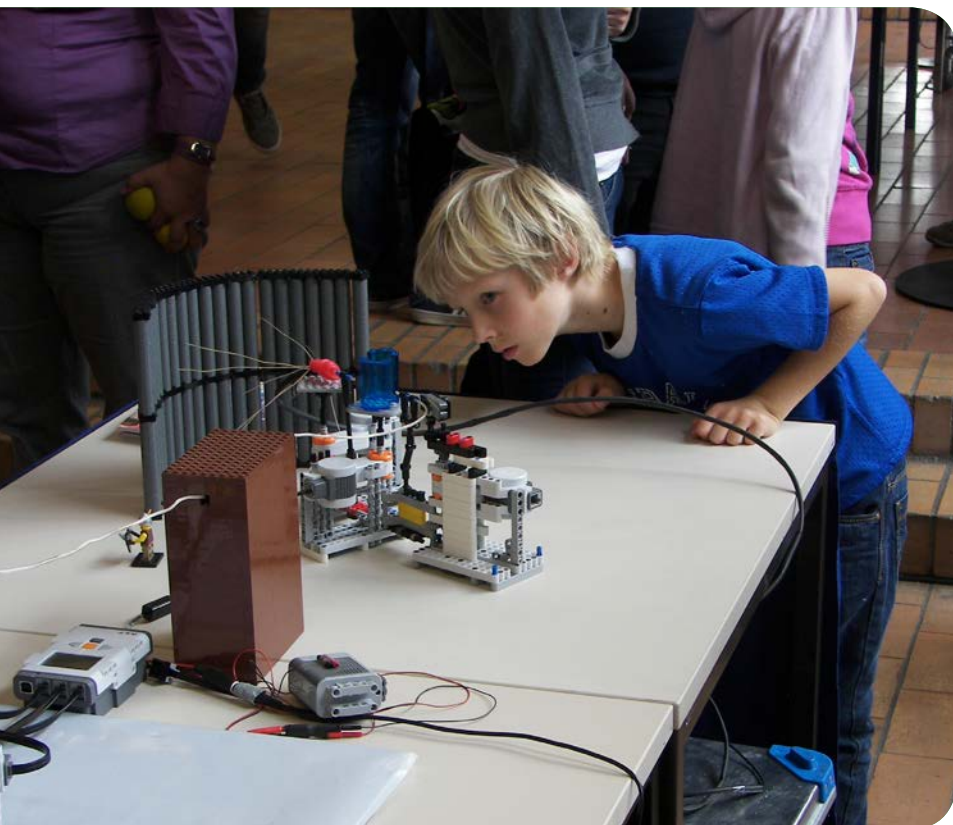


**September 13<sup>th</sup>**

Garching's mayor Dietmar Gruchmann tries his luck at the neutron ball toss during the Garching Herbsttage.

**September 30<sup>th</sup>**

The annual FRM II summer excursion takes us to a historical lift for ships in the environs of Nuremberg and to the castle of Nuremberg.

**October 11<sup>th</sup>**

The Garching Campus opens its doors, as does the FRM II. More than 10,000 visitors were attracted by the whole campus, of which 505 visitors made a tour through the FRM II. A stand with information about radiation protection as well as one with Lego models of neutron scattering instruments and our neutron ball toss close to the queue for registration attracted not only children.

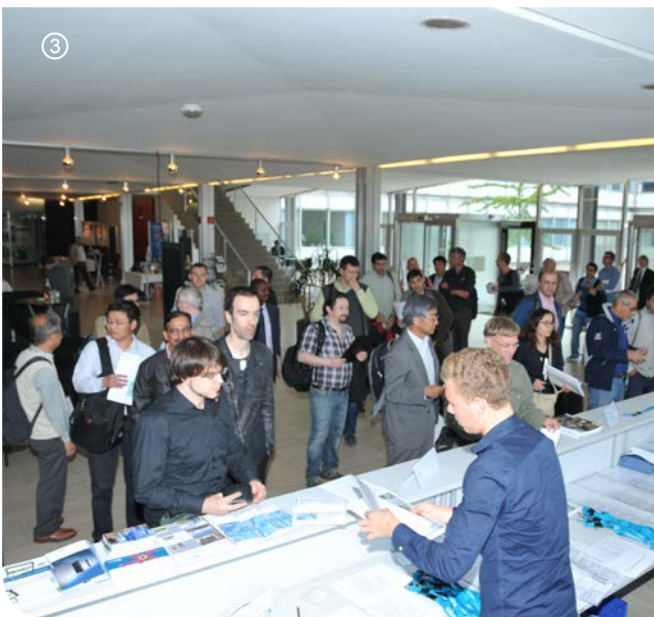
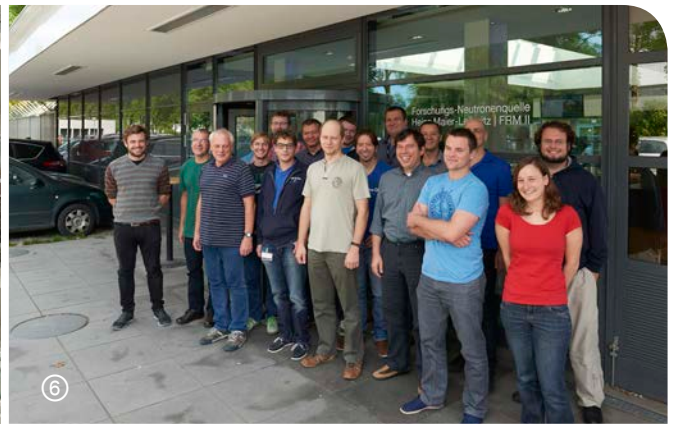
**November 11<sup>th</sup>**

A hall is constructed north of the FRM II premises. It will house the mock-up for the cooling systems of the ultracold neutron source.



# Workshops, Conferences and Schools

①	Neutrons in Research and Industry, weekly seminar	13 January – 15 December	Garching, TUM
②	NEUWAVE-6, Workshop on NEUtron WAVElength-dependent imaging	6 – 9 April	Garching, TUM
③	PSND 2014, International Workshop on Position Sensitive Neutron Detectors	2 – 4 June	Jülich, JCNS
④	Multi-TAS Workshop about application of Multi-analyser-detectors on triple axes spectrometer instruments	4 – 5 August	Garching, MLZ
⑤	18 <sup>th</sup> JCNS Laboratory Course - Neutron Scattering	1 – 12 September	Garching, JCNS
⑥	Jana2006, Workshop on crystallographic computing system	18 – 19 September	Garching, MLZ



⑦	VDI-TUM Expertenforum, Industrial Workshop on non-destructive testing for the mobility and energy of the future	11 September	Garching, TUM, VDI
⑧	Denim, Engineering workshop in the field of neutron scattering instruments	18 – 19 September	Garching, JCNS
⑨	ESS Science Symposium, Surface and interface reconstruction: a challenge for neutron reflectometry	24 – 26 September	Bernried, TUM
⑩	JCNS Workshop 2014, Trends and perspectives in neutron scattering	20 – 23 October	Tutzing, JCNS
⑪	McPhase 2014, Workshop on mean-field Monte-Carlo program	6 – 7 November	Garching, MLZ



Detailed reports on the workshops, conferences and schools can be found in the Newsletter MLZ News12 and 13 and at [www.mlz-garching.de/englisch/news-und-media/brochures-und-films/newsletter.html](http://www.mlz-garching.de/englisch/news-und-media/brochures-und-films/newsletter.html).

Surface studies with top-most layer sensitivity using slow positrons at NEPOMUC.



# Instrumental Upgrades & Services

# Instrumental Upgrades

V. Hutanu<sup>2,6</sup>, T. Keller<sup>3</sup>, J. Voigt<sup>2</sup>, T. Reimann<sup>1</sup>, M. Hofmann<sup>1</sup>, Z. Revay<sup>1</sup>, A. Houben<sup>2</sup>, A. Koutsioumpas<sup>2</sup>, O. Sobolev<sup>4</sup>, N. Walte<sup>5,1</sup>, T. Lauer<sup>1</sup>, Y. Su<sup>2</sup>, C. Hugenschmidt<sup>1</sup>, S. Söllradl<sup>1</sup>, O. Soltwedel<sup>3</sup>

<sup>1</sup>Heinz Maier-Leibnitz Zentrum (MLZ), Technische Universität München, Garching, Germany

<sup>2</sup>Jülich Centre of Neutron Science (JCNS) at MLZ, Forschungszentrum Jülich GmbH, Garching Germany

<sup>3</sup>Max Planck Institut für Festkörperforschung, Stuttgart, Germany

<sup>4</sup>Institut für Physikalische Chemie, Georg-August Universität Göttingen, Göttingen, Germany

<sup>5</sup>Bayerisches Geoinstitut, Universität Bayreuth, Bayreuth, Germany

<sup>6</sup>Institut für Kristallographie, RWTH Aachen, Aachen, Germany

**A**n asset of the MLZ instrument suite is its continuously growing diversity. Not only new instruments, but also the inclusion of new options or sample environments at the instruments during routine operation increase the experimental potential for our users' research. Keeping up to date with the instrument components is an ongoing effort. Here, we report on the challenge this presents for the instrument teams.

## Dedicated beam line for the polarised single crystal diffractometer POLI

Spherical neutron polarimetry was performed on the **Polarisation Investigator (POLI)** using the beam-port of the instrument HEiDi in 2010. We now report on the successful installation of POLI at its dedicated beam port, SR9a.

The biological shielding adapted in the meantime at the beam port SR9 now makes place for a second set of monochromators obtaining their hot neutrons through the beam channel SR9a. A double focusing mosaic crystal Cu 220 and a vertically focusing and horizontally bent perfect crystal Si 311 are the two non-polarising monochromators for POLI. Subsequent beam polarization is achieved by <sup>3</sup>He



Figure 1: V. Hutanu at POLI on its own new beam port (position).



Figure 2: The neighbours side by side: on the right, access to the instrument POLI, through the left door to HEiDi.

spin-filter cells. Cu 220 at the take-off angle of  $25^\circ$  is dedicated to the shortest wavelength of  $0.55 \text{ \AA}$  and Si 311 at the take-off angle of  $41^\circ$  is designed for the longest available wavelength of  $1.15 \text{ \AA}$  on POLI. A few different wavelength values between these two values are also available. Tuning the pressure in the <sup>3</sup>He spin filter cell optimises the polarisation parameter for any available wavelength.

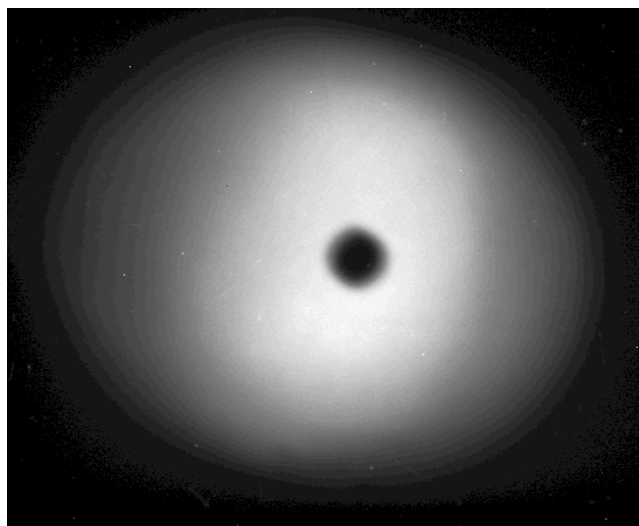


Figure 3: Homogeneous illumination with monochromatic neutron beam. The picture was taken using a neutron camera behind the sample. Black spot in the middle: 6 mm diameter Cd disc at the sample position on POLI.



Figure 4: The Si 311 monochromator for POLI.

During the first neutron test in February 2014, a flat Cu 220 crystal plate similar to that which will be used in the focussing monochromator was adopted. The result exceeded our expectations: at the selected wavelength of  $0.9 \text{ \AA}$ , a flux density of  $6 \times 10^6 \text{ n/s/cm}^2$  at the sample position was achieved. According to

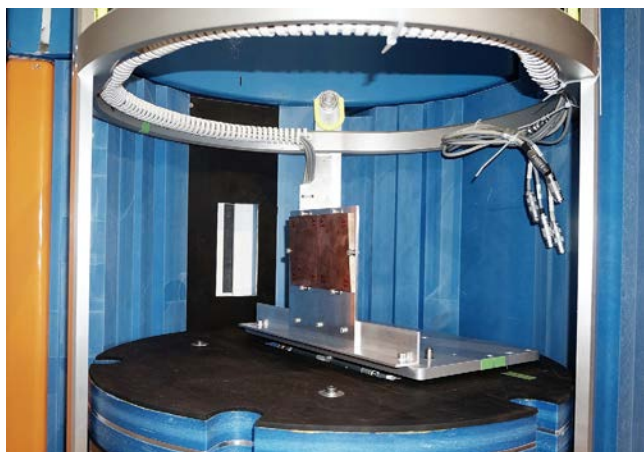


Figure 5: Single crystal Cu plate mounted at the position of the POLI monochromator used for the test experiments in February 2014.



Figure 6: Crane transport of the POLI diffractometer to its new "home" on the beam line SR9a.

our calculations, the use of focusing should increase the flux density by a factor of 5. The production of the dedicated Cu monochromator at the Institut für Physikalische Chemie of Göttingen University was completed in December 2014 and we are keen to install it on POLI in early 2015. The Si monochromator, which was produced by Bisson Technologies Inc. in cooperation with ILL Grenoble, was installed during the reactor shut down in March-August 2014. After the planned restart of the reactor and commissioning of the new Si monochromator in the fall of 2014, POLI performed the first user experiments on non-polarised diffraction in a magnetic field and spherical polarimetry on the new beamline. We are now looking forward to welcoming new users on POLI.

### New major components for TRISP

We redesigned two major components of TRISP, the monochromator and a support for the radio-frequency (RF) spin flip coils. Both components were constructed at the workshop of the MPI-FKF.

The mechanical parts of the previous monochromator at TRISP showed increased friction and backlash, leading to an inaccurate setting of the vertical and horizontal curvatures. We therefore decided to introduce a new design with a low friction curvature mechanism (2 dimensional), increased width and thicker PG crystals (3 mm instead of 1.5 mm). The enhanced crystal thickness allows for efficient use of the monochromator at the PG (004) reflection, where a typical reflectivity of around 30 % as compared to (002) in the range  $k_{\parallel} = 4\text{-}6 \text{ \AA}^{-1}$  is obtained. In combination with the velocity selector filtering the first order, the (004) reflection is an efficient alternative to a Cu (111) monochromator. The overall gain

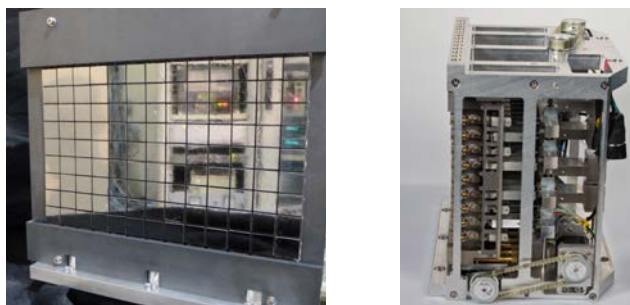


Figure 7: Front and side view of the redesigned monochromator for TRISP. PG crystal dimensions 20x18x3 mm<sup>3</sup>. All crystals were aligned individually. Construction at the workshop of the MPI-FKF.

from the new monochromator is around 20 % and about a factor two for the (002) and (004) reflection, respectively.

Pairs of RF spin flip coils at a separation distance of 500 mm form the spin echo precession regions at TRISP. The spin precession phase is proportional to this spacing. During a spin echo measurement, the spacing is varied by a few millimeters to determine the phase and amplitude of the neutron polarization. In the high resolution Larmor diffraction mode, where we aim to measure relative phase changes in the order of  $10^{-6}$ , the spacing must be kept constant to this relative precision. In the previous setup, the coils were mounted on an aluminum structure with a large thermal expansion coefficient of  $2 \times 10^{-5}/K$ . To eliminate thermal drifts, the new support consists of two tables, where the distance between the tables is defined by a Zerodur rod with a very small expansion coefficient ( $< 1 \times 10^{-7}/K$ ); one table is fixed to the aluminum support structure, while the second is kept at a constant distance and may float on a precision bearings with respect to the support. In addition, the first table incorporates a precise drive and optical encoder system to scan the spacing between the coils during spin echo measurements with sub- $\mu$ m precision. Precise linear bearings (Schneeberger) minimize pitching and rolling during translation.

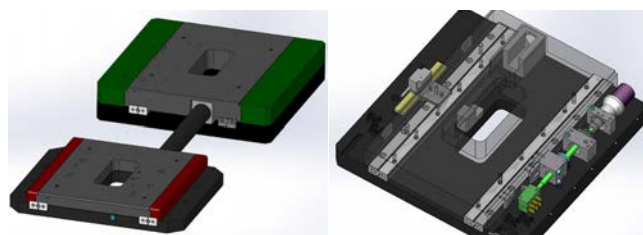


Figure 8: Support tables for the RF coils at TRISP. A Zerodur rod defines the spacing with a very low thermal drift ( $< 1 \times 10^{-7}/K$ ). The green table incorporates a precise linear drive with optical encoders.

### A big gift from Jülich

The construction of the thermal chopper spectrometer TOPAS is progressing steadily. In 2014 important steps towards the completion of the instrument were taken.

At the beginning of the year we completed the characterization of the <sup>3</sup>He detector tubes, from which we have built up the 16 m<sup>2</sup> detector array. This detector covers a solid angle of more than 3 steradian. In combination with the position resolution of the detectors, the excitation landscapes of novel materials can be mapped out efficiently by the instrument. The tests confirmed the specifications regarding the detection efficiency and the position resolution where completely fulfilled.

In addition, the spectrometer chamber was assembled and tested in the course of the last year. This 75 m<sup>3</sup> vessel, made from various stainless steels to meet the requirements of the polarization analysis, can, within 2 hours be pumped from ambient pressure to below the  $10^{-4}$  mbar necessary for cryogenic operations. The chamber and vacuum system were thoroughly tested. The control of the complex vacuum system and the sample area load lock was completed. It allows the separation of a 300 l volume from the main flight volume for a change of samples or sample environment.



Figure 9: Left: The spectrometer chamber assembled in Jülich. Right: Arrival in Garching.

Shortly before Christmas, a special present was sent from Jülich to Garching: The first section of the spectrometer chamber arrived in the early morning of 9 December and was stored at its future position in the neutron guide hall east. The remaining sections will follow in February.

This year will see the installation of the chamber in the guide hall, including the installation of the detectors inside the chamber. The second focus of the construction team is now on the primary spectrometer: While the housing and support were already completed last year, the chopper system consisting of the two Fermi choppers and the higher order removal chopper will be installed and tested again in Jülich before the next big gift will be sent to Garching.

### Improved shielding at PGAA

The improvement of the shielding at the PGAA facility is a continuous project. The latest construction is a combination of lead to attenuate gamma radiation, and boron- and lithium-containing absorbers against neutrons. Both neutron shielding materials emit secondary radiation: boron 478-keV gamma photons, lithium-6 fast neutrons, which cause neutron damage in the germanium crystal. Thus, lithium is never put into the direct beam. The beam is collimated and stopped using boron-containing materials (boron rubber, boron carbide), while the gammas emitted by it are stopped by a few centimeters of lead.

The arrangement of the improved shielding can be seen in Fig. 10. The guide chamber contains the elliptical neutron guide, which is interchangeable with a collimator. They are covered with a 3-5 cm thick boron rubber block on a moveable platform held by a newly-made cantilever. The neutron beam enters the sample chamber: an aluminum tube covered with a lithium-containing plastic sheet and is then stopped by a boron carbide plate in the beam stop. Perpendicular to the beam direction, a lead collimator allows the gamma rays into the germanium detector which is surrounded by an active shielding, the so-called Compton-suppressor, to reduce the spectral background originating from the photons scattered out of the detector. All units are covered by a 10 - 15 cm thick layer of lead.

The total count rate in the spectrum while acquiring the room background is about 3 - 5 counts per sec-

ond (depending on the operation of the neighboring instruments). When the collimated beam with a flux of  $2 \times 10^9 \text{ cm}^{-2}\text{s}^{-1}$  is on, the count rate increases with less than 10 counts per second, which makes possible the use of more than 3 orders of magnitude for the useful signals, as the digital spectrometer (ORETEC DSPEC-50) can handle about 30,000 cps. This low background allows for the irradiation of samples with the masses at the milligram level already in the collimated beam. The high-flux beam is 20 times stronger. The elliptical guide produces a highly divergent beam activating more structural materials. The background count rate in this setup is about 300 cps offering two orders of magnitude for the signal.

A low-background counting chamber was also installed next to the concrete bunker of the PGAA facility, which serves to measure the delayed gamma radiation from the activated samples. A HPGe detector with a relative efficiency of 30 % is cooled by a mechanical cooler, and is surrounded by 2 mm of tin to absorb the X-rays from lead, and the usual shielding components: lithium- and boron-containing plastic layers, and 10 cm of lead. The compact chamber accommodates samples with a volume of a few  $\text{cm}^3$ . The background count rate was 1.5 counts per second during the reactor break, while it is somewhat higher during the cycle: 2.5 cps. The counting chamber together with the irradiation opportunity at the PGAA facility permits in-beam neutron activation analysis.

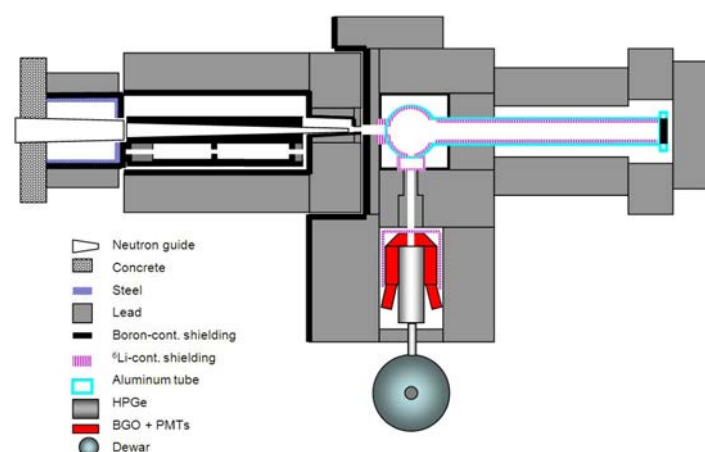


Figure 10: Shielding arrangement at the PGAA facility.

### POWTEX – ready for the Neutron Guide Hall East

In 2014, the POWTEX instrument passed several important milestones while awaiting the forthcoming on-site construction phase in the reactor and eastern guide-hall. The double-elliptic neutron-guide system was delivered by SwissNeutronics and is ready for installation. All components and housings of the four-disk chopper-system have been manufactured and the final assembly is currently underway at the Forschungszentrum Jülich. The successful prototype test of a tailor-made large-area  $^{10}\text{B}$ -detector led to the order of the full POWTEX detector from CDT GmbH, Heidelberg, in late 2013. Meanwhile, several production steps and, in particular, the boron sputtering process were significantly improved such that the first detectors and electronics passed series production. After having focused on the SR5 in-pile, the POWTEX engineering and construction team at ZEA-1 at the Forschungszentrum Jülich also started finalizing the construction and subsequent manufacture of the very last major components for POWTEX, e.g., the housing and shielding of the detector. Finally, the Monte-Carlo simulation of POWTEX was improved to gain more realistic diffraction patterns. These were used to investigate the potential benefits of a multi-dimensional Rietveld method which is currently in development mainly for POWTEX, but which was also successfully applied on data measured from POWGEN@ORNL.

In conclusion, the POWTEX instrument and its components are ready for the desired on-site construction phase once the time is ripe.

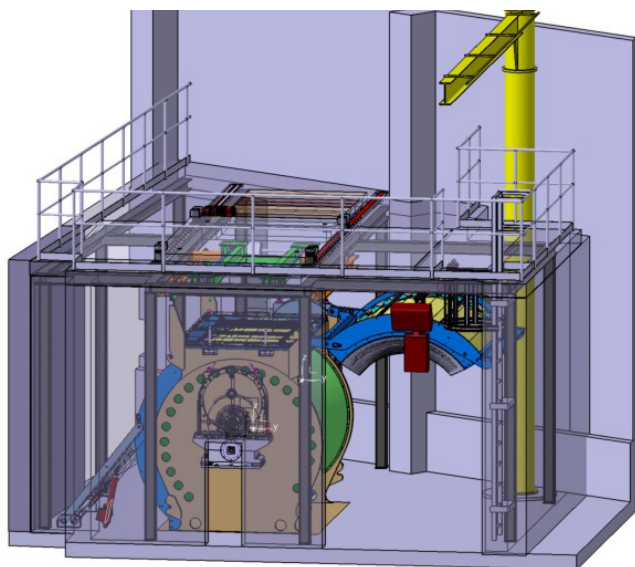


Figure 11: POWTEX detector (colored) and housing (gray) in the eastern guide hall.

### Instrumental updates related to Soft Matter on MARIA reflectometer

The usual practice when studying solid/liquid interfaces using neutron reflectometry is to vary the hydrogen content of the liquid as a means of obtaining reflectivity curves at various scattering length density contrasts. Such applications require the measurement of the absolute reflectivity of the interface

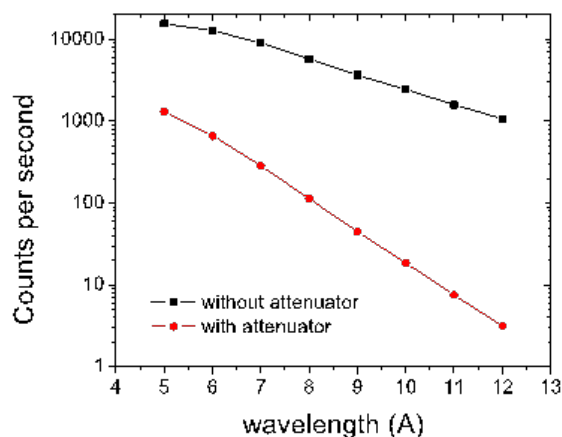


Figure 12: Characterization of installed attenuators.

(involving direct beam measurements). With this in mind, we installed a new set of beam attenuators on MARIA permitting the acquisition of direct beam measurements without saturating the detector.

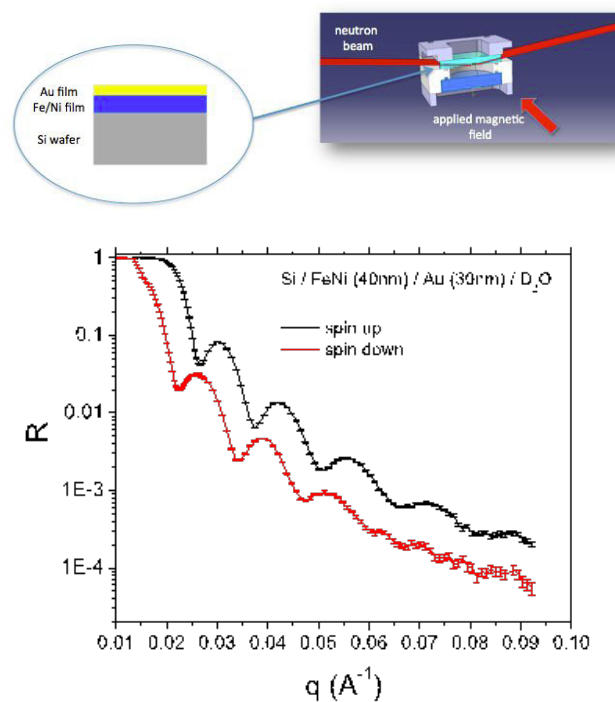


Figure 13: Full magnetic backing film concept and cell (top); first test measurement at MARIA (bottom).

Additionally, going beyond the need to exchange solvents in order to manipulate the scattering contrast of a system, we began implementing a method first devised at NIST that involves the use of ferromagnetic backing materials supported on a silicon wafer that possess a different sld, depending on the polarization of incoming neutrons. We have developed an appropriate liquid cell for implementing the method described above that is also adapted to the geometry of MARIA (beam focusing, magnet size etc. High quality ferromagnetic permalloy backing films were grown on silicon wafers, in cooperation with the MBE team.

### Expanding the capabilities of ANTARES: grating interferometry and monochromatic imaging

The spectrum of applications of the new ANTARES beam line has been expanded over the last year. Besides successful user experiments covering, for example, battery research, archeology and studies concerning hydrogen diffusion, a great deal of effort has been invested in further improving the capabilities of the beam line. In this context, a neutron grating interferometer (nGI) and double crystal monochromator (DCM) have been installed, each opening up new contrast mechanisms in neutron imaging in addition to pure neutron absorption.

nGI is based on two neutron absorption and one phase grating placed in the neutron beam which generate an interference pattern at the detector position with a periodicity of 4  $\mu\text{m}$ . The influence of a

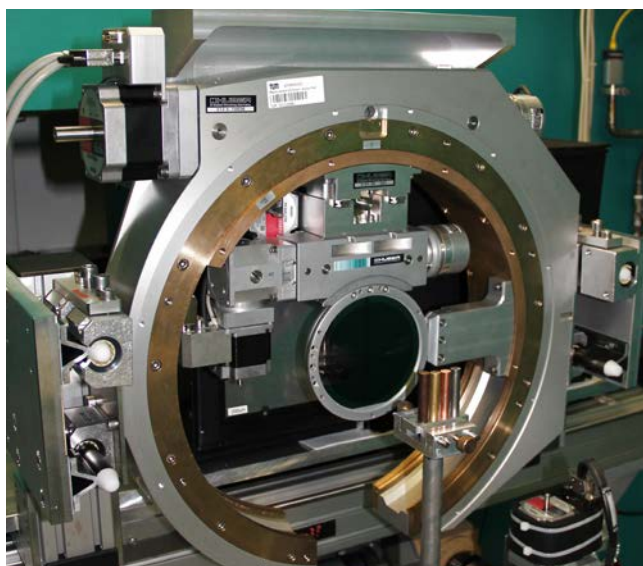


Figure 14: The nGI grating setup and the samples seen in Fig. 15.

sample on the interference fringes can be measured and separated into absorption, refraction and scattering contributions for each pixel. Hence, nGI simultaneously delivers the neutron transmission (TI), the differential phase contrast (DPC) and the dark-field image (DFI) in one measurement. The DFI, in particular, which identifies scattering at micron structures, has numerous applications in material testing on microstructural inhomogeneities, material distinction and imaging of domain structures e.g. in ferromagnets and superconductors. With a field of view of 100 mm the method is not restricted to small samples only.

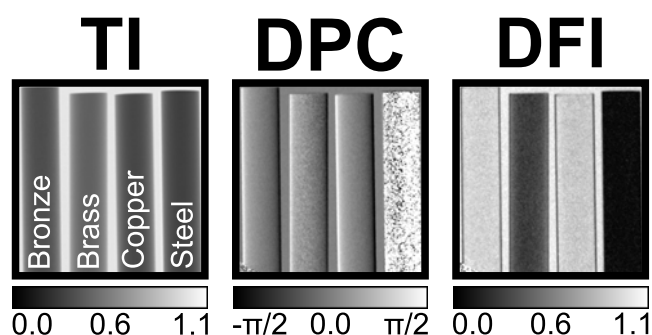


Figure 15: TI, DPC and DFI of four test materials. As the physical origin of the contrast is different the images contain complementary physical information.

The DCM consists of two graphite single crystals (mosaicity  $0.7^\circ$ ) aligned in parallel to each other. Via translation and rotation of the crystals, the desired wavelength can be selected in the range of 1.4 to 6.0  $\text{\AA}$  with  $\Delta\lambda/\lambda$  between 5 % and 1 %. Furthermore, the background at the detector position is strongly reduced by the beam dump placed in the direct beam direction.

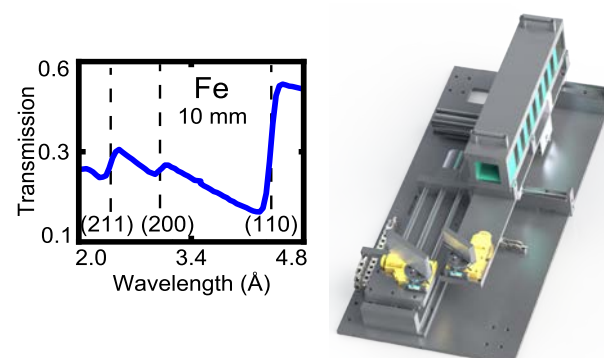


Figure 16: Left: Neutron transmission spectrum of iron showing characteristic Bragg edges; right: drawing of the new double crystal monochromator at ANTARES

Crystalline materials reveal sharp edges in their neutron transmission spectrum (Bragg edges), which depend on the local crystal lattice parameter. Hence, wavelength dependent imaging using a DCM can be used for material identification, stress and strain localization as well as for the evaluation of sample crystallinity. Furthermore, a highly monochromatic beam can be used for diffractive imaging, which is now also possible at ANTARES.

These new elements can easily be combined with various other beamline devices such as the velocity selector, polarizers and almost the whole FRM II sample environment. This makes ANTARES one of the most flexible Neutron Imaging beam lines available.

### New Detector at STRESS-SPEC

Quite recently the new 2d detector, developed in-house by the detector group, was mounted at STRESS-SPEC and first commissioning experiments have been conducted. Compared to the original delay line detector currently installed at



Figure 17: The back face of the new STRESS-SPEC detector in its housing before being closed for the commissioning tests.

STRESS-SPEC, it provides a much higher resolution and allows event mode type measurements (see the section by the detector group for details). Fig. 17 shows the detector in its new detector housing, which was built in cooperation with the technical services of the Helmholtz-Zentrum Geesthacht and the workshop of the Physics Department. The detector is integrated into the instrument control software using the QMesyDac interface developed by the instrument control group of TUM. First results of these experiments show a performance increase of almost a factor 2 compared to the current delay line detector.

The new detector will be fully operational and available for users after final installation of the optical elements for local strain and texture analysis from the second cycle of 2015.

### New Monochromator and Polarization analysis at PUMA

In addition to the available PG(002), Cu(220) and recently commissioned Cu(111), PUMA received the new double focused Ge(311) monochromator designed and built at the University of Göttingen. The main advantage of the new monochromator is the absence of the second order contamination in the monochromatised neutron beam and better resolution in comparison to the PG(002).

Fig. 18 shows the neutron intensity at the sample position delivered by different monochromators. If the neutron intensity is the most important factor, the PG(002) is still the best choice for measurements when the incident energy is lower than 60 meV. For

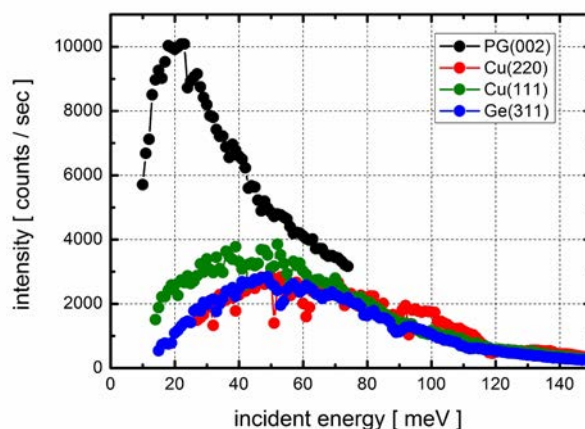


Figure 18: Intensity of neutrons scattered by the polyethylene sample measured without analyser and filters.

other cases, users can choose between three other monochromators, depending on the sensitivity to the background conditions or required resolution.

The recently commissioned multianalyser system of PUMA in combination with polarization analysis makes it possible to measure spin-up and spin-down scattering simultaneously using a special combination of polarisers (deflectors) consisting of FeSi polarizing supermirrors on Si-wafer substrate (SwissNeutronics,  $m = 4.5$ ). They are oriented in the scattered beam at critical angle  $\theta_c$  ( $-\theta_c$ ), so that the neutrons polarised in parallel direction ( $\uparrow$ ) are transmitted, whereas neutrons with spin-down polarisation are reflected.

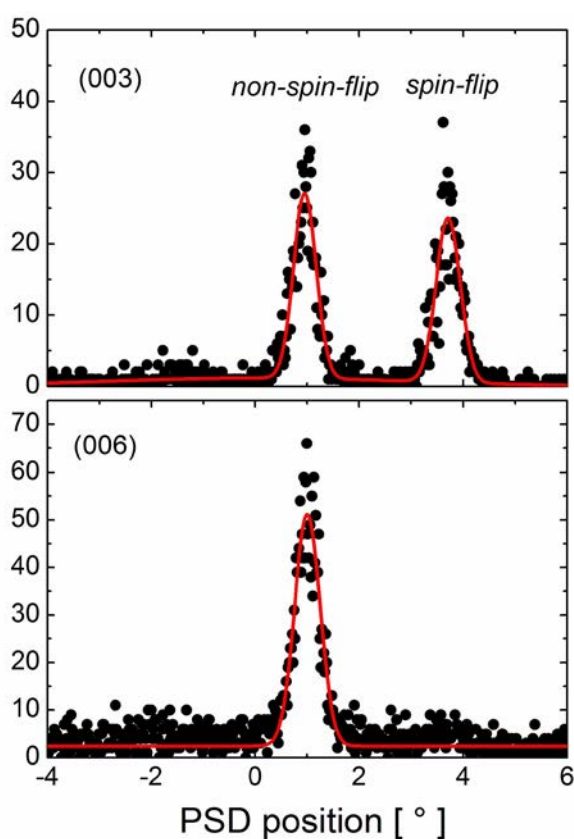


Figure 19: Bragg scattering from the hematite ( $\text{Fe}_2\text{O}_3$ ) sample: anti-ferromagnetic reflex (top) and nuclear reflex (bottom).

Both components hit different analyser blades of the PUMA multianalyser where the neutrons are reflected towards the corresponding detectors.

In September, first test experiments were performed in order to check the performance of the deflectors. A simplified set-up was used: In place of the multianalyser system we used a position sensitive detector

in order to see the angular distribution of neutrons scattered by the sample behind the deflectors and to find the optimal configuration for the multianalyser system. The incoming neutron beam was polarised by a  $^3\text{He}$  filter.

The first results using the double deflector system prove the feasibility of this novel method. Fig. 19 shows the measured Bragg intensity from the hematite ( $\text{Fe}_2\text{O}_3$ ) sample. In the case of nuclear reflex (006) only the non-spin-flip (transmitted) signal is recorded, whereas the anti-ferromagnetic scattering (003) shows both signals: transmitted and reflected corresponding to the spin-flip and non-spin-flip channels. These signals show a very good separation; they can therefore easily be detected by the multianalyser system.

#### Development and offline operation of SAPHiR in the neutron guide hall east

SAPHiR is one of the new instruments in the Neutron Guide Hall East; its aim is to provide extreme pressure and temperature conditions for time-of-flight neutron diffraction and radiography for research in the earth and material sciences and solid state physics. SAPHiR will share a thermal neutron beam line with a wavelength of 1 - 2.4 Å with the upstream instrument PowTex (Fig. 20). The multi anvil press of SAPHiR has been in place for two years and is currently operated offline (Fig. 21). The focusing neutron guide with a varying super mirror coating  $m = 1.5 - 4$  and the disc overlap chopper was manufactured in 2014 and is ready for setup in the eastern hall. The TOF neutron diffraction detector banks will surround the press in the backscatter, forward scatter, and at  $90^\circ$  angles to analyze diffracted neutrons that exit the sample through the anvil gaps (Fig. 20). The backscatter detectors consist of wave-length-shifting fiber scintillator detectors built by the ZEA Jülich. The two  $90^\circ$  detectors and the forward scatter detector were developed by the FRM II detector group. Prototypes for the detector modules are currently being built; each consists of 48 position sensitive  $^3\text{He}$  detector tubes assembled in curved detector banks to maintain a constant distance of 150 cm for each detector tube from the sample centre.

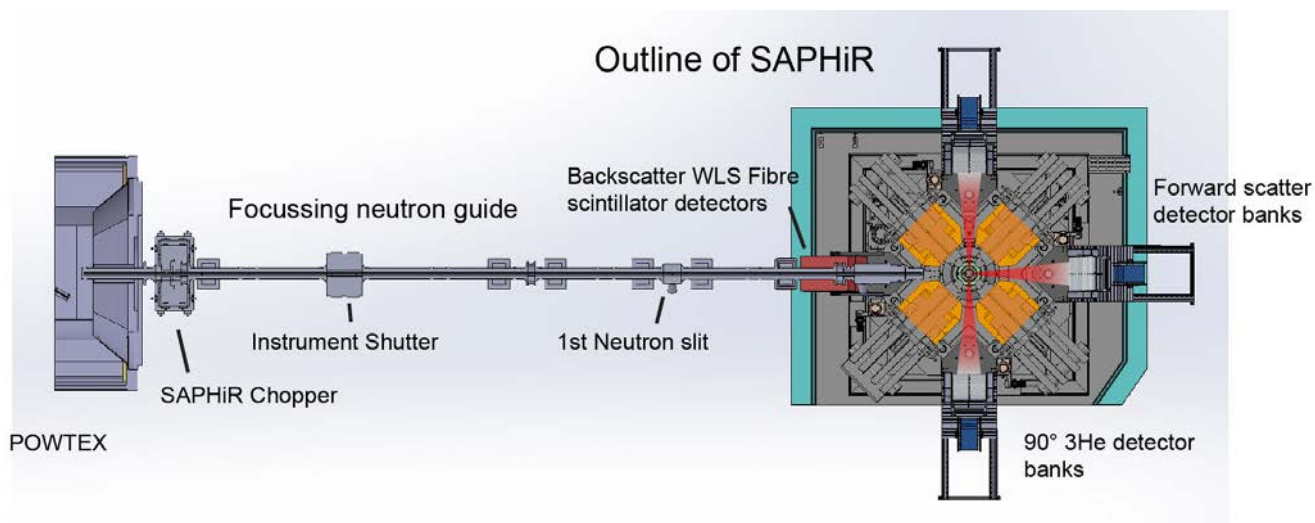


Figure 20: Outline of SAPHiR with the three-axis multi anvil press, the neutron guide, and the detector banks.

Construction of the detector frame and the detector shielding had to meet the requirement to keep the full positioning capability of SAPHiR in the x-y-z and rotation direction, while maintaining the relative position of the detectors to the sample throughout all movements. Thus, the detector frame was directly attached to the press and the frame for the much heavier boron PE shielding was attached to the positioning table to allow x-y-rotation positioning, while being supported on the floor by ball casters (Fig. 21). The biological shielding will be installed close to the sample inside the press to minimize large-scale shielding around SAPHiR.

Meanwhile, the three-axis press has been used for further development of the sample environment and to perform off-line experimental studies. The particularity of neutron diffraction requires a compara-

bly large sample volume of ca. 20 mm<sup>3</sup> as opposed to only ca. 1 mm<sup>3</sup> that is commonly used at high pressures and temperatures in the latest generation of three-axis presses. Hence, new larger sample assemblies were developed that contain sample capsules of size up to 3 x 4 mm. For heating, the sample assembly contains a Pt or Re metal foil furnace that is heated by thermal resistivity, and the temperature is controlled by a D-type thermocouple that is in contact with the top of the sample capsule. The new assemblies have been used and tested via off-line studies. As an example, Fig. 22 shows two polycrystalline olivine samples that have been deformed by pure shear at a strain rate of  $\sim 8 \times 10^{-7} \text{s}^{-1}$  for four days at 1300 °C and 1500 °C and at a pressure of  $\sim 8$  GPa. These experiments were performed to simulate the conditions of the earth at a depth of 200 - 300 km in order to understand the deformation



Figure 21: (left) View of the three-axis press before attachment of the detector frames. (middle) The stack of secondary anvils with the sample assembly is placed between the primary anvils before compression. (right) Installation of the detector frame and the instrument shielding for the left 90° detector bank.

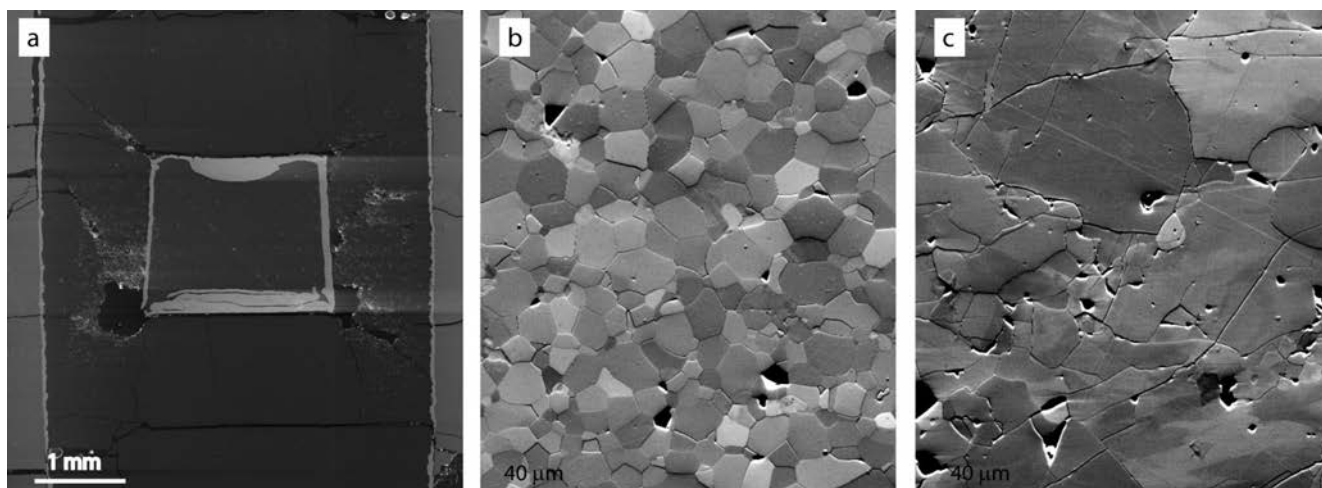


Figure 22: Scanning electron microscopy images of SAPHIR samples. (a) Section through an assembly after deformation showing a sample capsule in the centre and the vertical heating foil furnace on the outside. (b-c) Microstructure of polycrystalline olivine samples deformed at a strain-rate of  $\sim 8 \times 10^{-7} \text{ s}^{-1}$  at  $T = 1300 \text{ }^\circ\text{C}$  and  $1500 \text{ }^\circ\text{C}$ , respectively. Axis of compression is vertical; axis of extension is horizontal.

mechanisms and the seismic structure of the upper mantle, which requires long-term experimental stability under high P and T and a sub-micron precision of the anvil displacement. Future neutrons will allow measurement of the instantaneous strain rate during deformation by radiography, while the flow stress can be determined *in situ* by neutron diffraction as a function of other parameters such as temperature, water content, oxygen fugacity, pressure, and chemical composition.

#### Development and test of a neutron guide system for ultracold neutrons for the future UCN source at the FRM II

Ultracold neutrons (UCN), neutrons with energies on the neV scale, are unique probes for testing our actual understanding of particle physics and the universe. Destined to play a leading role in the worldwide UCN business in future, important projects, e.g. the development of a powerful UCN source and the installation of flagship experiments such as the nEDM and n-lifetime, began some time ago at the FRM II in collaboration with the universe cluster and the department of physics. In order to achieve the highest performance within these projects, dedicated neutron optical devices for the UCN transport, storage, polarization and detection are mandatory. Since 2012, a unique sputtering infrastructure has been established at the Maier Leibnitz laboratory (Coulombwall 6). Beginning in 2013, these coating facilities allow the upcoming fundamental neutron community at the MLZ to develop and produce requested UCN and cold neutron optics and hardware in-house.

#### UCN guide development

At various institutes around the world, ultracold neutron sources of high intensity are currently under construction or in the commissioning phase. Neutron guides connecting the UCN production or intermediate storage volumes and the experiments are among crucial components that need to be developed, produced and tested for these sources. The world's largest UCN guide, located in the guide hall east, which will deliver UCN from the powerful FRM II UCN source to future experiments will have an overall length of 28 m and an inner diameter of 115 mm. The transport of UCN over such long distances in standard UCN guides made from polished stainless steel tubes is associated with significant losses of UCN ( $>$  factor of 20). In addition, long guides act as an intermediate storage volume and therefore storage losses resulting from material choice, slits, surface contamination and poor vacu-

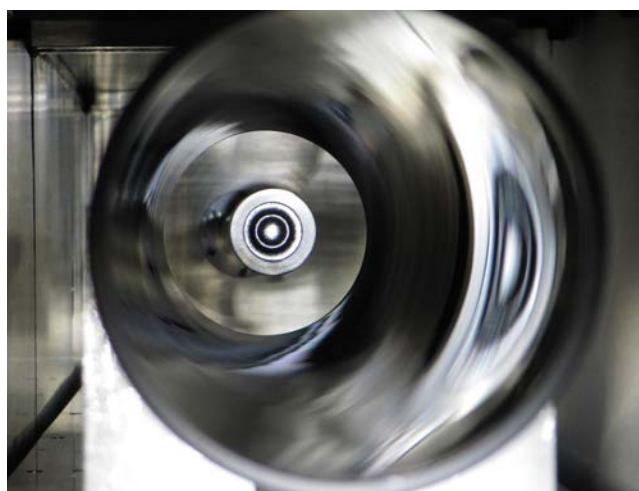


Figure 23: View inside of the UCN guide sputtering facility after completing a 1.5 m guide element.



Figure 24: Hands on the first 1.5m long UCN guide element produced at the MLZ.

um conditions are of great importance. In order to obtain the best performance for the Munich UCN source, we became interested in two different guide concepts, both dealing with a decrease in surface roughness. Some first guide prototypes successfully passed tests at the ILL. The first guide concept which is commercially available uses the so-called replication technique. Float glass with a minimal roughness of a few angstrom is coated on one side with a material of high neutron optical wall potential e.g. Nickel or its nonmagnetic compounds. Following galvanic reinforcement of this layer, a self-sustaining sheet can be peeled off from the substrate, resulting in a perfect copy of the glass surface. Starting with optimal parameters of 99 %/m in transmission (2011) for guides produced from these sheets, further tests showed some degradation in performance, finally reaching a transmission of 97 %/m (2013). At the same time, UCN guides produced from glass tubes coated inside with various nonmagnetic Ni compounds were investigated. Notwithstanding its lower cost, this guide technique delivered similar performance. Based on these results and the existing know-how, a dedicated and unique UCN guide coating facility was developed and built. With its total length (vacuum chamber) of 3.6 m, tubes with a maximal length of 1.6 m and a maximal outer diameter of 200 mm can be coated inside with almost all common materials used in neutron optics. As the FRM II is located in the industrial environment of Munich (glass tube supply) and with the great support of the neutron optics group at the facility, dedicated UCN guide components such as UCN guides bent up to 90° and UCN beam splitters can also be produced. In order to test the performance of a future UCN

guide system for the FRM II, a full sized UCN guide system of 17 m (10 UCN guide segments with a length of 1.5m with additional bends) was produced and transported to UCN turbine PF2 at the ILL in Grenoble (France).

#### UCN guide characterization with UCN at the ILL

The first experimental test of the largest UCN guide system worldwide was performed during a UCN beam time in June/July 2014 using ultracold neutron from the Pf2 port "Testbeam". In various experimental arrangements, including time of flight and storage measurements both with the complete guide system and single guide segments, the preferred glass guide idea was able to be characterized in detail. Following a first analysis, the huge amount of data collected successfully proved the expected functionality of the guide concept. In addition, it was possible to demonstrate the reproducibility in the guide production quality by measuring each single element.

In time of flight mode, a UCN (50 - 190 neV) transmission of 32 % was measured for the whole guide system (see Fig. 25), resulting in a transmission per meter of (96 +/- 3)%.

A scientific article with a detailed description of the guide production, the experimental setup at the ILL, the analysis of the data and additional transport simulation is in progress.



Figure 25: FRM II UCN guide system installed at the UCN turbine exit "testbeam" (on the left, not visible in the picture). More than half of the 17 m long glass guide coated with NiMo was mounted 3.5 m above the floor. UCN traveling from the turbine exit through the guide are detected by a  $^{10}\text{B}$  coated CascadeU detector at the end of the guide (lower right corner).

Based on the results obtained, the implementation of the UCN guide system using coated glass tubes feeding the nEDM setup (guide hall east) with UCN from the FRM II solid deuterium source (guide length 28 m) would result in a total UCN flux of approximately  $2.0 \times 10^7$  UCN/s (factor of 3 less than at the SR6 exit).

### Upgrade of the positron beam facility and positron instruments at NEPOMUC

In addition to the spectrometers and the beam lines to the instruments, two main parts in particular – the NEPOMUC source itself and the positron remoderator – received an overhaul from which all attached positron beam instruments benefit.

The positrons, which are created and moderated in the platinum foils of the in-pile positron source, are extracted and accelerated by a set of different electric lenses floating on high voltage. Therefore, well-defined electrical potentials of the head section of the positron source are crucial for the positron extraction and beam formation. After ten years of operation, corresponding electronic components showed the first signs of deterioration in long-term stability during the last reactor cycle. For this reason, these parts were replaced by new computer controllable high voltage equipment and integrated into the central beam line control software. This al-

lows automatic optimization of the high voltage settings for positron beam transport. Hence, this option greatly facilitates the use of the primary positron beam at different energies for planned experiments e.g. at the open beam port.

The remoderation device of NEPOMUC enhances the brightness of the positron beam and hence permits positron experiments with high spatial or time resolution. The remoderator is based on the stochastic positron cooling in a W(110) single crystal and the reemission of thermalized positrons into the vacuum with discrete energy. Since the degenerated crystal used had been replaced, the crystal clamping system was also reconstructed mainly in order to account for two issues. First, higher temperatures can be achieved by flashing the crystal using newly designed current heating. This is required to increase the positron moderation efficiency by removing adsorbates from the crystal surface. Second, the system is now reusable for the test and application of promising new remoderating materials.

Since distortion-free transport of the remoderated positron beam is of prime importance, the existing magnetic field coils and their feed lines were rearranged. Furthermore, new magnetic correction coils, which are used for an optimized injection of the remoderated positron beam into the magnetic

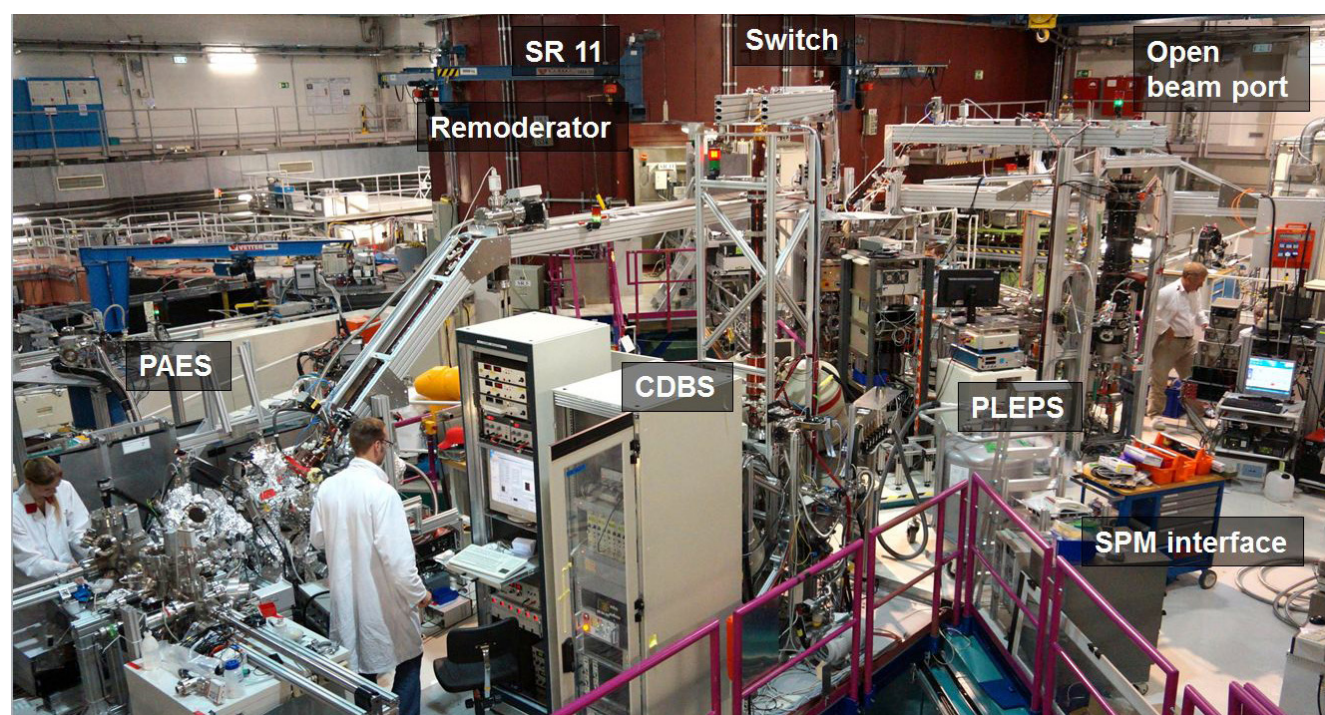


Figure 26: The Positron Source Nepomuc and its connected instruments in 2014.

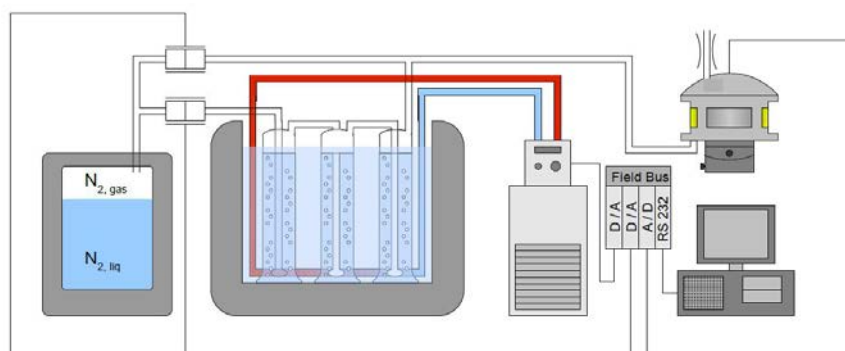


Figure 28: Liquid Nitrogen serves as gas reservoir. Arbitrary atmospheres are generated by a sensor controlled flux regulation of pure and saturated  $N_2$ . Chamber temperature is adjustable via the water bath. To keep environmental conditions at the sample position stable, a computer communicates and controls all components via a field bus.

guiding field, were mounted at the remoderator. As a result, the beam quality was enhanced and e.g. the entrance aperture at the Coincidence Doppler Broadening Spectrometer (CDBS) could be reduced again by a factor of four without losing counting rate. Therefore, the measurement time of experiments where a high spatial resolution is required could be reduced. At the Pulsed Low Energy Positron System (PLEPS) the benefits are comparable, but in the time domain. i.e. the timing resolution and, more importantly, the peak to background they could be further enhanced. In addition, the whole UHV system of the beamline and the positron instruments was maintained.

At the CDBS, new devices were installed in order to allow the variation of the distance between the high purity Germanium detectors and the sample as well as the positioning of two larger pixelated Germanium detectors. At the surface spectrometer, several parts have been replaced (e.g. a not well aligned linear feedthrough) or newly installed such as a new coolable and heatable sample stage, which allows the orientation of the sample with greatest accuracy.



Figure 27: The new monochromator drum and the neutron velocity selector at DNS.

### New monochromator shielding and velocity selector at DNS

Due to the increased neutron flux after the upgrade of the neutron guide sections at NL6 in 2013, the instrument upgrade at DNS was essentially oriented to the improvement of radiation shielding. During the long reactor shutdown period in 2014, a new monochromator drum with much-improved radiation shielding was installed. In addition, a neutron velocity selector was installed and successfully commissioned in the last reactor cycle in 2014. The DNS velocity selector allows the high-order contamination of the monochromatized beam to be suppressed. Alternatively, it can be used to switch from a certain incoming wavelength  $\lambda$  to  $\lambda/2$  without moving the secondary spectrometer.

### Controlled atmosphere conditions for NREX

To enlarge the field of investigation in soft matter at NREX and make use of the unique option of in-situ X-ray and neutron reflectometry at the same spot and at the same time, an arbitrary atmosphere generator is under development. The first major step, a stable controllable humidity, is already being implemented and demonstrated its performance at the end of 2014. Basically the generator mixes two adjustable streams of gases. Thus, for example, an arbitrary humidity (0 - 100 % r.h.) in the nitrogen atmosphere could be realised to within 1 % accuracy. Moreover, by mixing  $H_2O/D_2O$  in the gas wash bottles to certain ratios, SLD-contrast experiments are feasible. Adjustment of the desired relative humidity to within a minute range will be improved significantly by a redesigned sample cell with reduced dead volume. In addition, the available temperature range inside the new chamber will be adjustable between 10 - 60 °C by an external water bath thermostat. Beside humidity sensors, it is foreseen that the system will also work with ethanol, toluene, acetone and other sensitive gas-sensors. Thus, disjoining pres-

sure effects on thin soft films can be investigated routinely with neutron and X-ray reflectivity at NREX.

### Installation and successful test of a Fast Neutron Gamma-Ray Spectrometer at SR10

In 2014, an extension for the instruments MEDAPP and NECTAR became available at SR 10. It was developed within the framework of the **TransActinide Nuclear Data Evaluation and Measurement (TANDEM)** collaboration. The mobile gamma-ray spectrometer (Fig. 29) was installed for the first time at MLZ in November 2014. It is expected to investigate the inelastic-scattering reaction ( $n, n'\gamma$ ) of fission neutrons with an energy of 1.8 MeV with different sample nuclei. The so-called **Fast Neutron Gamma-ray Spectrometer (FaNGaS)** was developed at Forschungszentrum Jülich by the department of Nuclear Waste Management and Reactor Safety within the framework of the TANDEM collaboration with the aim of obtaining inelastic-scattering cross sections for the non-destructive investigation and quantification of actinides in radioactive waste. In the decommissioning of nuclear installations, a detailed knowledge of the enclosed actinides is especially important in order to allow for the safe treatment and storage of those materials.

Last November the necessary infrastructure, which contained massive shielding comprising different materials (Fig. 30) against neutron and gamma radiation was transported to MLZ and assembled in the bunker of the MEDAPP instrument. The first step was to determine the efficiency of the gamma spectrometer using radioactive sources. To extend the calibration spectrum to energies of up to 9 MeV,

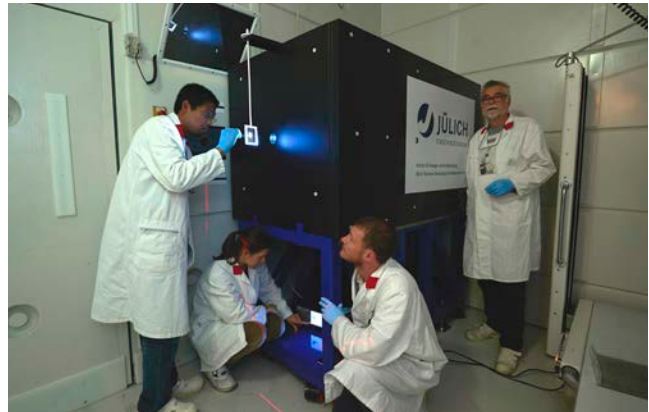


Figure 29: Matthias Rossbach (from right to the left) with Stefan Söllradl, Petra Kudejova and Tsitohaina Randriamalala during the fine tuning of the gamma-ray spectrometer.

prompt gamma-ray activation measurements were first performed with a thermal neutron beam. Optimization of the shielding around the detector and collimator resulted in the improved detection power of prompt and delayed emitted gamma radiation. Due to the high room background from scattered neutrons and generally small interaction cross sections of ( $n, n'\gamma$ ) prompt gamma reactions from metal foils need 10 to 12 hours of irradiation for most elements. Besides inelastic scattering, ( $n, p$ ), ( $n, \alpha$ ), and in some cases even ( $n, 2n$ ) product nuclei can be registered in the decay spectra of the irradiated materials. Using these reactions for a detailed energy and flux evaluation of the actual neutron beam, important reaction cross sections of other samples will be determined and gamma emission rates calculated. In particular, these data will be determined for some important actinides such as  $^{238}\text{U}$ ,  $^{232}\text{Th}$ ,  $^{237}\text{Np}$ ,  $^{242}\text{Pu}$  or  $^{241}\text{Am}$  to develop non-destructive tools for analysis of these isotopes in nuclear waste and residues from dismantling activities.

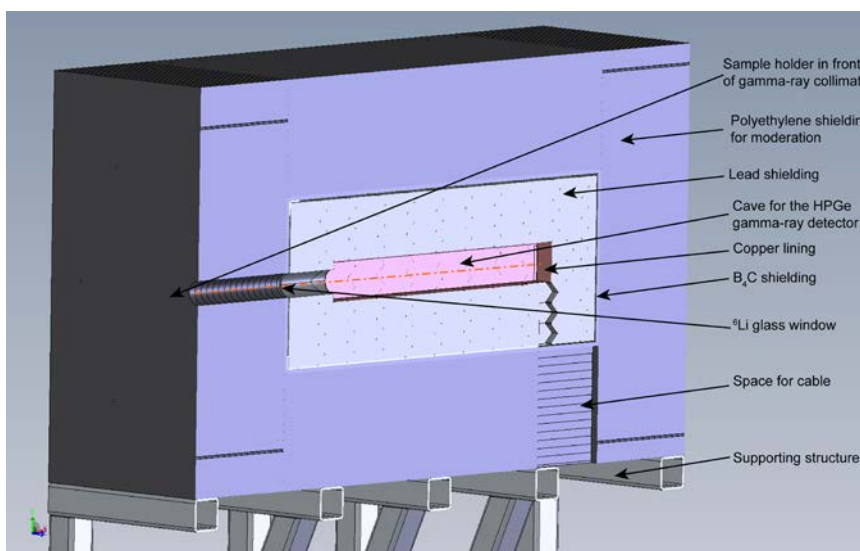


Figure 30: Schematic sketch of the sandwich construction, used in the FaNGaS setup. Of particular importance is the large polyethylene shielding surrounding the detector to slow down fast neutrons before absorption in the boron shielding can take place.

## Beyond the instruments – laboratories and service groups

N. Arend<sup>2</sup>, K. Bingöl<sup>2</sup>, A. Kriele<sup>3</sup>, J. Krüger<sup>1</sup>, P. Link<sup>1</sup>, S. Masalovich<sup>1</sup>, J. Peters<sup>1</sup>, J. Pulz<sup>1</sup>, S. Pütter<sup>2</sup>, H. Reithmeier<sup>1</sup>, T. Schrader<sup>2</sup>, H. Wenninger<sup>1</sup>, J. Wuttke<sup>2</sup>, K. Zeitelhack<sup>1</sup>

<sup>1</sup>Heinz Maier-Leibnitz Zentrum (MLZ), Technische Universität München, Garching, Germany

<sup>2</sup>Jülich Centre of Neutron Science (JCNS) at MLZ, Forschungszentrum Jülich GmbH, Garching Germany

<sup>3</sup>German Engineering Materials Science Centre (GEMS) at MLZ, Helmholtz-Zentrum Geesthacht GmbH, Garching, Germany

Successful experiments require high-performance instruments. Equally important are the services that support the instruments offered by the MLZ central groups covering subjects such as detector development, sample environments, scientific computing, neutron optics, IT services, instrument control software and general infrastructure. Furthermore, a number of laboratories such as materials science, biology and thin film laboratories etc. may be accessed by the instrument users for particular sample preparation or characterization in connection with proposed experiments at the neutron instruments.

### Neutron Guides and Mirrors

A challenge arose in 2014 when the Neutron Optics Group had to move the whole of their equipment into new laboratories (Fig. 1) due to the demolition of the old building. Nevertheless, the production of neutron guide elements was continued. In total, more than 20 m of neutron guide was built. Besides elements belonging to the new cold neutron guide at SR4b, sections of NL1 were rebuilt within the ongoing program of guide replacement due to irradiation



Figure 1: The new neutron guide assembly workshop: Josef Weber working on a two channel neutron guide element.

aging. In addition, a fast replacement of damaged guide elements was needed at the beamline SR8a. The team operating the high-resolution neutron powder diffractometer SPODI reported a reduction in the neutron flux at the sample position. From August 2012 until January 2014, the neutron flux at SPODI had been gradually reduced by about 15 % (dependent on the wavelength), resulting in a corresponding increase in the exposure time required per a single diffraction pattern. A visual inspection of the supermirror coating of the SR8a neutron guide (self-supported, vertically divergent) close to the reactor polygon indicated serious radiation damage to the borofloat glass on the side-plates of the neutron guide. The situation required immediate intervention and, therefore, two segments (each 2 m long) resembling the previous design of the SPODI neutron guide (but using Boron free float glass) were manufactured by the neutron optics group at short notice. The exchange of the damaged neutron guide segments was accompanied by an optimization of the helium inlet scheme for the guide (carried out by the SPODI group). Due to these measures, the initial neutron flux at SPODI was fully recovered. The concept of a new neutron guide in a jacket tube was jointly proposed by the SPODI team, the Neutron Optics group and JCNS (ZEA-1), which eliminates the need to regulate the helium atmosphere in the guide by a gas handling system and guarantees its safer use by encapsulating the guide. The new neutron guide and its adjacent parts are now in the design phase.

Further, a number of instruments have been assisted in the optical alignment of their neutron guides, or in surveys of their instrument components during construction or instrument modification. The reinstallation of the beam splitter unit NL6-13 built by Swiss-Neutronics reopened the NL6-N neutron guide for the instrument MIRA-1. Using a higher m-value of the supermirror coating of the silicon wafers, which

mirrors the NL6-N beam out of the NL6 beamline, shorter wavelength neutrons, down to  $\lambda = 8 \text{ \AA}$ , have now become available at MIRA-1.

### Neutron beam polarization with $^3\text{He}$ Neutron Spin Filters

The newly installed instrument POLI (designed for experiments using polarized hot neutrons) was provided with polarized  $^3\text{He}$  gas on a regular basis. This instrument is expected to become the most frequent user of spin filter cells using polarized  $^3\text{He}$  gas at HELIOS, our  $^3\text{He}$  gas polarization facility. Moreover, in 2014, the neutron spin filter cells were also used at the instruments RESEDA, REFSANS and PUMA for experiments using neutron polarization analysis. At PUMA, for example, these cells ensured a high polarization of the primary neutron beam, which helped to perform an accurate (and successful) test of the new multi-analyzer system developed at PUMA.

The adiabatic fast passage (AFP) spin-flipper, previously developed by the Neutron Optics Group, was finalized and became a robust device which had, in the course of 2014, already been used for a number of different measurements. Currently, two AFP spin-flippers are available.

### The new high resolution detector of Stress-Spec

Besides the standard activities concerning the service and maintenance of neutron detectors installed at the MLZ scientific instruments, 2014 was characterized by the completion of an important long-term detector development program undertaken by the detector group:

The construction of a new high resolution 2D-position sensitive detector was completed and the detector installed for the first commissioning experiments at the materials science and engineering diffractometer Stress-Spec. The design of the Multiwire Proportional Counter with 250 mm x 250 mm active area (Fig. 2) is based on a concept developed within the "MILAND" Joint Research Activity of the NMI3 consortium within the framework program 6 of the EC and has as its aim a position resolution  $\Delta_{x,y} < 1.3 \text{ mm}$  (FWHM) in both directions. It is filled with a gas mixture of 4 bar  $^3\text{He}$  + 2 bar  $\text{CF}_4$ , which results in a detection efficiency  $\varepsilon \approx 70 \%$  for thermal neutrons.

The impact position of a neutron is determined by reading the individual charge induced on each of the 256 cathode wires stretched in both the x- and y-directions. The Time-over Threshold method is used to determine the individual charge collected on a wire. The impact position is obtained by using a Centre-of-Gravity algorithm and the total charge released per neutron event is obtained by summing up all charges on both cathode grids. Finally, the VME64x-based readout electronics delivers the "Energy" of the neutron event in 8-bit resolution, the x- and y-impact position in 10-bit resolution, respectively, and the impact time in 19-bit resolution (100 ns binning) in list mode.

The position resolution and linearity of the detector was investigated using a collimated beam of 4.73  $\text{\AA}$  neutrons at the TREFF testing beamline at MLZ. The incident neutron beam was collimated to 0.25 x 0.25 mm<sup>2</sup>. The detector was mounted on a precision x-y linear stage table and moved in small steps of 0.25 mm width in both directions for a fine scan and in steps of 100 mm when performing a rough scan. The position of the incident neutron was determined by using a Center-of-Gravity algorithm.

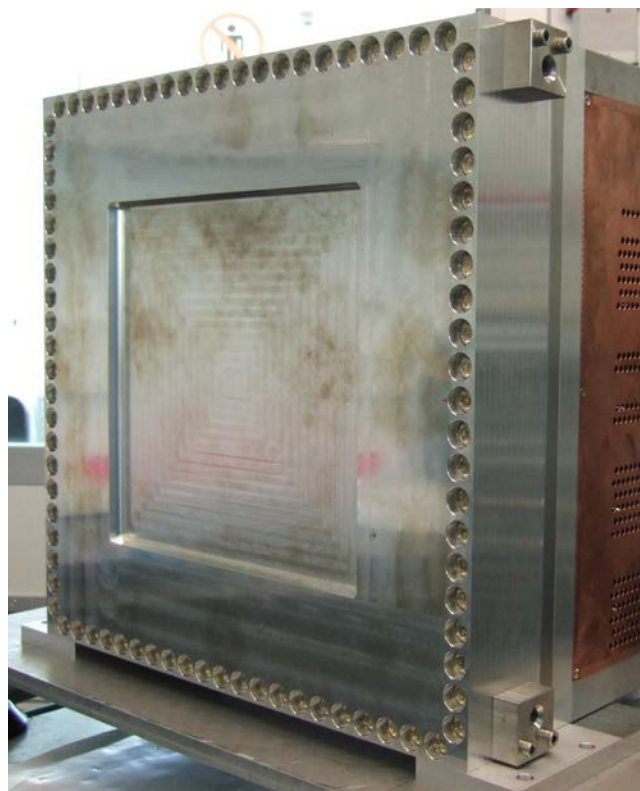


Figure 2: Front view of the new 250 mm x 250 mm active area MWPC for Stress-Spec with the 16 front end electronics modules mounted at the rear of the device in an EMV housing.

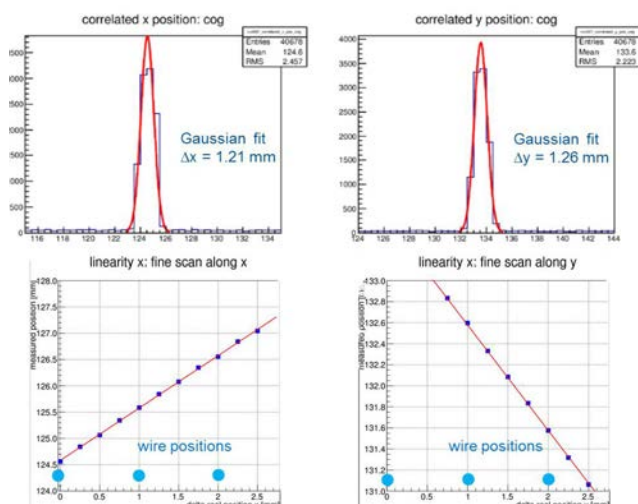


Figure 3: Top: Position spectrum of a collimated neutron beam in x- and y-coordinates determined with a Center-of-Gravity algorithm.

Bottom: Fine scan of the detector. Measured position of the incident beam versus the “true” position derived from the precision linear stage.

Figure 3 top shows the resulting position spectra for the x- and y-coordinate. Figure 3 bottom displays the measured impact position of the beam (peak position of the fit) as a function of the true position derived from the stepper motor of the precision linear stage for x- and y-coordinates. In both directions the detector reveals very good linearity.

In December 2014 the detector was mounted in its new detector housing at Stress-Spec and first commissioning experiments were successfully performed (see section on Stress-Spec of this report). It will be fully operational and available for users in the second reactor cycle.

### Magnets and low temperatures – News from the Sample Environment Group

A new cryogen-free Multi-Purpose-Magnet with a maximum field of  $H_{\max} = 2.2$  T, manufactured by HTS 110 New Zealand was delivered in early 2014 (Fig. 4). The acceptance test at FRM II revealed a performance exceeding its specifications. The magnet control rack was designed and manufactured by the SE Group.

The cryogen-free split pair magnet system operates with a coil set made of high temperature superconducting material. The coils are cooled by a powerful SHI SRDK 415 cold head manufactured by Sumitomo Cryogenics. The extremely compact magnet provides room temperature bores in all three spatial directions, one window with  $150^\circ$  horizontal and  $40^\circ$

vertical access and four conical windows with  $40^\circ$  horizontal and  $40^\circ$  vertical access. The magnet can be operated in arbitrary orientation, providing both vertical and horizontal operational field modes. The free sample volume equivalent to an 80 mm room temperature bore offers a broad range of different experimental applications such as low temperatures, high temperatures or pressure cells etc.

First user experiments have been successfully undertaken at the Instrument POLI. The low stray field of 5 mT at a distance of 1,8 meters allows for experiments using polarized neutrons. Some further work has to be done on embedding the system into the MLZ Instrument control software TACO.

To allow for temperatures down to 400 mK and bulky samples, a new bottom loading refrigerator (CC) operating with a  $^3\text{He}$  Joule-Thompson Stage has been developed. Experiments using gas pressure sample cells up to 0,4 GPa and down to 500 mK were performed at the instrument PANDA, which is equipped with a high pressure gas capillary (Fig. 5).



Figure 4: The new 2.2 T Multi-Purpose-Magnet.

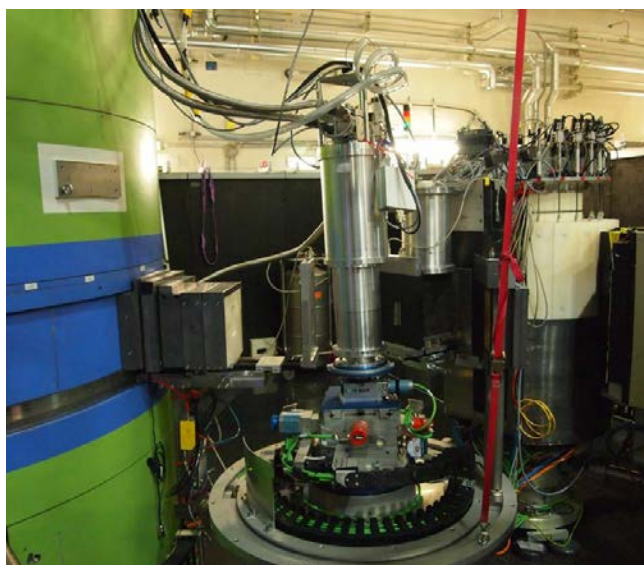


Figure 5: Experimental setup with the new bottom loading low temperature refrigerator at PANDA (Courtesy of Astrid Schneidewind).

### Project groups “Electronics” and “Engineering”

The project groups at the MLZ coordinate activities in the areas of instrument development, commissioning tasks, and technical service. They act as the interface between instrument scientists, technical support groups or companies, and management. The project groups cooperate mainly with the service groups for instrument control at MLZ and the Central Institutes for Engineering and Electronics (ZEA-1 and ZEA-2) of the Forschungszentrum Jülich GmbH in the fields of electronics and automation, neutron detectors, control software, and mechanical engineering.

The most notable projects in 2014 included

- Upgrading DNS
- New KWS-2  $^3\text{He}$  detector system
- Electromagnetic compatibility and interference (EMC/EMI)
- Instrument control software and code development platforms
- Shielding and selector modifications at KWS-3

The diffuse neutron scattering spectrometer DNS received a major upgrade that involved mechanical, electrical, and software components (Fig.6). To increase the neutron flux and instrument performance the neutron guide was replaced. As a consequence, the existing shielding was no longer sufficient and both monochromator area and flight path had to be redesigned and manufactured anew. In parallel, the instrument control software was relocated to NICOS and Tango. In October 2014, all mechani-

cal components were installed and commissioned by ZEA-1 and JCNS. The NICOS/Tango relocation will be completed in early 2015 in cooperation with ZEA-2. Furthermore, the electronics of the new PSD  $^3\text{He}$  detection system were successfully tested with the data acquisition software QMesyDAQ, which is used at MLZ in combination with MesyTec modules. The small angle scattering machine KWS-2 will receive a detector upgrade with a  $^3\text{He}$ -based system developed by General Electric/Reuter Stokes in cooperation with JCNS, ZEA-2, and the FRM II detector group. Specifications with respect to count rate performance, stability, electromagnetic compatibility, and mechanics had to be defined and discussed with the General Electric development team. In November 2014, a first prototype module (“8-pack”) was successfully tested and characterized at KWS-2 and TREFF.

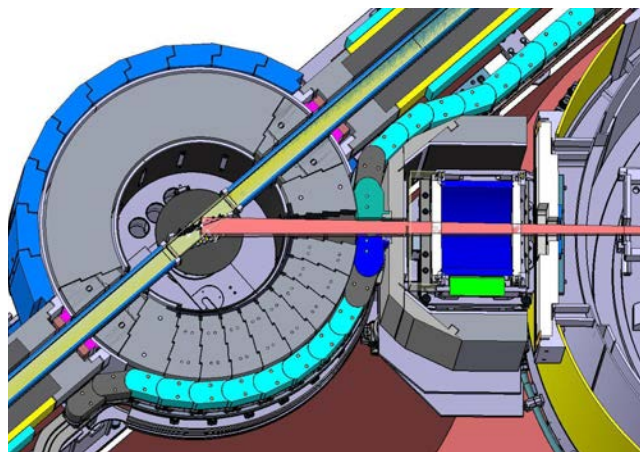


Figure 6: The newly designed shielding and flight path at the diffuse neutron scattering spectrometer DNS.

As a result of repeatedly observed noise and data corruption at several detector systems in the neutron guide hall west, a few years ago considerable effort was invested to understand and eliminate EMI issues at the MLZ instruments. In 2014 those efforts were intensified: a certified expert compiled an assessment of the EMC-relevant status of the new guide hall east, including grounding and electrical grid quality, as well as recommendations for infrastructure and instrumentation (in cooperation with JCNS, the MLZ project group electronics, and the electronics development group at DESY). In May 2014, a positively received workshop on EMC was held at MLZ to bring the necessity of a clean electrical environment to the attention of the instrument scientists and technical personnel.

Considerable progress was made in the area of software development and the closer integration of the team working, off-campus in Jülich, on the development process and platforms at MLZ. The project group and ZEA-2 were able to relocate two more instruments – BIODIFF and DNS – to NICOS, the common MLZ instrument control solution.

KWS-3 received an add-on to its selector system, which can now be tilted in order to reach smaller neutron wavelengths and extend the instruments' capabilities. Furthermore, in mid-2014, sliding radiation shielding was constructed and installed in cooperation with ZEA-1. This allows for significantly better access during maintenance.

### **NICOS – an ongoing success story for instrument control**

The success story of NICOS continues. Due to the modularity of the instrument control software, consisting of NICOS and various TACO/TANGO hardware device drivers, we were able to install the NICOS based instrument control system on the following four instruments:

- BIODIFF
- DNS
- NECTAR
- SANS-1

The power of the modularity of the instrument control was demonstrated in particular on the basis of the replacement of the NECTAR instrument control software. Due to the reuse of many existing TACO/TANGO servers and NICOS components, which are also used in the ANTARES instrument control software, the task was completed within a few days. Most of the remaining work to be done was confined to the installation and configuration of software components (TACO/TANGO servers and NICOS).

In addition to setting up these four instruments, a lot of work was carried out on improving the NICOS system, evident in the number of changes and contributions to the sources, amounting to 840 in 2014. At the MLZ, there are now in total 10 instruments running with the standard instrument control software NICOS in cooperation with TACO/TANGO servers.

Rolling out software is always a challenge that leads to a lot of manual work and sometimes unexpected

problems. Following the decision to use primarily Debian based Linux distributions such as Ubuntu or Linux Mint as the operating systems, it became obvious that it would be helpful to have our software in a Debian software repository. In this way, the installation of selected software components can be carried out very easily using the system tools.

Thus, the creation of a software repository was realized last year. We were therefore able to publish all our self-developed software, including the TACO/TANGO servers, in the form of directly installable software packages. This means that we are now able to install the necessary software in the standard way, while complying with the distribution rules. The benefit is an increase in the speed of software installation on the target machines. It is also more systematic and less error prone.

In the wake of these Debian packages, the software for the TACO boxes was also changed to a Debian based distribution in 2014.

The building of the packages as well as the updates of the TACO box software images can now be automated with the help of the productivity suite installed, consisting of a ticket system (Redmine), code review (Gerrit), and automatic testing and building (Jenkins).

Based on the experiences gained from our suite, we organized a workshop for the TANGO community to present the power of our work flow. The workshop was held on 23/24 July 2014 at the FRM II and enjoyed considerable success.

Together with the detector electronics group of the FRM II, support for the newly developed “Multi wire proportional chamber” was integrated into the QMesyDAQ software. The electronics was designed to support the same protocol as the Mesytec electronics to reduce the development effort. With the help of one of the new single board computers (CubieBoard which is comparable to a Raspberry Pi) the connection between the hardware from the detector electronics group and the QMesyDAQ software was realized. This development was successfully tested at the instrument Stress-Spec in December 2014.

Another project of the instrument control group was creating the specification for a unified interface for remote access to a PLC (programmable logic controller). At the moment, most of the interaction with a PLC is specific to the PLC and its programmer, leading to much effort being made to implement the techniques to access the PLC. To unify the access, a specification was elaborated that defines some device classes and their parameters, together with their addresses on the communication bus. This procedure allowed us to write a single TACO/TANGO device server, which can be reused by other projects through simple reconfiguration.

### Scientific Computing --- a European Endeavor

The Scientific Computing Group has deepened its international embedding by participating in the elaboration of workpackage 10, data treatment software, of the EU INFRADEV proposal SINE2020. Representatives of five European neutron facilities agreed to share the burden of software development by declaring each facility responsible for one software package, serving the needs of one large class of instruments (Table 1). Each facility will publish its software as open source. EU funding will be used to improve the software, especially in view of its use across facilities.

Technique	Software	Lead
Imaging	MuhRec&KipTool	PSI
Reflectometry & GISAS	BornAgain	MLZ
SANS	SASView	ESS
TOF & QENS	Mantid	ISIS
Atomistic modeling	nMoldyn, DFT	ILL

Table 1. Software to be further developed in WP10 of SINE2020.

The work already invested by the MLZ Scientific Computing Group in the development of a new software, BornAgain, for grazing-incidence small-angle scattering (GISAS) has been fully recognized: BornAgain will be the main contribution of MLZ to this workpackage, and will be extended to cover, in addition, conventional reflectometry and off-specular scattering.

### BornAgain: Software for grazing-incidence scattering

As already reported last year, the Scientific Comput-

ing Group is concentrating much of its resources into developing BornAgain, a software package to simulate GISAS experiments, and to fit one- and two-dimensional data sets. This software is intended to serve both in-house experimental analysis, such as those from the instruments MARIA and REFSANS, and the GISAS community at large, comprising neutron (GISANS) and X-ray (GISAXS) experiments.

This year, the development was mainly centered around three themes. First, a graphical user interface (GUI) was built to allow easier access to BornAgain's functionality. A beta version of this GUI was released in December 2014, and version 1.0 will appear at the beginning of 2015. Second, the simulation of polarized neutron scattering was added to the core of BornAgain. This new functionality, missing in established GISAXS software, is of critical importance for the analysis of scattering on magnetic systems, which forms a large part of the typical applications of our in-house reflectometers. Third, a final focal point consisted of elaborating good user documentation describing both installation issues and the program's features and usage.

The next steps will consist of finalizing the GUI, by exposing all existing functionality in the core library, and extending our documentation system with an easy-to-navigate website. A great deal of effort will also be dedicated to the analysis and simulation of experiments in which the computing group actively collaborates.

### Time-of-flight data reduction, MLZ data format

The other major project currently undertaken by the Scientific Computing Group is the support of time-of-flight spectrometers at MLZ. These instruments are TOFTOF, DNS, which are undergoing a major upgrade, and TOPAS (under construction). We need to offer MLZ users software for data reduction and analysis.

First, we had to define a new data format for TOFTOF and DNS. We thoroughly evaluated the much advertised neutron, X-ray and muon data format NeXuS, and even contributed substantially to a re-factoring of its documentation. We concluded, however, that NeXuS imposes impractical constraints that are not outweighed by any substantial advantage. The closer we looked into the details, the more

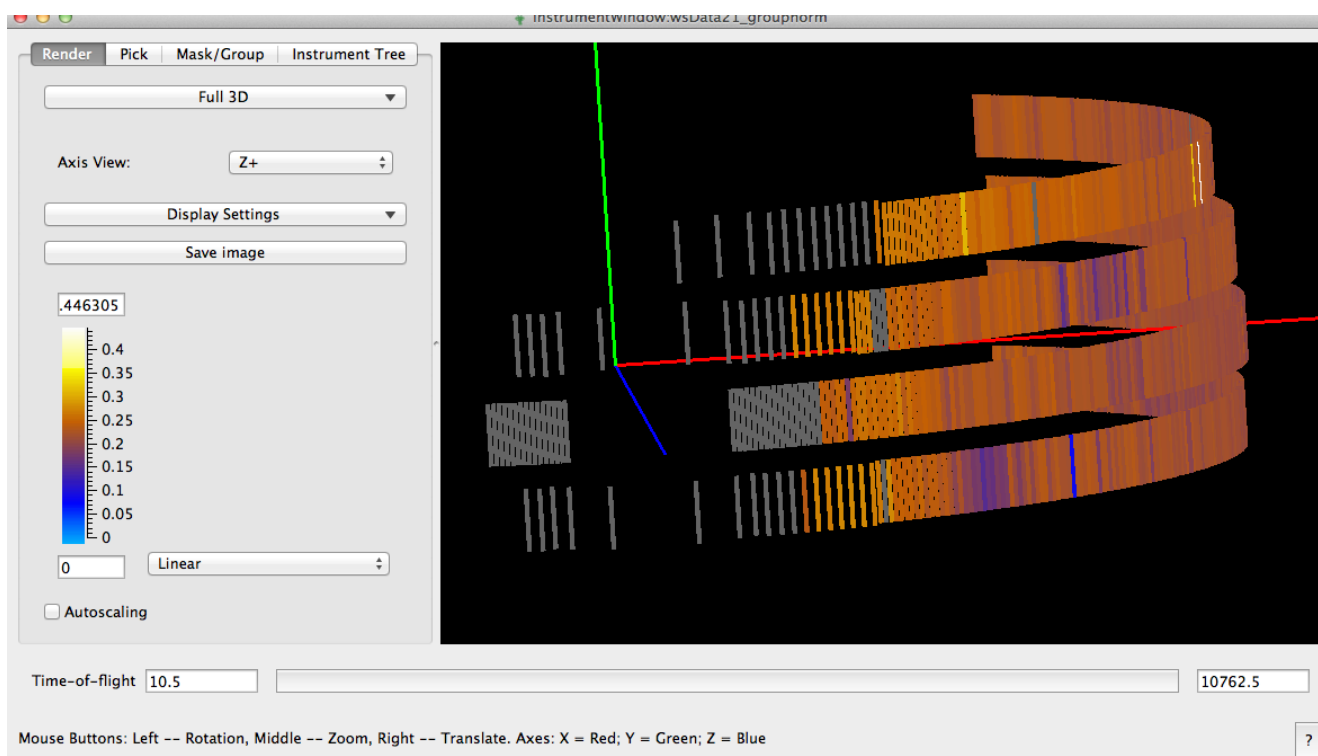


Figure 7: Mantidplot instrument view, displaying the detector geometry of TOFTOF.

improbable the promise that NeXuS make concerning the interoperability of raw data between different facilities. Instead, we decided to define a lightweight MLZ format, using the equivalent standard container formats JSON or YAML. Data exchange with other facilities will be supported by the NeXuS export functions, to be written as the need arises.

Within the framework of international cooperation, as described above, we follow the lead of the spallation sources ISIS and SNS in time-of-flight data reduction: we will adapt their software platform Mantid to our spectrometers. The Mantid project, which began in 2007, is indeed a major international collaboration involving a growing number of neutron and muon facilities. It is an open-source, multi-platform software. It offers a GUI as well as some scripting capabilities, three-dimensional plotting, fitting, and live data displays. It provides a framework to which users can contribute. In this way, more than 500 algorithms have been implemented.

To make Mantid work for our spectrometers, several pieces of software had to be written: scripts to generate instrument definition, files that describe the geometry of our instruments, and loaders that read our MLZ data format as well as the binary event-mode format of DNS as imposed by the detector electron-

ics. More surprisingly, we also had to develop algorithms for calibration and normalization because of subtle differences between the reactor and spallation-source instruments in data acquisition logic and raw data structure.

In close cooperation with those responsible for the TOFTOF instrument, we are currently testing the Mantid based raw data reduction, and validating it against legacy software (Fig. 7). In parallel, we are preparing for the forthcoming time-of-flight mode at DNS. All developments made now for TOFTOF and DNS will also serve TOPAS at a later date.

### News from the Software Group

For many years, the Organizational Software Group has been providing Software for staff and users of the FRM II / MLZ.

An important ongoing project of the group is the WKP-DoRIS application, which underwent a thorough overhaul. The new system was put into service in January 2014. This comprehensive software solution provides services for the operational division of the FRM II, which include the tracking of recurring checks (WKP) and the life cycle of the technical equipment.

One other part of DoRIS is Notifications of Changes (Änderungsanzeigen-DoRIS). Integration into DoRIS2 was the first attempt to manage the notifications of changes at the FRM. In 2014, this DoRIS module was modernized and currently its new release is underway. The new version of the system is better adapted to the current workflow experienced at the FRM II and provides user-friendly tools, e.g. for locking, releasing and changing notifications.

Although the Radiation Tracking Database used by the Radiation Protection Group represents comprehensive software which has already been successfully launched, an improvement on this system is required, as in recent times the need for better manageability for workplace safety has evolved.

In February 2014, the former Account Management System was modified and re-released as a web project within the FRM II website. The Account Management System provides a user-friendly interface, which guides and supports users in tracking their orders and business trips.

Parallel to this, the development of a tool for the Administration Department was initiated. Both programs operate on the same data. The new tool is able to analyze complex search processes and provides a customizable user interface. The application was put into operation in May 2014 and has been upgraded since to include a business trip module. Today, most software of the software group (except web projects) is available for installation on the System Center („Angekündigte Programme ausführen“). The procedure for annual safety training was changed from watching an instructional film to a web-based system called UWEB. The users can now choose themselves when to do the training and get an email reminder when the training is due. The account management for safety training is integrated with the admissions office and the user office systems.

The user office system was expanded to include a sample tracker, which also allows the Radiation Protection Group to register and control samples which get activated during measurement.

### Replacing and extending – the IT service group at MLZ

As already stated in last year's annual report, there was an ongoing effort to get rid of almost all machines running Microsoft(R) Windows(R) XP. The deadline for this task was set for the end of April 2014 and was completed on time. Only a really small number of machines were left afterwards owing to highly specific soft- or hardware that is used by these systems. It's an ongoing challenge to search for solutions to further replace old machines, even highly specialized ones.

Early this year, we relocated all client computers to our newly set up and completely virtualized Terminal Server farm, as was announced last year. The relocation itself went pretty smoothly and the farm is serving our clients very well, providing good performance and easy access to the applications hosted. Over the last years, the demand for disk space has escalated due to the amount of data generated together with the growing number of employees and projects. To meet the requirements and for reasons of redundancy, we have put a completely new and extendable storage system into operation. The storage system itself consists of a disk processor enclosure with two redundant service processors. Additionally, this enclosure contains 25 fast SAS hard disks. Connected to the disk processor enclosure are two additional disk array enclosures, each equipped with 15 high capacity SATA hard disks. To provide access to the storage system, a completely redundant Fibre Channel based storage area network (SAN) was built up from scratch. The service processors of the storage system are each connected to the SAN via two links. All relevant servers are equipped with two Fibre Channel host bus adapters and connected to the SAN. The whole system is in productive operation and works flawlessly, giving high performance.

To extend the overall availability of wireless networks at MLZ, two redundant management controllers and a bunch of new Access Points were ordered. We plan to bring the management controllers into operation in early 2015. Access points that have already been installed will then be relocated to the controller based solution. All new Access Points will be mounted and put into operation during the remaining part of 2015.

### Infrastructure group

As one of several important milestones for the supply of neutrons to the new neutron guide hall east (UYM), construction work on the new connecting building between the experimental hall and UYM was completed in 2014 (see Fig. 8). The new connecting building is now awaiting the installation of the technical infrastructure, e.g. several cranes for the handling of heavy components (see Fig. 9).

A further important milestone, this time for the supply of thermal neutrons to the instruments planned to be operated at 3 neutron channels of beam line SR5 in the new neutron guide hall east, and will be the replacement of the existing Plug JMA05 by a new one provided with 3 neutron channels (see Fig. 10). This plug has a shutter function which provides the necessary shielding effect in the closed position and transports neutrons to the instruments in the open position. Presently, there is only one instrument (TRISP) operating at one of two channels available at beam line SR5 in the experimental hall. Planning to replace the plug JMA05 is a very demanding task, since its built-in position is close to the reactor core. It requires approval from the authorities and has to scrupulously respect radiologi-



Figure 8: Exterior view of the new connecting building from the north side.



Figure 9: Interior view of the new connecting building from the south side.

cal considerations during the replacement work and, also, for its subsequent disposal. Moreover, since the existing Plug JMA05 is not accessible for radiological measurements at present, all radiological aspects of the replacement work had to be evaluated by the application of Monte Carlo simulations.

The technical aspects of replacing the plug JMA05 commence with cold tests. The subsequent hot phase begins with the removal and partial disposal of the Instrument TRISP in order to free up the necessary working space. Only when the area in front of the beam tube SR5 has been cleared is it possible to proceed with the plug exchange (Fig. 11).

The existing plug JMA05 will be pulled out from the beam tube SR5 with the help of the one machine specially conceived for the purpose (SRWM). After that, the front part of the Plug will be covered with a dedicated shielding device. In this way, the plug will be accessible and it will be possible to dismantle it safely into two parts, so that each can be lifted us-



Figure 10: The new plug JMA05 with 3 neutron channels.

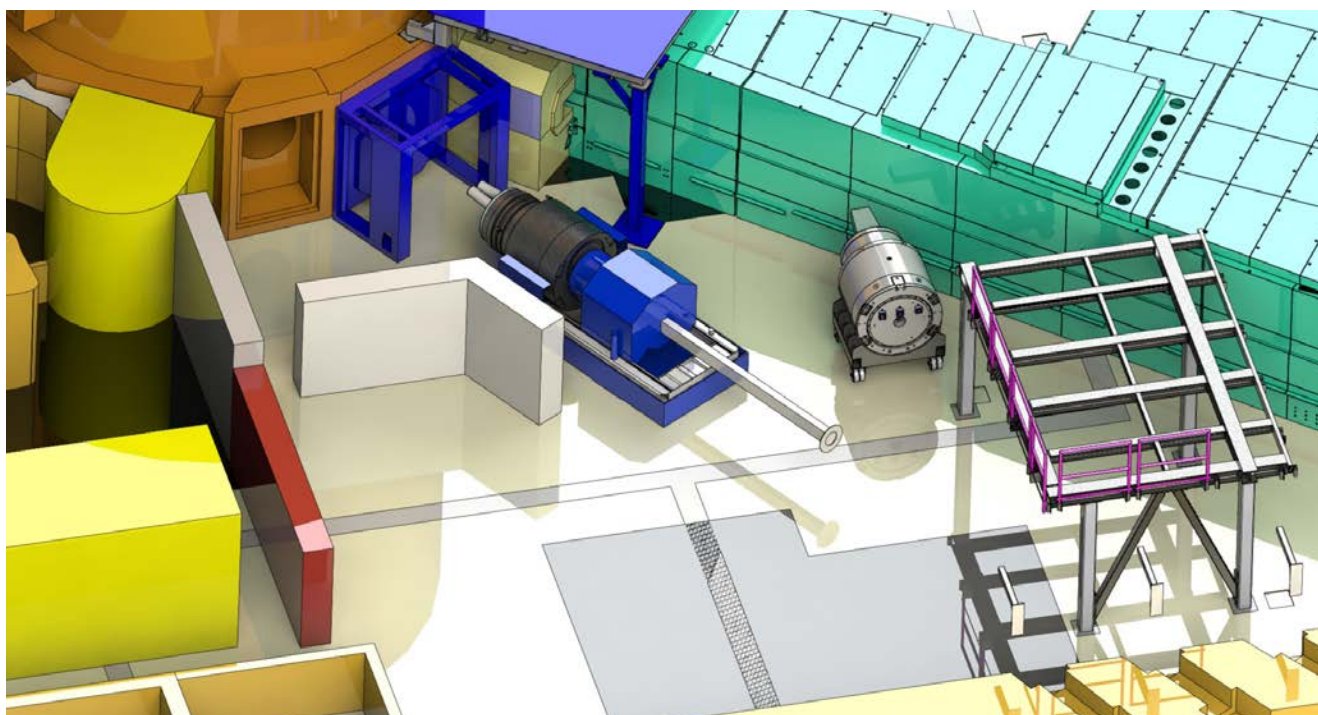


Figure 11: SR5 area with SRWM, shielding door, shielding device, radioactive plug JMA05 and the new plug JMA05.

ing the hall crane and handed over to the company entrusted with its disposal. After this, and again with the help of the SRWM, the new plug will be placed into the beam tube SR5 and, after tuning-work, will be fixed at its built-in position and connected to its driving and controlling systems. With final approval from the authorities, the new plug JMA05 can be put into operation.

An advanced project at the existing instruments in the neutron guide hall west (UYH) was the improvement of the cooling water system FAK-40 for these instruments. Here, the upgrade of the leakage mon-



Figure 12: Removal of the old concrete floor inside a dust cover to protect the vicinal instruments from dust released during the concreting work.

itoring system at these instruments was continued in 2014. The new system also comprises improved detection of possible leakages of the cooling water system and the instantaneous elimination of the leakage by closure of a gate valve, by measurement and recording of physical parameters of the cooling water (as e.g. pressure, temperature and flow rate) for failure analysis.

At the present time, all instruments situated on the northern side of UYH (and partially also on the southern side) are already equipped with the new leakage monitoring system. It is planned to continue the upgrades in early 2015 so that all instruments in UYH will be fully equipped with the new leakage monitoring system by July 2015.



Figure 13: The finished new granite floor for instrument KOMPASS.

An example of the realization of an instrument-specific requirement is the construction of a new granite floor in the neutron guide hall west (UYH). It was installed for the instrument KOMPASS in the experimental area to provide a strong, planar surface for easy movement of the heavy spectrometer components mounted on air-lubricated bearings.

For that, the old concrete floor had to be removed cautiously (see Fig. 12). The granite floor was then built-up out of massive granite slabs and finally polished carefully to fulfill the instrument's demanding planarity requirements. A picture of the completed granite floor is shown in Fig. 13.

### MBE system for thin film sample fabrication opened as user facility

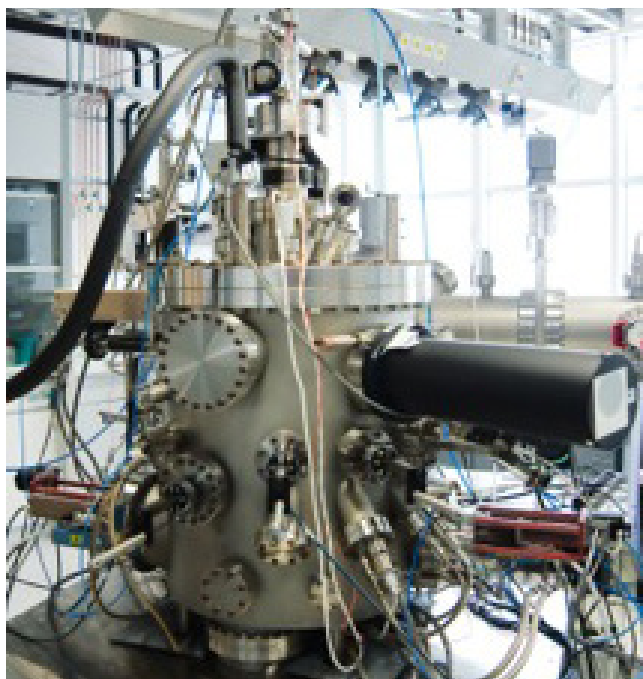


Figure 14: The MBE Setup.

To fabricate high quality metal and complex oxide thin film heterostructures such as e.g.  $\text{La}_{1-x}\text{Sr}_x\text{MnO}_3/\text{SrTiO}_3$  or Cu/Fe multilayers, the MBE system in the thin film laboratory is utilized (Fig. 14). Recently, it was opened to users and may now be accessed via the MLZ user office system in combination with application for beam time at neutron instruments such as MARIA or NREX.

Two access concepts are pursued: For remote access, the thin film laboratory scientist fabricates the sample. However, a prerequisite is that the laborato-

ry staff has already gained experience in fabrication of the desired material system. The second concept is collaborative access which means that the user fabricates the thin film sample with the on-site help of the thin film laboratory scientist. This type of access is necessary if research on the proper growth conditions for thin film preparation is required.

A crucial feature of the MBE system is script supported film growth. Once the fabrication procedure for the sample has been elaborated in detail, the MBE system may be operated via recipes to go through all fabrication steps automatically such as e.g. sample heating and shutter opening of evaporation sources. This ensures very high sample reproducibility. The recently installed LN<sub>2</sub> phase separator continuously supplies the MBE system with liquid nitrogen which enables automated sample fabrication over a long period.

### Brand-new X-ray Diffractometer for the Materials Science Lab

The Materials Science Laboratory is equipped with several analytic instruments, for instance X-ray Diffractometer (XRD), Differential Scanning Calorimeter (DSC), Micro-Hardness and Optical Microscopes to perform complementary analytics. In addition, it offers the possibility of preparing samples (polishing, cutting, etching and annealing) for subsequent neutron scattering measurements.

Since August 2014, the lab offers a brand-new Empyrean® X-ray Diffractometer from PANalytical (Fig. 15), mainly for battery research. In-situ XRD measurements of batteries in operando facilitate the investigation of effects during the charging and discharging of batteries under various conditions as well as the characterization of single battery components.

The instrument was co-financed by HZG and is therefore equipped with numerous options which cater for the high demand of the very varied requirements (phase and structure-analysis, thin film measurements, stress and texture) and the different types of samples (bulk, powder, alloys, polymers, thin films). Reflection- and Transmission measurements can be performed as well as Grazing Incident Diffraction. A high temperature vacuum chamber allows in-situ XRD analysis during the annealing of samples up



Figure 15: The new Empyren X-ray Diffractometer has been part of the Materials Science Lab equipment since August 2014.

to 1600°C, which is essential for high-performance materials such as Cobalt-Rhenium alloys used in gas turbines or memory shape materials such as Nickel-Manganese-Aluminium alloys.

With the reflection option of the XRD instrument, thin film properties such as thickness, roughness, crystallinity and stress can be analyzed. This is used, for instance, by the MLZ members of the MBE group as well as those from the UCN group to analyze their in-house fabricated Strontium-Titanate and Iron-Copper multilayer MBE thin films in addition to sputtered Nickel-Molybdenum-Titan films for Ultra Cold Neutron (UCN) super-mirrors, respectively.

The Differential Scanning Calorimeter DSC used for measuring phase-transition-temperatures and heat capacity, respectively, covers a temperature range from -180 °C up to 650 °C with an accuracy of +/- 0.05°. It has been mainly used to investigate soft materials such as di-block copolymers as well as hard materials such as AlFeNi and NiMnInCo-memory alloys and materials for new high density reactor fuels based on Uranium-Molybdenum (UMo) alloys. The Micro Hardness Tester makes it possible to measure the Vickers hardness of soft (e.g. polymers) up to hard materials (metals, alloys) in the range of 10 g – 10 kg (HV 0.1 – 10). It has been used, for example, to investigate the influence of nano-particle additives to dental composite materials and the effect of the subsequent UV- light hardening process with respect to the penetration depth and, therefore, to the degree of polymerization.

A high resolution digital optical microscope with considerable filter and contrast capabilities as well as

a digital stereo-microscope completes the analytical equipment of the lab.

Due to limited lab space, two instruments (Small Angle X-Ray Scattering SAXS, Laser Diffraction Particle Analyzer) have been outsourced to the TUM, Physics Department E13 on permanent loan. MLZ members still have access to these instruments.

### New sample characterization techniques available in the Biology lab of MLZ

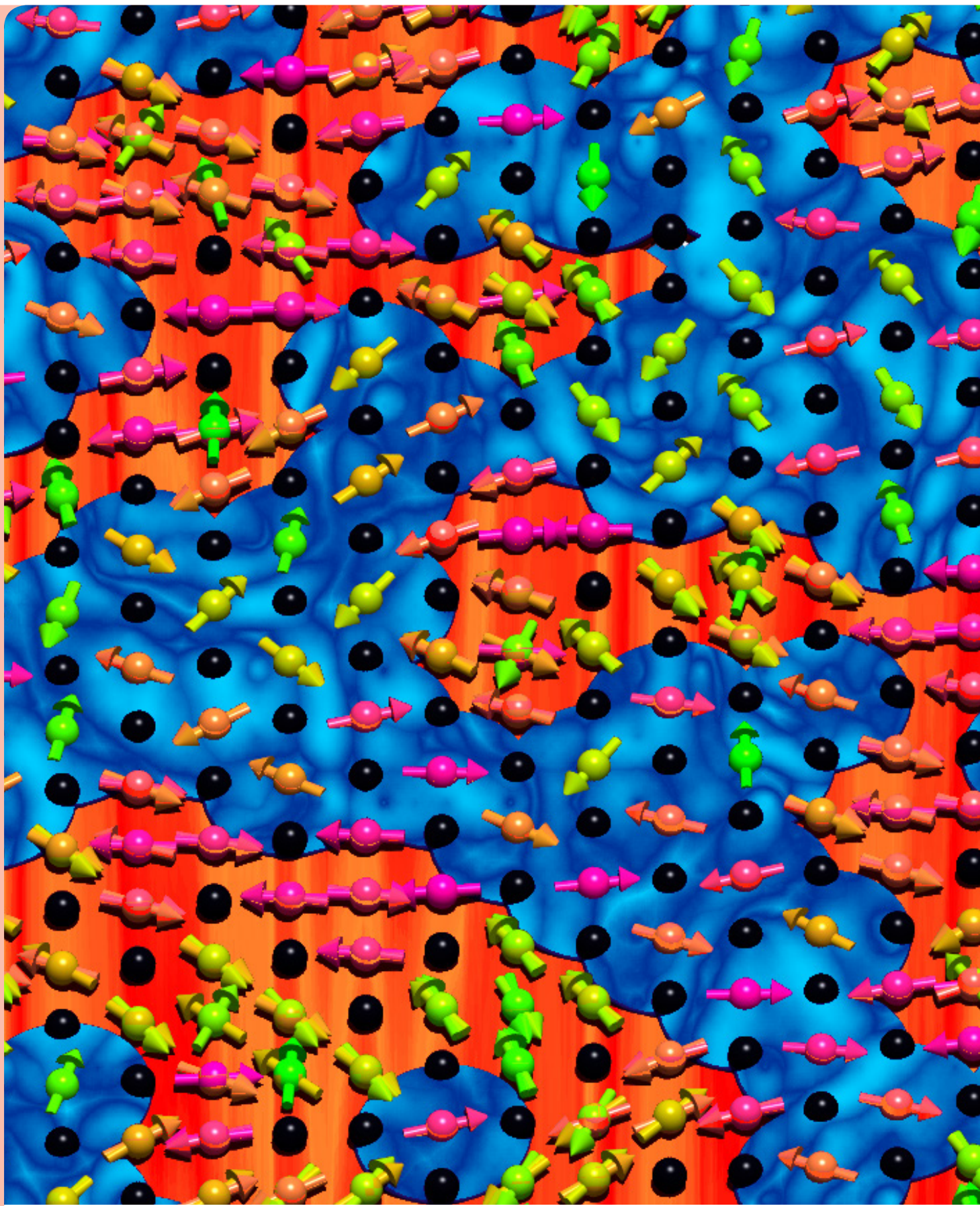
The biology Lab of the MLZ offers several techniques for the preparation and characterization of biological or soft matter samples. Recently, a UV-visible spectrometer Nanodrop from the company Thermo Scientific was added to the suite of instruments which can also be used in the neutron guide hall close to the small angle scattering instruments. This allows the sample concentration to be controlled using their light absorption finger print. Another valuable method for sample pre- and post-characterization is dynamic light scattering. Figure 16 shows the newly installed Malvern Zetasizer Nano S instrument connected to a lap-top computer in the biology lab. It allows the measurement of hydrodynamic radii in the range of 1 nm to 6 µm. It can also be brought to the neutron guide hall close to the instruments.

The web page of the Biology lab is currently under construction to include more detailed information on the available instruments and their manuals. A recent picture is provided for each instrument as well as a short version of the manual and a sample measurement. It is also indicated whether the instrument can be used in the guide halls and whom to ask in order to arrange for that via e-mail prior to the beam time.



Figure 16: Picture of the Malvern Zetasizer Nano dynamic light scattering instrument. It can be operated from a lap-top computer.

Charge distribution with nanostructure: In a cobalt oxide crystal Max Planck researchers found two different zones in the nanometer range, which are rich (blue) or poor (red) in charge carriers, respectively. At the same time, they investigated the magnetic correlations in this material using neutrons with the instrument PUMA. The arrows and colours reflect the orientations of the electron spin or magnetic moments of the individual atoms.



# Scientific Highlights

# Nematic spin correlations in the tetragonal state of uniaxial strained $\text{BaFe}_{2-x}\text{Ni}_x\text{As}_2$

X. Lu<sup>1</sup>, J. Park<sup>2</sup>, R. Zhang<sup>1</sup>, H. Luo<sup>1</sup>, A. H. Nevidomskyy<sup>3</sup>, Q. Si<sup>3</sup>, P. Dai<sup>3,1</sup>

<sup>1</sup>Institute of Physics, Chinese Academy of Sciences, Beijing, China

<sup>2</sup>Heinz Maier-Leibnitz Zentrum (MLZ), Technische Universität München, Garching, Germany

<sup>3</sup>Department of Physics and Astronomy, Rice University, Houston, USA

Understanding the microscopic origins of electronic phases in high-transition temperature (high- $T_c$ ) superconductors is important when it comes to elucidating the mechanism of superconductivity. In the paramagnetic tetragonal phase of  $\text{BaFe}_{2-x}\text{T}_x\text{As}_2$  (where  $T$  is Co or Ni) iron pnictides, an in-plane resistivity anisotropy has been observed. Here, we use inelastic neutron scattering to show that low-energy spin excitations in these materials change from fourfold symmetric to twofold symmetric at temperatures corresponding to the onset of the in-plane resistivity anisotropy. Because resistivity and spin excitation anisotropies both vanish near optimal superconductivity, we conclude that they are likely to be intimately connected.

## Electronic nematic state in iron pnictides

Correlated electron materials such as high temperature superconductors harbour various exotic properties driven by electron correlations. One of them is the electronic nematic phase in iron pnictides [1]. A nematic phase was proposed to describe a state of cigar-shaped molecules in liquid crystal in which the molecules have no positional order, but their long axis is preferentially aligned in one direction, as shown in Fig. 1(a). Molecules in nematic phase can flow like a liquid. Meanwhile, they form a symmetry broken (anisotropic) pattern like that of crystal. Thus, the nematic phase can be viewed as an intermediate state between an isotropic liquid and a highly ordered crystal in view of the broken symmetry. The nematicity in iron pnictides was first discovered as in-plane resistivity anisotropy in  $\text{Ba}(\text{Fe}_{1-x}\text{T}_x)_2\text{As}_2$  ( $T = \text{Co}, \text{Ni}$ ). An example is shown in Fig. 1(b). This anisotropy indicates that electrons transport much more easily in one direction ( $a$  axis) than the other ( $b$  axis), even in the case of the tetragonal state of uniaxial-stress detwinned sample (Fig. 1 (b)). This

nematicity was also discovered as a splitting of  $d_{xz}$  and  $d_{yz}$  orbitals in the uniaxial-strain detwinned samples at a temperature above  $T_s$  [2]. It has been generally believed that the nematic phase is driven by a certain electronic degree of freedom such as charge/orbital fluctuations and spin fluctuations [3]. However, it has also been explained as arising from the anisotropic scattering of Co dopants rather than intrinsic properties of the system [4].

## Nematic spin correlations in $\text{BaFe}_{2-x}\text{Ni}_x\text{As}_2$

In the antiferromagnetically (AF) ordered state of a detwinned sample, magnetic Bragg peaks and low energy spin waves should occur at  $Q = (\pm 1, 0, L)$  ( $L = \text{odd}$ ). By contrast, in the paramagnetic tetrago-

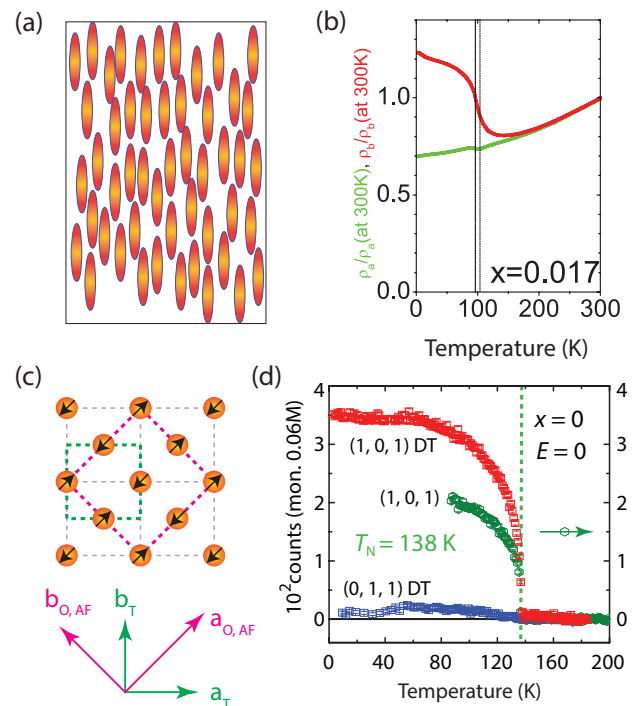


Figure 1: (a) Schematic of nematic phase in liquid crystal. (b) Resistivity anisotropy in uniaxial-stress detwinned  $\text{Ba}(\text{Fe}_{1-x}\text{Ni}_x)_2\text{As}_2$  ( $x = 0.017$ ) [6]. (c) The collinear C-type AF structure in the Fe plane. The green dashed box marks the tetragonal unit cell in the paramagnetic state and the magenta dashed box indicates the orthorhombic magnetic unit cell. (d) Magnetic Bragg peak intensity at the  $(1,0,1)$  and  $(0,1,1)$  positions for the  $\text{BaFe}_2\text{As}_2$  at zero pressure (green) and  $P \sim 15$  MPa uniaxial pressure along the  $b_0$  axis.

nal phase ( $T > T_s \geq T_N$ ), one would expect the spin excitations at the  $(\pm 1, 0)$  and  $(0, \pm 1)$  positions to have equal intensities. This dictates a symmetry change from  $C_4$  to  $C_2$  of the spin excitations in a detwinned sample across  $T_s$  and  $T_N$ , similar to resistivity. Thus, temperature dependence of the difference between spin excitations at  $(1, 0, 1)$  and  $(0, 1, 1)$  across  $T_N$  and  $T_s$  can conclusively determine whether there are nematic spin correlations in the tetragonal state. Searching for nematic spin correlations above  $T_N$  will be significant for understanding the origin of the nematic phase [3].

By carrying out a series of inelastic neutron scattering experiments on uniaxial-strain detwinned annealed  $\text{BaFe}_{2-x}\text{Ni}_x\text{As}_2$  ( $x = 0$ ,  $T_N = 138$  K, underdoped  $x = 0.085$ ,  $T_c = 16.5$  K,  $T_N = 44$  K and overdoped  $x = 0.12$ ,  $T_c = 18.6$  K) samples using the thermal triple-axis spectrometer PUMA, we have discovered nematic spin correlations in the tetragonal state.

Fig. 2(a) shows the temperature dependence of the spin excitations (signal above background scattering) across  $T_N$  and  $T_s$ . In the AF ordered state, we see only spin waves from the wave vector  $(1, 0, 1)$ . On warming to the paramagnetic tetragonal state above  $T_N$  and  $T_s$ , we see clear differences (nematic spin correlations) between  $(1, 0, 1)$  and  $(0, 1, 1)$  that vanish above 165 K, well above  $T_s$ , the same temperature below which anisotropy is observed in the in-plane resistivity. We conclude that the four-fold to two-fold symmetry change in spin excitations in  $\text{BaFe}_2\text{As}_2$  occurs alongside the resistivity anisotropy. To compare nematic spin correlations with resistivity data, we summarize our INS experiments on uniaxial strain detwinned  $\text{BaFe}_{2-x}\text{Ni}_x\text{As}_2$  in Fig. 2(b). The square red symbols indicate the temperature below which spin excitations at an energy transfer of  $E = 6$  meV exhibit a difference in intensity between the  $(\pm 1, 0)$  and  $(0, \pm 1)$  positions for undoped and electron underdoped  $\text{BaFe}_{2-x}\text{Ni}_x\text{As}_2$ . For electron overdoped  $\text{BaFe}_{1.88}\text{Ni}_{0.12}\text{As}_2$ , the same uniaxial pressure has no effect on spin excitations at wave vectors  $(\pm 1, 0)$  and  $(0, \pm 1)$ . As shown in Fig. 2(b), the resistivity anisotropy occurs near the spin excitation anisotropy temperature  $T^*$  determined from INS, indicating that the nematicity revealed by resistivity anisotropy is an intrinsic property and may have the same origin as nematic spin correlations. Our results revealed nematicity in the spin-excitation chan-

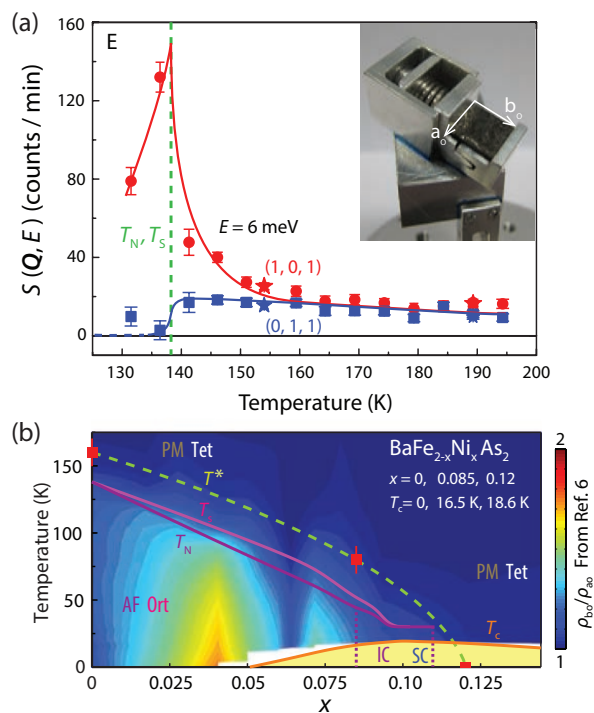


Figure 2: (a) Temperature dependence of the spin excitations at  $E = 6$  meV for  $(1, 0, 1)$  and  $(0, 1, 1)$ . The anisotropy in spin excitations vanishes around  $T = 160 \pm 10$  K. Inset: Detwining device mounted on the supporting sample holder. Uniaxial pressure can be applied by a steel spring driven by a screw. (b) The electronic phase diagram of  $\text{BaFe}_{2-x}\text{Ni}_x\text{As}_2$  from resistivity anisotropy ratio  $\rho_{b0}/\rho_{a0}$  obtained under uniaxial pressure [6]. The spin excitation anisotropy temperatures are marked as  $T^*$ .

nel and shed light on our understanding of the origin of nematic phase in iron pnictides. For detailed discussions, see ref. [5].

### Experiments at Puma

The success of the experiments presented depends on the high flux and excellent performance of the PUMA thermal-triple axis spectrometer. The configuration of the sample is shown in the inset of Fig. 2(a). In all experiments, horizontally and vertically curved pyrolytic graphite (PG) crystals were used as a monochromator and analyzer. To eliminate contamination from epithermal or higher-order neutrons, a sapphire filter was added in front of the monochromator and two PG filters were installed in front of the analyzer. All measurements were carried out with a fixed final wave vector,  $k_f = 2.662 \text{ \AA}^{-1}$ .

- [1] J. Chu et al., *Science* 329, 824 (2010).
- [2] M. Yi et al., *Proc. Natl. Acad. Sci. U.S.A.* 108, 6878 (2011).
- [3] R. Fernandes et al., *Nature Phys.* 10, 97 (2014).
- [4] S. Ishida et al., *Phys. Rev. Lett.* 110, 207001(2013).
- [5] X. Lu et al., *Science* 345, 657 (2014).
- [6] I. Fisher et al., *Rep. Prog. Phys.* 74, 124506 (2011).

# Real space description of excitations in $\text{SrCu}_2(\text{BO}_3)_2$ and spectral line shape at low temperatures

M. E. Zayed<sup>1,2,3</sup>, Ch. Rüegg<sup>3,4,5</sup>, Th. Strässle<sup>3</sup>, U. Stuhr<sup>3</sup>, B. Roessli<sup>3</sup>, M. Ay<sup>3</sup>, J. Mesot<sup>3,6,7</sup>, P. Link<sup>8</sup>, E. Pomjakushina<sup>9</sup>, M. Stingaciu<sup>9</sup>, K. Conder<sup>9</sup>, H. M. Rønnow<sup>2</sup>

<sup>1</sup>Department of Mathematics, Statistics and Physics, College of Arts and Science, Qatar University, Doha, Qatar

<sup>2</sup>Laboratory for Quantum Magnetism, École Polytechnique Fédérale de Lausanne (EPFL), Lausanne, Switzerland

<sup>3</sup>Laboratory for Neutron Scattering and Imaging, Paul Scherrer Institute, Villigen PSI, Switzerland

<sup>4</sup>DPMC-MaNEP, University of Geneva, Geneva, Switzerland

<sup>5</sup>London Centre for Nanotechnology and Department of Physics and Astronomy, University College London, London, United Kingdom

<sup>6</sup>Laboratory for Neutron and Synchrotron Spectroscopy, École Polytechnique Fédérale de Lausanne (EPFL), Lausanne, Switzerland

<sup>7</sup>Laboratory for Solid State Physics, ETH Zürich, Zürich, Switzerland

<sup>8</sup>Heinz Maier-Leibnitz Zentrum (MLZ), Technische Universität München, Garching, Germany

<sup>9</sup>Laboratory for Developments and Methods, Paul Scherrer Institute, Villigen PSI, Switzerland

**W**e explain the anomalous temperature dependence observed in magnetic excitations of the layered  $S = \frac{1}{2}$  2D quantum magnet  $\text{SrCu}_2(\text{BO}_3)_2$  via a simple model we have called ‘correlated decay of triplet excitations’. Triplet excitations in this frustrated spin system tend to remain localized and extend over several dimers. Using inelastic neutron scattering, we establish that these triplets are long lived when, in real space, they occur away from other triplets and decay rapidly when they overlap. The model quantitatively explains the previously elusive line shape and intensities of the excitations at finite temperature as well as their change with magnetic field as was measured on the PANDA spectrometer at MLZ.

## Inelastic neutron scattering experiments

Q-dependent triple axis measurements at zero field were performed on the TASP spectrometer at SINQ, PSI Switzerland, with 8 g single crystals and a fixed final neutron energy of 3.0 meV. The  $H = 8$  T INS measurements were obtained at the high flux triple axis spectrometer PANDA at MLZ, Garching, Germany, with a 3 g single crystal mounted in a 15 T cryomagnet with a and b axes in the scattering plane and  $H$  parallel to the c-axis. The spectrometer was operated at a fixed final neutron energy 5.0 meV with double focusing monochromator and horizontally focusing analyzer.

## Excitations at low temperature

$\text{SrCu}_2(\text{BO}_3)_2$  has been considered a model quantum magnet for the study of frustrated spin systems, as

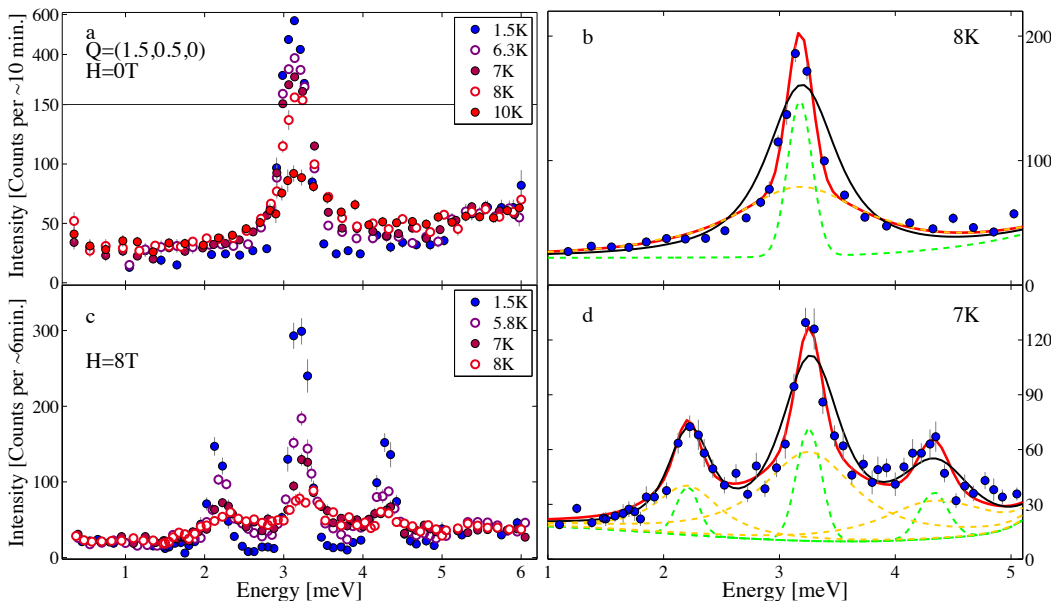


Figure 1: INS spectra at  $Q = (1.5;0.5;0)$  measured on a single crystal sample. (a) Zero field, (TASP). (b)  $T = 8$  K with fits: the red line is the total fit function consisting of a sharp component in green and a broad component in orange. The black line is a fit to a single DHO which fails to match the data. (c)  $H = 8$  T, (PANDA). (d)  $H = 8$  T at  $T = 7$  K, with fit lines as in (b). The DHOs are convolved with the instrument resolution.

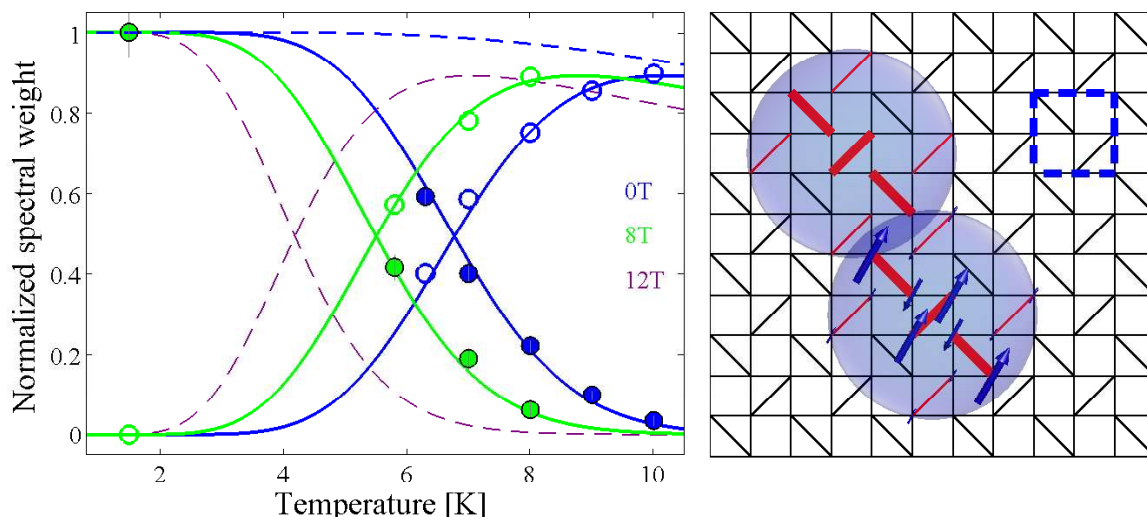


Figure 2: Left: Intensities of the sharp (closed symbols) and broad (open symbols) components. The dashed blue line is the isolated singlet population  $n_s(T) = (1 + e^{-\Delta/T})^{-1}$  at zero field. Full lines are the non-overlap probability  $P_s(T) = n_s(T)^{2m(2R/a)^2}$  and the overlap probability  $P_o(T) = n_s(T) - P_s(T)$ , with  $R$  the radius of the excited region, and  $a$  the lattice constant. The value of  $n_s(T)$  is modified in the presence of a magnetic field which accounts exactly for the observed intensities at  $H = 8$  T. Right: Sketch of two overlapping triplet excited regions (blue disks) in real space, with  $R = 1.3$   $a$  on the Shastry-Sutherland lattice. The magnetization pattern around the central dimer is indicated by up and down arrows with lengths proportional to the magnetization. The dashed square indicates a unit cell.

it is the only spin  $S = 1/2$  realization of the Shastry-Sutherland model that has an exactly solvable ground state. While the ground state is well known to be a direct product of singlets, knowledge of the excited states and, thus, of the finite temperature properties of the system is more elusive [1]. In  $\text{SrCu}_2(\text{BO}_3)_2$  the magnetic excitation, representing the transition from a spin singlet to a spin triplet state, displays peculiar behavior: although the spin gap  $\Delta$  is about 35 K, the peak intensity when measured by inelastic neutron scattering (INS) is strongly suppressed above 5 K and disappears into a seemingly flat continuum around 15 K ( $< \Delta/2$ ).

### Broad and sharp components

With detailed INS measurements on single crystals as a function of momentum and magnetic field, we found [2] that the low temperature properties of  $\text{SrCu}_2(\text{BO}_3)_2$  can still be described by a 35 K gapped system provided one accounts for two types of triplet excitations: damped and un-damped. We model the line shape of the excitation by a damped harmonic oscillator (DHO) convoluted with a Gaussian instrumental resolution. The sharp excitation remains resolution limited, while the broad one has a finite width that increases with temperature. A sum two DHO (one broad and one sharp) per triplet mode matches the INS data very well, while a single DHO per mode fails (Fig. 2).

### Correlated decay model

These two excitations are differentiated only by the

location where they occur in real space. A triplet will be damped if occurring in the vicinity of another triplet, and will otherwise remain sharp. The statistics for these 2 different types of events explain the intensities of the excitations at all measured temperatures and magnetic fields. When a triplet is formed on a particular dimer, it also polarizes neighboring dimers, giving an extended magnetized region in real space. We model the decay of the excitation to occur only when two such regions overlap. Our model of correlated decay, combined with the INS data, enabled us to calculate the real space radius of the triplet excitation in  $\text{SrCu}_2(\text{BO}_3)_2$ . It was found that the radius of 1.3 lattice units matches the experimental INS data. This value is found to be in agreement with independent theoretical perturbative continuous unitary transformation method (PCUT) calculations on the triplet magnetization pattern [3].

The finite temperature line shape observed in  $\text{SrCu}_2(\text{BO}_3)_2$  contrasts with recent reports of non-Lorentzian asymmetric spectral functions for certain gapped low-dimensional dimer systems such as the alternating chain  $\text{Cu}(\text{NO}_3)_2 \cdot 2.5 \text{H}_2\text{O}$  and the layered dimer material  $\text{Sr}_3\text{Cr}_2\text{O}_8$  [4,5].

[1] S. Miyahara and K. Ueda, *J. Phys. Condens. Matter* **15**, R327 (2003).

[2] M. E. Zayed et al., *Phys. Rev. Lett.* **113**, 067201 (2014).

[3] J. Dorier et al., *Phys. Rev. Lett.* **101**, 250402 (2008).

[4] D. A. Tennant et al., *Phys. Rev. B* **85**, 014402 (2012).

[5] J. Jensen et al., *Phys. Rev. B* **89**, 134407 (2014).

# Nano phase separation responsible for hour-glass spectra in $\text{La}_{2-x}\text{Sr}_x\text{CoO}_4$

A.C. Komarek<sup>1</sup>, Z. W. Li<sup>1</sup>, Y. Drees<sup>1</sup>, A. Ricci<sup>2</sup>, M. Rotter<sup>1</sup>, O. Sobolev<sup>3,4</sup>

<sup>1</sup>Max-Planck-Institute for Chemical Physics of Solids, Dresden, Germany

<sup>2</sup>Deutsches Elektronen-Synchrotron DESY, Hamburg, Germany

<sup>3</sup>Heinz Maier-Leibnitz Zentrum (MLZ), Technische Universität München, Garching, Germany

<sup>4</sup>Institut für Physikalische Chemie, Georg-August-Universität Göttingen, Göttingen, Germany

The so-called hour-glass magnetic excitation spectrum has fascinated physicists for many years. This phenomenon has so far been found only in copper oxide based high-temperature superconductors. It is widely believed that fluctuating charge stripes are involved in the physics of these peculiar excitation spectra. Here, we have studied an isostructural but insulating cobaltate that also exhibits an hour-glass magnetic spectrum. We can exclude not only Fermi surface effects, but also any substantial role attributable to charge stripes in the hour-glass spectrum in this cobalt oxide material. Instead, we observe electronic and magnetic nano phase separation within the cobalt oxygen planes and unravel a microscopically split origin of hour-glass spectra on the nano scale.

The appearance of a magnetic excitation spectrum with an hour-glass shape in energy-momentum space is a characteristic property of high-temperature superconducting cuprates. Despite numerous studies, the origin of this peculiar excitation spectrum is not well understood. Therefore, the recent observation of hour-glass shaped magnetic excitation spectra in isostructural cobaltate materials has stimulated the study of hour-glass spectra within insulating reference systems where Fermi surface effects play no role [1,2]. The cobaltate initially studied,  $\text{La}_{5/3}\text{Sr}_{1/3}\text{CoO}_4$ , exhibits broad magnetic peaks roughly around one-third-integer positions in reciprocal space. At about the same positions in reciprocal space, magnetic reflections appear in the isostructural nickelate  $\text{La}_{5/3}\text{Sr}_{1/3}\text{NiO}_4$  which exhibits robust diagonal charge stripe ordering. Thus, the presence of disordered diagonal charge stripe phases were also assumed in the cobaltates and, hence, the importance of charge stripe phases for the emergence of hour-glass spectra.

## Charge correlations and our nano phase separation scenario

In neutron and X-ray diffraction experiments we were not able to detect any signatures of charge stripe phases, neither in  $\text{La}_{5/3}\text{Sr}_{1/3}\text{CoO}_4$  nor in  $\text{La}_{1.6}\text{Sr}_{0.4}\text{CoO}_4$  [2,3]. Instead, we observe broad peaks at half-integer positions in reciprocal space very similar to those in the ideally half-doped checkerboard charge ordered compound  $\text{La}_{1.5}\text{Sr}_{0.5}\text{CoO}_4$  with a high charge ordering temperature far above 800 K. Thus, in the layered cobaltates, rather robust checkerboard charge ordering correlations still persist distinctly below half-doping down to 1/3 hole-doping. In compounds with less than 50 % hole-doping, the additional electrons have to be distributed in some way into the cobalt oxygen planes. Since no signatures of charge stripes could be observed within these strongly localized insulators, the emergence of the islands in the form of the undoped parent insulator  $\text{La}_2\text{CoO}_4$  appears to be an unavoidable consequence. Therefore, we propose a novel nano phase separation scenario where checker-

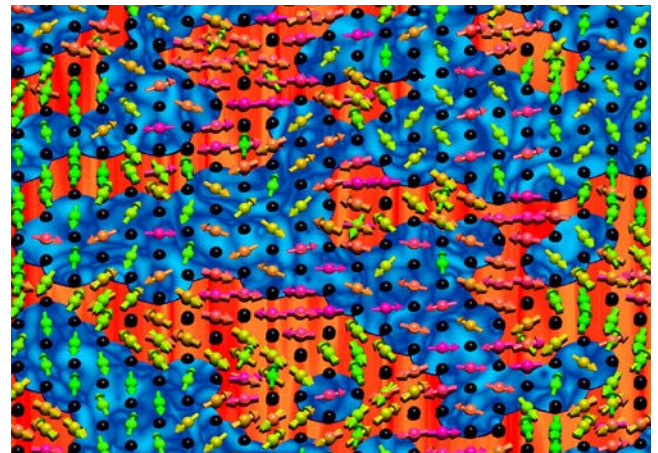


Figure 1: A graphical presentation of the core results of our spinwave calculations according to our nano phase separation model. First of all, non-collinear magnetic structures appear due to frustration. At higher energies the checkerboard charge ordered regions (blue) barely participate in the excitations and basically the undoped regions (red) exhibit strong excitations as visualized here by the additional drawing of additional spin directions during an excitation.

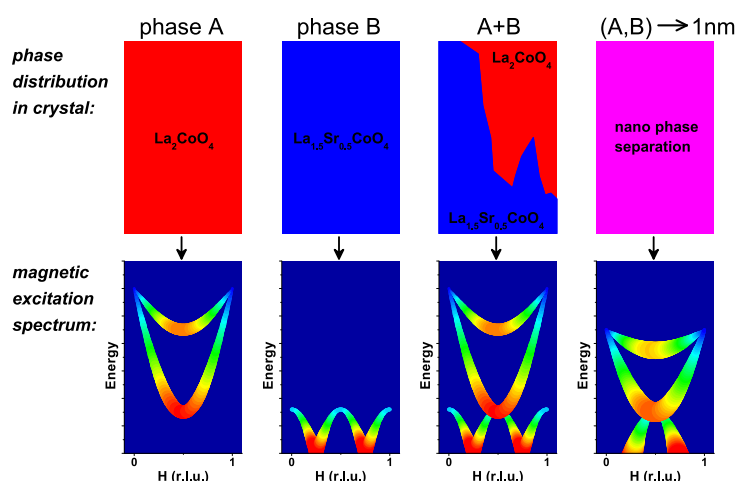


Figure 2: In the first two columns a schematic presentation of magnetic excitations in undoped (red) and half-doped (blue) cobaltate phases A and B is shown. In the third column the case of conventional phase separation is shown where the former two phases A and B coexist. Finally, in the last column is shown what happens once the A and B domain sizes get close to the dimensions of a few unit cells i.e. roughly nanometer-sized.

board charge ordered regions are interspersed with undoped islands on the nanometer-scale. Indeed, our analysis of microdiffraction measurements at the synchrotron corroborates this scenario [3].

### The novel high energy magnetic mode

Another interesting discovery that emerged was the observation of a hitherto unknown additional high-energy magnetic mode above the entire hour-glass shaped magnetic spectrum with polarized neutrons. Thus, the part of the spectrum above the crossing of the hour-glass somehow resembles the magnetic excitation spectrum of  $\text{La}_2\text{CoO}_4$ . Therefore, the question arises as to whether the magnetic excitations in the upper part of the spectrum are basically hosted within the nanometer-sized undoped islands of  $\text{La}_2\text{CoO}_4$ -type.

### Hole-doping and temperature dependence

Comparing  $\text{La}_{5/3}\text{Sr}_{1/3}\text{CoO}_4$  and  $\text{La}_{1.6}\text{Sr}_{0.4}\text{CoO}_4$  the additional high-energy magnetic mode seems to be distinctly weaker in  $\text{La}_{1.6}\text{Sr}_{0.4}\text{CoO}_4$ . Since the fraction of undoped islands should be much smaller in  $\text{La}_{1.6}\text{Sr}_{0.4}\text{CoO}_4$  than in  $\text{La}_{5/3}\text{Sr}_{1/3}\text{CoO}_4$  this is, indeed, evidence for our nano phase separation scenario [3]. Since the hole-concentration is closer to the half-doped than to the undoped material, the high energy magnetic excitations are in general weaker. Also the study of the temperature dependence of the magnetic excitations in  $\text{La}_{5/3}\text{Sr}_{1/3}\text{CoO}_4$  corroborates our novel nano phase separation scenario: e.g. the temperature-induced broadening of the low-energy magnetic excitations usually anticipated is not visible when the temperature rises. Within our model, this would naturally follow from the limiting factor of the static domain size of the checkerboard charge ordered regions, which is temperature-independent [3].

### Magnetism and nano phase separation

Finally, we conducted spin wave calculations for our nano phase separation model which are able to describe the observations within our neutron scattering experiments. These simulations clearly show that at higher energies basically the undoped islands can be excited [3], see Fig. 1. Hence, we did not only observe nano phase separation in the charge sector (nanometer-sized checkerboard charge ordered regions and undoped islands) but a kind of magnetic nano phase separation due to a strong decoupling of spins within checkerboard charge ordered regions with very small exchange interactions  $J'$  and spins within undoped islands with large exchange interactions  $J \gg J'$ . This novel electric and magnetic nano phase separation effect is very different from conventional phase separation since these Co oxide materials are homogenous. Furthermore, the total magnetic excitation spectrum is not simply a superposition of the excitation spectra of  $\text{La}_2\text{CoO}_4$  and  $\text{La}_{1.5}\text{Sr}_{0.5}\text{CoO}_4$  that is to be expected for conventional phase separation (see the schematic presentation in Fig. 2). In principle, this kind of nano phase separation appears in the limit for vanishing fraction of domain volume and dominating fraction of 'domain walls' (regions close to the 'border' of two phases) such that the excitation spectrum is not a simple superposition of the excitation spectra expected to occur within the volume of each type of domain.

[1] A. T. Boothroyd et al., *Nature* 471, 341 (2011).

[2] Y. Drees et al., *Nat. Commun.* 4, 2449 (2013).

[3] Y. Drees et al., *Nat. Commun.* 5, 5731 (2014).

# Triplet superconducting correlations in oxide heterostructures with noncollinear magnetization

Y. N. Khaydukov<sup>1,4,6</sup>, G. A. Ovsyannikov<sup>2,3</sup>, A. E. Sheyerman<sup>2</sup>, K. Y. Constantinian<sup>2</sup>, L. Mustafa<sup>1</sup>, T. Keller<sup>1,4</sup>, M. A. Uribe-Laverde<sup>5</sup>, Y. V. Kislinskii<sup>2</sup>, A. V. Shadrin<sup>2,3</sup>, A. Kalabukhov<sup>3</sup>, B. Keimer<sup>1</sup>, D. Winkler<sup>3</sup>

<sup>1</sup>Max Planck Institute for Solid State Research, Stuttgart, Germany

<sup>2</sup>Kotel'nikov Institute of Radio Engineering and Electronics of Russian Academy of Sciences, Moscow, Russia

<sup>3</sup>Department of Microtechnology and Nanoscience, Chalmers University of Technology, Gothenburg, Sweden

<sup>4</sup>Max-Planck-Institute for Solid State Research at MLZ, Garching, Germany

<sup>5</sup>Department of Physics and Fribourg Centre for Nanomaterials, University of Fribourg, Fribourg, Switzerland

<sup>6</sup>Skobeltsyn Institute of Nuclear Physics, Moscow State University, Moscow, Russia

**C**oexistence of ferromagnetic and superconducting order rarely occurs because of the antagonistic nature of the two phenomena. The strong exchange coupling in ferromagnets tries to align electron spins in parallel, incompatible with antiferromagnetically aligned spins of a Cooper pair. This conflict can be resolved in the case of triplet superconductivity where electron pairs with parallel spins are not destroyed by the exchange field of ferromagnets [1]. In this work, we have studied triplet superconducting correlations in all-oxide heterostructures composed of ferromagnetic  $\text{La}_{0.7}\text{Sr}_{0.3}\text{MnO}_3$ ,  $\text{SrRuO}_3$  and superconducting  $\text{YBa}_2\text{Cu}_3\text{O}_x$  using SQUID, PNR and transport measurements [2].

## Sample preparation and neutron scattering

Heterostructures with composition  $\text{La}_{0.7}\text{Sr}_{0.3}\text{MnO}_3/\text{SrRuO}_3/\text{YBa}_2\text{Cu}_3\text{O}_x$  (LSMO/SRO/YBCO) were fabricated on (110)  $\text{NdGaO}_3$ , (001)  $\text{LaAlO}_3$  or (001)  $(\text{LaAlO}_{3/0.3})_2(\text{Sr}_2\text{AlTaO}_6)_{0.7}$  substrates by pulsed

laser ablation and then covered in-situ by Au films. Square mesa-structures with in-plane size  $L = 10 - 50 \mu\text{m}$  were fabricated on  $\text{NdGaO}_3$  substrates [3].

The PNR experiment was conducted on the reflectometer NREX. A polarized neutron beam with wavelength  $4.26 \text{ \AA}$  and 99.99 % polarization falls on the sample under the grazing incidence angles  $\theta_i = [0.15 - 1]$ . The divergence of the beam  $\Delta\theta_i = 0.025^\circ$  was set by two slits in front of the sample. The polarization of the reflected beam was analyzed by a polarization analyzer with 98 % efficiency. An in-plane magnetic field was applied parallel to the one edge of the sample. Before the measurements, the sample was cooled down to  $T = 80 \text{ K}$  in  $H = 5 \text{ kOe}$  to align the magnetic domains in the direction parallel to the external field. Subsequently, the magnetic field was decreased to  $H = 30 \text{ Oe}$  and reflectivity curves were measured.

Spin-polarized reflectivity curves taken at  $T = 80 \text{ K}$  are shown in Fig. 1a. The NSF curves  $R^{++}$  and  $R^{-}$  are characterized by total reflection from the substrate with critical wave vector transfer  $Q_{\text{crit}} = 0.15 \text{ nm}^{-1}$

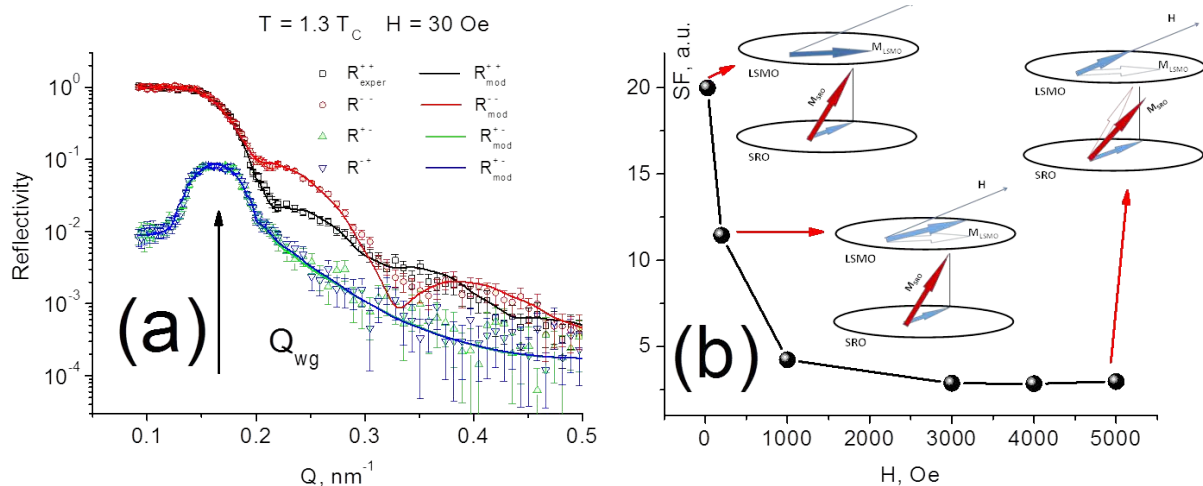


Figure 1: (a) Experimental (dots) reflectivity curves measured at  $T = 80 \text{ K}$  and  $H = 30 \text{ Oe}$  on the sample  $\text{Au}(20\text{nm})/\text{LSMO}(14\text{nm})/\text{SRO}(15\text{nm})/\text{YBCO}(100\text{nm})$ . Model reflectivity curves are shown by solid lines. The vertical arrow shows the center of the waveguide peak. (b) Integral of the waveguide spin-flip peak as a function of magnetic field measured at  $T = 10 \text{ K}$ . Insets: Sketch of the vector magnetic profile of the LSMO/SRO magnetic sub-system at different magnetic fields.

and Kiessig fringes. The difference between  $R^{++}$  and  $R^-$  indicates the presence of a collinear component of the magnetization. The SF scattering, in turn, shows that an in-plane non-collinear component of the magnetization exists. The sharp peaks in the SF channels around  $Q_{\text{crit}}$  with intensity of about 10 % originate from the waveguide-like structure formed by capping the system with the layer of gold. The parameters of this peak (width, height and area) are very sensitive to the magnetic state of the system [4]. In particular, the magnetic field dependence of the peak area is shown in Fig. 1b. One can see that the intensity of SF scattering is rapidly decreased in the range of magnetic field  $H = [0-1]$  kOe and stays almost zero at magnetic fields up to  $H = 5$  kOe. The sensitivity of the waveguide SF peak is explained by significant enhancement of neutron density in the waveguide mode. According to our calculations, the neutron density in the vicinity of the magnetic layers is enhanced by a factor of 20 - 30 with respect to the intensity of the incoming beam [2], thus allowing the sensitivity of PNR in the determination of the in-plane non-collinear moment to be significantly increased.

Analysis of PNR and SQUID data allowed us to restore field evolution of the 3D vector profile of the magnetic sub-system (see insets in Fig. 1b). In small magnetic fields (order of tens of Oersteds) magnetic moment of LSMO layer  $3.2 \mu_B/\text{Mn}$  lies in-plane along the easy axis, which made an angle of  $45^\circ$  with respect to the direction of external field. The magnetic moment of SRO  $1.3 \mu_B/\text{Ru}$  is inclined on angle  $80^\circ$  to the sample plane (left inset in Fig. 1b). The subsequent increase of the external magnetic field to  $H \sim 1$  kOe leads to a rotation of the LSMO magnetization vector towards the magnetic field, while the direction of the SRO magnetization remains the same (middle inset in Fig. 1b). The magnetic field of half a Tesla was not enough to align moments of LSMO and SRO collinear (right inset in Fig. 1b). Thus, a combination of PNR and SQUID allowed us to experimentally prove that the non-collinear alignment of the LSMO and SRO magnetization vectors remains virtually unchanged in the range of applied magnetic fields  $H = [0-5]$  kOe that enables generation of a triplet condensate.

### Transport measurements

To probe possible triplet superconducting correlations in the ferromagnetic layers, a mesa-structure

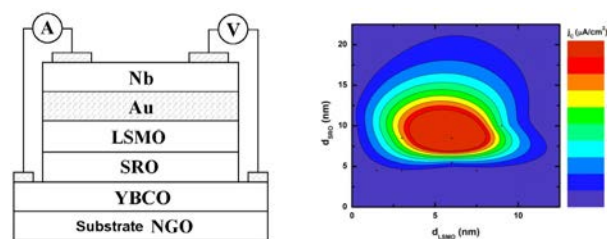


Figure 2: (a) Sketch of the transport experiment. (b) Dependence of the critical current density  $j_c$  measured at  $T = 4.2$  K on  $d_{\text{SRO}}$  and  $d_{\text{LSMO}}$ . Colored contours are shown to guide the eye. Experimental data are shown by black points.

with two superconducting electrodes was studied (Fig. 2). The second electrode was a Nb film deposited on top of the Au/LSMO/SRO/YBCO structure [3]. A superconducting current was observed in all mesa-structures with LSMO/SRO total thickness  $d_M = d_{\text{LSMO}} + d_{\text{SRO}}$  up to 53 nm (Fig. 2b), which is much larger than the coherence length of both ferromagnets  $\xi_F \sim 5$  nm [3]. The measurements also showed that a critical current exists even in the fields of several kOe. It would be surprising for a singlet superconducting current to exist at  $H$  fields up to 100 times stronger than the period of critical current oscillation ( $\sim 10$  Oe). As was directly shown by PNR and SQUID measurements, the presence of critical currents at such high magnetic fields is explained by strong non-collinear alignment of magnetic moments of LSMO and SRO layers.

### Conclusion

We have directly probed non-collinear magnetism on metal-oxide heterostructures by means of SQUID magnetometry and PNR. The dependence of the observed superconducting current in the mesa-structures Nb/Au/LSMO/SRO/YBCO on thicknesses of LSMO and SRO was studied and compared with theoretical predictions. The Josephson effect observed in these structures is explained by the penetration of the long-range triplet component of the superconducting correlations into the magnetic layer. Further work is required to elucidate the magnetic structures at the interfaces and their influence on the propagation of supercurrents, as well as the possible role of d-wave pairing.

[1] F. S. Bergeret et al., Rev. Mod. Phys. 77, 1321 (2005).

[2] Y. N. Khaydukov et al., Phys. Rev. B 90, 035130 (2014).

[3] G. A. Ovsyannikov et al., J. Exp. Theor. Phys. Lett. 97, 145 (2013).

[4] Y. N. Khaydukov and Yu. V. Nikitenko, Nucl. Instrum. Meth. A 629, 245 (2011).

# Competing ferromagnetic and antiferromagnetic interactions in the 2D spiral magnet $\text{Sr}_3\text{Fe}_2\text{O}_7$

J.-H. Kim<sup>1</sup>, A. Jain<sup>1,2</sup>, M. Reehuis<sup>3</sup>, G. Khaliullin<sup>1</sup>, D. C. Peets<sup>1</sup>, C. Ulrich<sup>1,4,5</sup>, J. T. Park<sup>6</sup>, E. Faulhaber<sup>6</sup>, A. Hoser<sup>3</sup>, H. C. Walker<sup>7</sup>, D. T. Adroja<sup>7,8</sup>, A. C. Walters<sup>1</sup>, D. S. Inosov<sup>1,9</sup>, A. Maljuk<sup>1,10</sup>, B. Keimer<sup>1</sup>

<sup>1</sup>Max-Planck-Institut für Festkörperforschung, Stuttgart, Germany

<sup>2</sup>Solid State Physics Division, Bhabha Atomic Research Centre, Mumbai, India

<sup>3</sup>Helmholtz-Zentrum Berlin für Materialien und Energie, Berlin, Germany

<sup>4</sup>School of Physics, University of New South Wales, Sydney, Australia

<sup>5</sup>Australian Nuclear Science and Technology Organisation, Lucas Heights, Australia

<sup>6</sup>Heinz Maier-Leibnitz Zentrum (MLZ), Technische Universität München, Garching, Germany

<sup>7</sup>ISIS Facility, STFC, Rutherford Appleton Laboratory, Chilton (Oxfordshire), United Kingdom

<sup>8</sup>Physics Department, University of Johannesburg, Auckland Park, South Africa

<sup>9</sup>Institut für Festkörperphysik, Technische Universität Dresden, Dresden, Germany

<sup>10</sup>Leibniz-Institut für Festkörper- und Werkstofforschung, Dresden, Germany

We use inelastic neutron scattering to investigate the spin dynamics of the stoichiometric bilayer perovskite  $\text{Sr}_3\text{Fe}_2\text{O}_7$ , which undergoes a temperature driven metal-insulator transition (MIT) and a transition to helical magnetic order. We show that the measured magnetic excitation spectra can be well described within the framework of an effective Hamiltonian with up to third-nearest-neighbor exchange interactions. The estimated strengths of ferromagnetic double-exchange and antiferromagnetic superexchange interactions are comparable, indicating that competition between such antagonistic exchange interactions stabilizes helical magnetism near the MIT.

## Magnetic dynamics in the proximity of the metal-insulator transition

Despite recent progress in the theoretical description of metal-insulator transitions (MITs), the understanding of magnetic correlations near MITs remains challenging. Following dynamical mean-field theory, it is generally believed that in transition-metal oxides (TMO) localized spins in insulating Hubbard-like bands interact via antiferromagnetic superexchange interactions, whereas ferromagnetic double-exchange interactions are driven by itinerant electrons in their metallic bands [1]. According to a long-standing theoretical prediction [2], the competition between antiferromagnetic superexchange interactions and ferromagnetic double-exchange interactions can lead to noncollinear magnetic structures in the vicinity of MITs. However, alternative interpretations have also been proposed. Specifi-

cally, the ferromagnetic double-exchange interaction alone can generate a spiral magnetic phase in TMOs with metal ions in high oxidation states [3]. The difference between the two scenarios is the magnitude and spatial range of the exchange interactions, which can be tested by measuring spin-wave dispersions by means of inelastic neutron scattering (INS). To the best of our knowledge, however, INS measurements on stoichiometric model compounds have thus far not been carried out, mainly due to difficulties in obtaining large enough single crystals of sufficient quality.

We have used the clean and fully oxygenated stoichiometric compound  $\text{Sr}_3\text{Fe}_2\text{O}_7$  ( $T_N = 115$  K,  $T_{\text{MIT}} = 340$  K) to study the magnetic structure and dynamics by neutron scattering.

## Spiral magnetic order

First, single crystal and powder neutron diffraction measurements were carried out on the E5 and E6 diffractometers at BER-II (Helmholtz-Zentrum Berlin, Germany), respectively, to determine its magnetic

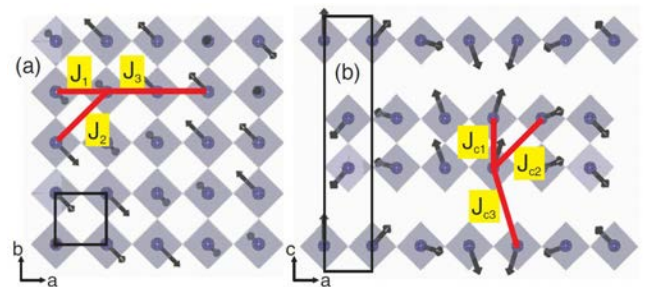


Figure 1: Helical magnetic structure of  $\text{Sr}_3\text{Fe}_2\text{O}_7$  projected onto the (a)  $ab$  and (b)  $ac$  planes. The rectangle indicates the tetragonal unit cell. Spheres and octahedra represent the Fe ions and  $\text{FeO}_6$  units, respectively. Arrows indicate the spin directions. Lines indicate the spin exchange couplings  $J$  included in the theoretical fits.

structure. The magnetic structure of  $\text{Sr}_3\text{Fe}_2\text{O}_7$  obtained, based on refinement of diffraction data, is an elliptical helix with a  $c$  component significantly smaller than its  $ab$  components. As illustrated in Fig. 1, all spins lie in a plane perpendicular to the  $[110]$  direction. Along the  $c$  axis, the spins of the iron atoms at  $(0\ 0\ \pm z)$  are antiparallel with those at  $(0.5\ 0.5\ 0.5\ \pm z)$  [see Fig. 1(a)], which yields the component of the propagation vector  $k_z = 1$ .

### Magnetic excitation spectra and calculations

To study the magnetic dynamics in  $\text{Sr}_3\text{Fe}_2\text{O}_7$ , we performed a series of INS measurements at the three-axis spectrometers PANDA (cold neutrons) and PUMA (thermal neutrons) on a single crystal with diameter 5 mm and length 50 mm. During the INS experiments both at PANDA and PUMA, we used a double-focusing PG(002) monochromator and analyzer to maximize the neutron flux at the sample position while preserving reasonable instrumental resolution. To eliminate higher-order neutron contamination, a Be filter before the analyzer was used at PANDA and a sapphire filter and two PG filters were inserted before the monochromator and after the analyzer at PUMA, respectively. The final neutron wave vector was fixed to  $k_f = 1.57\ \text{\AA}^{-1}$  on PANDA and to  $2.662\ \text{\AA}^{-1}$  on PUMA.

The upper panels of Fig. 2 show the scattered neutron intensity distribution in momentum and energy below  $T_N$  ( $T = 7\ \text{K}$ ). The neutron scattering dataset in the first two upper panels was obtained on PUMA, measuring along the  $[H00]$  (left) and  $[HH0]$  (middle) directions up to 14 meV. While sharply dispersive spin-wave branches are clearly seen, the features close to the zone center remain ambiguous. To further resolve the low-energy magnetic excitations, we have mapped out the spin-wave excitations up to 6 meV along  $[HH5]$  on PANDA with better energy and momentum resolution (Fig. 2 upper right), where no significant spin anisotropy gap was seen. To fit the observed spin-wave dispersion and intensities, we carried out standard linear spin-wave calculations [4], using a minimal set of input parameters in the following equation:

$$H = \sum_{ij} J_{ij} \mathbf{S}_i \cdot \mathbf{S}_j + \Delta \sum_i S_{ix}^2$$

where  $J_{ij}$  represents the Heisenberg coupling between the  $i$ -th and  $j$ -th spins  $\mathbf{S}$ ,  $\Delta > 0$  is the easy (110) plane anisotropy parameter, and  $\mathbf{S}_\alpha$  refers to the spin

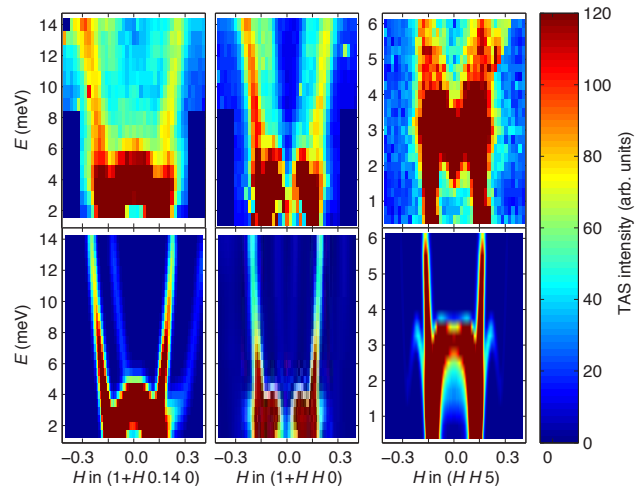


Figure 2: (Upper panels) Contour maps of spin-wave dispersions in  $\text{Sr}_3\text{Fe}_2\text{O}_7$  at 7 K along the (left)  $[H00]$ , (middle)  $[HH0]$ , (right)  $[HH5]$  directions. Upper panels show the theoretical dispersions and neutron scattering intensities (convoluted with the instrumental resolution), calculated with the parameters described in the text.

component along the  $[110]$  axis. The lower panels in Fig. 2 represent the results of calculations with the following parameters:  $J_1 = -7.2\ \text{meV}$ ,  $J_2 = 1.05\ \text{meV}$ ,  $J_3 = 2.1\ \text{meV}$ ,  $J_{c1} = -5.1\ \text{meV}$ ,  $J_{c2} < 0.01\ \text{meV}$ ,  $J_{c3} = 0.01\ \text{meV}$  and  $\Delta = 0.06\ \text{meV}$ . Here, positive values of  $J$  represent antiferromagnetic interactions. The calculations are in excellent agreement with the measured spin excitation spectra (Fig. 2).

### Confirmation of long-standing theory

The competition between ferromagnetic double-exchange interactions and antiferromagnetic superexchange interactions is controlled by the degree of itinerary or localization of the conduction electrons, and a strong modification in electron correlations near the MIT region can generate a fine balance between them. Based on this scenario, the sign and relative strength of exchange interactions extracted from the magnon dispersion of  $\text{Sr}_3\text{Fe}_2\text{O}_7$  with a quasi-two-dimensional spiral state near a MIT are in line with theoretical estimations [1]. Thus, our spin excitation measurements, together with calculations, provide a quantitative confirmation of a decades-old theoretical prediction [2] and a firm experimental basis for further experimental and theoretical work on TMOs near MITs.

[1] G. Khaliullin, *Prog. Theor. Phys. Suppl.* 160, 155 (2005).

[2] P.-G. de Gennes, *Phys. Rev.* 118, 141 (1960).

[3] M. Mostovoy, *Phys. Rev. Lett.* 94, 137205 (2005);

Z. Li et al., *Phys. Rev. B* 85, 134419 (2012).

[4] G. Khaliullin and R. Kilian, *Phys. Rev. B* 61, 3494 (2000).

# Exchange-bias-like coupling in a ferrimagnetic Fe/Tb multilayer with planar domain walls

S. Mukherjee, W. Kreuzpaintner, P. Böni, A. Paul

Physik-Department E13, Technische Universität München, Garching, Germany

**F**ield cooling of a transition metal–rare earth (TM–RE) Fe/Tb-multilayer system is shown to form a double hysteresis loop with exchange-bias-like shifts along and opposite to the field cooling axis below the ordering temperature of the RE. The measured polarized neutron reflectivity data at various applied fields confirm an antiferromagnetic alignment between the individual layers of Fe and Tb associated with a significant value of the magnetic moment for the Tb layers, even at room temperature. We attribute the shifts of the hysteresis loops to the formation of  $2\pi$ -domain walls by the interface moments that are pinned by the magnetically hard Tb layers forming bidomain-like states in this layered artificial ferrimagnetic system. This excludes an explanation in terms of  $\pi$ -domain walls, which are believed to be responsible for the exchange bias in other RE–TM bilayer systems.

## Planar domain wall in exchange coupled system

Multilayers of rare earth (RE) such as Gd, Sm, Dy and Tb and ferromagnetic (FM) elements are known to show exchange bias effects. In these kinds of multilayer systems, a hard (RE) and a soft (FM) magnetic layer are combined which are antiferromagnetically (AF) coupled at the interface, forming essentially a ferrimagnetic system. In an alloyed  $\text{Gd}_{40}\text{Fe}_{60}/\text{Tb}_{12}\text{Fe}_{88}$  exchange-coupled bilayer system (for e.g.), both negative and positive bias, depending upon the cooling field, have been observed. It has been shown that reversal of the soft layer induces a magnetic planar domain wall (DW) at the interface which in FM–RE systems resides in the soft FM owing to the strong anisotropy in the RE. In this report we focus on field cooling experiments of Fe/Tb multilayers showing in-plane magnetic anisotropy. We observe antiferromagnetic coupling be-

tween the Tb and Fe layers. Thus, the Fe/Tb system effectively represents a layered artificial ferrimagnet. It shows double hysteresis loops (DHLs) with anomalously large exchange bias-like shifts along the negative and positive field cooling axes. In an usual AF–FM system, the shift is always opposite to the cooling field. We use polarized neutron reflectivity (PNR) which is an effective tool to probe such challenging ferrimagnetic systems. The temperature evolution of the coercivities and the PNR data, along with model simulations, do not indicate that a decoupled system is at the origin of the DHLs. The loop shifts are attributed to the formation of bidomain-like states in the AF layers that are larger than the FM domains. Further, we can rule out the possibility of formation of commonly observed  $\pi$ -domain walls in the softer Fe layers, pinned by the harder Tb layers. We argue that the formation of  $2\pi$ -DWs, with right and left handedness, within the Fe layers are responsible for the observed exchange bias [1].

## Specular neutron scattering

We prepared the sample by dc magnetron sputtering using Si(100) as substrate. A multilayer consisting of five bilayers of Fe/Tb, i.e.,  $[\text{Fe}(3.0\text{ nm})/\text{Tb}(6.0\text{ nm})]_5/\text{Fe}(4.5\text{ nm})$  was used. The thickness of the layers is chosen such that the anisotropy is confined to the film plane. Depth sensitive polarized neutron scattering at the TREFF reflectometer at the MLZ was measured for the non spin-flip (NSF) ( $R_{++}$  and  $R_{--}$ ) cross sections in accessing the longitudinal components of magnetization with respect to the guiding field. The specimens are field cooled in a field  $H_{\text{FC}} = 4.0\text{ kOe}$  inside a cryostat at the instrument.

## Double hysteresis loop and planar domain wall formation

The hysteresis loops for the sample at 50 K is shown in Fig. 1 (top panel) after field cooling. The hysteresis loop consists of a primary (soft) and a secondary

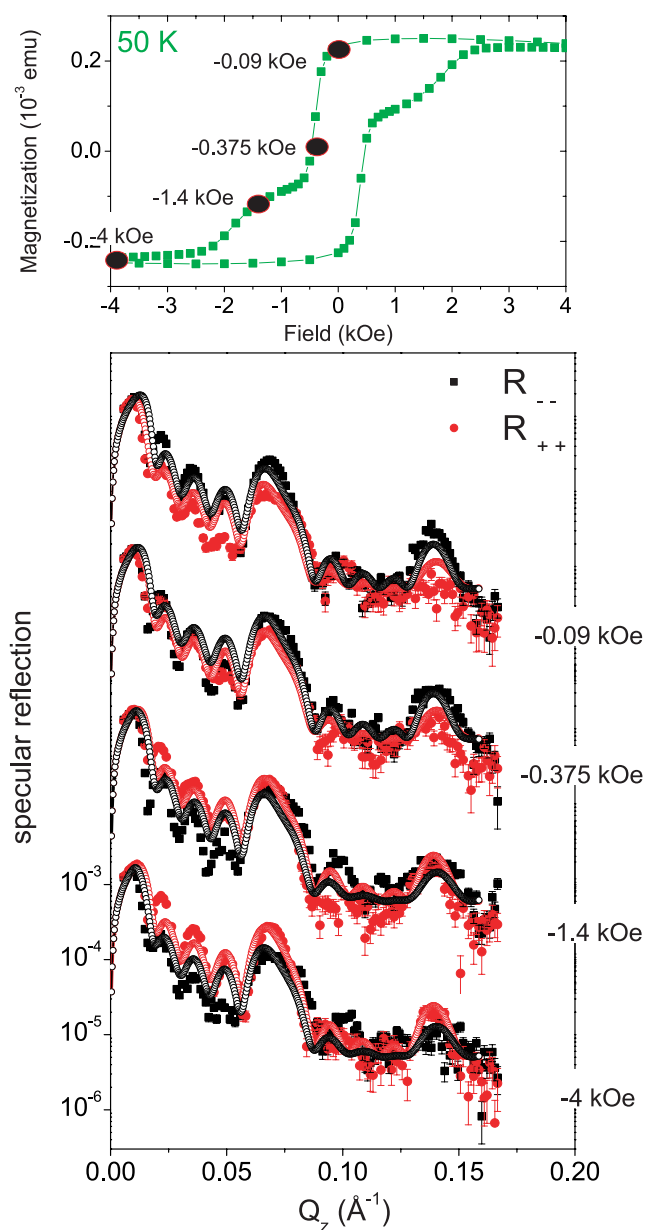


Figure 1: The top panel shows the hysteresis loop at 50 K. The bottom panel shows the PNR curves for spin-up and spin-down polarizations measured at various applied fields  $H_a$  along the decreasing branch of the hysteresis loop along with their best fits (open symbols). The field values for neutron measurements are indicated alongside (marked in circles in the top panel).

loop (bottom half) that is shifted opposite to the field cooling axis (negative shift), i.e., along the decreasing branch of the hysteresis loop. However, we observe a similar shift (top half) along the increasing branch of the same loop as well. Such a superposition of two secondary loops is known as DHL. Such DHLs are probably due to the formation of planar domain walls which have proportions of left-handed and right-handed configurations. Fig. 1 (bottom panel) displays specular PNR data measured at 50 K for various applied fields  $H_a$ . The sample was first saturated in a field of 4 kOe before the measurements

were started at -0.09 kOe and onwards. From the fits to the data we find magnetic moments of Tb at 50 K (and also at 300 K) which is a result of induced magnetization from the TM proximity. The 3d -5d hybridization not only produces significant 5d density at the RE sites, but is also responsible for the crucial coupling between the RE and TM moments. The layers are seen to flip their direction before and after the coercive field. Upon magnetization reversal, the magnitude of the magnetic moment of each of the individual Tb or Fe layers remains (almost) unchanged but, due to the strong AF coupling at the interfaces, the entire ferrimagnetic Tb/Fe entity flips its direction, showing up as DHLs.

As Fe is the softer material, it is expected that the nucleation of the DW takes place within the Fe layers, because the magnetization of the Tb layer is constrained by its strong anisotropy. In the case where the Tb layer was replaced by a usual AF layer, coupled to a FM layer, the DWs would have a tendency to propagate from one Fe layer to the other Fe layer. In the present case, they are blocked on their way as they are compressed against the anisotropic Tb layer. However, due to the presence of the Tb layer on both sides of each Fe layer, it is more likely that the DW propagates via  $2\pi$ -DWs (with opposite handedness, left and right) instead of  $\pi$ -DWs, commonly observed in hard-soft (RE-TM) bilayers (or TM-RE-TM) trilayer interfaces when each of the FM layers has only one interface to the RE layer. This can be attributed to the observation of the DHLs in the multilayer.

## Conclusion

In RE-TM systems AF-coupling at the interface helps in forming planar domain walls at the interface. Field cooling of a (Fe/Tb) multilayer system was shown to form DHL with exchange-bias-like shifts along and opposite to the field cooling axis below the ordering temperature of the RE. The possible formation of  $2\pi$ -DWs within the Fe layers was attributed to the origin of the exchange bias. More specifically, it is plausible that a mixture of regions containing left-handed DW and right-handed DW has led to such DHL.

[1] A. Paul et al., Phys. Rev. B 89, 144415 (2014).

# Critical spin-flip scattering at the helimagnetic transition of MnSi

J. Kindervater<sup>1</sup>, W. Häußler<sup>1,2</sup>, M. Janoschek<sup>3</sup>, C. Pfleiderer<sup>1</sup>, P. Böni<sup>1</sup>, M. Garst<sup>4</sup>

<sup>1</sup>Physik-Department, Technische Universität München, Garching, Germany

<sup>2</sup>Heinz Maier-Leibnitz Zentrum (MLZ), Technische Universität München, Garching, Germany

<sup>3</sup>Los Alamos National Laboratory, Los Alamos, USA

<sup>4</sup>Institute for Theoretical Physics, University of Cologne, Cologne, Germany

Second-order phase transitions between two phases of matter, at which collective fluctuations extend over macroscopic length scales, show spectacular cooperative phenomena such as critical opalescence. Interestingly, an excess of such fluctuations changes the character of these transitions profoundly, driving them first-order [1]. Such fluctuation-induced first-order transitions are at the heart of a plethora of systems such as liquid crystals, superconductors, cold atom systems or phase transitions in the early universe; However, only recently was the helimagnet MnSi identified as the first clear experimental example of such a transition via unpolarized SANS [2]. Our recent polarized study [3] using the new miniaturized spherical neutron polarimetry setup MiniMuPAD, also demonstrates quantitative agreement of the critical spin-flip scattering with the minimal model of the proposed Brazovskii transition.

## Spherical neutron Polarimetry with MiniMuPAD at RESEDA

Shown in Fig. 1 (a) is a schematic depiction of the miniaturized SNP setup developed for our study. Pairs of crossed precession coils (PC) before and after the sample permit the polarization of the incoming and scattered neutron beam to be rotated in any arbitrary direction and, therefore, to perform full spherical neutron polarimetry (SNP). Parasitic rotations of the polarization are minimized by the very compact design and the  $\mu$ -metal yokes (MM) around the precession coils, which short circuit both the external and precession fields.

The measurements reported here were performed at the beam-line RESEDA at MLZ. Neutrons were polarized with a cavity and analyzed with a bender at a neutron wavelength of  $\lambda = 4.5 \text{ \AA}$ . Data were re-

corded with a CASCADE [4] area detector. For our study, we used the MnSi single crystal investigated in Ref. [2]. The combination of the large window of the PCs with a PSD detector and the possibility for rotation of the sample by an angle  $\phi$  with respect to its vertical  $[1\bar{1}2]$  axis, see Fig. 1 c), allowed us to track various points in reciprocal space going well beyond previous work.

## Spin resolved critical scattering at the transition

For the spin resolved scattering from helimagnets, we focus on the magnetic contribution which consists of a symmetric and an antisymmetric part

$$\sigma_{mag}(Q, \hat{e}_{in}) = \sigma_{mag}^S + (\hat{Q} \hat{e}_{in}) \sigma_{mag}^A,$$

where the latter is weighted by the scalar product of the direction of the scattering vector  $\hat{Q}$  and the

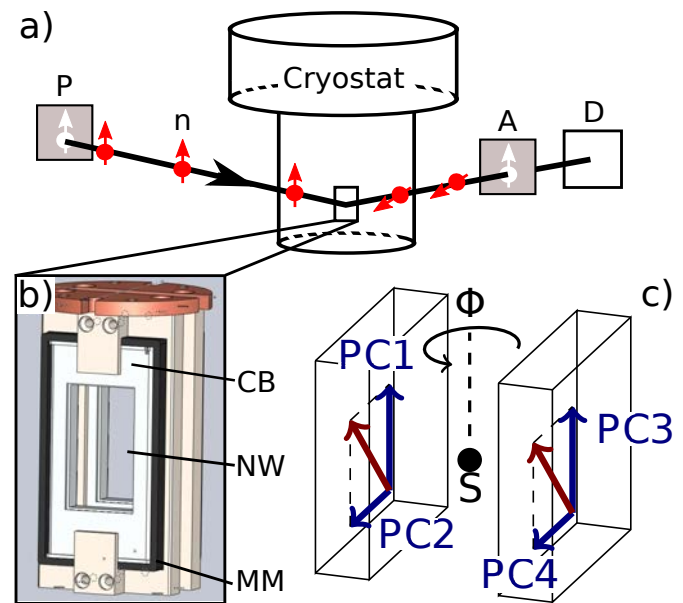


Figure 1: Schematic depiction of the SNP device. (a) Overview of the complete setup with cryostat, polarizer (P), analyzer (A), and detector (D). (b) Close-up view of the SNP device, as composed of the coil bodies (CB) with the neutron window (NW). The coils are surrounded by  $\mu$ -metal yokes (MM). (c) Orientation of the precession coils (blue arrows), local magnetic field (red arrow), and sample (S).

incoming polarization  $\hat{e}_in$ . Based on the theory for chiral magnets [5], for  $T > T_c$  one expects the spin-flip scattering to assume the following simple form:

$$\sigma_{mag}^S \mp \sigma_{mag}^A = \frac{Ak_B T}{(|Q| \pm k)^2 + \kappa^2(T)},$$

where  $k_B$  is the Boltzmann constant,  $k$  is the helix wavevector and  $A$  is a constant that depends on the magnetic form factor of MnSi. The inverse correlation length  $\kappa(T)$  represents the point of contact with the different theoretical proposals of the helimagnetic transition that motivated our study. In particular, for very weak cubic anisotropies in a Brazovskii scenario chiral paramagnons develop isotropically and become soft on a sphere in momentum space as  $\kappa(T)$  vanishes [2]. These chiral paramagnons effectively display a one-dimensional character, resulting in strong renormalizations suppressing the mean field transition by  $\Delta T = T_{MF} - T_c \approx 1.5$  K, driving it to first-order.

Fig. 2 a) and b) display the temperature dependence of the spin-flip scattering  $\sigma_{\pm\mp}^S(\mathbf{Q})$  measured on a sphere with a radius corresponding to the helical modulation  $k = 0.039 \text{ \AA}^{-1}$ . Approaching  $T_c$  the chiral magnetic ordering indeed develops isotropically, resulting in a negligible dependence on the orientation of  $\mathbf{Q}$ .  $\sigma_{+}$  reflect the strong  $T$ -dependence of  $\kappa$  close to  $T_c$ , while  $\sigma_{-}$  is barely temperature dependent as it is suppressed by the additional factor  $4k^2$  in the denominator of Eq. (1). Using the published results for  $\kappa(T)$ , we are left with a single fitting parameter, namely the Amplitude  $A$  in Eq. (1), in addition to a temperature and  $\mathbf{Q}$ -independent incoherent background  $\sigma_{inc}^S$  shown as the dotted line in Fig. 2 b). We find a remarkably good fit for both cross sections, as shown by the solid lines.

## Conclusion

We have investigated the critical spin-flip scattering close to the helimagnetic transition in MnSi. Furthermore, we developed a miniaturized, low-cost SNP device for swift experiments at scattering angles up to  $15^\circ$ . Considering carefully the importance of incoherent scattering, we find excellent quantitative agreement of the temperature dependence of the critical spin-flip scattering at various sample orientations with the Brazovskii scenario of a fluctuation-induced first order transition. Our study thereby provides a quantitative connection of the magnetic

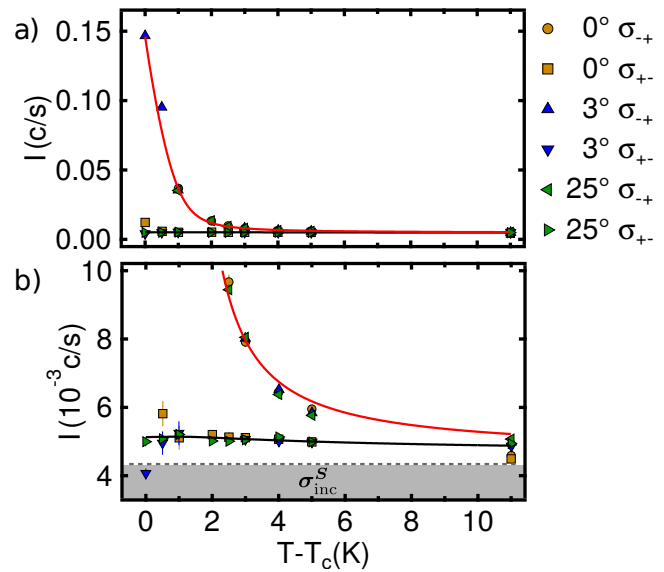


Figure 2: (a) Temperature dependence of the spin-flip scattering cross section of MnSi  $\sigma_{\pm\mp}^S(\mathbf{Q})$  with  $|\mathbf{Q}| = k$  close to the critical temperature  $T = T_c$ , for different orientations specified by the angle  $\phi = 0^\circ, 3^\circ$ , and  $25^\circ$ . For  $\phi = 0$ ,  $\hat{Q} \parallel [1\bar{1}1]$ . (b) same data but on a different intensity scale. The dashed line represents the background of the incoherent spin-flip scattering.

scattering with magnetization-, susceptibility-, and specific heat-data [1], completing a remarkably comprehensive account in a minimal model that does not require any additional phenomenological parameters such as those necessary in a proposal [6] for the prediction of skyrmion formation at zero magnetic field in bulk chiral magnets.

- [1] S. A. Brazovskii, Sov. Phys. J. Exp. Theor. Phys. 41, 85 (1975).
- [2] M. Janoschek et al., Phys. Rev. B 87, 134407 (2013).
- [3] J. Kindervater et al., Phys. Rev. B 89, 180408(R) (2014).
- [4] W. Häußler et al., Rev. Sci. Instrum. 82, 045101 (2011).
- [5] S. V. Grigoriev et al., Phys. Rev. B 72, 134420 (2005).
- [6] U. Rößler et al., Nature 442, 797 (2006).

# Studying the interactions between liposomes and silica nanoparticles using SANS, NSE and DLS

I. Hoffmann<sup>1,2</sup>, R. Michel<sup>1</sup>, M. Sharp<sup>2</sup>, O. Holderer<sup>3</sup>, M.-S. Appavou<sup>3</sup>, F. Polzer<sup>4</sup>, B. Farago<sup>2</sup>, M. Gradzielski<sup>1</sup>

<sup>1</sup>Stranski-Laboratorium für Physikalische und Theoretische Chemie, Institut für Chemie, Technische Universität Berlin, Berlin, Germany

<sup>2</sup>Institut Max von Laue-Paul Langevin (ILL), Grenoble, France

<sup>3</sup>Jülich Centre for Neutron Science (JCNS) at MLZ, Forschungszentrum Jülich GmbH, Garching, Germany

<sup>4</sup>TEM Group, Institute of Physics, Humboldt Universität zu Berlin, Berlin, Germany

We studied the interactions between DOPC liposomes and small silica nanoparticles (SiNPs). To do so, we performed SANS, NSE, DLS and cryo-TEM measurements. The interactions between liposomes and nanoparticles are of fundamental scientific interest as liposomes can serve as model systems for biological cells. Therefore, these measurements are important for an understanding of the effect of nanoparticles on living cells. Using SANS, it could be shown that the SiNPs have almost no effect on the structure of the liposomes despite almost complete adsorption, as evidenced by DLS and TEM. We proceeded to investigate the influence of the SiNPs on the liposomes' membrane dynamics using NSE and found that the membrane is softened by the binding of the SiNPs to the membrane surface. This surprising result may help in future understanding of the effects of nanoparticles on biological cells.

Vesicles are closed bilayers, dividing an interior part from the bulk solution, very much like cells. If the bilayer consists of phospholipids, as does most of any biological membrane, they are referred to as liposomes and serve as simple model systems for biological cells [1].

With the increasingly wide-spread use of nanoparticles in our daily environment, their interactions with cells have gained quite some interest, whether it is to be able to assess their risks (nanotoxicity) or their benefits in nano medicine [2-4].

To fully understand the effect of nanoparticles on the cell membrane, it is not only necessary to investigate the influence on the structure but also on the dynamics and the stiffness of the membrane.

We have investigated the interactions between liposomes consisting of the phospholipid DOPC (1,2-Dioleoyl-*sn*-glycero-3-phosphocholine, 0.1 wt%), prepared by extrusion through a 100 nm membrane and SiNPs at a concentration of 0.085 wt% with a radius of 8.4 nm in dilute aqueous solution. To do so, several complementary methods were employed [5].

## Structure of the Liposomes

To study the influence on the membrane dynamics, it was necessary to investigate an interacting system, which does not undergo a major structural reorganization. As the contrast of silica is relatively low in neutron scattering, small angle neutron scattering (SANS) is well suited to examination of the structure of the liposomes. Therefore, measurements were performed on the instrument KWS 2 at MLZ to verify the size of the liposomes and their structural stability against the SiNPs. As can be seen in Fig. 1, the curves look almost identical, regardless of the presence or absence of the nanoparticles, which means that the structure of the liposomes is not altered. Furthermore, the size of the liposomes can be determined to be 43.5 nm, as can be seen from the kink at about 0.07 1/nm. This confirms results ob-

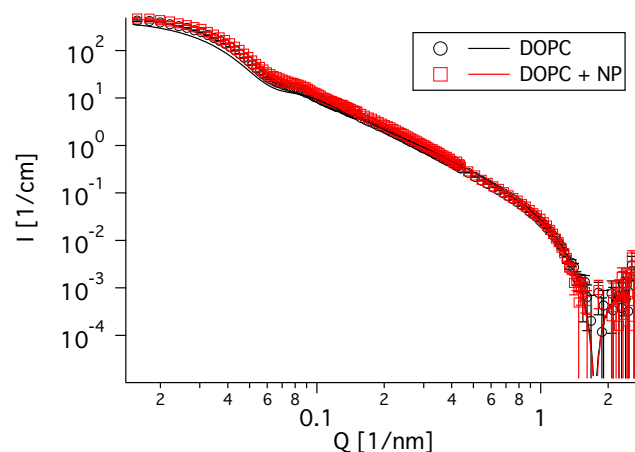


Figure 1: SANS curves of pure DOPC liposomes and DOPC liposomes with SiNPs added. Almost no structural change can be seen (KWS 2, MLZ).

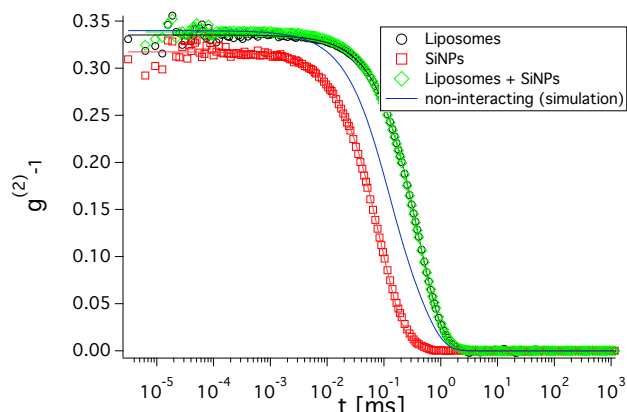


Figure 2: DLS curves of DOPC liposomes (black circles), SiNPs (red squares) and liposomes with SiNPs added (green diamonds). All curves show a single exponential decay. The blue curve is the bi-exponential decay that would result if the SiNPs were free.

tained from cryo-TEM. The identical position of the dip at about 2 1/nm shows that the thickness of the membrane was not changed, either.

From the SANS measurements alone, it is not clear if the SiNPs are adsorbed on the liposomes. Therefore, dynamic light scattering (DLS) measurements were performed (Fig. 2). They allow one to determine the translational diffusion coefficients of objects in solution, which are related to the sizes of the diffusing objects. The advantage of knowing the translational diffusion coefficient is two-fold. First, it makes it possible to check if the SiNPs are adsorbed and second, translational diffusion also contributes to the signal measured in NSE. Knowing it a priori makes the determination of the membranes' bending rigidity from NSE more reliable. As the SiNPs have a relatively high contrast in light scattering, the fast diffusion of unbound SiNPs would lead to a significantly faster decay of the curve for the sample with liposomes and SiNPs. The simulated curve in Fig. 2 corresponds to the combination of the individual curves from liposomes and SiNPs weighted with their respective intensities, which would result if the SiNPs were not adsorbed on the liposomes. However, the measured curves are almost identical for the liposomes with and without added SiNPs. This indicates that they are bound to the vesicles and further confirms our finding from SANS that the structure of the liposomes is not changed. The diffusion coefficient determined from the decay of the DLS curves will be used in the analysis of the NSE measurements.

### Membrane Dynamics

NSE allows the dynamics of objects on a timescale

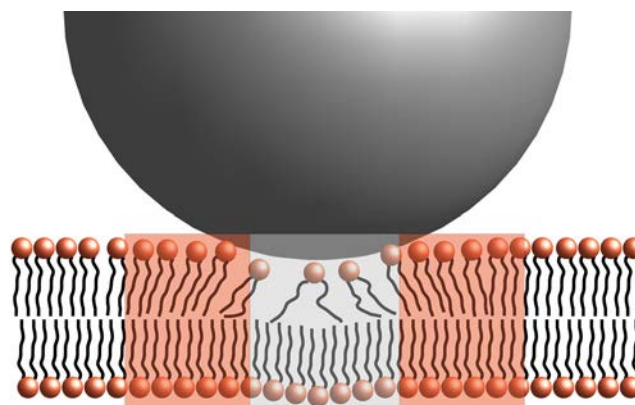


Figure 3: SiNP adsorbed on the liposome membrane; where it is directly adsorbed, undulations are suppressed (grey background) but in its vicinity (red background) the structural distortion of the bilayer causes a softening of the membrane.

from less than a nanosecond to several hundred nanoseconds and on a size range from less than a nanometer to tens of nanometers to be monitored. It is the neutron scattering method that allows the smallest changes in energy (longest time scales) to be measured. Its size and energy range are well suited to an investigation of the dynamics of biological membranes. Therefore, we performed NSE measurements on the instruments J-NSE (MLZ) and IN15 (ILL).

The data could be described as a combination of translational diffusion and membrane undulations in the framework of the Zilman-Granek model[6], which predicts the bending modulus  $\kappa$  to scale with the experimentally determined relaxation rate  $\Gamma$  as  $\Gamma \sim (1/\kappa)^{0.5}$ . Using the translational diffusion coefficient previously determined by DLS, the only free parameter is the bending rigidity and it was found that the bending rigidity decreases upon addition of the SiNPs. This is a surprising result, as the adsorption of rigid particles would be expected to stiffen the membrane. However, the adsorption of the SiNPs introduces disorder in the bilayer, which softens it in the vicinity of the adsorption site as depicted in Fig. 3. Together with the stiffening of the membrane directly at the adsorption site, this leads to a small but pronounced net softening of the membrane.

[1] D. D. Lasic, *Liposomes: from physics to applications*, Elsevier Amsterdam (1993).

[2] R. Michel and M. Gradzielski, *Int. J. Mol. Sci.* 13, 11610 (2012).

[3] R. Michel et al, *Soft Matter* 9, 4167 (2013).

[4] A. H. Bahrami et al., *Adv. Colloid Interface Sci.* 208, 214 (2014).

[5] I. Hoffmann et al., *Nanoscale* 6, 6945 (2014).

[6] A. G. Zilman and R. Granek, *Phys. Rev. Lett.* 77, 4788 (1996).

# Internal nanosecond dynamics in the intrinsically disordered myelin basic protein

A. Stadler<sup>1</sup>, L. Stingaciu<sup>2</sup>, A. Radulescu<sup>3</sup>, O. Holderer<sup>3</sup>, M. Monkenbusch<sup>1</sup>, R. Biehl<sup>1</sup>, D. Richter<sup>1</sup>

<sup>1</sup>Jülich Centre for Neutron Science (JCNS) and Institute for Complex Systems (ICS), Forschungszentrum Jülich GmbH, Jülich, Germany

<sup>2</sup>Jülich Centre for Neutron Science (JCNS) at SNS, Forschungszentrum Jülich GmbH, Oak Ridge, USA

<sup>3</sup>Jülich Centre for Neutron Science (JCNS) at MLZ, Forschungszentrum Jülich GmbH, Garching, Germany

Intrinsically disordered proteins lack a well-defined folded structure and contain a high degree of structural freedom and conformational flexibility. In solution, the myelin basic protein belongs to that class of proteins. Using small-angle scattering, the protein was found to be structurally disordered, similar to ideal Gaussian chains. Modelling via a coarse-grained structural ensemble indicated a compact core with flexible ends. Neutron spin-echo spectroscopy measurements revealed a large contribution of internal dynamics to the overall diffusion. In an alternative approach, we investigated whether models from polymer theory are suitable for the interpretation of the observed motions.

## Intrinsically Disordered Proteins

The expected structural and dynamic properties of intrinsically disordered proteins (IDPs) range from very soft structures, through folded elements connected by extended and flexible loops, to fully disordered polypeptide chains. Crystallographic structures of IDPs do not exist due to the existence of a large number of different conformational states. However, at low resolution the protein structure in solution can be well characterized by small-angle scattering of X-rays (SAXS) or neutrons (SANS), while neutron spin-echo spectroscopy (NSE) is a method well-suited to the study of polymer dynamics [1] and functional relevant motions of protein domains [2].

The myelin basic protein (MBP) is a major component of the myelin sheath in the central nervous system. In aqueous solution, MBP is primarily unstructured and is classified as intrinsically disordered. In this context, we investigated the nature and extent of large conformational motions in MBP as an example of their role in IDPs [3].

## Small-Angle Scattering and NSE Experiments

SANS was measured on the instrument KWS-1 at the MLZ in Garching. SAXS was measured on the instrument BM29 at the ESRF, Grenoble, France. NSE measurements were carried out at the J-NSE spectrometer at the MLZ.

## Solution Structure of MBP

Small-angle scattering was measured to gain information about the solution structure of MBP as a prerequisite for the NSE experiments. Measured SAXS and SANS form factors of MBP are given in Fig. 1. Both curves show power law scattering at  $q > 0.1 \text{ \AA}^{-1}$  with a power law coefficient of  $-2.1$ . A power law coefficient of  $-2$  is the characteristic sign of Gaussian chain polymers in  $\Theta$  solvent and in the melt. The slightly steeper slope of the measured data indicates a more compact conformation as compared

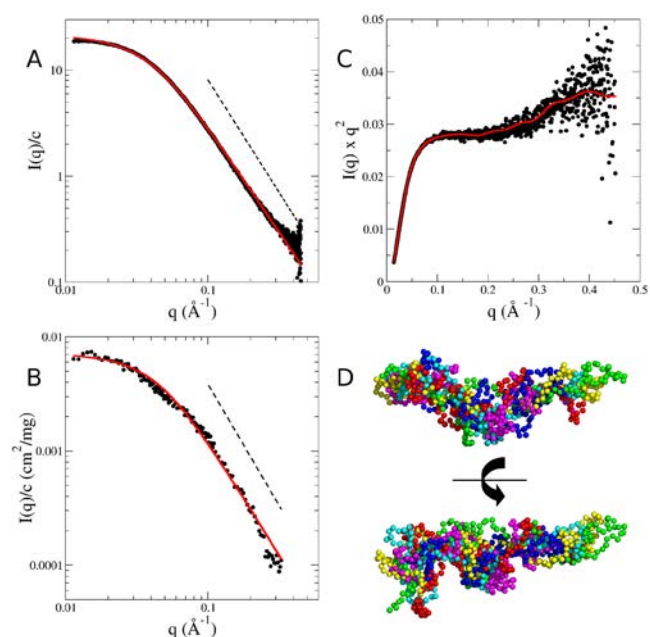


Figure 1: Measured small-angle scattering of MBP with structural models. (A) SAXS and (B) SANS data of MBP. The solid lines are fits with the Debye equation for Gaussian chains. Power law scattering behaviour above  $q > 0.1 \text{ \AA}^{-1}$  is indicated by the straight dashed lines. (C) Kratky-plot of the measured SAXS data. The solid line is the calculated scattering curve of the conformational ensemble. (D) Representative coarse-grained conformations (different colours) of MBP. The structures are rotated by  $90^\circ$  in the lower part of the figure.

to a Gaussian chain. The SAXS and SANS curves measured can be described using the Debye equation for Gaussian chains. Reverse Monte Carlo simulations were applied to generate a coarse-grained ensemble representing the structural characteristics of MBP. The general features of the selected coarse-grained conformations indicate a central core region with flexible termini, while the overall shape appears to be slightly bent (Fig. 1 (D)).

### Dynamics of MBP Measured by NSE

Collective motions of MBP were explored using NSE. The measured NSE spectra of a 54 mg/mL solution are shown in Fig. 2. In general, protein dynamics measured by NSE in solution consist of global diffusion and internal conformational motions. In a first approach we use the structural ensemble determined by small-angle scattering to interpret the NSE spectra, see Fig. 2 (A). Typically, the observed relaxation due to internal protein dynamics decays significantly faster than global protein diffusion, which is the remaining contribution to the NSE spectra in the long-time limit. At shorter times the contribution of internal protein dynamics to the spectra becomes directly visible as compared to the long time limit.

To interpret the observed internal protein dynamics in more detail, the lowest lying collective excitations of the structural ensemble were calculated using normal mode analysis. The calculated displacement patterns of the first and second non-trivial normal

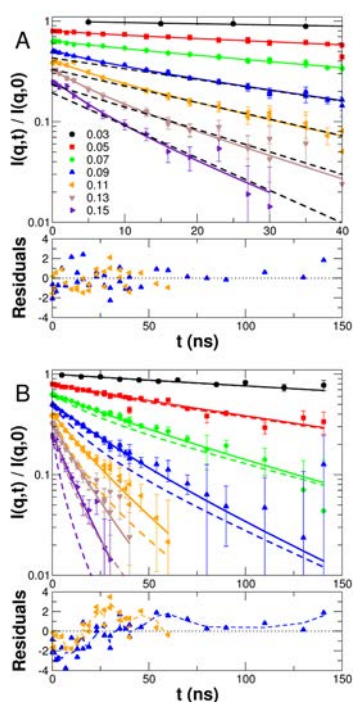


Figure 2: Measured NSE data of MBP. The residuals are given for  $q = 0.09$  and  $0.11 \text{ \AA}^{-1}$  below the graphs. (A) The solid lines are fits to the NSE data using a representative structural model. The data and fits are shown only up to 40 ns for better visibility of the short-time behaviour. The dashed lines are exponential fits to extrapolate the long-time diffusion limit. A clear separation between internal dynamics and global protein diffusion is distinctly visible at short times. (B) The dashed lines are calculated curves using the Zimm model; the solid lines are fits with the ZIF model.

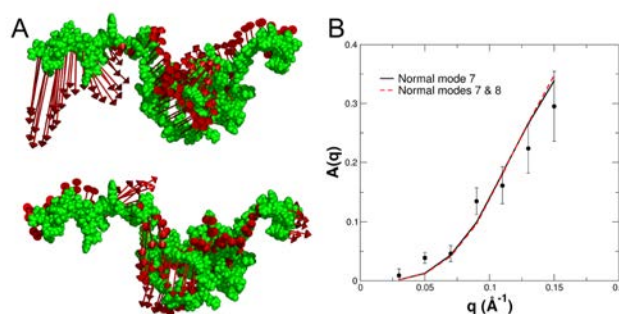


Figure 3: (A) Calculated first and second non-trivial normal modes 7 and 8 (NM 7 upper part, NM 8 lower part). (B) Contribution of internal protein dynamics to the NSE spectra  $A(q)$  and fits with normal modes 7 and 8.

modes (NMs 7 and 8) of a representative conformation are shown in Fig. 3 (A). The normal modes were used to describe the measured contribution of internal dynamics  $A(q)$  to the NSE spectra, see Fig. 3 (B). NM 7 is the dominating collective excitation of the protein and fully reproduces the measured  $A(q)$ .

In an alternative approach we tested whether the dynamics of MBP can be described using simplified models from polymer theory. The classical Zimm model is a coarse-grained description of the dynamics of polymers in solution. To account for additional microscopic interactions - such as, for example, internal barriers, hindered dihedral rotations, side-chain interactions, or hydrogen bonding - the Zimm model was extended to the Zimm models with internal friction (ZIF). The fits with the Zimm and ZIF models to the NSE spectra are shown in Fig 2 (B). The classical Zimm model does not represent the measured data. The ZIF model shows small but systematic deviations from the measured data. The large value of the internal friction also leads to the breakdown of the mathematical structure of the Zimm model.

### Conclusions

The NSE experiments showed a high flexibility of the structural ensemble. Our results are important for a biophysical understanding of the nature and extent of large-scale conformational motions in IDPs. Our experiment clearly demonstrates the potential of neutron scattering for the investigation of IDPs.

- [1] D. Richter et al., *Advances in Polymer Science: J. Neutron Spin Echo in Polymer Systems*, Vol. 174, Springer, Berlin (2005).
- [2] R. Inoue et al., *Biophys. J.* 99, 2309 (2010).
- [3] A. M. Stadler et al., *J. Am. Chem. Soc.* 136(19), 6987 (2014).

# From molecular dehydration to excess volumes of demixing thermo-responsive polymer solutions

M. Philipp<sup>1</sup>, K. Kyriakos<sup>1</sup>, L. Silvi<sup>1,2</sup>, W. Lohstroh<sup>1,2</sup>, W. Petry<sup>1,2</sup>, J. K. Krüger<sup>3,4</sup>, C. M. Papadakis<sup>1</sup>, P. Müller-Buschbaum<sup>1</sup>

<sup>1</sup>Physik-Department E13, Technische Universität München, Garching, Germany

<sup>2</sup>Heinz Maier-Leibnitz Zentrum (MLZ), Technische Universität München, Garching, Germany

<sup>3</sup>Laboratoire de Physique des Matériaux, Université du Luxembourg, Luxembourg, Luxembourg

<sup>4</sup>Fakultät für Werkstoffwissenschaften, Universität des Saarlandes, Germany

**E**nvironmentally responsive polymers are of interest in view of their current use, and foreseen future implementation in everyday life. Typical fields of application are soft robotics, sensors, drug delivery systems, and stimuli-responsive surfaces. The working principle of these smart polymeric materials is based on a demixing phase transition, leading to massive changes in volume and elasticity. To elucidate the underlying mechanisms of phase separation, we investigate the dehydration of model thermo-responsive polymers in an aqueous environment using the time-of-flight spectrometer TOF-TOF. Our neutron scattering studies are of particular value for a deeper understanding of the nature of the molecular driving mechanisms of the demixing process, their impact on macroscopic order parameter susceptibilities, and a better theoretical description of the dehydration.

## Environmentally responsive polymers in an aqueous environment

In engineering, bioengineering and medicine there is a huge demand for tailor-made polymeric materials that possess the ability to undergo massive changes in their volume, their elasticity or related properties when exposed to small stimuli [1]. In order to design novel stimuli-responsive materials with the desired switching behavior, a multitude of complex architectures of responsive hydrogels, brushes, thin films, colloids and micellar systems have been synthesized. The switching mechanism is generally provoked by a sharp demixing phase transition, which is often of the lower critical solution temperature type for aqueous systems. In the case of hydrogels the phase separation is commonly denoted as a volume phase transition, which hints at the fact that the volume expansion coefficient can be considered as the macroscopic order parameter

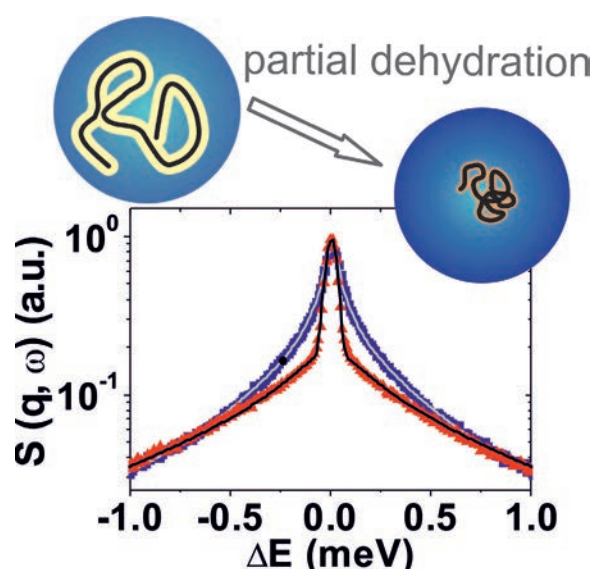


Figure 1: Investigation of the diffusion dynamics of the hydration water and the almost freely diffusing water during the partial dehydration of the classical responsive polymer PNIPAM in aqueous solution. Central part of quasi-elastic neutron scattering spectra recorded for the homogeneous solution (in blue) and the phase-separated solution (in red).

ter susceptibility. On the molecular scale, important variations in hydrophobic interactions and hydrogen bond interactions seem to govern the phase separation and provoke a coil-to-globule transition in the case of individual polymer chains [2]. As a consequence, important changes in structure and in molecular diffusion occur.

One prerequisite for major progress and future innovation in this growing field of smart synthetic polymeric materials is a more fundamental understanding of the molecular driving mechanisms of the phase separation. Another crucial point is the elucidation of the impact of the molecular processes on those properties, which are strongly coupled to the macroscopic order parameter. In order to contribute to these issues, we study the demixing transition of model responsive materials, namely aqueous solutions of the classical thermo-responsive polymer

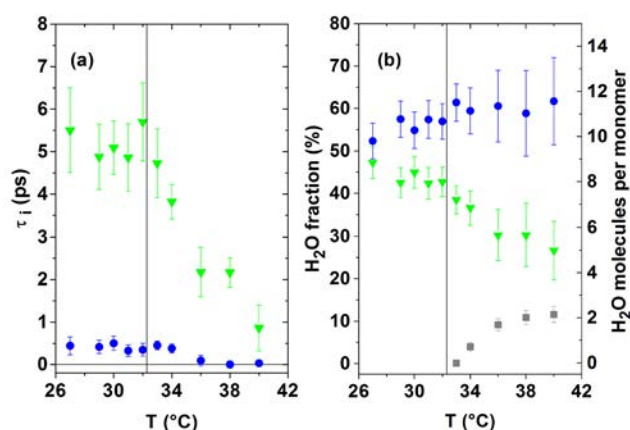


Figure 2: (a) Residence time of hydrogen atoms of water molecules versus temperature, indicating the expulsion of water molecules from the hydration shells of PNIPAM. (b) Fraction of water molecules belonging to the different water populations. Green symbols: weakly bound hydration water, grey symbols: strongly bound hydration water, blue symbols: almost freely diffusing water.

called poly(N-isopropylacrylamide) (PNIPAM) [4,5]. The study of simple PNIPAM solutions – as compared to the above-mentioned technologically more valuable materials such as hydrogels, or thin films – enables us to concentrate on the basics of the phase transition by avoiding its interference with mechanical constraints exerted on the macromolecules by covalent network knots or by interfacial interactions.

### Dehydration behavior of phase-separating, thermo-responsive solutions

Changes in intermolecular interactions and in molecular transport are at the origin of the phase separation [1–5]. Here, we focus on the diffusion dynamics of the hydration water and the almost freely diffusing water across the demixing transition of a concentrated aqueous solution of 25 mass% PNIPAM with the aim of accessing the molecular order parameter [5]. Its demixing temperature lies at 32.2 °C. The incoherent neutron scattering experiment was performed at the cold neutron time-of-flight spectrometer TOF-TOF at the MLZ in Garching. Fig. 1 shows that the central part of the spectra significantly varies as the demixing temperature is crossed. A schematic drawing of the partial dehydration and the structural changes of a macromolecule subjected to the related coil-to-globule transition is also included in the figure. The scattering curves below and above the phase transition have been analyzed assuming a diffusion model of two different water populations, which will be denoted in the following weakly bound water and almost freely diffusing water (plus the elastic contribution). As expected, the isotropic jump

diffusion model is applicable to both water populations and the average residence time  $\tau_1$  and the relative fractions are shown in Fig. 2. The average residence times, before jumping to another position, of the weakly bound hydration water clearly decreases in a remarkably continuous manner as it is expelled from the hydration shells. It approaches the value observed for the almost freely diffusing water of the phase-separating solution. The fraction of the different water populations also changes upon demixing (see Fig. 2(b)). Whereas most of the weakly bound hydration water is expelled from the hydration shells during phase separation, our studies indicate that the mobility of part of the hydration water is significantly reduced above the demixing temperature. This can be concluded from the increase of the observed elastic intensity (Fig. 2(b), grey symbols). Hence, only a partial dehydration of the macromolecules seems to occur and the hydration number decreases by about six for the considered demixing 25 mass% PNIPAM solution.

### Impact of dehydration on the excess volumes released during phase separation

We elucidated the impact of molecular dehydration on the macroscopic order parameter susceptibility by studying, in addition, the volume expansion coefficients  $\alpha(T)$  of phase-separating dilute to concentrated aqueous PNIPAM solutions [5]. Since  $\alpha(T)$  shows a peak-like feature during phase separation, the demixing solutions significantly expand. This is attributed to a less dense packing of the water molecules, as they are expelled from the hydration shells that envelop the PNIPAM chains. A qualitative understanding of the relationship between the molecular and macroscopic key processes governing the demixing transition could be provided in the frame of the immense strain-softening of the ferroelastic-like, phase-separating solutions [4,5]. To conclude, our incoherent neutron scattering experiment provides important insight into the molecular-mechanistic origins of demixing transitions, as well as of the dehydration process of PNIPAM, and related synthetic and biological polymers.

- [1] I. Tokarev et al., *Soft Matter* 5, 511 (2009).
- [2] Y. Maeda et al., *Langmuir* 16, 7503 (2000).
- [3] A. Laschewsky et al., *Prog Colloid Polym Sci* 140, 15 (2013).
- [4] M. Philipp et al., *Soft Matter* 9, 5034 (2013).
- [5] M. Philipp et al., *J. Phys. Chem. B* 118, 4253 (2014).

# Polyethylene glycol polymer layers – studies from tethered lipid bilayers to protein-cell interactions

P. J. F. Röttgermann<sup>1</sup>, S. Hertrich<sup>1</sup>, I. Berts<sup>1</sup>, A. Rühm<sup>2</sup>, J.-F. Moulin<sup>3</sup>, J.O. Rädler<sup>1</sup>, B. Nickel<sup>1</sup>

<sup>1</sup>Fakultät für Physik & CeNS, Ludwig-Maximilians-Universität, München, Germany

<sup>2</sup>Max Planck Institute for Intelligent Systems, Stuttgart, Germany

<sup>3</sup>German Engineering Material Science Centre (GEMS) at MLZ, Helmholtz-Zentrum Geesthacht GmbH, Garching, Germany

The structural design and analysis of bio-mimicking surfaces is of great importance for the design of artificial environments for cell adhesion. Such bioavailable surfaces can be mimicked by tethered, solid-supported lipid bilayers (TLB) using polyethylene glycol (PEG) as a cushion. PEG can also be used for the spatial organization of proteins and PEG linked as a copolymer on a surface. Thus, cell motility can be tuned by variation of the surface parameters.

## PEG-Tethered Lipid Bilayers

Solid-supported lipid bilayers can act as a workbench for the study of membrane processes. The realization of tethered lipid bilayers is difficult. Here, we designed TLBs with a cushion thickness comparable to a bilayer dimension [1]. LipoPEG was used, as PEG is a weakly interacting cushion material. The PEG end is grafted onto the solid surface and the lipid end can anchor a lipid bilayer (Fig. 1).

Using FRAP measurements, we determined a diffusion constant of  $2.1 \pm 0.1 \mu\text{m}^2\text{s}^{-1}$  for the TLB which is only 12 % lower than the diffusion constants of sup-

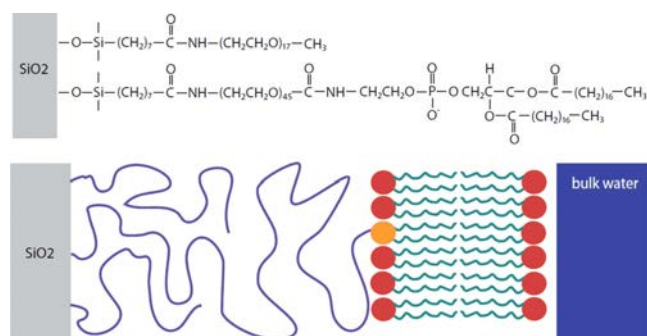


Figure 1: Structure of the tethered lipid bilayer (TLB): (a) Chemical composition of the silane and PEG–lipid cushion. (b) Cartoon of the structure of the TLB consisting of the silicon oxide surface, the PEG cushion, one tethered lipid (yellow head), and several lipids in the bilayer (red heads). Bulk water is represented in blue. [1]

ported lipid bilayers (SLB). This suggests that the bilayer exhibits only a small immobile fraction without any grafted lipids as obstacles. Specular x-ray and neutron reflectivity (NREX at MLZ) were performed to determine the structural layer composition of the TLB. A three layer model consisting of a silicon oxide layer, a PEG layer and a lipid chain region fits the neutron reflectivity (Fig. 2). The PEG interlayer of the TLB is highly hydrated, with a water content of  $90 \pm 3 \%$ .

AFM indentation measurements at 50 different spots proved (i) the PEG perpendicular layer softness and (ii) its homogeneity along the surface. As the TLB ruptures occur only after deformation of about 40 Å compared to 20 Å for a SLB, the additional deformation can be attributed to the compression of the PEG cushion. Possible applications of such elevated lipid bilayers are, for example, the study of membrane-perforating proteins or binding studies of membrane-associated proteins.

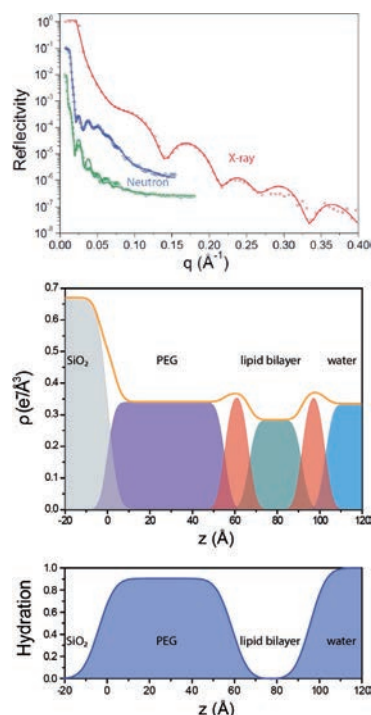


Figure 2: (a) Normalized neutron and X-ray reflectivity data and fit (b) Electron density of the different layers of the system, extracted from the X-ray measurement. (c) Hydration of lipid bilayer and PEG cushion extracted from the difference of the neutron models at different contrasts ( $\text{D}_2\text{O}$  and  $\text{D}_2\text{O}/\text{H}_2\text{O}$  mix with  $\text{SLD } 4.0 \times 10^{-6} \text{ \AA}^{-2}$ ). [1]

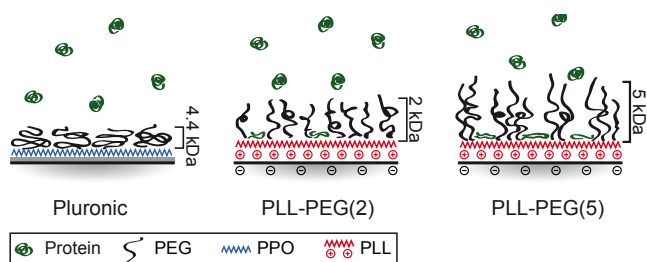


Figure 3: Interpretation based on the neutron SLD profiles of the adsorption of FN in the three different polymer coatings Pluronic (PPO-PEG), PLL-PEG(2) and PLL-PEG(5). In the first case, FN is not adsorbed on the Pluronic, while on the PLL-PEG samples FN penetrates the extended PEG layers to attach to underlying PLL. The higher PEG density leads to stiffer chains and therefore higher protein adsorption. [3]

### Cell Motility on PEG-Copolymers

To understand how cells and proteins interact on PEG copolymer surfaces, structural analysis is needed. It has been previously observed that cells are able to migrate on passivated PEG areas which were exposed to proteins such as fibronectin (FN) [2]. Here, we employed neutron scattering (REF-SANS at MLZ) to probe the structure of different PEG layers and determine the amount and distribution of FN in these PEG layers [3]. We focused our study on two polymer constructs: first, PEG (4.4 kDa) grafted onto a hydrophobic polymer anchor polypropylene oxide (PPO), and second, PEG chains of 2 and 5 kDa grafted in a ratio of 3.5 onto the poly-L-lysine (PLL-PEG(2) and PLL-PEG(5)). The REFSANS data revealed that PEG repellence is mainly influenced by the underlying polymer-layer and secondly by the PEG density. Hydrophobic layers such as PPO are shielded by the PEG chains and are, therefore, highly protein repellent. In the moiety of hydrophilic layers (PLL) protein adsorption of  $0.4 \text{ mg/cm}^2$  for PLL-PEG(2) and  $0.7 \text{ mg/cm}^2$  for PLL-PEG(5) was found. Higher PEG densities lead to higher protein repellence. However, too high a PEG density (e.g. surface density  $\sigma = 1.99 \text{ \AA}^{-2}$  for PLL-PEG(5)) can lead to a contrary effect of increased protein adsorption. PEG brushes probably become stiffer and are not that flexible anymore (Fig. 3).

Surface properties were compared with cell behavior. No cell adhesion was noticed as no protein is adsorbed on the PEG linked PPO polymer (Pluronic). By contrast, cell spreading was observed on PLL-PEG. Cell spreading on PLL-PEG(5) is comparable to that on pure FN surfaces. Apart from different spreading, cell motility also correlates with different surface properties. Cell motion was tracked by time-

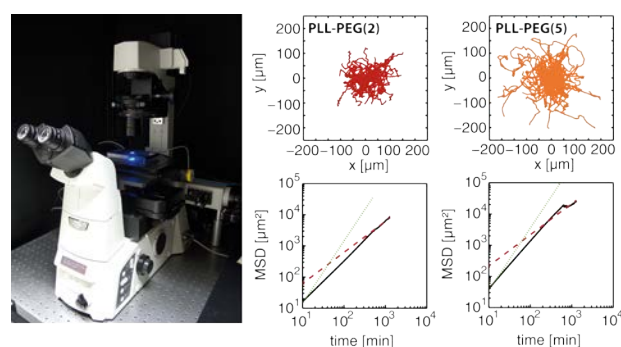


Figure 4: (a) Setup for time-lapse fluorescence microscopy for cell tracking. (b) Representative cell trajectories on the two different substrates over a period of 24 h: PLL PEG(2) (red), PLL PEG(5) (orange) (c) Mean square displacements (MSD) (black curves) are plotted against time for the various substrates. As a guide to the eye, the MSD dependence for directed motion (dotted green curve, slope 2) and diffusive motion (dashed red curve, slope 1) are indicated. [3]

lapse fluorescence microscopy (Fig. 4). The longest persistence time of cell motion is observed on a pure FN surface, whereas the highest velocity is observed on PLL PEG(5) (Fig. 4). As cells polarize in one direction (mostly random in the absence of a chemo-attractant), they have a higher probability of moving forward in the same direction instead of turning towards any other direction if the amount of protein is high. The highest speed is measured on PLL PEG(5). It exhibits fewer adhesion points than pure FN layers which leads on the one hand to more frequent interruption in the migration and on the other hand to faster movement, possibly due to faster detachment.

We generated artificial surfaces with TLBs which could provide a more natural and cell-like surrounding. Further studies on the membrane interaction of living cells on solid surfaces containing FN and PEG are needed, using neutron reflectivity. Information on the surface interaction of macromolecular biomolecules paves the way for more advanced micro-structured surfaces which can be used for cell migration assays or high-throughput single cell analysis.

### Acknowledgements

Financial support by the Deutsche Forschungsgemeinschaft (DFG) via project B1 within the SFB 1032, the Excellence Cluster 'Nanosystems Initiative Munich (NIM)', the Center for NanoScience (CeNS), FP7 EU grants NanoTransKinetics and NanoMILE, and by BMBF-05K13WM1 and 05K10WM1 is gratefully acknowledged.

[1] S. Hertrich et al., *Langmuir* 30, 9442 (2014).

[2] P. J. F. Röttgermann et al., *Soft Matter* 10, 2397 (2014).

[3] P. J. Röttgermann et al., *Macromol. Biosci.* 14, 1755 (2014).

# Structural insights into nanoparticles containing Gadolinium complexes as potential theranostics

L. Paduano<sup>1</sup>, A. Luchini<sup>1</sup>, N. Szekely<sup>2</sup>, V. Pipich<sup>2</sup>

<sup>1</sup>Department of Chemical Sciences, University of Naples "Federico II", Napoli, Italy

<sup>2</sup>Jülich Centre for Neutron Science (JCNS) at MLZ, Forschungszentrum Jülich GmbH, Garching, Germany

The term "theranostics" refers to the currently expanding research field where suitably designed systems, able to combine diagnostic (PET and SPECT in combination with CT and/or MRI) and therapeutic modalities in one unified material, have promising applications. These multifunctional systems provide the opportunity to develop individually designed therapies against various diseases to achieve personalized medicine. In recent years, supramolecular aggregates containing Gd(III) complexes have been proposed as MRI Contrast Agents. In the present report, the design and characterization of 1-Oleyl glycerol (MO) based nanostructures doped with a synthetic amphiphilic gadolinium complex (C18)<sub>2</sub>DTPA(Gd) are presented. The aim of this research is the development of well-defined and stable highly-ordered three dimensional mesophases for potential application as highly efficient MRI contrast agents. Moreover, drug-loading of the anticancer doxorubicin (Dox) in such nanostructures was also investigated for potential theranostic applications.

## Development of a theranostic device

Among the recently proposed theranostic devices, liposomes, obtained via amphiphilic gadolinium complexes or by their co-aggregation with surfactants, as well as micelles, display higher efficacy with respect to MRI contrast agents based on isolated Gadolinium complexes. In addition to liposomes and micelles, amphiphilic molecules also aggregate in a water solution, giving a variety of higher order two (2D) or three (3D) nanostructures. In particular, 2D inverse hexagonal and 3D inverse cubic structures can be dispersed as stable particles, offering substantial advantages as compared to traditional supramolecular aggregates. Indeed, these nanostructures present much higher payloads of Gadolinium ions than micellar and liposomal systems with an expected increased relaxivity rate ( $1/T_1$ ) [2,3,4]. The improved relaxivity values are due to the presence of nano-scale water channels that offer a better environment for diffusion and fast exchange between gadolinium coordinated water and bulk water.

Here, we report on the structural characterization of new gadolinium based contrast agents obtained by

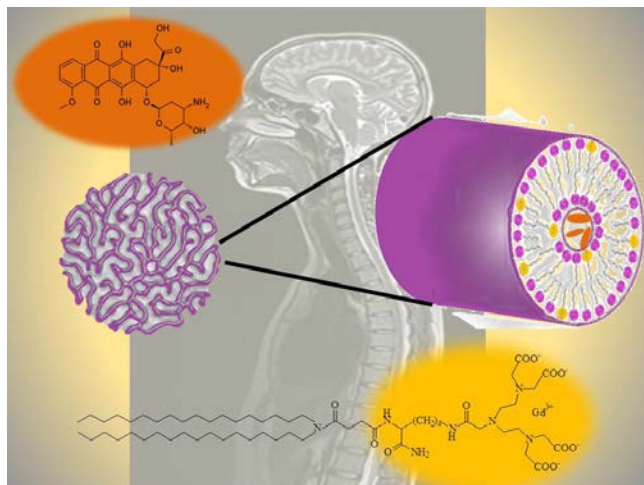


Figure 1: Bicontinuous Nanoaggregates Containing Gadolinium complexes and Doxorubicine as potential theranostics.

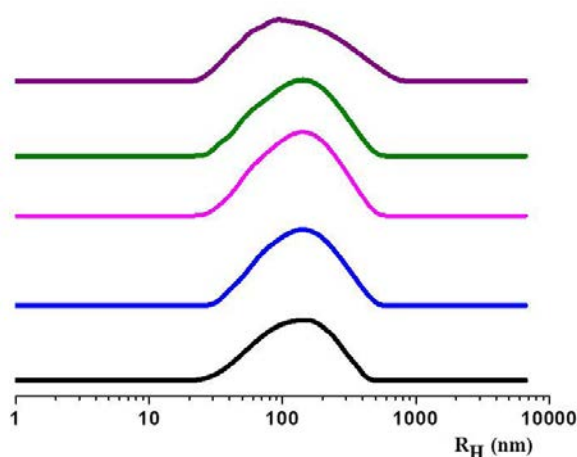


Figure 2: Example of the hydrodynamic radii distribution at 90°. For all the systems the total concentration was 0.2 mmol kg<sup>-1</sup>.

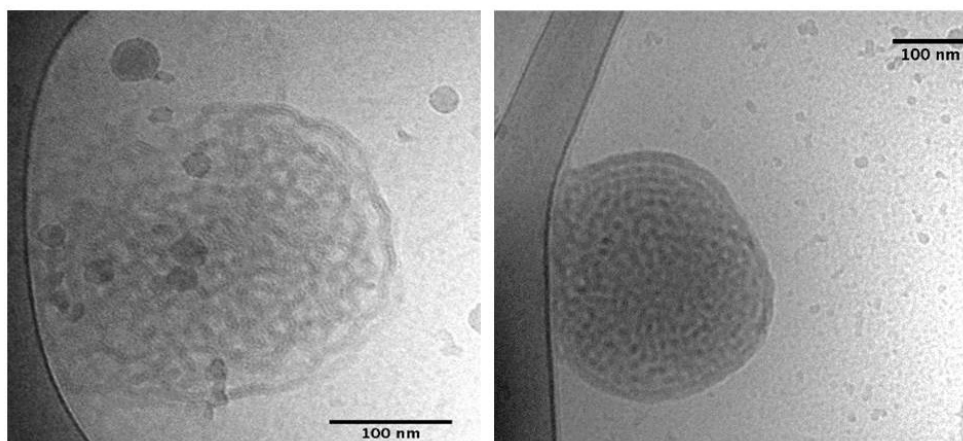


Figure 4: Cryo-Tem Image on bicontinuous aggregates present in samples containing 1 % mol (left) and 10 % mol (right) of amphiphilic gadolinium complex.

co-aggregation of an amphiphilic gadolinium complex,  $(C18)_2DTPA(Gd)$ , with monoolein (MO). The nanostructures obtained display high relaxivity values. Since these nanostructures are also of interest for their application in drug controlled-release, their doxorubicin encapsulation capability was also evaluated.

### Structure revealed by light and neutrons

Monolein (MO) nanoaggregates containing different amounts (in mol.) of  $(C18)_2DTPA(Gd)$  amphiphilic gadolinium complex (0 %, A1; 1 %, A2; 5 %, A3; 10 %, A4 and 20 %, A5) and Pluronic F127 (PF127) at 15 % w/w were formulated.

The structural characterization was carried out by combining information obtained through Dynamic Light Scattering (DLS) and Small-Angle Neutron Scattering (SANS) measurements. In all the samples investigated, the DLS data revealed the presence of a single broad distribution of aggregates with mean hydrodynamic radius in the range of 70-

200 nm (Fig. 2). The morphology of these aggregates, and their geometrical characteristics, were obtained through SANS measurements. Scattering cross sections for all systems studied (Fig. 3) showed the presence, in the low region, of a power law decay:  $(d\Sigma/d\Omega) \propto q^\alpha$ , with  $\alpha$  of about -3. According also to the Cryo-TEM image performed on selected samples (Fig. 4), this is due to the presence of bicontinuous aggregates. Fitting optimization, with an appropriate model of  $d\Sigma/d\Omega$  vs.  $q$  made it possible to obtain structural parameters of the aggregates. The thickness of the bilayers was evaluated to be about 3 nm and the mean distance between the centers of the layers about 5 nm. All the different aggregates showed high relaxivity values per Gd complex ( $r_{1p} \approx 11 \text{ mM}^{-1}\text{s}^{-1}$  at 20 MHz and 298 K) and a Drug-Loading Capability (DLC) with respect to doxorubicin encapsulation of about 95 % at drug/lipid (w/w) ratio of 0.10.

### Nanoparticles containing Gd-complex: major results

With the aim of introducing novel theranostic agents, the preparation and characterization of nanoaggregates of MO/PF127 containing the amphiphilic Gd-complex  $(C18)_2DTPA-Gd$  were presented. Experimental evidence indicates that these are bicontinuous aggregates. The relaxometric properties, the size and shape of the nanostructure, as well the Doxorubicin loading ability suggest the nanocompounds obtained could act as theranostics for simultaneous cancer therapy and MRI visualization.

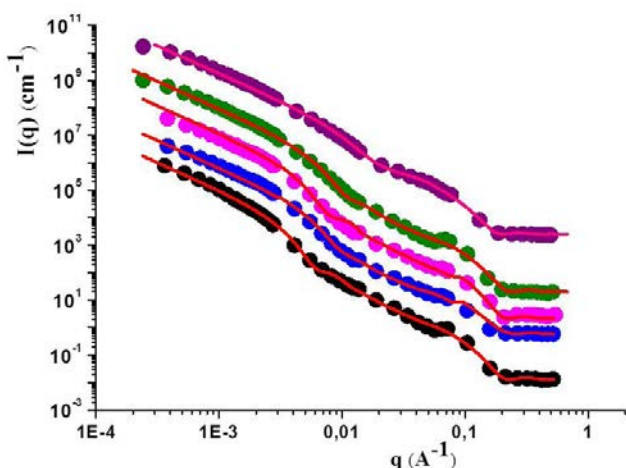


Figure 3: Neutron scattering profiles of the systems studied.

- [1] A. Accardo et al., *Colloid Polym Sci* 292(5), 1121 (2014).
- [2] A. Accardo et al., *J. Pept. Sci.* 19(4), 190 (2013).
- [3] A. Accardo et al., *Mol. BioSyst.* 6(5), 878 (2010).
- [4] M. Vaccaro et al., *ChemPhysChem* 8(17), 2526 (2007).

# Quasielastic neutron scattering insight into the molecular dynamics of all-polymer nano-composites

D. Bhowmik<sup>1</sup>, J. A. Pomposo<sup>2,3</sup>, F. Juranyi<sup>4</sup>, V. García Sakai<sup>5</sup>, M. Zamponi<sup>6</sup>, Y. Su<sup>6</sup>, A. Arbe<sup>2</sup>, J. Colmenero<sup>1,2</sup>

<sup>1</sup>Donostia International Physics Center, San Sebastián, Spain

<sup>2</sup>Centro de Física de Materiales (CSIC-UPV/EHU), Materials Physics Center (MPC), San Sebastián, Spain

<sup>3</sup>IKERBASQUE - Basque Foundation for Science, Bilbao, Spain

<sup>4</sup>Laboratory for Neutron Scattering, Paul Scherrer Institut, Villigen, Switzerland

<sup>5</sup>ISIS Facility, Rutherford Appleton Laboratory, Harwell Science & Innovation Campus, Didcot, United Kingdom

<sup>6</sup>Jülich Centre for Neutron Science (JCNS) at MLZ, Forschungszentrum Jülich GmbH, Garching, Germany

**Q**ENS has selectively revealed the component dynamics in isotopically labelled nano-composites (NCs) where single-chain nano-particles (SCNPs) based on PMMA [poly(methyl methacrylate)] are mixed with PEO [poly(ethylene oxide)]. Effects on the  $\alpha$ -methyl group dynamics of SCNPs have been characterized. PEO dynamics shows deviations from Gaussian behavior which become more pronounced with increasing concentration of SCNPs.

jects showing unique and remarkable physicochemical, rheological and sensing properties as a result of their locally collapsed structure and ultra-small size [1]. They are also promising candidates for mixing with linear polymers, leading to novel NCs with tunable properties.

Here, we investigated the component dynamics of two NCs consisting of mixtures of linear PEO chains with PMMA-based SCNPs (see Scheme 1, [2]), which show large dynamic asymmetry due to the huge difference in the glass-transition temperatures  $T_g$  of the components. We focused on two SCNPs' concentrations: 25 wt% [3] and 75 wt% [4]. To selectively follow one component, the other was deuterated. The coherent contribution was characterized by DNS (MLZ). Combining SPHERES (MLZ), IRIS (ISIS) and FOCUS (PSI), we covered a large dy-

## QENS and Diffraction with Polarization Analysis: Right Tools to Unravel Component Dynamics in Novel Nano-Composites

SCNPs obtained by intramolecular cross-linking of linear macromolecules are emerging soft nano-ob-

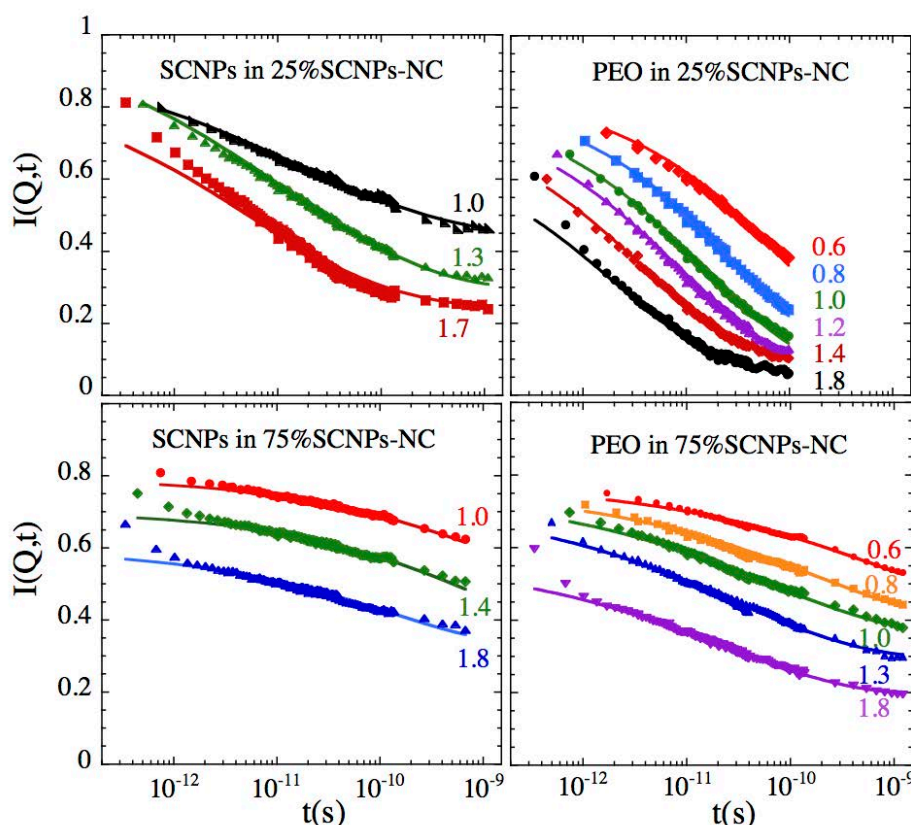
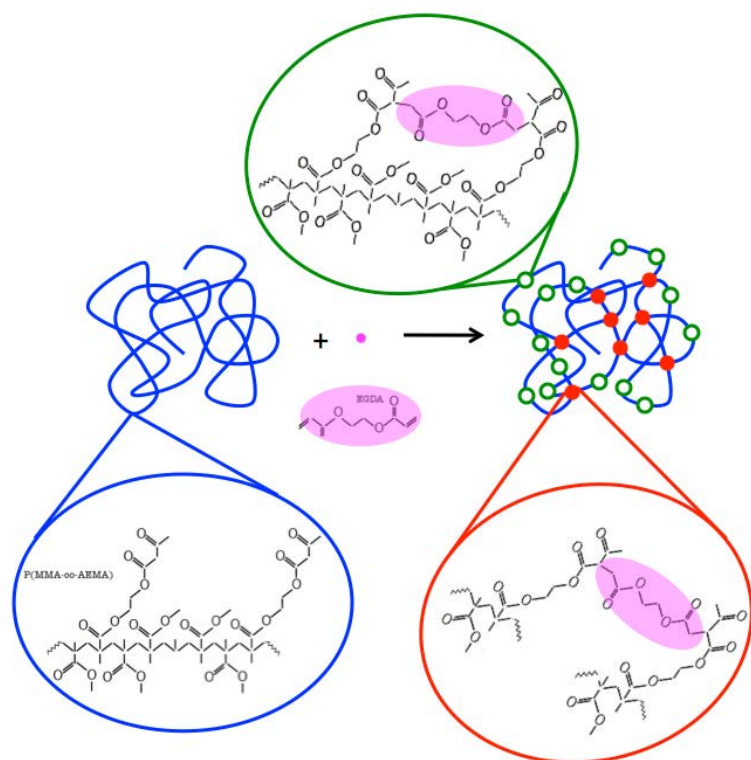


Figure 1: Intermediate scattering function obtained by Fourier transformation and deconvolution of the spectra measured by different spectrometers on the distinctly labeled samples. Lines are fits to the RRDM (PMMA-SCNP's-component) and to stretched exponentials (PEO-component) [3,4]. Different curves correspond to the different  $Q$ -values indicated (in  $\text{\AA}^{-1}$ ).



Scheme 1: Schematic illustration of the synthesis of PMMA-SCNPs through Michael addition-mediated multidirectional self-assembly using random copolymers of methyl methacrylate (MMA) and (2-acetoacetoxy)ethyl methacrylate (AEMA) as precursors, and ethylene glycol diacrylate (EGDA) as intrachain cross-linking agent (see, e.g. Ref. [2]).

dynamic range (see e.g. Fig. 1), essential to a study of the dynamics in such complex materials.

### SCNPs Dynamics: Methyl-Group Rotations

In the range investigated, SCNPs' dynamics is dominated by the  $\alpha$ -methyl group motions of PMMA. Analysis in terms of the rotation rate distribution model (RRDM) [5] - taking into account the disorder in amorphous samples - revealed an average rate higher than in bulk PMMA for the PEO-rich sample [3]. This could be due to the plasticization effect induced by the fast PEO. In the other system [4],  $\alpha$ -methyl groups are hardly affected by PEO except for hints of a more heterogeneous environment than in bulk.

### PEO Dynamics: Deviations from Gaussian Behavior and Confining Effects by SCNPs' matrix

QENS results on the PEO-rich sample [3] revealed slightly slowed down dynamics with respect to the bulk and indications for distributed chain mobility. At local scales, deviations from Gaussian behavior occur. They were described by the anomalous jump diffusion model [6], which assumes a distribution of elementary jumps at the origin of the sublinear diffusion of the atoms. The most probable jump distance  $l_0$  turned out to be rather similar in bulk and NC samples.

A more exotic behavior was found in the SCNPs-rich NC [4]. When approaching  $T_g$ , PEO dynamics shows confinement effects as a result of the dramatic slowing down of the SCNPs. Well above  $T_g$ , PEO dynamics exhibits anomalously strong deviations from Gaussian behavior, which, interestingly enough, grow with increased mobility of the SCNPs. If this behavior is interpreted in terms of the anomalous jump diffusion model, the value of  $l_0$  dramatically increases with respect to those deduced for the other NC or in bulk. In the presence of a majority of SCNPs, PEO segments seem to be trapped in effective cages imposed by the SCNPs for a very long time - more than two orders of magnitude longer than in bulk - before the sub-diffusive process leading to segmental relaxation sets in. Local loops in the SCNPs may play an important role in this trapping mechanism.

[1] L. Oria et al., *Adv. Mater.* 22, 3038 (2010).

[2] A. Sanchez-Sanchez et al., *ACS Macro Lett.* 2, 491 (2013).

[3] D. Bhowmik et al., *Macromolecules* 47, 304 (2014).

[4] D. Bhowmik et al., *Macromolecules* 47, 3005 (2014).

[5] See, e.g. J. Colmenero et al., *Prog. Polym. Sci.* 30, 1147 (2005).

[6] A. Arbe et al., *Phys. Rev. Lett.* 89, 245701 (2002).

# Highly asymmetric genetically encoded amphiphiles

I. Weitzhandler<sup>1</sup>, J. R. McDaniel<sup>1</sup>, S. Prevost<sup>2</sup>, M.-S. Appavou<sup>3</sup>, M. Gradzielski<sup>2</sup>, A. Chilkoti<sup>1</sup>

<sup>1</sup>Department of Biomedical Engineering and Research Triangle MRSEC, Duke University, Durham, North Carolina, USA

<sup>2</sup>Stranski-Laboratorium für Physikalische und Theoretische Chemie, Institut für Chemie, Technische Universität Berlin, Berlin, Germany

<sup>3</sup>Jülich Centre for Neutron Science (JCNS) at MLZ, Forschungszentrum Jülich GmbH, Garching, Germany

**E**lastin-like polypeptides (ELPs) are a class of biopolymers consisting of the pentameric repeat unit  $(VPG_{\alpha}G)_{n}$  based on the sequence of mammalian tropoelastin that display a thermally induced phase transition in aqueous solution. We have discovered a remarkably simple approach to driving the spontaneous self-assembly of high molecular weight ELPs into nanostructures by genetically fusing a short 1.5 kDa  $(XG_{\gamma})_{8}$  assembly domain to one end of the ELP. Classical theories of self-assembly based on the geometric mass balance of hydrophilic and hydrophobic block copolymers suggest that these highly asymmetric polypeptides should form spherical micelles. Surprisingly, when sufficiently hydrophobic amino acids (X) are presented in a periodic sequence such as  $(FGG)_{8}$  or  $(YG)_{8}$ , these highly asymmetric polypeptides self-assemble into cylindrical micelles whose morphology can be tuned by the sequence of the assembly domain. These nanostructures were characterized by cryogenic transmission electron microscopy and small angle neutron scattering in order to gain a detailed mesoscopic picture of the self-assembly.

Elastin-like polypeptides (ELPs) are recombinantly synthesized polypeptides with the monomeric repeat unit of VPGXG where the guest residue X can be any amino acid except proline. ELPs are frequently termed “smart” biomaterials because they exhibit highly tunable lower critical solution temperature (LCST) phase transition behavior. Because of this precise control of the polymerization product, as well as their non-toxicity and biodegradability, ELPs are very attractive materials for biomedical applications [1-3].

Previous publications by our group describe a remarkably simple approach to building self-assembled ELP nanoparticles. Functionalization of the C-terminus of an ELP with a short  $(CGG)_{8}$  domain provides eight unique sites to which hydrophobic small molecules (e.g. small-molecule chemotherapeutics) can be covalently attached, thereby providing the polymer with sufficiently amphiphilic character to self-assemble into spherical micelles [3-5].

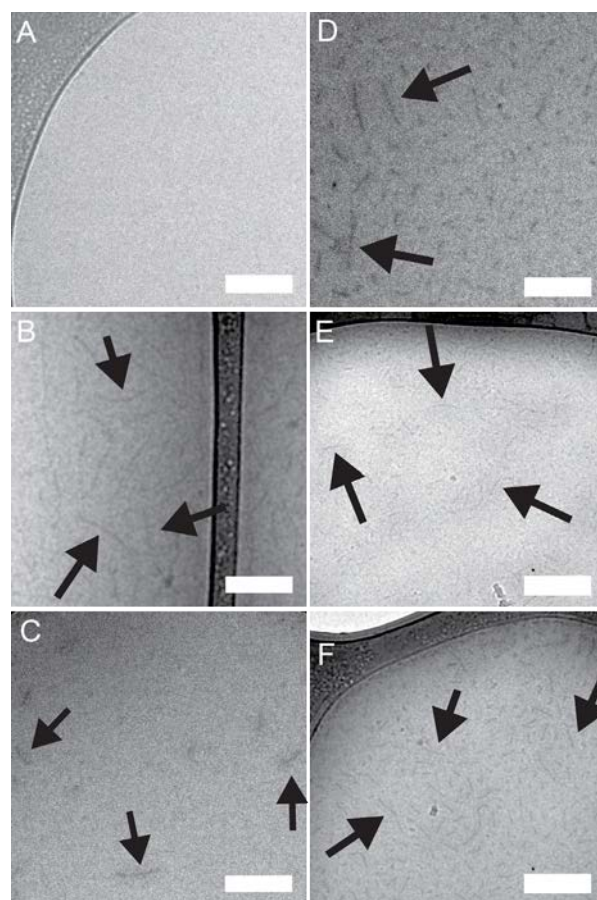


**Figure 1:** Cryo-TEM micrographs of genetically encoded asymmetric amphiphiles. (A–C) A160- $(YGG)_{8}$ , A160- $(YG)_{8}$ , and A160- $Y_{8}$ , respectively. (A) Constructs such as A160- $(YGG)_{8}$  that do not self-assemble could not be visualized by cryo-TEM because of their high levels of hydration and low densities. (B,C) Changing the assembly domain from  $(YG)_{8}$  (B) to  $Y_{8}$  (C) causes a significant decrease in the length of the cylindrical micelles. (D–F) A160- $(FGG)_{8}$  (D), A80- $(FGG)_{8}$  (E), and A40- $(FGG)_{8}$  (F) self-assemble into cylindrical micelles with similar aspect ratios. Scale bar represents 200 nm.

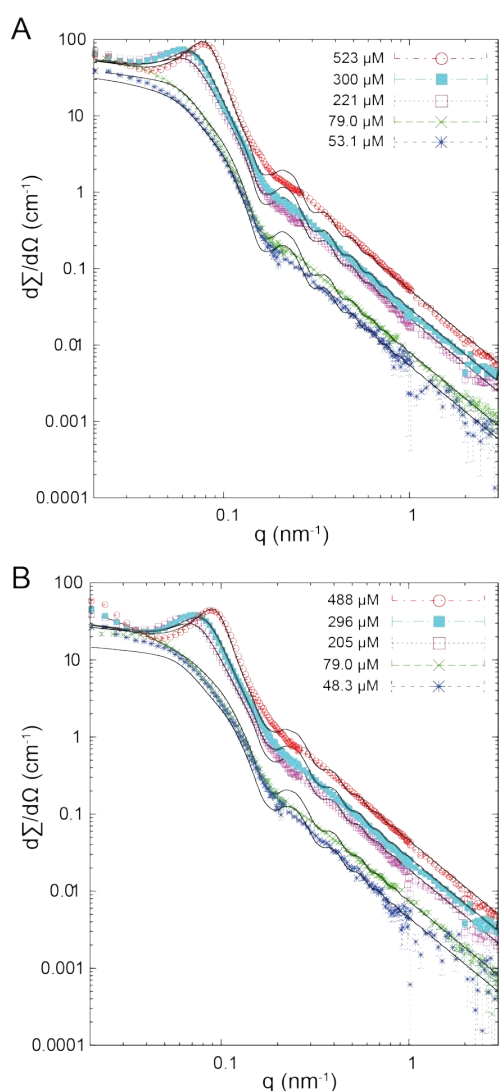


Figure 2: SANS spectra and analytical model fits (solid lines) for A160-(FGG)<sub>8</sub> (A) and A160-(YG)<sub>8</sub> (B). The  $q^{-2}$  slope in the mid to high  $q$  region is characteristic of the polymer chains in the hydrophilic part of the nanostructures. The structure factor peak at low  $q$  is caused by repulsive interactions between structures.

The structural similarity of the small molecules previously studied to aromatic amino acid side chains led us to hypothesize that a short (XGG)<sub>8</sub> domain (where X is a hydrophobic amino acid such as Y, F, or W) could similarly drive self-assembly. The structure of these highly asymmetric amphiphiles follows the motif: (M)SKGPG – (αGVPG)<sub>n</sub> – (XG<sub>y</sub>)<sub>8</sub>, where alanine (A) is the guest residue,  $n$  is the number of pentameric repeats, X is the identity of the amino acid hydrophobe responsible for driving self-assembly, and  $y$  is the number of glycine (G) spacers. To investigate this hypothesis, we explored the self-assembly behavior of a subset of these sequences by independently modulating these variables.

We find that self-assembly of these peptide-based polymers is governed at the sequence level by both the hydrophobicity of the amino acid X and the number of glycine spacers ( $y$ ). These studies yielded the unexpected observation that some of these block copolymers assemble into cylindrical micelles rather than the expected star-like morphology despite their high degree of asymmetry, with a hydrophilic fraction that exceeds 0.95 in some cases. These morphologies suggest that the self-assembly of our peptide-based polymers is not driven solely by hydrophobicity, but also by specific interactions between amino acids that are provided for by their perfectly controlled stereochemistry.

### Consistent self-assembly into cylinders

The morphology as determined by cryo-TEM and SANS remained remarkably constant for most self-assembling amphiphiles. Cryo-TEM (Fig. 1) revealed cylindrical structures with apparent aspect ratios ranging from 5 to 11, with all but one (A160-Y<sub>8</sub>) between 9 and 11. Additionally, SANS spectra of two asymmetric amphiphiles (A160-(YG)<sub>8</sub> and A160-(FGG)<sub>8</sub>) were obtained.

Based on cryo-TEM data, we chose a model of isotropically oriented homogeneous cylindrical micelles that also incorporated scattering from individual polypeptide chains at smaller length scales [6–8]. To obtain a robust set of output parameters, we simultaneously fitted all spectra from a given amphiphile with the same parameter set, thus covering a wide concentration range. For A160-(FGG)<sub>8</sub> and A160-(YG)<sub>8</sub> the cylinder lengths obtained from the model are 174 and 164 nm and the radii are 24 and 21 nm, respectively, corresponding to an axial ratio  $\epsilon$  of  $\sim 4$ , which is significantly smaller than the apparent aspect ratios ranging from 9–11 determined by cryo-TEM. The  $R_g$  of the individual polymer chains (the hydrophilic ELP brush) is 11 nm and the hydration of the micelles (the volume fraction of the nanostructure occupied by water) is 0.94.

- [1] J. R. McDaniel et al., *Nano Lett.* 14, 6590 (2014).
- [2] S. R. Macewanand and A. Chilkoti, *Nano Lett.* 12, 3322 (2012).
- [3] J. A. MacKay et al., *Nat. Mater.* 8, 993 (2009).
- [4] J. R. McDaniel et al., *J. Control. Release* 159, 362 (2012).
- [5] J. R. McDaniel et al., *Angew. Chem. Int. Ed. Engl.* 52, 1683 (2013).
- [6] A. G. Fournet, *J. Polym. Sci.* 19, 594 (1956).
- [7] P. Debye, *J. Phys. Colloid. Chem.* 51, 18 (1947).
- [8] M. S. Wertheim, *Phys. Rev. Lett.* 10, 321 (1963).

# Free volume in new and used high free volume thin film composite membranes

T. Koschine<sup>1</sup>, K. Rätzke<sup>1</sup>, F. Faupel<sup>1</sup>, M. M. Khan<sup>2</sup>, T. Emmeler<sup>2</sup>, V. Filiz<sup>2</sup>, V. Abetz<sup>2,3</sup>, L. Ravelli<sup>4</sup>, W. Egger<sup>4</sup>

<sup>1</sup>Institute of Materials Science, Chair for Multicomponent Materials, University of Kiel, Technical Faculty, Kiel, Germany

<sup>2</sup>Institute of Polymer Research, Helmholtz-Zentrum Geesthacht, Geesthacht, Germany

<sup>3</sup>Institute of Physical Chemistry, University of Hamburg, Hamburg, Germany

<sup>4</sup>University of the German Federal Armed Forces, Neubiberg, Munich, Germany

**P**olymeric gas separation membranes frequently undergo the phenomenon of aging, that is, performance parameters such as permeability decrease with storage or usage time. Previous experiments [1] have shown that this decrease is clearly correlated with a reduction in free volume, in particular at the surface. Here, we report on a new approach to reducing aging by incorporating functionalized multiwalled carbon nanotubes into a polymer of intrinsic microporosity.

Nowadays, membranes are also important for gas separation on an industrial scale, as they allow e.g. lower process temperatures and can be produced cost effectively. Membranes are most efficient if they have a high throughput, i.e. high permeability as well as high separation efficiency for the desired gas mixtures. One of the best materials today is the high free volume polymer PIM-1 [2]. PIM-1 is a polymer of intrinsic microporosity, which means that the porosity stems only from the molecular structures and is independent of the thermal or processing history of the material. In the application of membranes, their thickness is very important, as thin membranes reduce the flow resistance. However, in the case of thin polymeric samples, the problem of physical aging arises, which leads to a reduction in membrane performance with time [3,4]. This is well correlated to a lower free volume and can be measured using positron annihilation lifetime spectroscopy (PALS) [1,2,5]. In the present investigation, the membranes were not just stored but also actively used for gas separation and their mechanical and gas separation properties were improved by incorporating f-MWCNTs. At 2 wt% loading of f-MWCNTs, the permeability is up to four times higher (for CH<sub>4</sub>), while the selectivity of certain gas pairs, for instance CO<sub>2</sub>/CH<sub>4</sub> is slightly lower [5]. The aim of the present

work, which forms part of work [6] already published, is to correlate these effects with free volume measurements made using PALS. PALS in connection with an energy tunable beam for the analysis of thin films is a suitable tool for measuring the aging of the free volume and also high free volume polymers [1]

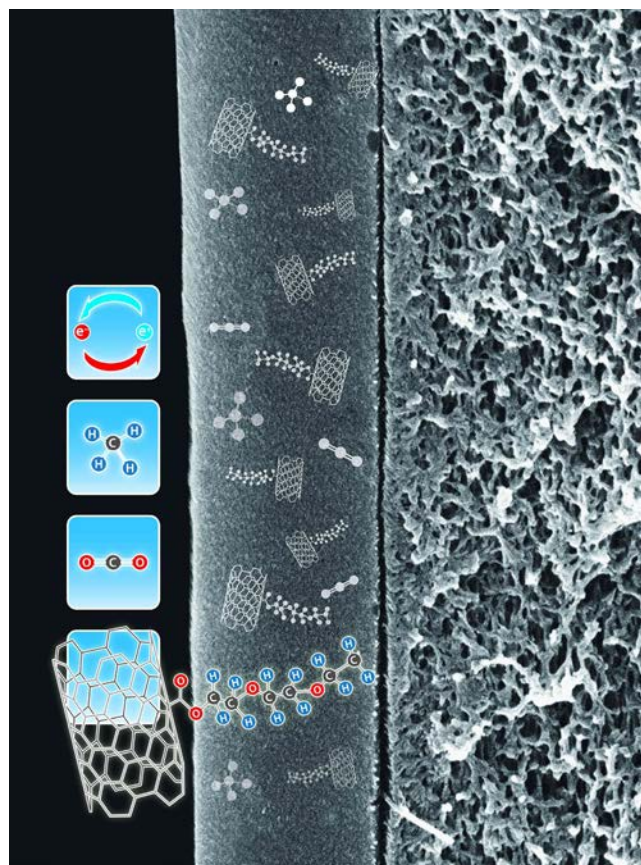


Figure 1: Illustration based on a SEM cross-section of meshy support and the thin membrane films with schematic of carbon nanotubes and the gas molecules.

## Positron lifetime analysis with PLEPS

Sample preparation and characterization are described elsewhere in detail [6]. Here, we focus on the positron lifetime analysis with the Pulsed Low Energy Positron Source (PLEPS) at the MLZ in Garching. The most important feature of this setup is the moderation of the implantation energy and, there-

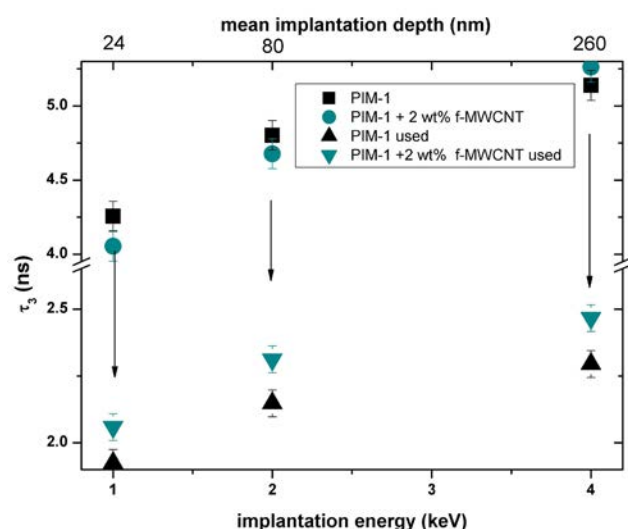


Figure 2: o-Ps lifetime versus the implantation energy for samples with and without CNT before and after usage.

fore, the variation in the implantation depth. Selecting the right implantation energy ensures that all positrons will annihilate inside the film and not in the support layer. Three different implantation energies, i.e. 1, 2 and 4 keV were chosen, leading to mean implantation depths of 24, 80 and 260 nm, respectively. At least  $3 \times 10^6$  counts ensure sound statistical evidence. The peak to background ratio was better than 3000:1. The resolution function with a SiC reference sample had a FWHM of around 260 ps. The spectra were evaluated with LT9.2.0. Details of the evaluation are given elsewhere [6].

### Characterization of modern polymeric membrane materials using positrons

A detailed discussion, including references to other work, is given in Ref. 6. The o-Ps lifetime of the pure unused PIM-1 measured (see Fig. 2) is in the range of values [1] reported in the literature and at 4 keV in the range of bulk PIM-1. The first observation is the reduction in the o-Ps lifetime towards the surface, which has been discussed by Harms et al. [1]. They proposed a faster aging at the surface due to an out-diffusion of free volume. The second trend is the strong reduction in the o-Ps lifetime after 300 days of usage in both samples. This effect is very similar to physical aging effects reported in high free volume polymers [5]. The lower free volume is explained by a collapse of the large free volume holes and fewer connections between them. The third effect is the influence of the f-MWCNTs on the free volume. In the unused samples, the size of the free volume holes is not affected by the CNTs, because the o-Ps lifetime

is nearly the same as for the two cast samples at all implantation energies. This effect is not unusual for CNTs in a polymer network. Still, it is possible that the f-MWCNT introduce directed channels along the nanotubes. In other polymers, these also lead to larger free volume holes at the interfaces [7], but these may not be detected here by PALS since the o-Ps will only probe the shortest diameter of a free volume hole and the free volume holes in the PIM-1 are already very large. In the used f-MWCNT containing PIM-1 membrane samples, the o-Ps lifetime and the o-Ps intensity are systematically higher, indicating that the free volume is less reduced by the incorporation of f-MWCNTs. As detailed in the original paper [6], these results are in good accordance with the permeability measurements.

In summary, positron annihilation lifetime spectroscopy is a suitable tool to support characterization of modern polymeric membrane materials in real applications.

### Acknowledgements

This work was in part financially supported by BMBF “Posimethod” 05K10FKB and the 7<sup>th</sup> Framework Program research EU-project “HARCANA” (Grant Agreement No: NMP3-LA-2008-213277).

- [1] S. Harms et al., *J. Adhes.* 88, 608 (2012).
- [2] P. M. Budd et al., *J. Membr. Sci.* 325, 851 (2008).
- [3] B. W. Rowe et al., *Polymer* 50, 5565 (2009).
- [4] M. M. Khan et al., *Nanoscale Res. Lett.* 7, 504 (2012).
- [5] X. Y. Wang et al., *J. Phys. Chem. B* 110, 16685 (2006).
- [6] T. Koschine et al., *J. Polym. Sci. Part B Polym. Phys.* 53(3), 213 (2015).
- [7] S. K. Sharma et al., *Phys. Chem. Chem. Phys.* 14, 10972 (2012).

# Neutron cryo-crystallography sheds light on heme peroxidases reaction pathway

C. Casadei<sup>1,2</sup>, M. Blakeley<sup>2</sup>, T. Schrader<sup>3</sup>, A. Ostermann<sup>4</sup>, E. Raven<sup>5</sup>, P. Moody<sup>1</sup>

<sup>1</sup>Department of Biochemistry and Henry Wellcome Laboratories for Structural Biology, University of Leicester, Leicester, UK

<sup>2</sup>Institut Laue-Langevin (ILL), Grenoble, France

<sup>3</sup>Jülich Centre for Neutron Science (JCNS) at MLZ, Forschungszentrum Jülich GmbH, Garching, Germany

<sup>4</sup>Heinz Maier-Leibnitz Zentrum (MLZ), Technische Universität München, Garching, Germany

<sup>5</sup>Department of Chemistry, University of Leicester, Leicester, UK

**H**eme peroxidases are a family of catalytic iron-containing proteins that are found in nearly all living organisms. These enzymes catalyze the H<sub>2</sub>O<sub>2</sub>-dependent oxidation of a substrate, thereby removing this potentially hazardous molecule from the cell. Heme peroxidases share a common reaction mechanism that involves the presence of two intermediate species known as Compound I and Compound II. Compound I contains an oxidized ferryl heme, plus either a porphyrin  $\pi$ -radical or a protein radical. Reduction of Compound I by one electron equivalent yields the closely related Compound II intermediate. Heme peroxidases have been the object of extensive studies in the last decades: of particular interest is the structural characterization of the active site in the transient Compound I. The protonation state of the iron bound oxygen ligand in Compound I has become a key question in the study of heme enzymes, due to its implications for the reaction mechanism. In particular, attention has been focused on whether the ferryl can be formulated as Fe(IV)=O or Fe(IV)-OH.

## Neutron cryo-crystallography - the method of choice

The methodologies that were traditionally employed to address this question appeared to be inadequate. Early approaches to the problem used resonance Raman methods to examine the iron-oxygen bond as an indirect reporter on the oxygen protonation state. However, the photolability of Compound I during laser excitation is well documented and results in ambiguous experimental findings. More recently, X-ray crystallography was employed with the purpose of inferring the ligand protonation state from the study of the iron-oxygen distance. However, the catalytic centre in these proteins is particularly sensitive to radiation damage effects and X-ray determined Fe-O distances are now considered unreliable.

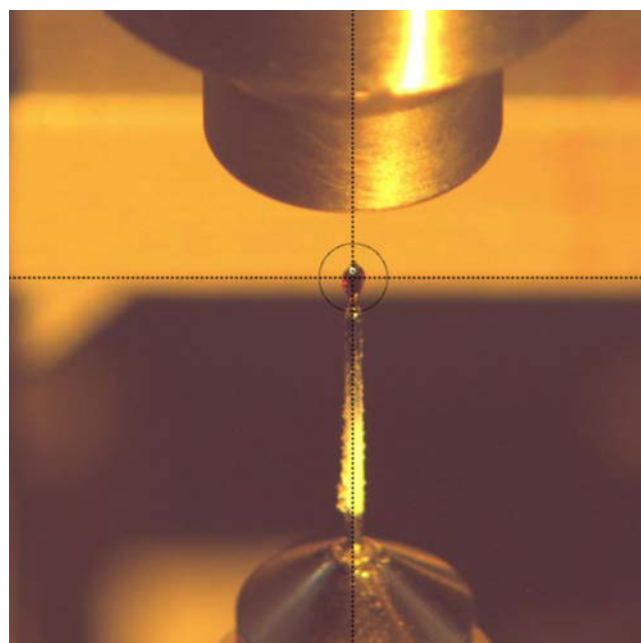


Figure 1: Deuterium exchanged crystal of CcP transient Compound I (center of the cross-hair) in the cryostream at BIODIFF (MLZ).

For these reasons we adopted a different approach. Neutron crystallography allows the localization of deuterium substituted hydrogen atoms in medium resolution nuclear scattering density maps. By contrast, hydrogen atoms are localized in X-ray maps only at high resolutions of 1.2 Å or beyond. The high

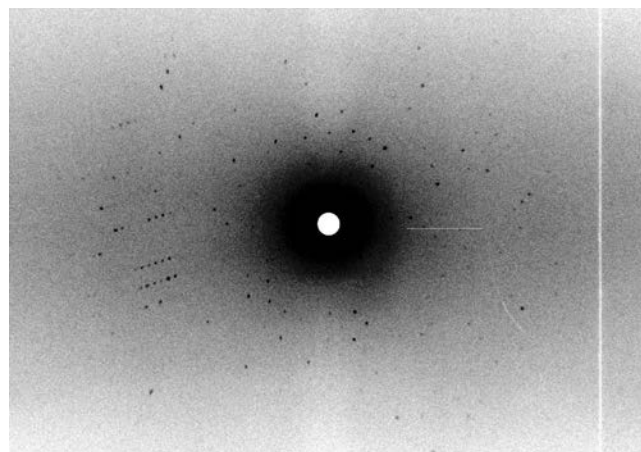


Figure 2: Monochromatic neutron diffraction pattern of CcP transient Compound I collected at BIODIFF (MLZ).

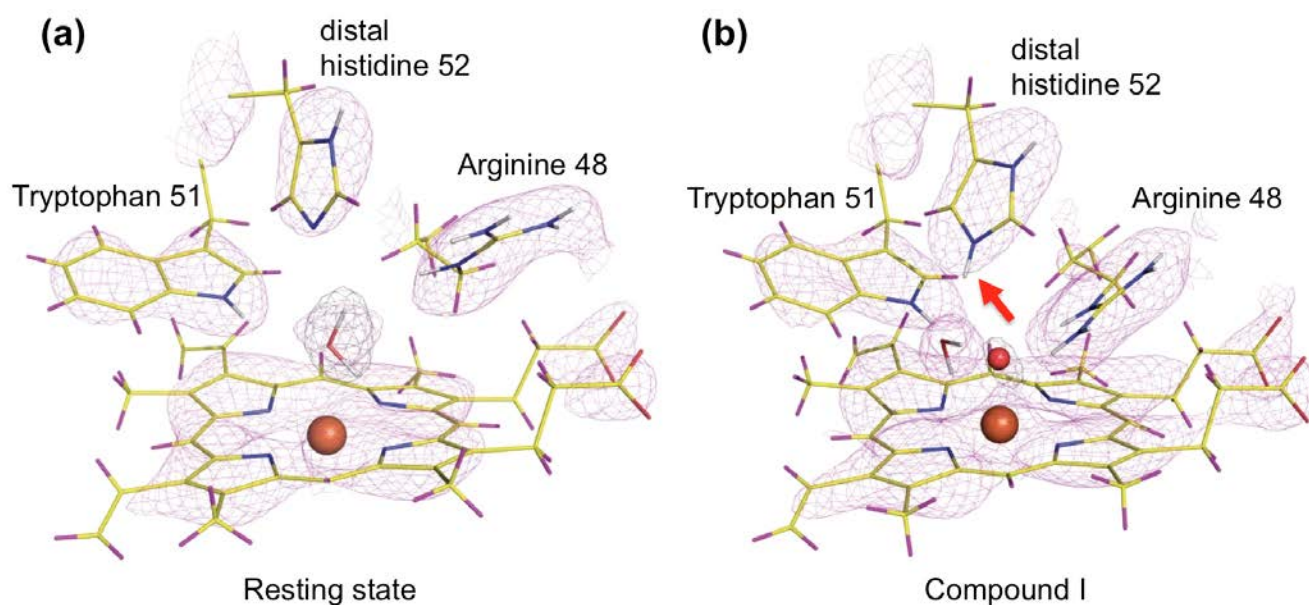


Figure 3: Neutron scattering density maps of Cytochrome c Peroxidase in the resting state (a) and of transient Compound I (b).  $2F_o - F_c$  neutron map shown in magenta. The additional proton (deuteron) at the distal histidine in the transient Compound I is marked by an arrow. The oxygen atom (red sphere) which is bound to the iron atom (brown sphere) in Compound I is not protonated.

X-ray dose required for ultra-high resolution data collection cannot be employed in the study of heme enzymes due to their sensitivity to radiation damage.

Due to the lack of radiation damage effects and its capability of localizing deuterons, neutron crystallography is an excellent tool for the study of hydrogen related biochemistry such as the determination of the protonation state of key residues and ligands, the position of water molecules in the active site and the study of hydrogen bond networks. Neutron crystallography data collection from cryo-trapped reaction intermediates is a unique tool for probing reaction mechanisms, but presents a number of challenges, in particular the need to flash cool the large crystals required for neutron crystallography down to the cryogenic temperature required for the study of transient species.

### Structure determination of Compound I

We determined the neutron structure of the transient Compound I of the heme enzyme Cytochrome c Peroxidase (CcP) at 100 K: a deuterium exchanged CcP single crystal was reacted to form Compound I and subsequently cryo-cooled at 100 K (see Fig. 1). Monochromatic neutron data were collected at the instrument BIODIFF at the MLZ (see Fig. 2). We obtained the first cryo-trapped enzyme intermediate structure determined by neutron crystallography. For

a direct comparison we also determined the neutron structure of CcP in the resting state, using the quasi-Laue diffractometer LADI III, at the ILL. The data were collected at room temperature on a deuterium exchanged single crystal.

The structures showed that the distal histidine residue in the active site is neutral (single protonated) in the resting state but doubly protonated in Compound I, which was unexpected (see Fig. 3). The iron axial ligand in Compound I is an oxygen atom, and it is non-protonated. The oxygen forms hydrogen bonds to the residue Tryptophan 51 and Arginine 48. Our observations indicate that the widely assumed role of the distal histidine in Compound I formation needs to be reassessed and we proposed a possible alternative mechanisms for O-O bond cleavage [1].

This work shows the feasibility of using neutron cryo-crystallography for the clarification of the reaction mechanism in enzymatic pathways.

[1] C. M. Casadei et al., *Science* 345, 193 (2014).

# Structure solution of a new ordered mixed imide-amide compound for hydrogen storage

E. Napolitano<sup>1</sup>, F. Dolci<sup>1</sup>, R. Campesi<sup>1</sup>, C. Pistidda<sup>2</sup>, M. Hoelzel<sup>3</sup>, P. Moretto<sup>1</sup>, S. Enzo<sup>4</sup>

<sup>1</sup>Institute for Energy and Transport, European Commission - DG Joint Research Centre, Petten, the Netherlands

<sup>2</sup>Institute of Materials Research, Helmholtz-Zentrum Geesthacht, Geesthacht, Germany

<sup>3</sup>Heinz Maier-Leibnitz Zentrum (MLZ), Technische Universität München, Garching, Germany

<sup>4</sup>Dipartimento di Chimica e Farmacia, Università degli Studi di Sassari and INSTM, Sassari, Italy

In order to elucidate the reaction pathways in complex hydrogen storage materials, the compound  $\text{KMg}(\text{NH})(\text{NH}_2)$  was synthesized from the reversible dehydrogenation process of a  $\text{Mg}(\text{NH}_2)_2/\text{KH}$  mixture. Preliminary powder X-ray diffraction patterns on specimens without any deuteration were supplemented with neutron powder diffraction studies on the reaction products from deuterated precursors with the intent of solving the crystal structure. The compound presents the orthorhombic space group  $\text{Pnma}$  (62) with lattice parameters:  $a = 9.3497(3)\text{\AA}$ ;  $b = 3.6631(1)\text{\AA}$ ;  $c = 9.8901(3)\text{\AA}$ , respectively. The coexistence of imide/amide groups in the same compound allows us to notice for the first time a heptahedral geometry arrangement around potassium atoms by imide and amide units.

In the field of solid-state hydrogen storage, the alkali amides and alkaline-earth analogues show remarkable reversibility in terms of hydrogen release and up-take processes [1]. Unfortunately, the formation of new unknown phases during intermediate steps of the absorption/desorption reaction pathways may constitute a severe limitation to understanding the basic mechanisms of the reaction kinetics. Recently, the formation of a new unknown  $\text{KMg}(\text{NH})(\text{NH}_2)$

Atom type	Wyckoff site	$x_N$	$y_N$	$z_N$	$B_{\text{iso}} / \text{\AA}^2$
K	4 (c)	0.2189(7)	0.75	0.1540(6)	2.3(1)
Mg	4 (c)	0.0321(3)	0.25	0.3956(4)	0.52(6)
N1	4 (c)	0.1238(2)	0.75	0.4540(3)	0.69(4)
N2	4 (c)	0.4772(2)	0.25	0.3048(3)	1.48(5)
D1	4 (c)	0.2276(5)	0.75	0.4440(4)	3.02(8)
D2	8 (d)	0.4351(4)	0.0430(8)	0.3570(3)	4.4(1)

Table 1: Atomic coordinates obtained from Rietveld refinement of the RT neutron diffraction data.

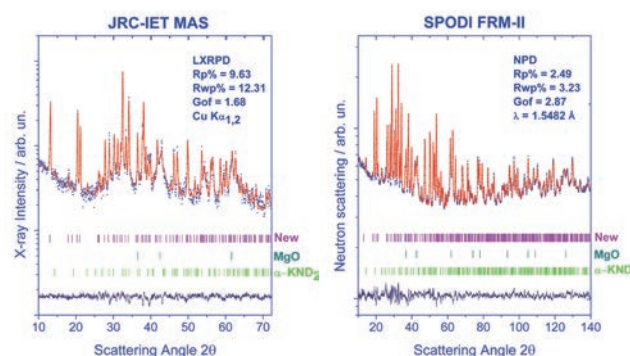


Figure 1: Rietveld refinement of laboratory X-ray (left) and neutron (right) powder diffraction patterns of the  $\text{KMg}(\text{ND})(\text{ND}_2)$  compound.

compound was reported by Wang et al. [2], unfortunately without its crystal structure being established.

In such cases, where compounds with hydrogen atoms are concerned, deuteration and neutron powder diffraction patterns combined with the so-called *ab-initio* [3] approach appear well suited to shed light on the hydrogen atom interactions and to solve the complete structure of an unclassified new compound.

## Experimental methods and numerical data analysis

The  $\text{KMg}(\text{ND})(\text{ND}_2)$  compound was prepared applying the synthetic procedure reported by Wang et al. [2]. The deuterated reagents were produced as described by Napolitano et al. [4]. Two experimental diffractograms were collected in order to solve the crystal structure of the unknown phase: a laboratory X-Ray powder diffraction pattern (JRC-IET MAS,  $\text{Cu K}\alpha$ , RT), collected in a Bragg-Brentano setting, and a Neutron powder diffraction pattern carried out in transmission geometry at the SPODI instrument (MLZ,  $\lambda = 1.5481 \text{\AA}$ , RT) Fig.1. Preliminary phase identification analysis was conducted using X'Pert Highscore [5] software and the indexing step us-

ing the McMaille program [6]. The crystal structure model was carried out using the ab-initio methods applying the Direct-Space approaches [7] using Endeavour [8] software and the Maud [9] program for the Rietveld refinement.

The X-Ray and neutron diffraction patterns were subjected to parallel data treatment. The phase identification analysis revealed the presence of minor polycrystalline compounds:  $\alpha$ -KNH<sub>2</sub> and MgO. The remaining unassigned peaks were indexed in the orthorhombic crystal system with space group Pnma and lattice parameters:  $a = 9.3497(3)$  Å;  $b = 3.6631(1)$  Å;  $c = 9.8901(3)$  Å [10]. Starting from the assumption that the chemical composition of the unclassified phase was KMg(ND)(ND<sub>2</sub>), based on previous reported infrared results [2], the Direct-Space Method was applied in order to the unknown crystal structure. A total of 28 atoms were placed inside the unit cell, consisting of 4 asymmetric units and a calculated density of 1.91 g/cm<sup>3</sup>. During the final Rietveld refinement, microstructure and structure parameters were optimized, yielding the best fit with satisfactory residual values (Fig. 1- Tab. 1).

### Crystal structure description

The crystal structure of KMg(ND)(ND<sub>2</sub>) composite contains features of both alkali and alkali metal earth imides and amide compounds. Each Mg<sup>2+</sup> cation is tetrahedrally coordinated by three ND<sup>2-</sup> imide units (N1 atoms) with an Mg-N1 average distance of ca. 2.1 Å and one amide ND<sup>2-</sup> group (N2 atom) with Mg-N2 distance ca. 2.05 Å. Every N1 atom adopts a distorted tetrahedral coordination sphere by three

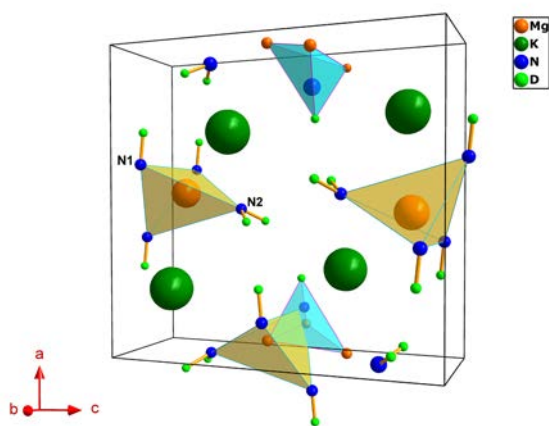


Figure 2: Unit cell content view of KMg(ND)(ND<sub>2</sub>). Imide and amide units present different N-D distances: N1-D 0.975 Å and N2-D 0.998 Å, respectively.

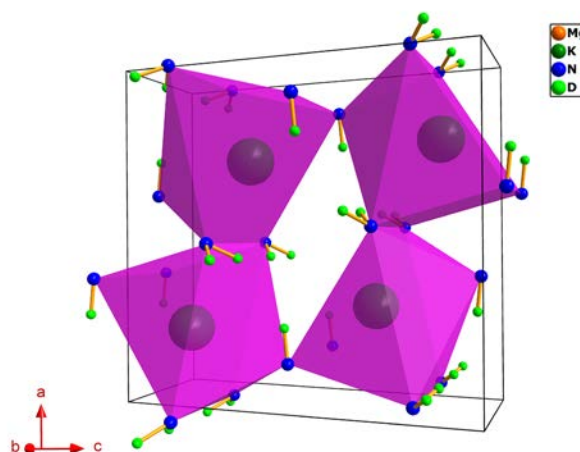


Fig 3. Representation of the chemical coordination sphere of potassium cations inside the unit cell. The trigonal prismatic mono-capped polyhedrons KN7 are shown.

Mg cations and one D1 atom (Fig. 2). The potassium cations experience a heptahedral coordination environment creating a trigonal prismatic mono-capped polyhedron with K-N distances ranging from 2.94 Å to 3.1 Å. Also, five of the eleven deuterium atoms present a distance K-D < 3 Å, showing the key role of potassium cations in sustaining the activation of N-D bonds (Fig. 3).

In this work, we report the crystal structure solution of the mixed imide-amide potassium-magnesium composite using X-Ray and Neutron powder diffraction data.

The KMg(ND)(ND<sub>2</sub>) compound presents imide and amide groups coexisting and interacting with magnesium atoms in tetrahedral coordination, and shows for the first time a imide/amide heptahedral coordination arrangement around the potassium atoms.

- [1] P. Chen et al., *Nature* 420, 302 (2002).
- [2] J. Wang et al., *ChemSusChem* 4,1622 (2011).
- [3] K. D. Harris et al., *Angew. Chem. Int. Ed.* 40, 1626 (2001).
- [4] E. Napolitano et al., *Int. J. Hydrog. Energy* 39, 868 (2014).
- [5] PANalytical. X'pert Data Collector and X'pert Highscore. PANalytical BV, Almelo, The Netherlands (2003).
- [6] A. Le Bail, *Powder Diffr.* 19, 249 (2004).
- [7] R. Černý and V. Favre-Nicolin, *Z. Kristallogr.* 222, 105 (2007).
- [8] Endeavour - Crystal Impact - [www.crystalimpact.com/endeavour](http://www.crystalimpact.com/endeavour).
- [9] L. Lutterotti The MAUD Program, [www.ing.unitn.it/~maud/](http://www.ing.unitn.it/~maud/)
- [10] E. Napolitano et al., *Int. J. Hydrog. Energy* 39, 8181 (2014).

# On the complex H-bonding network in paravauxite, $\text{Fe}^{2+}\text{Al}_2(\text{PO}_4)_2(\text{OH})_2 \cdot 8\text{H}_2\text{O}$

G. D. Gatta<sup>1</sup>, P. Vignola<sup>1,2</sup>, M. Meven<sup>3,4</sup>

<sup>1</sup>Dipartimento di Scienze della Terra, Università degli Studi di Milano, Milano, Italy

<sup>2</sup>CNR-Istituto per la Dinamica dei Processi Ambientali, Milano, Italy

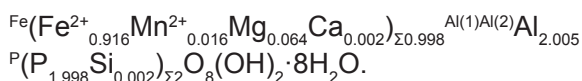
<sup>3</sup>Institut für Kristallographie, RWTH Aachen, Aachen, Germany

<sup>4</sup>Jülich Centre for Neutron Science (JCNS) at MLZ, Forschungszentrum Jülich GmbH, Garching, Germany

Phosphate minerals represent the major host for transition metals and  $\text{H}_2\text{O}$  in pegmatitic rocks, playing an essential geochemical role in the evolution processes of pegmatites. A good knowledge of their crystal chemistry is therefore necessary to better understand the genesis of pegmatites. Paravauxite is a mineral found in hydrothermal tin veins and granite pegmatites [1,2]. Its ideal chemical formula is  $\text{Fe}^{2+}\text{Al}_2(\text{PO}_4)_2(\text{OH})_2 \cdot 8\text{H}_2\text{O}$ . Its crystal structure was solved and refined by Baur [3] in 1969 on the basis of single-crystal X-ray diffraction data. This structure model appears to be consistent. However, due to the technical limitations of X-ray diffraction, the refinement only provided the isotropic displacement parameters, and the positions of nine independent proton sites were assigned but not refined. This led to a poor description of (the expected) complex H-bonding scheme in the paravauxite structure. In light of this, the crystal structure of a natural paravauxite was reinvestigated using electron microprobe analysis in wavelength dispersive mode (EPMA-WDS) and single-crystal neutron diffraction in an attempt to resolve these open questions.

## Looking into a gem stone

A gemmy, pale green, single crystal of paravauxite (up to 9 mm in length and 5 mm in diameter) from the Siglo Veinte Mine, Bolivia, was used in this study. The determination of the chemical composition was performed by EPMA-WDS analysis on a polished crystal using a Jeol JXA-8200 microprobe with the following result:



A single-crystal neutron diffraction experiment was

performed using the hot source (fast neutrons) single-crystal diffractometer HEiDi of the neutron source FRM II. The diffraction data were collected at 293 K with a wavelength of the incident beam of 1.1680(2) Å. The unit-cell parameters were refined on the basis of the 42 Bragg reflections (space group: P -1,  $a = 5.240(6)$  Å,  $b = 10.567(7)$  Å,  $c = 6.698(9)$  Å,  $\alpha = 106.82(8)^\circ$ ,  $\beta = 110.77(9)^\circ$ ,  $\gamma = 72.23(9)^\circ$ ,  $V = 336.4(6)$  Å<sup>3</sup>). A total number of 4190 reflections were collected up to  $2\theta_{\text{max}} = 126.3^\circ$  and  $\sin(\Theta)/\lambda = 0.76/\text{Å}$ , respectively. The discrepancy factor for the symmetry related reflections (based on Friedel pairs) was  $R_{\text{int}} = 0.0442$ . The anisotropic structure refinement was then performed using the SHELX-97 software [4], starting from the atomic coordinates of Baur [3] without H sites. The structure refinement was conducted with: a) the neutron scattering length of iron at the octahedral Fe site and the scattering length of aluminum at the octahedral Al(1) and Al(2) sites, also refining their site occupancy factors (*s.o.f.*); b) the scattering length of phosphorous at the tetrahedral P site, with full occupancy; c) the scattering length of oxygen at the OP(1), OP(2), OP(3), OP(4), OH(5), OW(6), OW(7), OW(8) and OW(9), with full site occupancies. Then, a structure model was implemented with nine H sites, (*i.e.*, H(1), H(2), H(3), H(4), H(5), H(6), H(7), H(8) and H(9)) all at ~1 Å from the respective O sites. Given such a model, convergence was rapidly achieved. However, H(4) and H(9) showed unrealistically large displacement parameters, if compared to those of the other H sites. Further refinement cycles were then conducted splitting the H(4) and H(9) sites into two mutually exclusive sub-sites (*i.e.*, H(4A) and H(4B), H(9A) and H(9B)) only 0.4-0.6 Å apart. Their *s.o.f.* were not restrained. With this configuration, the refined displacement parameters had realistic values, convergence was achieved and the variance-covariance matrix showed no significant correlation among the refined parameters. No peak larger than

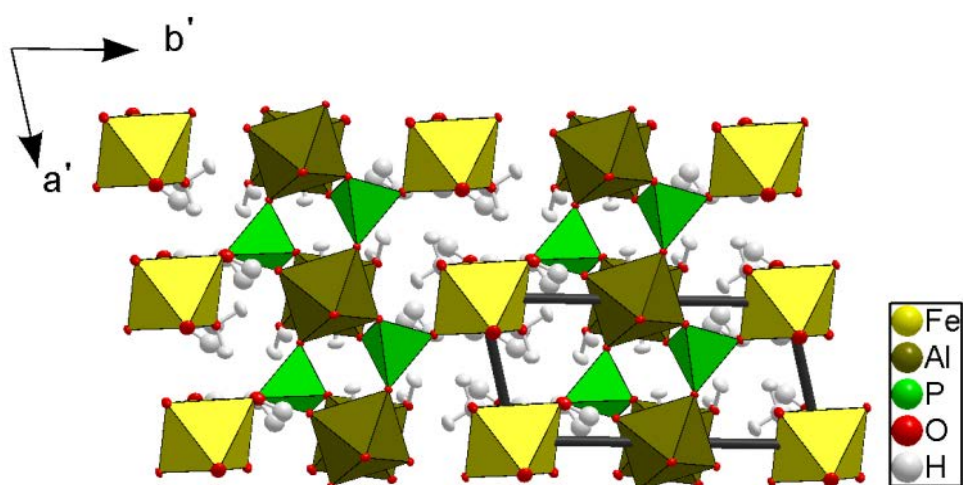


Figure 1: The crystal structure of paravauxite viewed down [001].

$\pm 1.3 \text{ fm}/\text{\AA}^3$  was present in the final difference-Fourier map of the nuclear density. The final statistical index  $R_1$  was 0.0495 for 194 refined parameters and 1678 unique reflections with  $F_o > 4\sigma(F_o)$ .

### Locating the hydrogen in paravauxite

This is the first study in which the crystal structure of paravauxite has been investigated on the basis of single-crystal neutron diffraction. Previous structure data available in the literature [3] are based on single-crystal X-ray diffraction. The structural refinement of this study confirms the former general structure model [3]. The structure of paravauxite is composed of chains of corner-sharing Al-octahedra, running along [001], linked by P-tetrahedra to form layers parallel to the *ac*-plane. These layers are connected by Fe-octahedra (Fig. 1). Two independent Al-octahedra (*i.e.*,  $\text{AlO}_4(\text{OH})_2$  and  $\text{AlO}_2(\text{OH})_2(\text{OH}_2)_2$ ), one independent Fe-octahedron (*i.e.*,  $\text{FeO}_4(\text{OH}_2)_2$ ) along with one independent  $\text{PO}_4$ -tetrahedron form the polyhedral “framework”, and at least one independent “zeolitic”  $\text{H}_2\text{O}$  lies in the cavities.

Using the neutron scattering length of iron at the Fe site, the refined occupancy factor is  $s.o.f. = 0.921(7)$ . This virtual partial site occupancy reflects the multi-elemental population at the Fe site, as shown by the EPMA-WDS [*i.e.*, with minor fractions of Mg (0.064 *a.p.f.u.*) and Mn (0.016 *a.p.f.u.*)]. The Al(1) and Al(2) sites were found to be fully occupied by aluminum (with refined  $s.o.f. = 1.02(2)$  and  $1.05(2)$ , respectively). The  $s.o.f.$  of the subsites H(4A) and H(4B), and H(9A) and H(9B) were re-

finned without any restraint, and the sum [ $s.o.f.(\text{H4A}) + s.o.f.(\text{H4B})$ ] = 0.94(3) and [ $s.o.f.(\text{H4A}) + s.o.f.(\text{H4B})$ ] = 1.02(2) suggest full site occupancies within  $2\sigma$ . The structure model with the sub-sites H(4A) and H(4B), and H(9A) and H(9B) is the best fit to the observed intensity data (at 293 K), with realistic displacement parameters.

The complex H-bonding scheme in the paravauxite structure is now well defined, with twelve independent H-bonds. Some of the H-bonds appear to be stronger than others. The weaker are characterized by low O-H...O angular values (*i.e.*,  $123 - 146^\circ$ ). Some H-bonds connect the Al-octahedra with the Fe-octahedra. The zeolitic  $\text{H}_2\text{O}$  molecule (*i.e.*, H(8)-OW(9)-H(9AB)) is connected via H-bonding to OP(1) (*i.e.*, the bridging oxygen between the Al(1)-octahedron and the P-tetrahedron), OP(3) (*i.e.*, the bridging oxygen between the Fe-octahedron and the P-tetrahedron) and OW(6) (*i.e.*, belonging to the Al(2)-octahedron). Further structural details are reported in [5].

- [1] S. G. Gordon, *Proc. Acad. Nat. Sci. Philadelphia* 75, 261 (1922).
- [2] S. G. Gordon, *Proc. Acad. Nat. Sci. Philadelphia* 96, 279 (1944).
- [3] W. H. Baur, *Neues Jahrbuch für Mineralogie Monatshefte* 1969 430 (1969).
- [4] G.M. Sheldrick, *Acta Crystallogr. Sect. A* 64, 112 (2008).
- [5] G. D. Gatta et al., *Mineralogical Magazine* 78, 841 (2014).

# CN-mayenite $\text{Ca}_{12}\text{Al}_{14}\text{O}_{32}(\text{CN})_2$ – a new kind of solid anion conductor with a mobile molecular anion

A. Schmidt<sup>1</sup>, J.-P. Eufinger<sup>2</sup>, M. Hoelzel<sup>3</sup>, J. Janek<sup>2</sup>, M. Lerch<sup>1</sup>

<sup>1</sup>Institut für Chemie, Technische Universität Berlin, Berlin, Germany

<sup>2</sup>Physikalisch-Chemisches Institut, JLU Gießen, Gießen, Germany

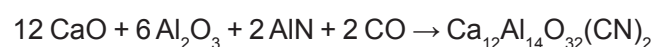
<sup>3</sup>Heinz Maier-Leibnitz Zentrum (MLZ), Technische Universität München, Garching, Germany

**C**N-mayenite,  $\text{Ca}_{12}\text{Al}_{14}\text{O}_{32}(\text{CN})_2$ , an anti-zeolite-type material, shows surprisingly high ionic conductivity and can be considered as the first example of a new kind of solid anion conductor with a mobile molecular anion (cyanide). With the help of neutron diffraction studies at SPODI, it was possible to establish that the orientation of the cyanide ions in the cages is tilted slightly towards the  $\bar{4}$  axis. The high-temperature behavior of CN-mayenite shows certain similarities to O-mayenite; a “smearing” of the nuclear density distribution is observed as an indication of increased mobility of the cyanide ions.

group  $\bar{4}3d$ ,  $a \sim 12 \text{ \AA}$ ,  $Z = 2$ ) contains twelve of these cages, two of them occupied by an oxide ion in a random manner (see Fig. 1). As this extra-framework oxygen, also known as ‘free oxygen’, is highly mobile at elevated temperatures, mayenite is an excellent oxide ion conductor with values of only one magnitude lower compared to those of yttria-stabilized zirconia [1,2]. Substituting the extra-framework oxygen atoms by other anions appears to offer a promising path to solid electrolytes with very unusual mobile anions. In recent years we successfully prepared mayenite-based materials containing different anions such as nitride, sulfide, chloride, nitrite or cyanide [3]. The latter phase (CN-mayenite,  $\text{Ca}_{12}\text{Al}_{14}\text{O}_{32}(\text{CN})_2$ ) is stable up to temperatures of more than 1300 K and therefore a promising candidate for a high-temperature solid cyanide ion conductor.

## From simple ingredients to a complex structure

CN-mayenite was synthesized at 1423 K in nitrogen atmosphere [4].



High-temperature neutron scattering investigations were performed at the powder diffractometer SPODI (wavelength 154.8 pm) at temperatures of 298, 673, 973, 1173 and 1323 K using a niobium container and a high-temperature vacuum furnace ( $p \approx 10^{-6}$  bar).

## Detecting the mobile cyanide

To determine the cyanide ion positions in the cages, we began the Rietveld refinement procedure by refining the framework atoms exclusively. The calculated difference Fourier map is shown in Fig. 2 for 298 K. It should be noted that, due to the local  $\bar{4}$  axis, the residual *average* scattering density is produced by at least four differently oriented CN species. A total refinement of the crystal structure

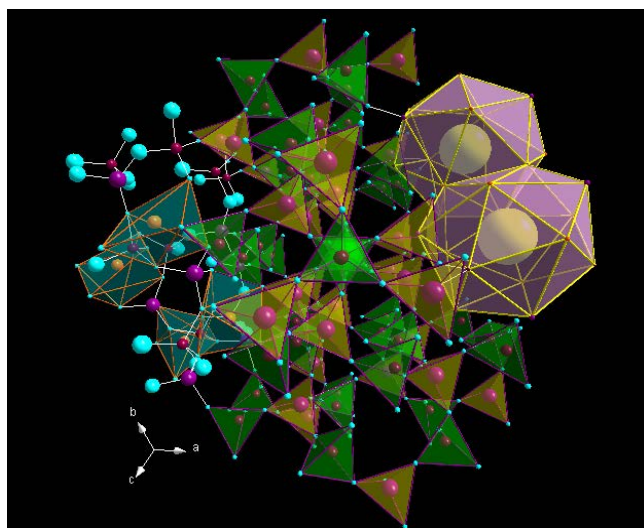


Figure 1: Crystal structure of mayenite, highlighting the coordination polyhedra around Ca (orange)/Al (pink) and two large cages around the extra-framework oxide anions (yellow).

## Mayenite - a solid cyanide ion conductor

Mayenite ( $\text{Ca}_{12}\text{Al}_{14}\text{O}_{33}$ ) exhibits a quite uncommon crystal structure which may be described as some kind of anti-zeolite, as it forms positively charged cage-like structures, partially occupied by anions. Calcium, aluminum and 32 of the 33 oxygen atoms form huge cages connected by large “windows” with diameters of up to 380 pm. The cubic unit cell (space

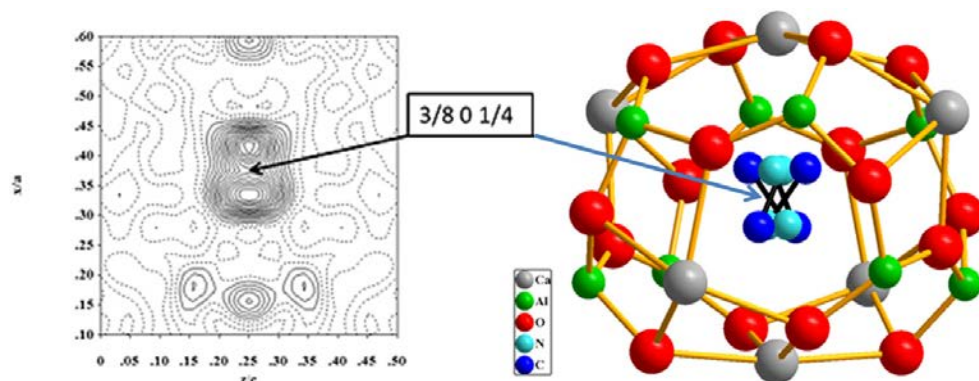


Figure 2: Left: difference Fourier plot after exclusive refinement of framework atoms at 298 K, showing the  $(x\ 0\ z)$  section ( $\bar{4}$  axis vertical). Right: cage within the mayenite structure. The triple bond between carbon and nitrogen of the cyanide anion is marked by a black line. The original cage center position at  $(3/8\ 0\ 1/4)$  is marked by arrows.

including the cyanide anions was carried out, using two 48 e  $(x, y, z)$  atomic positions, one for carbon and one for nitrogen. The final results are depicted on the right in Fig. 2. As expected, the orientation of the anion was found not to be parallel to the  $\bar{4}$  axis. The C-N bond length was determined to be 125(2) pm at 298 K, also remaining nearly constant within the error margin at high temperatures.

From the corresponding difference Fourier maps at high temperatures, the atom distribution seems to “smear out”, indicating an elevated motion of the cyanide ions, but no sign of continuous pathways for the diffusion of  $\text{CN}^-$  between the cages could be detected. Consequently, it is not possible to give an unambiguous statement on the conductivity behavior of CN-mayenite from neutron powder investigations alone.

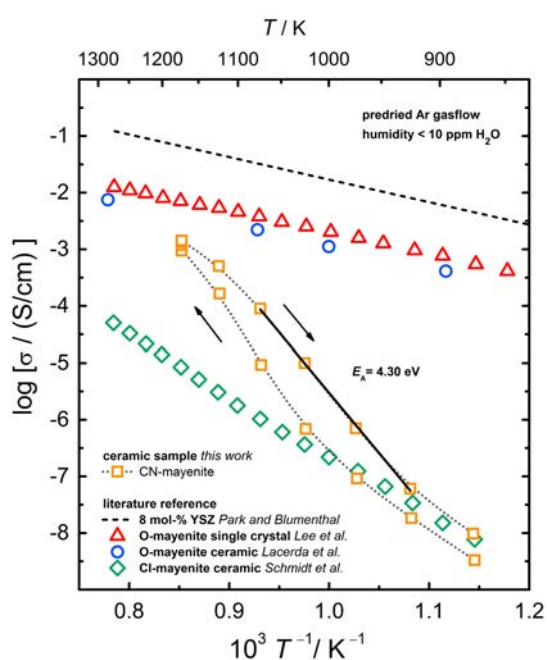


Figure 3: Total conductivity of  $\text{Ca}_{12}\text{Al}_{14}\text{O}_{32}(\text{CN})_2$  as function of reciprocal temperature together with reference samples.

In order to obtain more detailed information on the ion mobility, the total electrical conductivity of CN-mayenite was measured as a function of temperature in dehumidified argon atmosphere (impedance spectroscopy, see Fig. 3). It was found to be  $\sigma(1173\ \text{K}) = 1.4 \cdot 10^{-3}\ \text{S/cm}$  which is only one order of magnitude lower than that of O-mayenite. The conduction originates mainly from ion mobility ( $t_e < 0.1$ ) [3], and the electronic conductivity was found to be rather low with values between  $\sigma_e = 10^{-4}$  and  $10^{-5}\ \text{S/cm}$ . From these findings, we conclude that the cyanide anions in the cages are the main charge carrier, making CN-mayenite the first known high-temperature solid cyanide ion conductor.

### Mobility of the cyanide ions

We have succeeded in preparing a mayenite phase with cyanide ions in the cages. The existence of the cyanide ions was proven by means of IR,  $^{13}\text{C}$ -MAS-NMR and elemental analysis methods. With the help of neutron diffraction studies, it was possible to show that the orientation of the cyanide ions in the cages is tilted slightly towards the  $\bar{4}$  axis. At high-temperatures, a “smearing” of the nuclear density distribution is observed, which may be an indication of increased mobility of the cyanide ions between the cages. This is clearly corroborated by impedance spectroscopy measurements.  $\text{Ca}_{12}\text{Al}_{14}\text{O}_{32}(\text{CN})_2$  can be considered as the first example of a new kind of solid anion conductor with a mobile molecular anion.

This work was supported by the Deutsche Forschungsgemeinschaft within the framework of the collaborative project PAK 956.

[1] M. Lacerda et al., *Nature* 332, 526 (1988).

[2] D. K. Lee et al., *Phys. Chem. Chem. Phys.* 11, 3105 (2009).

[3] J. P. Eufinger et al., *Phys. Chem. Chem. Phys.* 17, 6844 (2015).

[4] A. Schmidt et al., *Solid State Sciences* 38, 69 (2014).

# Low-temperature properties of single-crystal CrB<sub>2</sub>

A. Regnat<sup>1</sup>, A. Bauer<sup>1</sup>, C.G.F. Blum<sup>2</sup>, S. Gottlieb-Schönmeyer<sup>1</sup>, B. Pedersen<sup>3</sup>, A. Senyshyn<sup>3</sup>, M. Meven<sup>4,5</sup>, S. Wurmehl<sup>2,6</sup>, J. Kuneš<sup>7</sup>, C. Pfleiderer<sup>1</sup>

<sup>1</sup>Physik-Department, Technische Universität München, Garching, Germany

<sup>2</sup>Leibniz Institute for Solid State and Materials Research IFW, Dresden, Germany

<sup>3</sup>Heinz Maier-Leibnitz Zentrum (MLZ), Technische Universität München, Garching, Germany

<sup>4</sup>Institut für Kristallographie, RWTH Aachen at MLZ, Garching, Germany

<sup>5</sup>Jülich Centre for Neutron Science (JCNS) at MLZ, Forschungszentrum Jülich GmbH, Garching, Germany

<sup>6</sup>Institut für Festkörperphysik, Technische Universität Dresden, Dresden, Germany

<sup>7</sup>Institute of Physics, Academy of Sciences, Praha, Czech Republic

**W**e report on the low-temperature properties of <sup>11</sup>B enriched single-crystal CrB<sub>2</sub> as prepared from high purity Cr and B powder via a solid-state reaction and optical float-zoning. The temperature dependence of the electrical resistivity, Hall effect, magnetization, and specific heat suggest that CrB<sub>2</sub> develops weak itinerant antiferromagnetism below  $T_N = 88.5$  K in the presence of strongly enhanced antiferromagnetic spin fluctuations and geometric frustration [1]. Comprehensive neutron diffraction studies carried out on the instruments RESI, HEiDi, and SPODI reveal a complex incommensurate cycloidal magnetic structure.

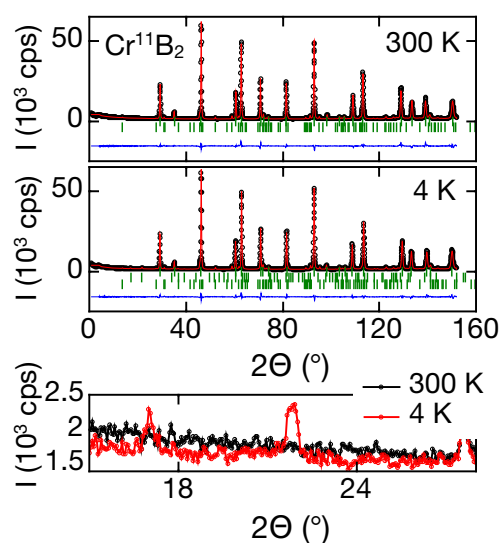


Figure 2: Powder neutron diffraction pattern of CrB<sub>2</sub> obtained at SPODI at 300 K (top) and 4 K (middle). Red lines correspond to the Rietveld refinement. Blue lines show the error of the refinement. Vertical green lines mark the Bragg positions. (bottom) The blow-up shows the existence of magnetic satellite peaks at 4 K (red curve) whereas no magnetic Bragg peaks are observed at room temperature (black curve).

CrB<sub>2</sub> belongs to the series of hexagonal C32 diborides (space group P6/mmm). Their crystal structure is characterized by an alternating sequence of hexagonal metal layers and honeycomb boron layers along the [001] direction. As a refractory metal, CrB<sub>2</sub>

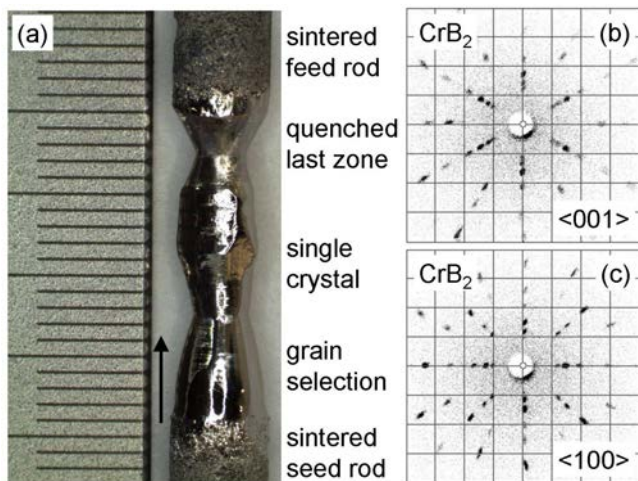


Figure 1: (a) CrB<sub>2</sub> rod after optical float zoning. Large facets and a clean metallic surface indicate high sample quality. (b) Laue X-ray diffraction pattern along the c axis showing the characteristic sixfold symmetry. (c) Laue x-ray diffraction pattern along the a axis.

had already attracted scientific interest in the late 1960s [2,3]. However, previous studies have either not addressed or not clarified key questions, e.g. what is the nature of the antiferromagnetic order of CrB<sub>2</sub>? What is the effect of magnetic fields on the antiferromagnetic transition temperature in CrB<sub>2</sub> and what does the magnetic phase diagram of CrB<sub>2</sub> look like? In view of the hexagonal crystal structure of CrB<sub>2</sub>, how important is geometric frustration?

## Single crystal growth and structure analysis

In order to answer these questions, we have grown high-purity single crystals by means of the optical float-zoning of sintered CrB<sub>2</sub> rods. Our samples were grown using 99 % enriched <sup>11</sup>B powder to permit detailed neutron scattering studies. Fig. 1 shows the float-zoned CrB<sub>2</sub> crystal and typical Laue x-ray pic-

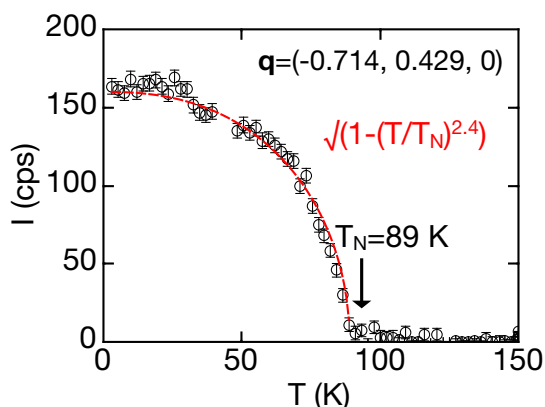


Figure 3: Temperature dependence of a magnetic satellite peak as measured at HEiDi. The red line is a fit to the integrated intensities.

tures of surfaces perpendicular to the  $c$  axis and the  $a$  axis, respectively [4]. The hexagonal lattice constants of  $\text{CrB}_2$  observed in powder neutron diffraction at SPODI (Fig. 2),  $a = 2.972 \text{ \AA}$  and  $c = 3.083 \text{ \AA}$ , are in close agreement with values reported in the literature [5]. Single crystal neutron diffraction experiments performed at RESI and HEiDi (Fig. 3) suggest a complex incommensurate spin structure. Our preliminary magnetic structure refinement is consistent with a spin cycloid with  $\mathbf{q} = 0.286 \mathbf{q}_{110}$ ,  $\mathbf{q}_{110} = 4\pi/a$  (Fig. 4) [6,7].

### Low-temperature bulk and transport properties

Low-temperature bulk and transport measurements reveal the hallmarks of itinerant antiferromagnetism. Most notably, we observe a lack of field dependence of the magnetic ordering temperature up to 14 T. Electrical resistivity as well as heat capacity data also provide evidence for the high quality of our single crystals, seen e.g. in a pronounced kink in the electrical resistivity, and a well-defined lambda anomaly at  $T_N$  (Fig. 5). From magnetization meas-

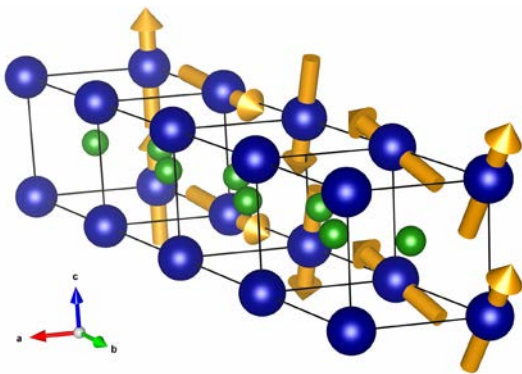


Figure 4: Schematic drawing of the incommensurate magnetic structure of  $\text{CrB}_2$ . The preliminary refinement yields a spin cycloid which is formed by magnetic moments,  $\mu \approx 0.4 \mu_B$ , turning in the  $a$ - $c$ -plane. In the interest of clarity not all moment vectors are shown.

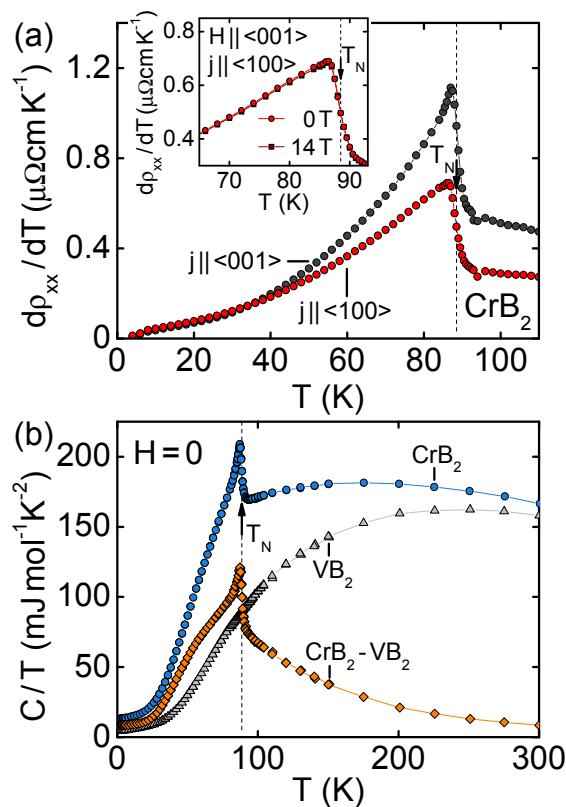


Figure 5: (top) Determination of the Néel temperature,  $T_N = 88.5 \text{ K}$ , from the derivative of the electrical resistivity with respect to the temperature.  $T_N$  does not shift in magnetic fields up to 14 T. (bottom) The magnetic phase transition at  $T_N$  manifests in a sharp  $\lambda$ -anomaly of the specific heat  $C$ . For low temperatures,  $T \rightarrow 0$ , specific heat divided by temperature,  $C/T$ , allows the electronic specific heat contribution,  $\gamma_0 = 13 \text{ mJ mol}^{-1} \text{ K}^{-2}$  to be determined. Data are shown for  $\text{CrB}_2$  and  $\text{VB}_2$ , where the latter is used for an estimate of the lattice contribution in  $\text{CrB}_2$ .

urements we deduce a large negative Curie-Weiss temperature,  $\Theta_{\text{CW}} = -750 \text{ K}$  and a large effective fluctuating moment,  $\mu_{\text{eff}} \approx 2\mu_B/\text{f.u.}$ , indicating the importance of spin fluctuations in this compound. The large ratio of the Curie-Weiss and Néel temperature,  $f = \Theta_{\text{CW}}/T_N \approx 8.5$ , is characteristic of strong geometric frustration [8,9]. All in all, our work identifies  $\text{CrB}_2$  as a weak itinerant antiferromagnet par excellence, providing perhaps the closest antiferromagnetic analog to the weak itinerant ferromagnets reported so far.

- [1] A. Bauer et al., *Phys. Rev. B* 90, 064414 (2014).
- [2] R. G. Barnes and R. B. Creel, *Phys. Lett. A* 29, 203 (1969).
- [3] J. Castaing et al., *Solid State Commun.* 7, 1453 (1969).
- [4] A. Bauer, PhD thesis (2014).
- [5] P. Vajeeston et al., *Phys. Rev. B* 63, 045115 (2001).
- [6] S. Funahashi et al., *Solid State Commun.* 23, 859 (1977).
- [7] A. Regnat, forthcoming PhD thesis.
- [8] A. P. Ramirez, *Annu. Rev. Mater. Sci.* 24, 453 (1994).
- [9] M. Brasse et al., *Phys. Rev. B* 88, 155138 (2013).

# The mechanism of multiferroicity in melilite defined by Spherical Neutron Polarimetry

V. Hutanu<sup>1,2</sup>, A. Sazonov<sup>1,2</sup>, M. Meven<sup>1,2</sup>, G. Roth<sup>1</sup>

<sup>1</sup>Institut für Kristallographie, RWTH Aachen, Aachen, Germany

<sup>2</sup>Jülich Centre for Neutron Science (JCNS) at MLZ, Forschungszentrum Jülich GmbH, Garching, Germany

The emergence of ferroelectricity in selected representatives of the melilite family, including  $\text{Ba}_2\text{CoGe}_2\text{O}_7$ , below their magnetic ordering temperature has been recently discovered. The remarkable and complex response of these materials to magnetic and electric fields cannot be explained by the common mechanisms applied to the other multiferroics. A number of new microscopic mechanisms have recently been proposed. In order to distinguish between different scenarios, a spherical neutron polarimetry (SNP) experiment on the multiferroic antiferromagnet  $\text{Ba}_2\text{CoGe}_2\text{O}_7$  was performed on the diffractometer POLI. Using SNP, we refined the magnetic symmetry of the compound precisely and determined the distribution of the magnetic domains in zero field and under the influence of the magnetic and electric fields to check the agreement with proposed models.

## Peculiar multiferroicity in melilites

Magnetically induced ferroelectricity was recently found in  $\text{Ba}_2\text{CoGe}_2\text{O}_7$  below  $T_N = 6.7$  K [1,2]. The origin of the observed ferroelectric polarization is still an open question. It cannot be explained by the well-accepted spin-current model, nor by the exchange-striction mechanism. Instead, three new microscopic mechanisms for the magnetically-induced ferroelectricity have been proposed: (i) Spin-dependent metal-ligand  $p$ - $d$  hybridization [2]; (ii) the onset of spontaneous toroidal moment in the multiferroic phase of  $\text{Ba}_2\text{CoGe}_2\text{O}_7$  [3]; (iii) antiferroelectric polarization-polarization coupling present in the spin Hamiltonian [4]. In order to distinguish between the different microscopic mechanisms in this compound, we studied its magnetic symmetry using a combination of unpolarised and polarized neutron diffraction techniques.

## Unpolarised single crystal diffraction

The magnetic structure of  $\text{Ba}_2\text{CoGe}_2\text{O}_7$  at 2.2 K ( $T_N = 6.7$  K) was initially studied at HEiDi by unpolarised neutron diffraction [5] using magnetic symmetry analysis [6]. The results showed an antiferromagnetic (AFM) order of the Co magnetic moments within the  $(a,b)$  plane (Fig. 1), while neighbouring planes stacked along the  $c$  axis are ordered ferromagnetically (FM). The direction of the Co magnetic moments was assumed to be parallel to the  $[100]$  direction of the  $Cm'm2'$  magnetic cell, based on bulk magnetization measurements. This magnetic space group allows a spin canting, i.e. a FM component within the  $(a,b)$  plane, perpendicular to the direction of the primary AFM ordering. The magnitude of the ordered magnetic moment of  $\text{Co}^{2+}$  ions is found to be  $2.9 \pm 0.1 \mu_B$ .

Nevertheless, the precise moment direction within the  $(a,b)$  plane cannot be determined unambiguously by unpolarised neutron diffraction due to the presence of energetically equivalent magnetic domains in zero field. As a result, it is impossible to distinguish with the conventional diffraction technique between three possible magnetic space groups (MSG):  $P2_1'2_12_1'$ ,  $Cm'm2'$ , and  $P112_1'$  [6].

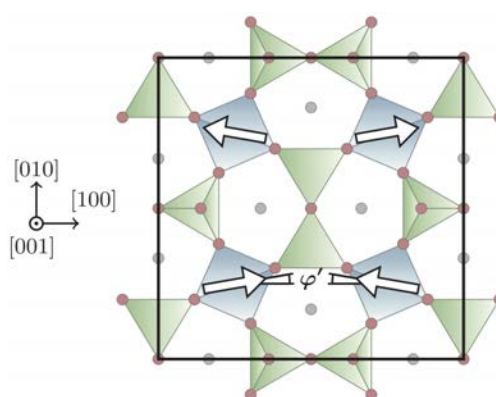


Figure 1: Magnetic structure of  $\text{Ba}_2\text{CoGe}_2\text{O}_7$  at 2.2 K: View from the  $[001]$  direction.

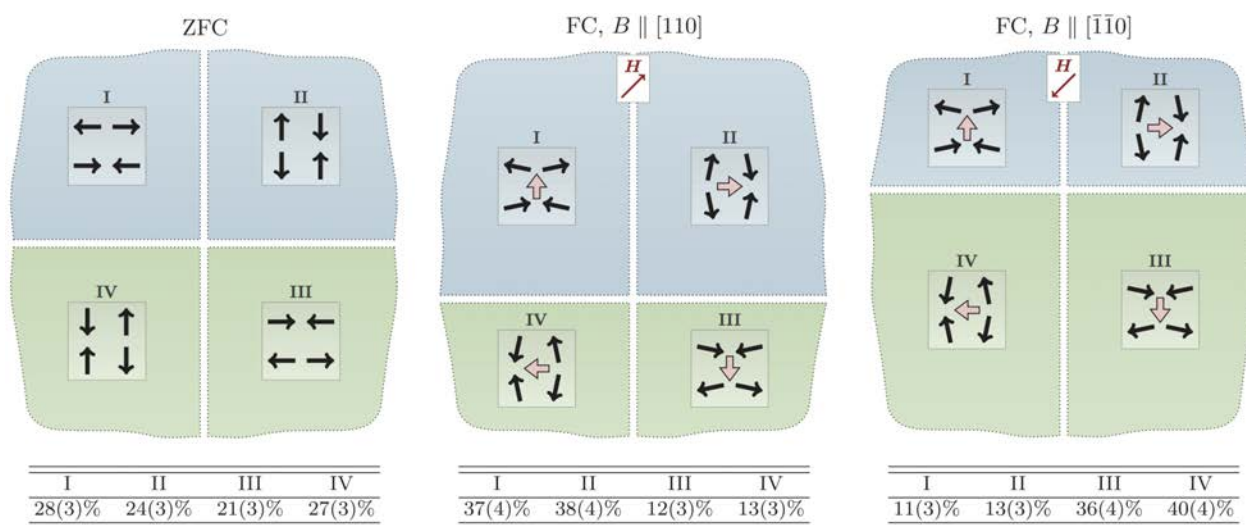


Figure 2: Influence of field cooling on domain imbalance revealed by SNP. Left panel: Zero-field cooling. Middle panel: Field cooling in  $B \parallel [110]$ . Right panel: Field cooling in  $B \parallel [\bar{1}\bar{1}0]$ .

### Neutron polarisation analysis

In order to determine the magnetic domain populations and to choose the proper MSG, SNP measurements have been performed with a Cryopad on the polarized single-crystal diffractometer POLI [7]. Measured polarization matrices were treated within two magnetic structure models: Calc110 and Calc100. For the model Calc110 the AFM component is fixed along the  $[110]$ , while for the Calc100 model the AFM component is along  $[100]$ . Both models fail to explain the observed polarization matrices assuming a single-domain state. Considering magnetic domains allowed by symmetry with equal populations gave much better agreement for the ZFC case. Finally, all three ZFC, FC110, and FC $\bar{1}\bar{1}0$  domain states are much better described in the model Calc100 ( $\chi^2 = 7\%$ ) than in the model Calc110 ( $\chi^2 = 25\%$ ). Hence, the model Calc110 can be ruled out and the sublattice magnetization parallel to  $[100]$  is found to be the genuine magnetic structure with  $Cm'm2'$  MSG.

Fig. 2 schematically describes the influence of fields parallel to the  $[110]$  and  $[\bar{1}\bar{1}0]$  axes on the domain imbalance within the Calc100 model. Following ZFC protocol, the allowed domains are equally populated within experimental accuracy (Fig. 2 left). In  $B = 20$  mT, domains I and II are energetically favorable compared to domains III and IV (Fig. 2 centre). Their volume covers about 3/4 of the crystal volume. Cooling with the same field strength, but applied along the opposite direction,  $[\bar{1}\bar{1}0]$ , reverses the situation (Fig. 2 right).

The change in volume ratio of the magnetic domain population is linear with field strength between  $B = 0$ , and 20 mT. This extrapolates to about 40 mT applied along  $[110]$ , which is required to fully suppress the energetically unfavoured domains in agreement with the static magnetization measurements [1]. This field value is much smaller than the critical field of about 1 T where the induced electric polarization disappears, ruling out the spin-dependent hybridization mechanism [2]. Moreover, the magnetic domain population is unaffected by the applied electric field up to 6 kV/mm, ruling out the mechanism based on spontaneous toroidal moment [3]. The SNP results support the existence of an antiferroelectric polarization-polarization coupling present in the spin Hamiltonian proposed in Ref. [4].

- [1] H. T. Yi et al., *Appl. Phys. Lett.* 92, 212904 (2008).
- [2] H. Murakawa et al., *Phys. Rev. Lett.* 105, 137202 (2010).
- [3] P. Toledano et al., *Phys. Rev. B* 84, 094421 (2011).
- [4] J. Romhányi et al., *Phys. Rev. B* 84, 224419 (2011).
- [5] V. Hutanu et al., *Phys. Rev. B* 86, 104401 (2012).
- [6] J. M. Perez-Mato, and J. Ribeiro, *Acta Crystallogr. Sect. A* 67, 264 (2011).
- [7] V. Hutanu et al., *Phys. Rev. B* 89, 064403 (2014).

# Lithium plating investigated by in situ neutron diffraction

V. Zinth<sup>1</sup>, C. von Lüders<sup>2</sup>, M. Hofmann<sup>1</sup>, J. Hattendorff<sup>3</sup>, I. Buchberger<sup>3</sup>, S. Erhard<sup>2</sup>, J. Rebelo-Kornmeier<sup>1</sup>, A. Jossen<sup>2</sup>, R. Gilles<sup>1</sup>

<sup>1</sup>Heinz Maier-Leibnitz Zentrum (MLZ), Technische Universität München, Garching, Germany

<sup>2</sup>Lehrstuhl für Elektrische Energiespeichertechnik, Technische Universität München, München, Germany

<sup>3</sup>Lehrstuhl für Technische Elektrochemie, Technische Universität München, Garching, Germany

**L**i plating, the deposition of metallic lithium onto the graphite anode of a Li-ion cell was studied using in situ neutron diffraction at Stress-Spec. Competing with the intercalation of lithium into graphite that takes place during the normal charging process, Li plating results in a lower degree of graphite lithiation during and after charge: After fast charge at  $-20\text{ °C}$ , neutron diffraction shows there is less highly lithiated  $\text{LiC}_6$  than after slower charge, although the cell stores the same amount of charge. Li plating uses up to 19 % of the active lithium in the cell. However, Li plating is mostly reversible and the metallic lithium slowly diffuses into the graphite during 20 h rest or is discharged prior to the lithiated graphite during immediate discharge [1].

## Lithium and Li-ion batteries

In rechargeable Li-ion batteries, Li ions are transported to the negative electrode (anode) during charge and move back to the positive electrode (cathode) during discharge. The first rechargeable lithium batteries developed in the 1970s used metallic lithium as anode material. Unfortunately, during repeated charging, metallic Li does not deposit in a uniform way on the Li anode, but forms dendrites that can lead to internal short circuits in the cell, in the worst case causing the cell to burn or even explode. Because of these hazards, rechargeable batteries with a Li anode were never commercialized [2].

The breakthrough and commercialization of rechargeable Li-ion batteries – used nowadays in many applications such as smart phones, cameras and laptops – came only in the 1990s with the use of the intercalation materials graphite and  $\text{LiCoO}_2$ . In graphite, Li is reversibly intercalated between the graphite layers while the cell is charged and the problem of dendrite formation is avoided under

normal operating conditions. Still, the potential of Li insertion into graphite is close to the potential for the formation of metallic lithium and during fast charge or at low temperatures, where the kinetics of intercalation are too slow, the deposition of metallic lithium on the graphite anode – so called Li plating – can still occur. Possible consequences are dendrite formation, faster capacity loss and cell aging. All these issues should be avoided in a safe and long-life Li-ion cell.

So far, evidence for Li plating has come only from a “bump” in the discharge curve (a so called high-voltage plateau) [3], some microscopic studies with cell designs far from standard commercial cells and ex situ studies, where aged cells were disassembled and metallic or white areas on the electrodes interpreted as the result of Li plating. Here, neutron diffraction offers a promising alternative for investigating Li plating in a commercial cell under operating conditions.

## Investigation of Li plating at STRESS-SPEC

While the metallic lithium cannot be observed directly due to its small quantity and scattering in compar-

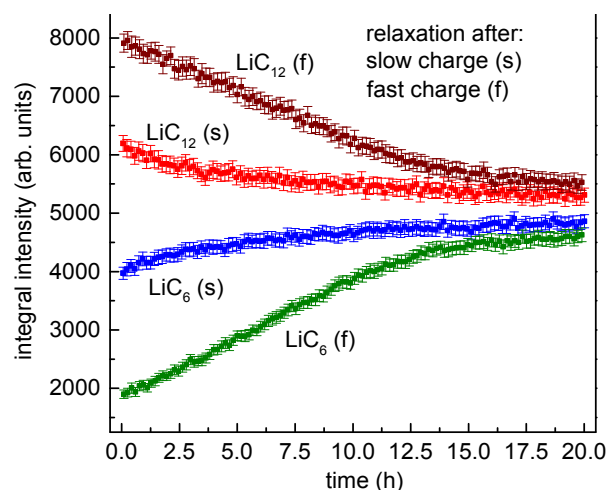


Figure 1: Changes of  $\text{LiC}_{12}$  and  $\text{LiC}_6$  reflection intensity during 20 h relaxation at  $-20\text{ °C}$  after slow (30 h) and fast (5 h) charge.

ison to the other cell components, its presence is implied by a lower degree of graphite lithiation, since Li ions can either be reduced to metallic lithium or intercalated in the graphite anode. Li intercalation into graphite proceeds via a number of stages from graphite to  $\text{LiC}_{12}$  and finally  $\text{LiC}_6$ , both easily identified by neutron diffraction because of their prominent (002) and (001) reflections. At Stress-Spec, the high neutron flux and the area detector make it possible to collect diffraction data on these reflections in ~5 min intervals during cell charge and discharge. Since Li plating is enhanced at low temperatures, experiments were performed at  $-20\text{ }^\circ\text{C}$  with the Li-ion battery, a commercial 18650 cell with a graphite anode and a  $\text{LiNi}_{0.33}\text{Mn}_{0.33}\text{Co}_{0.33}\text{O}_2$  cathode, being placed in a cryostat.

First, the cell was charged very slowly within 30 h and discharged again after a 20 h rest. In a second cycle, the cell was charged within 5 h, again followed by a 20 h rest. Comparison of the diffraction data collected at the end of the slow, 30 h charge and the fast, 5 h charge showed that after the 5 h charge the graphite was lithiated to a lower degree than after the 30 h charge. After the 5 h charge, less  $\text{LiC}_6$  – the most lithiated form of graphite – was present, and more  $\text{LiC}_{12}$  remained. At the same time, the charge put into the cell and extracted from it was almost the same, which means part of the charge must have been stored in the cell in a way different from lithiated graphite: as metallic lithium.

### What happens to Li plating after charge?

During a 20 h rest after charge, the  $\text{LiC}_6$  reflection intensity increases further and the  $\text{LiC}_{12}$  reflection intensity decreases (Fig. 1). The changes are more pronounced after fast charge. This means the graphite is further lithiated during rest, especially after fast charge, supposedly by the reaction of the plated metallic lithium with the graphite anode and diffusion of Li ions into the graphite particles. This shows a major part of Li plating is reversible and given enough time, the plated lithium may diffuse into the graphite.

### What happens to plated Li during discharge?

During discharge, Li deintercalates from the graphite.  $\text{LiC}_6$  is transformed first to  $\text{LiC}_{12}$  and then to a number of phases with lower lithium content that are found to coexist at low temperatures. However, if the

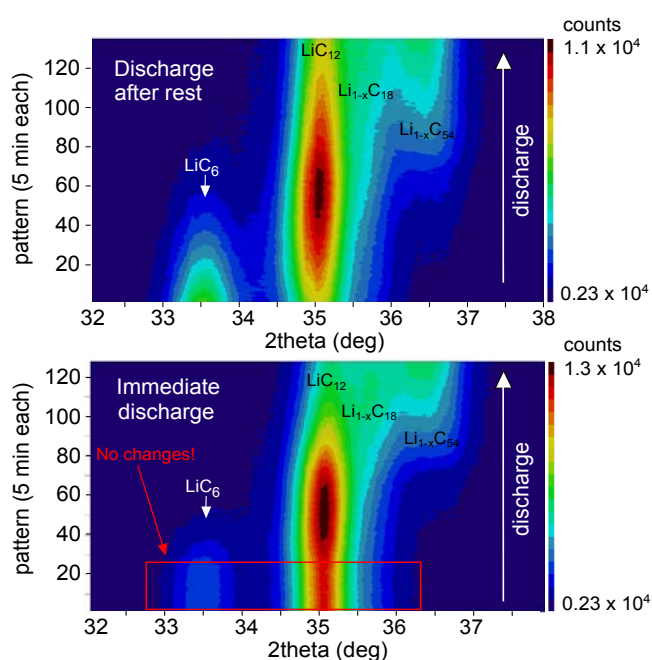


Figure 2: Diffraction data collected during discharge after rest (top) and immediate discharge (bottom), when Li plating is present.

cell is discharged directly after fast charge, at first we see no such changes. As Fig. 2 shows, there are no changes to the  $\text{LiC}_6$  and  $\text{LiC}_{12}$  reflections, although charge is extracted from the cell and consequently Li ions must move from anode to cathode. This means the metallic lithium is discharged first. Then, after a certain time, the discharge proceeds with the delithiation of the graphite, and the Li extraction from the graphite and  $\text{LiC}_6$  transformation to  $\text{LiC}_{12}$  begins. This coincides with the end of the above mentioned high voltage plateau, also observed in our experiment. From the charge extracted from the cell before the delithiation of graphite begins, we can estimate the percentage of metallic lithium, which is 19 % of the cyclable lithium in the cell.

So far, we have been able to estimate the amount of Li plating in a commercial Li-ion cell and show that most of that plating is reversible and can either diffuse into the graphite anode during a rest period or be discharged prior to the discharge of lithiated graphite. In situ neutron diffraction gives unique insights into the phenomenon of Li plating. In the future, a deeper understanding of Li plating may help provide better means to detect and prevent it.

[1] V. Zinth et al., *J. Power Sources* 271,152 (2014).

[2] J. B. Goodenough et al., *J. Am. Chem. Soc.* 135 (4), 1167 (2013).

[3] R. V. Bugga et al., *ECS Trans.* 25 (36), 241 (2010).

# Local structure and lithium mobility in intercalated $\text{Li}_3\text{Al}_x\text{Ti}_{2-x}(\text{PO}_4)_3$ NASICON type materials

K. Arbi<sup>1</sup>, M. Hoelzel<sup>2</sup>, A. Kuhn<sup>3</sup>, F. García-Alvarado<sup>3</sup>, J. Sanz<sup>1</sup>

<sup>1</sup>Instituto de Ciencia de Materiales de Madrid (CSIC), Madrid, Spain

<sup>2</sup>Heinz Maier-Leibnitz Zentrum (MLZ), Technische Universität München, Garching, Germany

<sup>3</sup>Departamento de Química, Universidad CEU San Pablo Facultad de Farmacia, Madrid, Spain

A combination of neutron diffraction and NMR spectroscopy provides new insights into structural factors that affect lithium mobility in NASICON lithium metal phosphates. Powder neutron diffraction was used to study the structure of lithium intercalated  $\text{Li}_3\text{Al}_x\text{Ti}_{2-x}(\text{PO}_4)_3$  compounds ( $x = 0, 0.2$ ) between 100 and 500 K. While Li occupies 6-fold M1 sites at ternary axes in pristine  $\text{Li}_{1+x}\text{Al}_x\text{Ti}_{2-x}(\text{PO}_4)_3$ , Li is located near M2 positions at M3/M3' 4-fold coordinated sites in lithiated  $\text{Li}_3\text{Al}_x\text{Ti}_{2-x}(\text{PO}_4)_3$  samples. The detection of twelve components in  $^7\text{Li}$  MAS-NMR spectra recorded at room temperature suggests the location of  $\text{Li}^+$  ions at three-oxygen faces that define M2 cavities.

Lithium metal phosphates are interesting candidates for use as solid electrolytes and insertion electrodes for high performance all-solid-state lithium-ion batteries, owing to their stability and good electrochemical performance [1-3]. In this work, lithium intercalated  $\text{Li}_3\text{Ti}_{2-x}\text{Al}_x(\text{PO}_4)_3$  were prepared by

chemical lithium insertion using n-butyl lithium, and special attention was paid to the location and mobility of Li at various temperatures [4].

## Powder neutron diffraction at SPODI

Neutron diffraction patterns were collected in the temperature range 5 - 500 K.

A wavelength of 1.548 Å was selected from a Ge monochromator. Cylindrical vanadium cans of 8 mm diameter were filled with 2-3 g of powder sample and patterns were collected for 4 h over the 5–160  $2\theta$  range.

## Structure analysis of $\text{Li}_3\text{Ti}_{2-x}\text{Al}_x(\text{PO}_4)_3$

The neutron diffraction pattern observed at 5 K and the calculated Rietveld profile of  $\text{Li}_3\text{Ti}_{1.8}\text{Al}_{0.2}(\text{PO}_4)_3$  is shown in Fig. 1. The Li insertion reduces the symmetry from R-3c to R-3.

The location of Li at M3 or M3' sites by means of Fourier map differences considerably improved agreement factors in refinements performed between 5 and 500 K. In pristine samples, Li ions occupy regular six-fold M1 coordinated sites (6b) at ternary axes, but in lithiated samples, Li ions occupy two distorted four-fold coordinated M3/M3' sites (18f) out of axes. The increment of Li content enhances Li–Li repulsions (distance M1–M3 ~ 3.7 Å), favoring the occupation of M3/M3' sites at the expense of M1 sites in lithiated samples. For lithiated  $\text{Li}_3\text{Ti}_{1.8}\text{Al}_{0.2}(\text{PO}_4)_3$ , the *a* lattice parameter increases from 8.35 to 8.40 Å with temperature, but the *c* lattice parameter decreases from 22.80 to 22.73 Å. It can be assumed that Li occupation of M1 sites produces the thermal expansion of the *c* axis, but that of M3/M3' sites favors the expansion of the *a* axis.

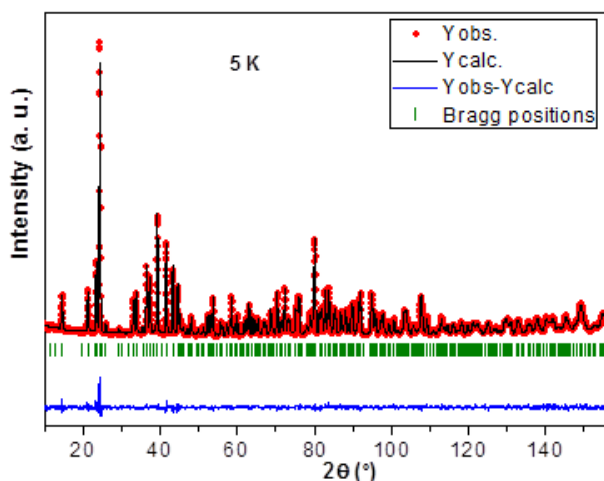


Figure 1: Neutron diffraction pattern of  $\text{Li}_3\text{Ti}_{1.8}\text{Al}_{0.2}(\text{PO}_4)_3$  at 5 K: experimental data (red points), calculated Rietveld profile (black), and difference profile (bottom, blue). The reflection positions calculated are shown as green ticks.

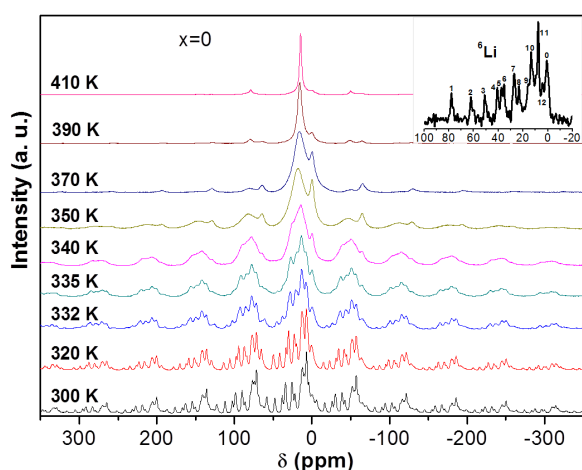


Figure 2: Temperature dependence of  ${}^7\text{Li}$  MAS-NMR spectra of  $\text{Li}_3\text{Ti}_{2-x}\text{Al}_x(\text{PO}_4)_3$  ( $x = 0$ ).

Atom	Wyckoff position	$x/a$	$y/b$	$z/c$	Occ
Li3	18f	0.030	0.319	0.045	0.72
Li3'	18f	0.055	0.373	0.117	0.34
Ti1	6c	0	0	0.145	1
Ti2	6c	0	0	0.348	1
P	18f	0.291	$y/b \sim 0$	0.250	1
O1	18f	0.167	0.216	0.089	1
O2	18f	0.136	0.229	0.398	1
O3	18f	0.197	0.992	0.193	1
O4	18f	0.911	0.145	0.299	1

Table 1: Structural model used for refinement of intercalated  $\text{Li}_3\text{Ti}_{2-x}\text{Al}_x(\text{PO}_4)_3$

### Lithium location:

#### In need of ${}^7\text{Li}$ NMR spectroscopy

${}^7\text{Li}$  MAS-NMR spectra of Li intercalated samples display lithium components that are shifted with respect to those of pristine samples, owing to paramagnetic interactions with  $\text{Ti}^{3+}$  cations [5].

In  $\text{Li}_3\text{Ti}_2(\text{PO}_4)_3$  twelve components were detected in  ${}^7\text{Li}$  MAS-NMR spectra recorded at 300 K (Fig. 2). Taking into account the structural refinements deduced from ND patterns at 5 K, only two Li components, ascribed to fourfold M3 and M3' sites, should have been detected. In order to explain the NMR results, it must be assumed that Li ions are shifted from fourfold to lower coordinated sites (Fig. 3).

The structural analysis of M2 cavities shows that eight oxygen atoms are located at shorter distances

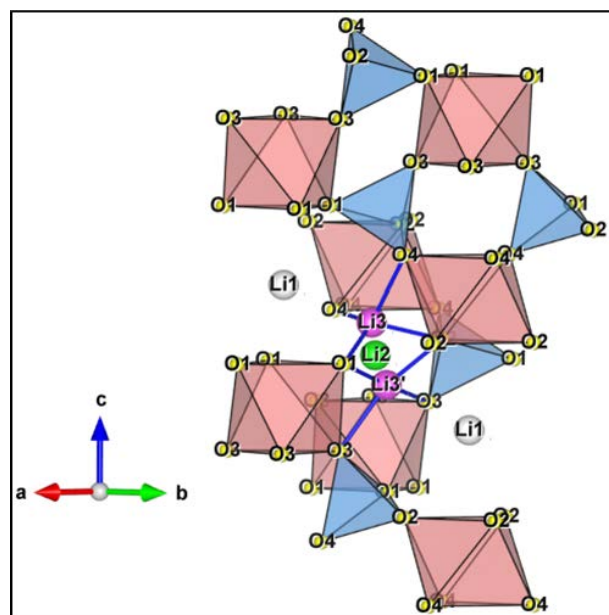


Figure 3: Schematic representation of conduction pathways and M2 cavities, where M3 and M3' sites are indicated.

than 3.1 Å. If it is assumed that Li ions are disposed near three-oxygen faces that define M2 cavities, the number of possible positions increases to twelve, which agrees with observations in  $\text{Li}_3\text{Ti}_2(\text{PO}_4)_3$ .

From the  ${}^7\text{Li}$  MAS-NMR spectra of  $\text{Li}_3\text{Ti}_{1.8}\text{Al}_{0.2}(\text{PO}_4)_3$  (two components), it must be concluded that structural disorder associated with Ti for Al substitution favors Li mobility, impeding at room temperature the detection of twelve NMR components.

In order to explain differences observed in ND and NMR results, structural analyses were performed at increasing temperatures. To that end, the location of lithium was investigated by Fourier map differences at 100, 300 and 500 K using structural models where Li ions were not included. This analysis showed, that occupation of M3/M3' sites decreases with temperature, being higher in all cases than that of M1 sites (Fig. 3). In agreement with NMR results, other sites near M1 were partially occupied. However, the existence of several small peaks makes the occupation of these sites difficult to analyze by Rietveld analysis. To investigate alternative sites, DFT calculations oriented to investigate Li coordination are necessary.

[1] J. M. Tarascon et al., *Dalton Trans.* 19, 2988 (2004).

[2] H. Huang et al., *J. Power Sources* 189, 748 (2009).

[3] Y. Lu et al., *J. Mater. Chem. A* 1, 68 (2013).

[4] K. Arbi et al., *Phys. Chem. Chem. Phys.* 16, 18397 (2014).

[5] Y. Joo Lee et al., *J. Am. Chem. Soc.* 120, 12601 (1998).

# Variant redistribution in a Ni-Mn-Ga shape memory alloy during thermo-mechanical treatment

Z. B. Li<sup>1</sup>, Y. D. Zhang<sup>2,3</sup>, W. M. Gan<sup>4</sup>, M. Hofmann<sup>5</sup>, C. Esling<sup>2,3</sup>, X. Zhao<sup>1</sup>, L. Zuo<sup>1</sup>

<sup>1</sup>Key Laboratory for Anisotropy and Texture of Materials (Ministry of Education), Northeastern University, Shenyang, China

<sup>2</sup>Laboratoire d'Étude des Microstructures et de Mécanique des Matériaux (LEM3), Université de Lorraine, Metz, France

<sup>3</sup>Laboratory of Excellence on Design of Alloy Metals for low-mAss Structures (DAMAS), Université de Lorraine, Metz, France

<sup>4</sup>German Engineering Materials Science Centre (GEMS) at MLZ, Helmholtz-Zentrum Geesthacht GmbH, Garching, Germany

<sup>5</sup>Heinz Maier-Leibnitz Zentrum (MLZ), Technische Universität München, Garching, Germany

Single crystal NiMnGa alloy can generate large magnetic-field-induced shape changes due to variant reorientation. Apparently, the high-cost fabrication of single crystals constitutes a severe obstacle for practical applications. In contrast, preparation of polycrystalline materials which can generate a large magnetic field-induced shape change due to variant reorientation is much simpler and of lower cost. However, the random distribution of crystallographic orientation in polycrystalline material greatly weakens the orientation dependence of magnetocrystalline anisotropy, which severely impairs the functional properties. Thus, microstructure texturing with proper processing routes could be seen as the best means of recovering the lost anisotropic features. Thermo-mechanical treatment (TMT) incorporating three cycles of uniaxial compression was introduced during martensitic transformation to modify the variant distribution of a polycrystalline Ni<sub>50</sub>Mn<sub>30</sub>Ga<sub>20</sub> alloy. The phase transformation processes under uniaxial compression were traced by *in-situ* neutron diffraction, and direct evidence of the variant redistribution was observed.

## ***In-situ* TMT and neutron diffraction experiments**

Uniaxial compressive load was applied via a rotatable multifunctional (tension/compression) load frame installed at STRESS-SPEC [1,2], using the “constant load” mode to ensure a fixed load. For the *in-situ* measurements of cyclic thermo-mechanical load, one cylindrical-shaped sample of polycrystalline Ni<sub>50</sub>Mn<sub>30</sub>Ga<sub>20</sub> alloy was first heated from room temperature (RT) to 393 K to reach the fully austenitic state. Then, a uniaxial compressive load of -10 MPa was applied along the solidification direction (SD). Finally the sample was cooled to RT at a cooling rate of 2 K/min under constant load, during

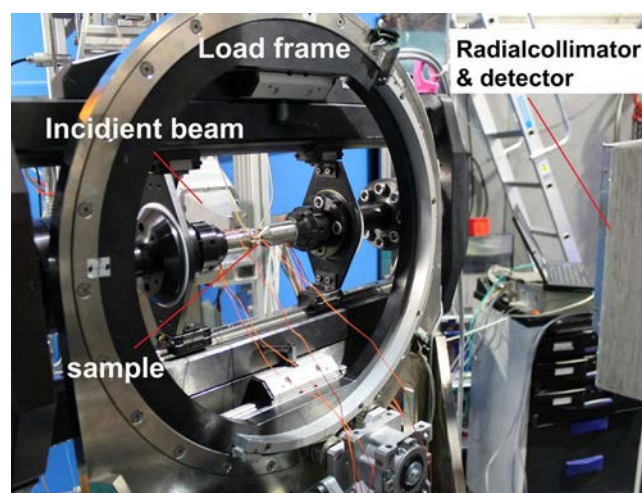


Figure 1: The unique tensile/compression rig was installed at STRESS-SPEC for *in-situ* diffraction patterns during cooling under load.

which neutron diffraction images were continuously recorded at an interval of 60 s by a two-dimensional (2D) detector at  $2\theta = 43.5^\circ$ . These two steps were considered as constituting Cycle 1 of the TMT. For Cycle 2 and Cycle 3, the experimental conditions were the same as those of Cycle 1, except that the constant compressive load was increased to -25 MPa and -50 MPa, respectively. The experimental setup is shown in Fig. 1.

## **Martensitic transformation**

For the present directionally solidified Ni<sub>50</sub>Mn<sub>30</sub>Ga<sub>20</sub> alloy, a martensitic start temperature  $M_s = 347.8$  K was determined from DSC measurements. Powder XRD analyses show that the alloy consists of a seven-layered modulated (7M) martensite at RT, having a monoclinic incommensurate superstructure [3]. In this superstructure, the easy magnetization axis of the 7M martensite corresponds to the  $b$  axis of the superstructure, *i.e.*  $[010]_{7M}$ .

The diffraction patterns on cooling across the martensitic transformation under the compressive load of -10 MPa (Cycle 1), -25 MPa (Cycle 2) and -50 MPa (Cycle 3), are shown in Fig. 2, respective-

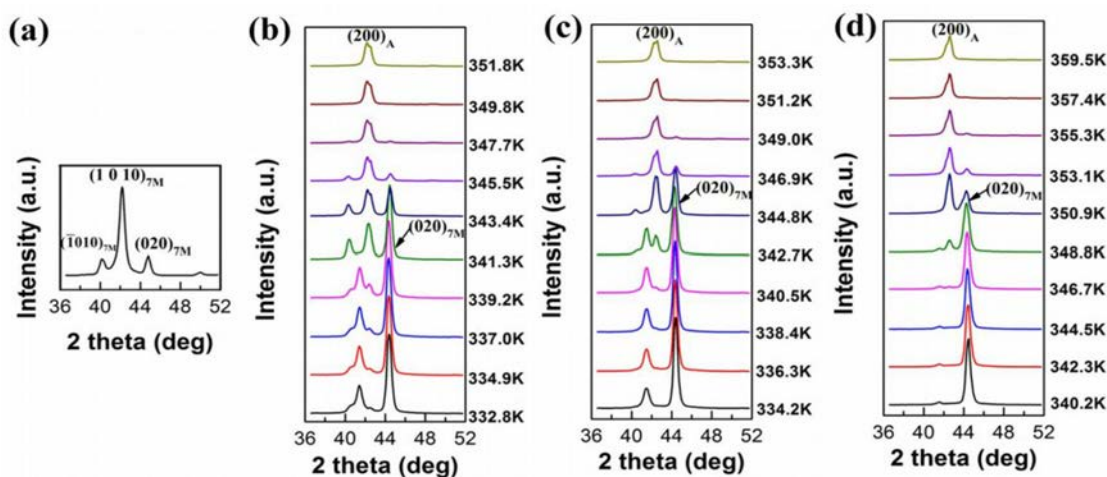


Figure 2: (a) Diffraction patterns measured on initial sample at  $\sim 303$  K. (b)-(d) Diffraction patterns measured on TMT sample during cooling under compressive loading of  $-10$  MPa (Cycle 1),  $-25$  MPa (Cycle 2) and  $-50$  MPa (Cycle 3).

ly. Compressive loading induced that the strongest diffraction peak of the 7M martensite changed from  $(1010)_{7M}$  to  $(020)_{7M}$  in the measured  $2\theta$  range. After three treatment cycles almost only the  $(020)_{7M}$  diffraction remained, suggesting a redistribution of martensitic variants induced by the load applied during the transformation. Moreover, with increasing load the amount of deformation associated with the phase transformation was also found to increase gradually.

According to the variations in the diffraction patterns, the uniaxial compressive load applied significantly influences the martensitic transformation thermodynamics, resulting in increased transformation temperatures. The shifts of transformation temperatures under uniaxial load  $\sigma$  can be well explained by the Clausius-Clapeyron equation [4].

### Texture evolution

Since the easy magnetization axis is an important parameter that accounts for the magnetocrystalline anisotropy in Ni-Mn-Ga alloys, we shall focus on the orientation distribution of the easy magnetization axis of 7M martensite (i.e.  $\langle 010 \rangle_{7M}$ ). Fig. 3a

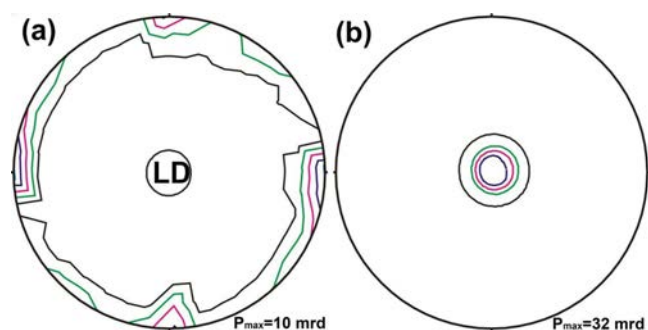


Figure 3: (a)  $(020)_{7M}$  pole figure of the initial sample. (b)  $(020)_{7M}$  pole figure of the sample with three cycles of treatment (LD – loading/compression direction) [4].

and Fig. 3b display the  $(020)_{7M}$  complete pole figures of the samples without and with the cyclic TMT, respectively. It can be seen that in the initial state (Fig. 3a), the  $\langle 010 \rangle_{7M}$  directions of 7M martensite tend to be perpendicular or parallel to the SD. After three cycles of treatment (Fig. 3b), the  $\langle 010 \rangle_{7M}$  directions become almost parallel to the LD (which is also the SD). Notably, a strong  $\langle 010 \rangle_{7M}$  preferential orientation along the LD was induced by the external compression during martensitic transformation [4]. Furthermore, magnetization measurements show that after cyclic TMT it is easier to reach saturation in the sample, suggesting the enhancement of magnetocrystalline anisotropy induced by the external compression during martensitic transformation.

In summary, direct experimental evidence was obtained on the redistribution of martensitic variants, triggered by uniaxial compression during martensitic transformation. The cyclic TMT resulted in large unidirectional lattice strains for the martensitic transformation and hence significant changes in the martensite microstructure. The 7M martensite plates formed with a strong  $\langle 010 \rangle_{7M}$  preferential crystallographic orientation along the loading axis, leading to an enhancement of the magnetocrystalline anisotropy. The present investigations may provide fundamental information on variant selection subjected to external stress field and the necessary guidelines for microstructure optimization of polycrystalline Ni-Mn-Ga alloys through external field training.

- [1] H. G. Brokmeier et al., Nucl. Instr. Meth. A 642, 87 (2011).
- [2] M. Hoelzel et al., Nucl. Instr. Meth. A 711, 101 (2013).
- [3] Z. B. Li, et al., J. Appl. Crystallogr. 43, 617 (2010).
- [4] Z. B. Li, et al., Appl. Phys. Lett. 105, 021907 (2014).

# Studies of early stage precipitation in a tungsten-rich nickel-base superalloy using SAXS and SANS

R. Gilles<sup>1</sup>, D. Mukherji<sup>2</sup>, H. Eckerlebe<sup>3</sup>, L. Karge<sup>1</sup>, P. Staron<sup>3</sup>, P. Strunz<sup>4</sup>, Th. Lippmann<sup>3</sup>

<sup>1</sup>Heinz Maier-Leibnitz Zentrum (MLZ), Technische Universität München, Garching, Germany

<sup>2</sup>Institut für Werkstoffe, Technische Universität Braunschweig, Braunschweig, Germany

<sup>3</sup>German Engineering Materials Science Centre (GEMS) at MLZ, Helmholtz-Zentrum Geesthacht GmbH, Garching, Germany

<sup>4</sup>Nuclear Physics Institute (NPI), Rez near Prague, Czech Republic

**C**haracterization of early stage precipitation is an important issue as it controls the emerging microstructure developed in Ni-based superalloys. These alloys are used as single crystal blades in gas turbines. The difficulty is that the  $\gamma'$  precipitation occurs at high temperatures and the reaction kinetic is extremely fast. Therefore, experimental methods with high time resolution are needed to monitor  $\gamma'$  precipitation. By using the high flux synchrotron instrument HARWI-II of the Helmholtz-Zentrum Geesthacht equipped with a fast data collection detector, it was possible to observe the creation of fine precipitates and their early growth in an alloy system of a tungsten-rich Ni-base superalloy [1,2]. The cooling down of the superalloy from the single-phase region to lower temperatures already leads to the formation of  $\gamma'$  precipitates in the size range of a few nm. In addition, SANS measurements were performed at the new SANS-1 instrument at MLZ to extend the results to larger precipitate sizes and to include initial growth [3].

## Tungsten rich Ni-based superalloy for high temperature application

An experimental single crystal alloy (nominal composition: Ni – 11.6 Al – 2.4 Ta – 3.5 W – 6.0 Cr – 1.3 Mo in at. %) was used for this study. The samples were prepared in solution heat-treated 1533 K/5 h/argon quenched and aged 1373 K/4 h + 1173 K/24 h/air cooled condition (designated W3SX STA). The microstructure of the alloy in the heat-treated condition is shown in Fig. 1. It can be seen that the  $\gamma'$  precipitates exist in two different morphologies after the heat treatments – namely, as large cuboidal particles (in the order of 400 nm to 500 nm) with rather sharp corners, which are arranged in a cubic array, and finer secondary  $\gamma'$  precipitates (< 100 nm) in the  $\gamma$  channels with more rounded corners but still with a cuboidal morphology.

## In-situ SAXS and SANS characterization of $\gamma'$ precipitates

The  $\gamma'$  precipitation kinetics of the W3SX alloy is extremely fast. A very fast quenching (at the rate of 750 K/min) from 1557 K was therefore adopted for the in-situ SAXS measurement. When the alloy is cooled from the high temperature, around one

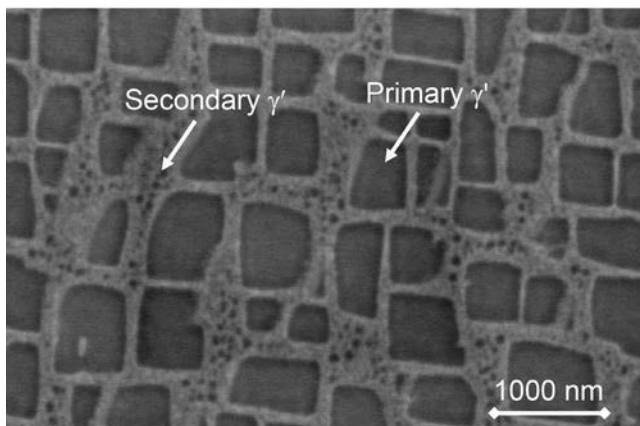


Figure 1: Scanning electron microscopy image of the microstructure of the W3SX STA sample used for SANS measurement. It reveals two distributions of large and fine  $\gamma'$  precipitates.

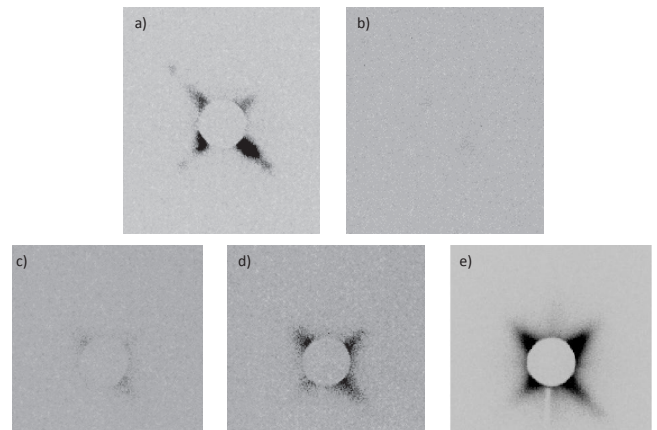


Figure 2: Five SAXS images of the W3SX STA sample during heating and cooling: before heating at RT (a), heated at 1557 K (b) and during the cooling at 1535 K (c), 1073 K (d) and RT after heating (e).

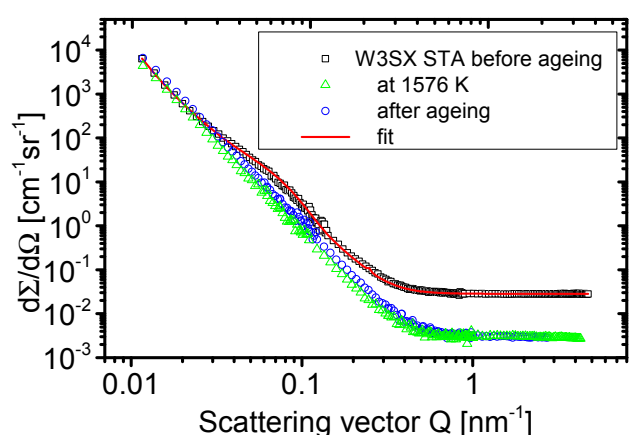


Figure 3: 1D SANS scattering curves of W3SX STA sample at RT before and after ageing and at 1576 K. The background was significantly reduced for the in-situ heating experiments by minimizing air scattering due to the vacuum furnace and a longer vacuum aperture nose in the setup resulting in smaller intensities at larger Q-values.

second after starting the cooling process the SAXS measurement were able to monitor the early stages of  $\gamma'$  nucleation (at particle sizes of  $\sim 12$  nm). During these measurements, about 500 images were collected (one every 3.5 seconds) from the 2D area detector. The sequence of detector images at some critical selected temperatures during heating and cooling is shown in Fig. 2. After heating, on holding at 1557 K,  $\gamma'$  precipitates (at least all the small precipitates) are dissolved. During the cooling process, the first detection of scattering from  $\gamma'$  precipitates becomes visible at 1535 K. The scattering signal gets stronger due to the formation of a higher volume of precipitates on continuing cooling to RT. More details can be obtained from reference [3].

Due to furnace limitations in the SANS measurements, only much slower cooling rates (20 K/min or 60 K/min) could be achieved. Therefore, only the growth of more or less unimodal precipitates ( $> 400$  nm) could be observed when the sample was cooled from 1573 K to RT. The size distribution of  $\gamma'$  precipitates obtained from the fit of the SANS data at RT before heating is shown in Fig. 3. The average precipitate size of the small  $\gamma'$  particles is 67 nm and that of the larger ones was found to be around 500 nm. The volume fractions of the two precipitate fractions are determined as 12 % for the fine cuboidal precipitates and approximately 56 % for the large cuboidal precipitates. This is in general agreement with the SEM image of the W3SX STA alloy (Fig. 1), although the size distribution and volume fraction of the large precipitates is not com-

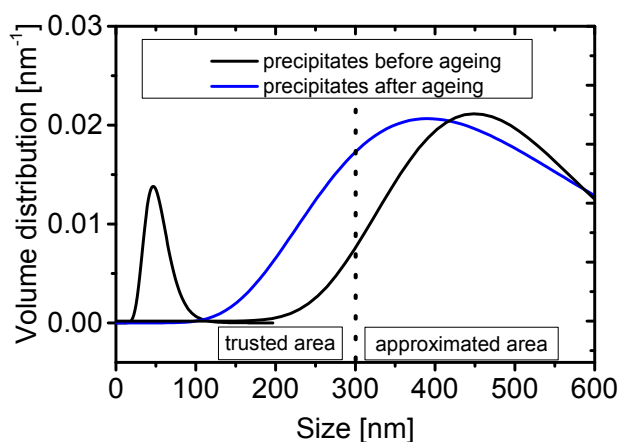


Figure 4: The  $\gamma'$  precipitate size distribution in W3SX STA sample obtained from SANS. The size distribution is bimodal consisting of larger and finer precipitates in the measurement at RT before and unimodal at RT after ageing. Before ageing, the small particles have a mean size of 67 nm and the large particles a mean size of  $\sim 500$  nm. After ageing only the large precipitates could be measured with a mean size of  $\sim 400$  nm.

pletely resolved by the measurement setup adopted at the SANS instrument (i.e. limited by the Q range). Hence, the size values reported can only be taken as a rough estimation. The precipitate size in the sample after in-situ ageing, measured at RT, shows an average size of slightly less than 400 nm with the precipitate size distribution more or less unimodal. It should be pointed out that continuous cooling during the in-situ cycle in the SANS experiment and the lack of holding at an ageing temperature prevents the nucleation of secondary  $\gamma'$ . The precipitating particles seem to grow rapidly after their first nucleation and already reach this large size after five minutes of continuous cooling.

#### Acknowledement

The authors would like to thank DFG for financial support for the Co-Re alloy development project (RO 2045/31-1 and GI 242/4-1) and the Helmholtz Zentrum Geesthacht for providing beam time at the former beamline HARWI II at DESY and Torben Fischer (HZG) for supporting the experiment. Our thanks are also due to the Maier-Leibnitz Zentrum for beam time and the support of the sample environment. One of the authors (Pavel Strunz) gratefully acknowledges the support by GACR (CZ) project No. 14-36566G.

[1] D. Mukherji et al., *Mater. Sci. Forum* 426, 815 (2003).

[2] R. Gilles et al., *Advanced Materials Research* 278, 42 (2011).

[3] R. Gilles et al., *J. Alloy. Compd.* 612, 90 (2014).

# Mapping the structure of a glass through its voids

M. Zanatta<sup>1</sup>, G. Baldi<sup>2</sup>, R. S. Brusa<sup>3</sup>, W. Egger<sup>4</sup>, A. Fontana<sup>3</sup>, E. Gilioli<sup>2</sup>, S. Mariazzi<sup>5</sup>, G. Monaco<sup>3</sup>, L. Ravelli<sup>3</sup>, F. Sacchetti<sup>1</sup>

<sup>1</sup>Dipartimento di Fisica e Geologia and IOM-CNR, Università di Perugia, Perugia, Italy

<sup>2</sup>Istituto dei Materiali per l' Elettronica ed il Magnetismo - CNR, Parma, Italy

<sup>3</sup>Dipartimento di Fisica, Università di Trento, Trento, Italy

<sup>4</sup>Institut für Angewandte Physik and Messtechnik, Universität der Bundeswehr München, Neubiberg, Germany

<sup>5</sup>Stefan-Meyer-Institut für subatomare Physik, Wien, Austria

**W**hat happens to vitreous silica  $v\text{-SiO}_2$ , the ubiquitous glass in nature, when it is compressed? Its density of course increases, but the real challenge is the description of this process down to the atomic length-scale. X-ray diffraction (XRD) and positron lifetime annihilation spectroscopy (PALS) were exploited to map the structure of a set of permanently densified  $\text{SiO}_2$  glasses. They provide a picture of silica as a porous medium where about 20 % of the volume is occupied by sub-nano voids whose density variation dominates both the compressibility and the medium range order up to densities close to that of  $\alpha$ -quartz.

## Order within disorder

Glasses are part of the wide family of disordered materials. This means that their structure lacks any long-range order even if it is far from being totally random [1]. First-neighbor atoms are often disposed in well-defined arrangements and almost ordered structures persist up to a few interatomic distances, leading to the so-called medium range order (MRO). The MRO is revealed by neutron or x-ray diffraction through the appearance of a first sharp diffraction peak (FSDP) in the measured static structure factor  $S(Q)$ . However, though it appears fundamental in the comprehension of glass phenomenology, a precise microscopic view of the MRO characteristic length scale still proves elusive.

Vitreous silica is characterized by a disordered open network formed by  $\text{SiO}_4$  tetrahedra. Permanent densification was achieved by using a high-pressure, high-temperature technique [2,3]. Samples were prepared under different pressures and cover a density range from that of normal silica ( $2.20 \text{ g/cm}^3$ ) up to a density 22 % higher than that ( $2.67 \text{ g/cm}^3$ ). Although subjected to a relevant density change,

XRD shows that the  $\text{SiO}_4$  tetrahedra are basically unaffected. This means that the main effects of densification need to be sought for in-between the tetrahedra, namely in the interstitial void spaces.

## Looking into the interstitial voids

PALS represents an unique tool for looking into the interstitial voids in glasses and mapping their evolution as a function of density. The main observable of a PALS experiment is the time that elapses between the positron  $e^+$  implantation and its annihilation. Different times correspond to different annihilation channels and these give information on the nature of the sample, see Fig. 1. In an insulator with open volumes,  $e^+$  can also form positronium (Ps), an  $e^+e^-$  bound state. Ps exists in two spin states: the singlet state para-positronium (pPs, lifetime in vacuum  $\tau_p=125 \text{ ps}$ ) and the long living triplet state ortho-positronium (oPs, lifetime in vacuum  $\tau_o=142 \text{ ns}$ ). In condensed matter, the latter lifetime is reduced via pickoff annihilation with the electron cloud limiting the void volume. However, the pickoff lifetime is still longer than that of the other annihilation processes and it conveys information on the void dimensions.

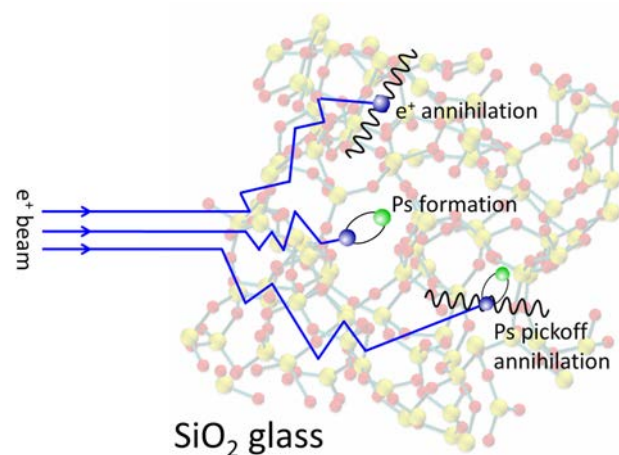


Figure 1: Pictorial view of the positron annihilation processes in  $v\text{-SiO}_2$ .

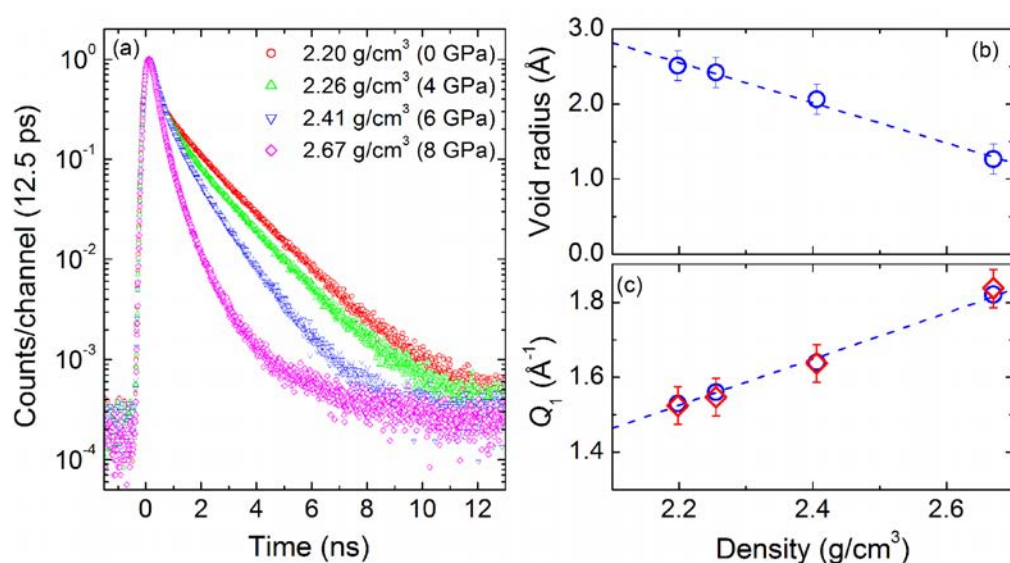


Figure 2: (a) Lifetime spectra measured at 18 KeV positron implantation energy in  $v$ -SiO<sub>2</sub> samples with increasing density (from top to bottom). Spectra are normalized to the peak height. (b) Void radius  $R$  as obtained from PALS data. (c) FSDP position  $Q_1$  as obtained by means of XRD (blue open circles) compared to the positions calculated using the void-cluster model of Ref. [6] (red open diamonds); data are from Ref. [2].

Experiments were performed at the pulsed low energy positron system (PLEPS), fed by the NEP-OMUC positron source of the FRM II reactor (Garching, Germany). PALS spectra were acquired at two implantation energies of 16 and 18 keV that correspond to average implantation depths ranging between 1 and 2  $\mu$ m. An example of PALS data is reported in Fig. 2(a).

### A porous view for $v$ -SiO<sub>2</sub>

The analysis performed with PATFIT shows the presence of three main lifetime components: (i) a short lifetime  $\tau_1$  which comes from pPs and e<sup>+</sup> annihilation in bulk silica; (ii) an intermediate lifetime  $\tau_2$  probably due to oPs or e<sup>+</sup> annihilation in small voids or vacant sites; (iii) a long lifetime  $\tau_3$  that is related to oPs pickoff in the intrinsic structural voids. The decrease in this longest decaying lifetime going from normal silica to the sample of highest density is evident from Fig. 2(a) and is related to the shrinking of the intrinsic voids in the silica samples. Being more quantitative, the oPs pick-off lifetime can be related to the interstitial voids dimension according to the Tao-Eldrup model [4,5]. We find that, on increasing the density by 22 %, the void radius shrinks linearly to half of its initial value, Fig. 2(b). Moreover, the intensity of the third lifetime component is also reduced, thus implying a diminution of the number of voids.

These results naturally suggest a description of  $v$ -SiO<sub>2</sub> as a porous medium whose structure is made up of an incompressible and a compressible part, namely SiO<sub>4</sub> tetrahedra and interstitial voids,

respectively. In normal silica, the compressible part occupies  $\sim$ 18 % of the total volume. Upon densification, the tetrahedra rotate almost rigidly to fill the interstitial voids so that the compressible part is reduced to  $\sim$ 3 % of its initial value [2].

### What about the medium range order?

The densification process also induces a modification in the MRO. With increasing density, the FSDP position  $Q_1$  shifts upwards by about 20 %. This behavior can be explained in terms of a reduction in the volume of the voids as well.

The vitreous silica network can be further described as an ensemble of voids surrounded, at a certain distance  $D$  from their centers, by quasi-spherical cation-centered clusters, i.e. SiO<sub>4</sub> tetrahedra separated by the Si-Si distance  $d$ . The void-cluster distance  $D$  can be viewed as the sum of the PALS void radius  $R$  and a screening distance depending on the tetrahedral structure. The two distances  $D$  and  $d$  are the main ingredients of the so-called void-cluster model for the FSDP [6]. Fig. 2(c) shows how PALS data allow us to describe with great accuracy both the FSDP position and its density dependence in absolute units, shedding some new light on the subtle nature of MRO [2].

[1] S. R. Elliott, *Nature* 354, 445 (1991).

[2] M. Zanatta et al., *Phys. Rev. Lett.* 112, 045501 (2014).

[3] M. Zanatta et al., *Phys. Rev. B* 81, 212201 (2010).

[4] S. J. Tao, *J. Chem. Phys.* 56, 5499 (1972).

[5] M. Eldrup et al., *Chem. Phys.* 63, 51 (1981).

[6] S. R. Elliott, *Phys. Rev. Lett.* 67, 711 (1991).

# Thin film annealing and alloying of a Au/Cu two-layer system studied with a positron beam

M. Reiner<sup>1,2</sup>, T. Gigl<sup>1,2</sup>, C. Piochacz<sup>1,2</sup>, C. Hugenschmidt<sup>1,2</sup>

<sup>1</sup>Heinz Maier-Leibnitz Zentrum (MLZ), Technische Universität München, Garching, Germany

<sup>2</sup>Physik-Department E21, Technische Universität München, Garching, Germany

The high temperature behavior of a Au( $d = 180$  nm)/Cu( $d = 480$  nm) two-layer system was studied using Positron Annihilation Spectroscopy (PAS). For this purpose, defect sensitive and element specific Coincident Doppler Broadening Spectroscopy (CDBS) with a monoenergetic positron beam was applied. In-situ CDBS during isothermal tempering at 633 K for 7 h enabled the observation of both annealing of the Au film and alloying of Au and Cu. The changes in the recorded spectra could be separated into two stages: In the first stage, annealing in the Au film was detected, whereas in the second stage intermixing of Au and Cu atoms was observed. The intermixing zone was found to be homogeneous up to a depth of more than 180 nm. In addition, ab initio calculations were performed in order to estimate the composition of the alloyed film, which was found to be  $\text{Au}_{0.7}\text{Cu}_{0.3}$ .

## Element specificity of PAS

In the present study [1], the high-intensity positron beam NEPOMUC at the MLZ was used in order to study the tempering of a two-layer system of Au and Cu on a Si substrate. Therefore, depth dependent CDBS of the positron annihilation line was applied. The Doppler broadening is caused by the momentum component of the annihilating electron-positron pair  $p_L$  longitudinal to the emission direction of the annihilation  $\gamma$ -quanta. With this technique, high Doppler shifts stemming from the annihilation with core electrons can be detected and hence, an element specific analysis of the surrounding of the annihilation site is possible. The interpretation of the data can be supported by the ab-initio calculation of CDB spectra. Moreover, the CDB signature can also be used to investigate the presence of open volume defects, which trap positrons with high efficiency.

Usually, not the raw CDB spectra are analyzed but the so-called ratio curves to a reference spectrum, which here has been measured for Cu.

## Depth profiling with positrons

The thin film system was produced by vapor deposition on a Si(100) substrate. A Au film of 180 nm thickness was deposited on top of a 480 nm thick Cu film. In EDX measurements, the chemical purity of the system was confirmed. X-ray diffraction revealed that both films were polycrystalline with a typical grain size around 30 nm. Afterwards, the system was investigated by depth dependent CDBS. The incident beam energy  $E_+$  was adjusted in order to probe different depth regions of the two-layer system. By precisely modelling both the positron implantation and diffusion, the  $E_+$  dependent depth distribution of the annihilating positrons can be determined. According to this information, Cu and Au reference spectra were superposed and the calculated spectra shown in Fig. 1 (solid lines) were obtained. One can see at  $E_+ = 6$  keV a CDB signature

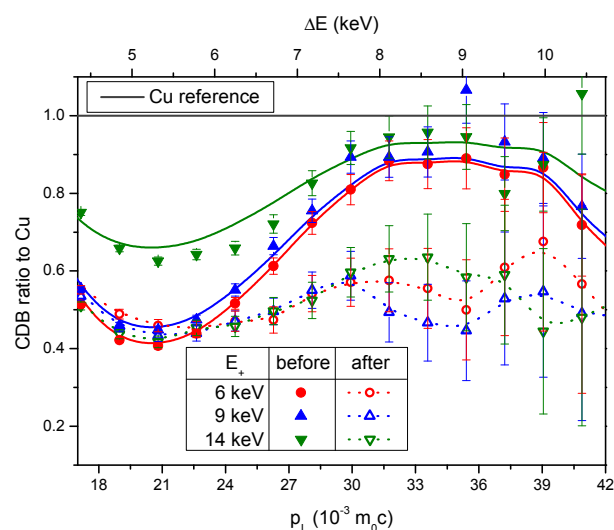


Figure 1: Depth dependent CDBS ratio curves taken at various incident positron energies  $E_+$  before (filled symbols) and after tempering (open symbols). The solid lines show calculated spectra for the Au/Cu two-layer before tempering. (from [1])

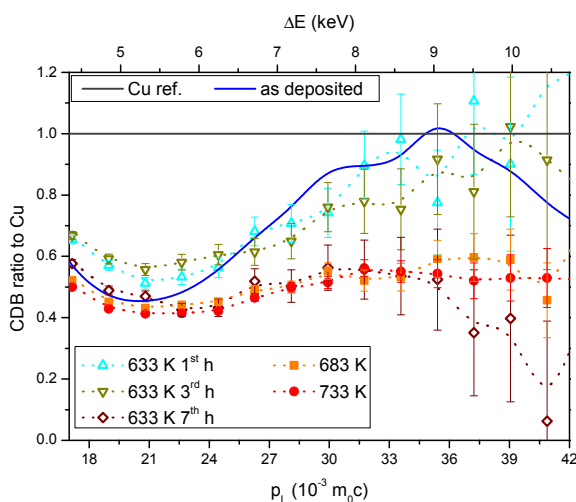


Figure 2: In-situ CDBS at high temperatures with ( $E_+ = 9$  keV): During tempering at 633 K thermodynamic equilibrium was reached after 7 h. Tempering for more than 7 h and heating up to 733 K do not change the spectra (dotted lines are guides to the eye). (from [1])

typical for Au. The approach of the ratio curves to the Cu reference with increasing  $E_+$  is caused by a higher fraction of positrons annihilating in the Cu film. Theoretical and measured spectra are in very good agreement in the element specific high momentum area, which clearly demonstrates the great potential of positron beams for the investigation of thin films and multilayer systems.

### In-situ CDBS at high temperatures

Then, the investigated system was heated up to a maximum temperature of 733 K and CDB spectra were detected in-situ. This experiment could only be conducted due to the extraordinarily high intensity of the NEPOMUC positron beam which allows high-quality CDB spectra to be detected within short measurement times. For this experiment, the new high-temperature sample holder of the CDB-spectrometer was used, which allows measurements at up to 1160 K with the sample biased to high voltages up to 30 kV. During tempering, spectra clearly kept changing at a temperature of 633 K for 7 hours (Fig. 2). Following a detailed analysis of the CDBS spectra (see [1] for details), these changes could be attributed to two effects: In the first three hours, it was mainly the annealing of the Au film that was detected. Later, the intermixing of Au and Cu atoms is the dominating process visible in CDBS, as shown in the following. Tempering for longer times or at higher temperatures did not further change the CDB spectra and hence, the examined system was in thermodynamic equilibrium.

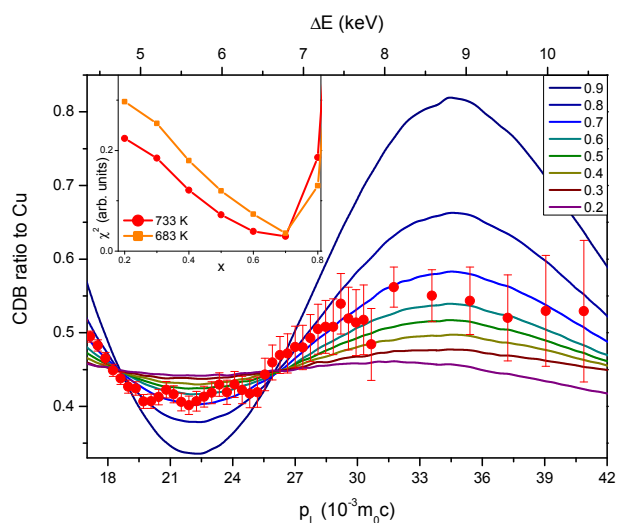


Figure 3: Calculational analysis of in-situ CDBS at 733 K ( $E_+ = 9$  keV): The comparison of the CDB spectra calculated for  $Au_xCu_{1-x}$  (solid lines) with that measured in the intermixing zone (symbols) shows excellent agreement for  $x = 0.7$ . The insert displays the fit error  $\chi^2(x)$ . (from [1])

### Calculational analysis of CDBS results

The CDB spectra detected in thermodynamic equilibrium are explained by the intermixing of Au and Cu atoms at the former interface of both layers. In order to estimate the Au content in the intermixing zone, CDB spectra were calculated for the disordered fcc phase of  $Au_xCu_{1-x}$  (see [3] for details). The Au content  $x$  was varied between 0.2 and 0.9 and the theoretical spectra were compared to the one measured at 733 K (Fig. 3). For  $x = 0.7$  very good agreement was found and hence, the composition of the intermixing zone can be estimated to be  $Au_{0.7}Cu_{0.3}$ . In order to probe the homogeneity of the intermixing zone, depth dependent CDBS was conducted after cooling down. Independently of the incident beam energy  $E_+$ , a CDB signature similar to the  $Au_{0.7}Cu_{0.3}$  one was found (Fig. 1). Hence, it is concluded that Cu atoms penetrated the complete Au film and that the intermixing zone is homogeneous in depth.

[1] M. Reiner et al., *J. Alloy. Compd.* 587, 515 (2014).

[2] M. Reiner et al., *J. Phys: Conf. Ser.* 443(1), 012071 (2013).

[3] M. Reiner et al., *J. Phys: Conf. Ser.* 505, 012025 (2014).

# Neutron spin echo spectroscopy under 17 T magnetic field at RESEDA

J. Kindervater<sup>1</sup>, N. Martin<sup>1,2,3</sup>, W. Häußler<sup>1,2</sup>, M. Krautloher<sup>4</sup>, C. Fuchs<sup>2</sup>, S. Mühlbauer<sup>2</sup>, J.A. Lim<sup>2,5,6</sup>, E. Blackburn<sup>6</sup>, P. Böni<sup>1</sup>, C. Pfeleiderer<sup>1</sup>

<sup>1</sup>Physik-Department, Technische Universität München, Garching, Germany

<sup>2</sup>Heinz Maier-Leibnitz Zentrum (MLZ), Technische Universität München, Garching, Germany

<sup>3</sup>DSM/IRAMIS/Laboratoire Léon Brillouin, CEA Saclay, Gif-sur-Yvette, France

<sup>4</sup>Max-Planck-Institut für Festkörperforschung, Stuttgart, Germany

<sup>5</sup>Institut für Festkörperphysik, Technische Universität Dresden, Dresden, Germany

<sup>6</sup>School of Physics and Astronomy, University of Birmingham, Birmingham, United Kingdom

A wide range of prominent scientific problems, such as the spectrum of thermal fluctuations stabilizing the Skyrmion lattice phase in chiral magnets [1,2], quantum phase transitions of transverse field Ising magnets [3] or field-induced Bose-Einstein condensation of magnons [4], involve high magnetic fields and simultaneously require neutron spectroscopy at sub- $\mu\text{eV}$  resolution. Despite this importance, very few studies of this kind have been reported in the literature. We have performed a proof-of-principle MIEZE (Modulation of Intensity with Zero Effort) [5] experiment at RESEDA (MLZ) under large magnetic fields which demonstrates for the first time the feasibility of applying strong magnetic fields up to 17 T at the sample while maintaining an excellent energy resolution [6].

## Spin echo techniques

Neutron spin echo (NSE) [6,7] encodes the information on energy transfers in scattering events in the polarization of the neutron beam. This permits complete decoupling of the energy resolution from the monochromaticity of the neutron beam. In turn, NSE techniques reach the highest energy resolution among all neutron spectroscopy techniques reported to date ( $\delta E \sim 1$  neV). On the downside, being based on polarized neutrons, it is crucial for conventional spin echo, i.e. NSE [6,7] and NRSE [8], that the neutron polarization is not changed in an uncontrolled manner, completely prohibiting depolarizing conditions (e.g. ferromagnetic) or the application of magnetic fields.

Approaches to overcome these constraints are realized in terms of Ferromagnetic NSE [7] or Intensity Modulation NSE [9]. However, the intrinsic loss of polarization and intensity strongly reduces their ef-

iciency. The resonant spin echo technique MIEZE allows these drawbacks to be overcome as all spin manipulations are performed in front of the sample, such that depolarizing environments at the sample have no influence on the measurement.

## MIEZE Setup at RESEDA

At the NRSE spectrometer RESEDA (MLZ), the MIEZE option has been implemented in terms of two different variants: (i) a conventional transverse (t-MIEZE) and (ii) a unique longitudinal MIEZE (l-MIEZE) setup, which differs in terms of the geometrical arrangement of the precession field. t-MIEZE uses transverse NRSE coils, akin to the standard

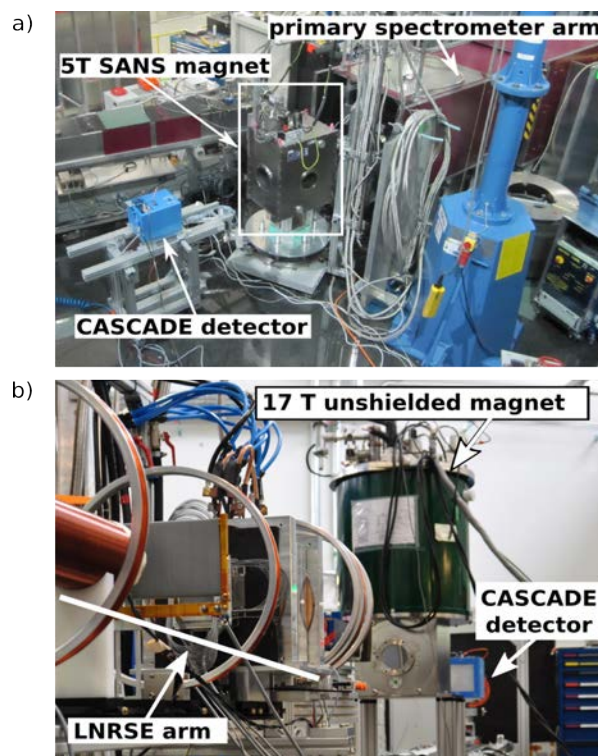


Figure 1: MIEZE and magnetic field setup at RESEDA. a) t-MIEZE setup as combined with an actively shielded 5 T SANS magnet from the MLZ sample environment group. b) l-MIEZE setup combined with the Birmingham 17 T magnet [13].

NRSE setup at RESEDA, where the main precession field is *perpendicular* to the neutron beam. In contrast, the I-MIEZE setup uses a field-geometry, where the main fields are *parallel* to the neutron beam (LNRSE) [10] as in NSE. The latter has the significant advantage that guide fields can be used to preserve the polarization so that no magnetic shielding is needed. Moreover, the similarity to NSE allows the same correction techniques to be employed. The LNRSE test setup already extends the highest spin echo time accessible at RESEDA by a factor of 10. Furthermore, LNRSE allows the application of effective field integral subtraction [11], extending the dynamic range towards lower spin echo times by two orders of magnitude.

### MIEZE resolution for different magnetic field configurations

For our proof of principle experiment, a shielded 5 T magnet and an unshielded 17 T magnet were used. The cryogen free 5 T magnet (c.f. Fig. 1 a)) was used with the t-MIEZE setup and the results for the neutron beam perpendicular a) and parallel b) are shown in Fig. 2. In both geometries, no reduction of the signal up to the maximum field of 5 T was observed.

The Helium cooled 17 T magnet, shown in Fig. 1 b), only allows for longitudinal magnetic fields [13]. Fig. 2 c) shows typical direct beam data measured with an applied field of 17 T when using the I-MIEZE setup. The scattering of the data points around the single exponential fit is caused by imperfect tuning due to time constraints. As seen in Fig. 2 c), the signal contrast achieved at a Fourier time  $\tau_{\text{MIEZE}} \approx 15$  ns is well above the resolution limit.

Setting up either magnet at RESEDA, including slight retuning of the instrument requires approximately half a day.

### Conclusion

We have demonstrated that large magnetic fields up to 17 T may readily be combined with the MIEZE technique at RESEDA. As the observed MIEZE resolution is independent of external conditions, field dependent studies are now possible. These results promise access to a wide range of scientific questions in hard and soft condensed matter by means of high-resolution neutron spectroscopy. Last but not least, the possibility of combining high-resolution neutron spectroscopy with high magnetic fields

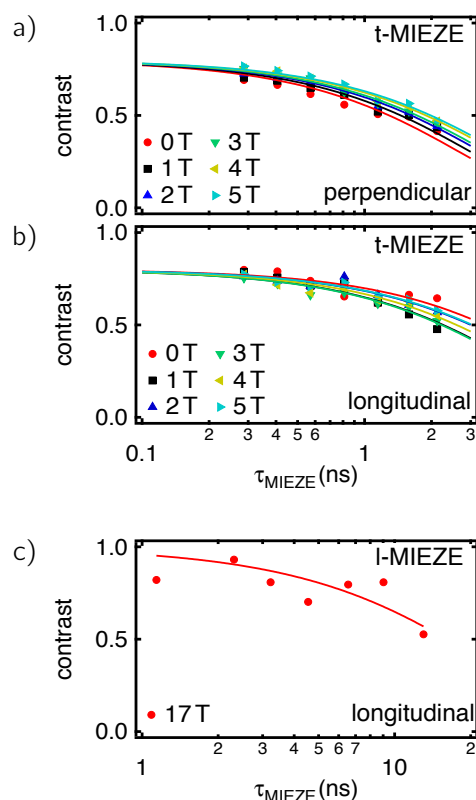


Figure 2: MIEZE resolution with magnetic field at the sample. Typical data as recorded with a 5 T SANS magnet, where the field was applied perpendicular a) and parallel b) to the neutron beam. c) Data recorded at 17 T applied longitudinal to the neutron beam using the Birmingham SANS magnet [13].

is also of great interest in the form of MIEZE as an add-on option for large scale SANS machines, bridging characteristic times of quasi-elastic measurements and stroboscopic studies in the range  $\Delta t \approx 1 \mu\text{s} - 1 \text{ms}$  in addition to SANS, TISANE and TAS/ToF.

- [1] S. Mühlbauer et al., *Science* 323, 915 (2009).
- [2] R. Georgii et al., *Appl. Phys. Lett.* 98, 073505 (2011).
- [3] R. Coldea et al., *Science* 327, 177 (2010).
- [4] A. Zheludev et al., *Phys. Rev. B* 76, 054450 (2007).
- [5] R. Gähler et al., *Phys. B Condens. Matter* 180, 899 (1992).
- [6] J. Kindervater et al., *EPJ Web of Conferences* 83, 03008 (2015).
- [7] F. Mezei, *Zeitschrift für Physik* 255, 146 (1972).
- [8] F. Mezei, *The principles of neutron spin echo* (Springer, 1980).
- [9] R. Gähler and R. Golub, *Z. Phys. B Condens. Matter* 65, 269 (1987).
- [10] B. Farago, and F. Mezei, *Phys. B, C* 136, 100 (1986).
- [11] W. Häußler et al., *Chem. Phys.* 292, 501 (2003).
- [12] W. Häußler and U. Schmidt, *Phys. Chem. Chem. Phys.* 7, 1245 (2005).
- [13] W. Häußler et al., *Rev. Sci. Instrum.* 82, 045101 (2011).
- [14] A. T. Holmes et al., *Rev. Sci. Instrum.* 83, 023904 (2012).

# Neutron reflectometry on samples with curved geometry

J. Fröh<sup>1</sup>, A. Rühm<sup>2</sup>, H. Möhwald<sup>3</sup>, R. Krastev<sup>4</sup>, R. Köhler<sup>5</sup>

<sup>1</sup>Harbin Institute of Technology, Harbin, China

<sup>2</sup>Max Planck Institute for Intelligent Systems, Stuttgart, Germany

<sup>3</sup>Max Planck Institute for Colloid and Interfaces; Potsdam-Golm, Germany

<sup>4</sup>Naturwissenschaftliches und Medizinisches Institut, University Tübingen, Reutlingen, Germany

<sup>5</sup>University of Technology Berlin and Helmholtz-Zentrum Berlin, Germany

For many decades, X-Ray and neutron reflectometry have proved to be versatile tools for the non-destructive determination of film thickness, roughness, and film composition on submicrometer and nanometer scales, both in soft and hard matter research. The basis of the reflectometry technique is the characteristic interference pattern resulting from coherent reflections of the incoming beam at the sample sub-interfaces. So far, this has limited the method to planar geometry. Our study shows how, by the use of modern 2D detectors and adequate alignment systems, the scope of reflectometry can be extended to curved geometries. This is equally important for fundamental and applied science, especially in the course of miniaturisation in technical applications, e.g. electronics, medical technology, and surface treatment.

## Improving a perfect tool?

For more than 80 years, the principle of X-ray reflectometry (XR) has been known as a tool for thin film and interface research. The more recent Neutron reflectometry (NR) is as potent as the established X-ray method, but complements it by virtue of its special features [1].

Both techniques are universally applicable methods, contact-free, and non-destructive. They deliver very precise information about the overall structure of films, and show material sensitivity. This made these techniques outstanding for interface science and indispensable in the course of the trend to miniaturized devices, functional coatings or smart interfaces.

The quintessence of the method is the reflection of the incoming beam at all sub-interfaces of the sample. The specularly reflected parts of the beam exhibit a fixed phase shift, yielding to a characteristic interference curve. Based on this curve, the film and

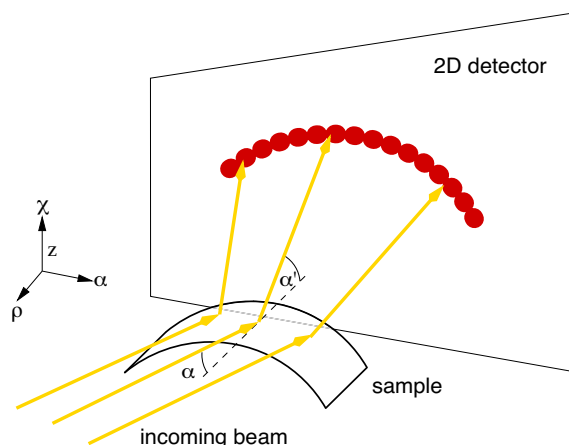


Figure 1: Principle of Reflectometry on curved samples: The sample is scanned around angle  $\alpha$ . Only the top of the sample fulfils the specular reflectivity condition (dashed line).

surface properties can be determined via fitting routines.

Both the XR and NR methods make high demands on the sample: homogeneity, low roughness, low waviness; i.e. planar and parallel interfaces are basic requirements. This excludes curved objects, which would be of special technological or scientific interest, e.g. shafts or tubes, but also coatings on curved objects.

Our approach illustrates that the capabilities of the newly available 2D detectors, combined with high-precision sample positioning devices, make it possible to extend NR to complex geometries.

## Principle and Challenges of NR on curved samples

For reflectometry on a planar sample, the height  $z$  and rocking angle  $\alpha$  have to be aligned. On curved objects, two further parameters are added: the rolling angle  $\rho$ , and twisting angle  $\chi$ . The chosen sample is axially symmetric around  $\rho$ , so only  $\chi$  remains to be aligned [3].

Fig. 2 presents the adjustment of angle  $\chi$  of a curved sample, with the properly aligned sample in the middle. The vast impact of the  $\chi$ -alignment on the reliability of the measurement is obvious.

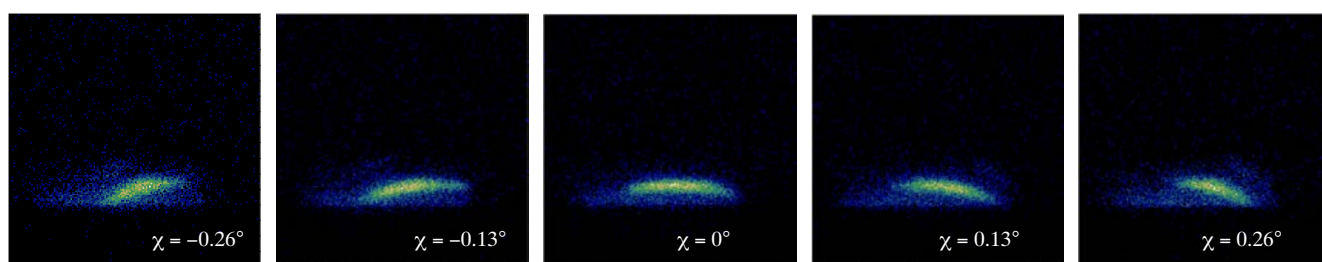


Figure 2: Alignment of the twist angle,  $\chi$ : Detector images of a scan around the vertical axis. The central image represents the accurately aligned sample. (Left to right, clockwise rotation. The direct beam is blocked.)

While measuring, sample and detector pivot around axis  $\alpha$ . Only the summit part of a curved sample is in specular condition (Fig. 1). To avoid any impact from the intensity scattered by the wings, the lateral reflection is blocked by a software mask [3].

### Reflectometry with PEM as the model system

Polyelectrolyte multilayers (PEM) are Soft matter films, stepwise adsorbed to solid substrate. Their structural properties are well known and easily tunable, making them well-suited model systems [2]. Three different samples are tested: glass slides, glass slides coated with PEM and glass slides with PEM featuring a deuterium-labelled sandwich structure. The samples are bent using a special device to obtain a defined curvature,  $R \approx 95$  mm. NR experiments are performed on N-Rex at MLZ and on the V6 device at HZB.

### Modified reflectometry method

The newly available 2D-detectors, together with high-precision adjustment systems, allow the classical reflectometry method to be adapted to more complex sample geometries. This clearly extends the applicability of XR and NR in interfacial science, making way for new experimental approaches and measurements on objects with curved or bent elements.

However, the mutual interaction of the angular resolution of the positioning system and the sample curvature is challenging. Together with the resolution of the 2D detector, it depicts device-related restrictions of the method. For increased sample curvatures, this is aggravated by the demand for reducing aperture size, which subsequently diminishes the signal quality.

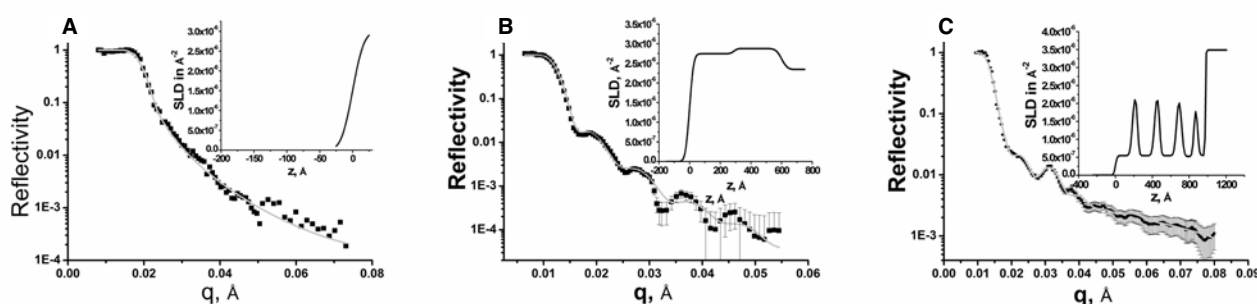


Figure 3: Reflectivity curves and fits: Bare substrate (A), PEM film on substrate (B), and layer-structured PEM on substrate (C). The insets present the SLD- thickness profiles. (Momentum transfer,  $q = 4\pi/\lambda \cdot (\sin \alpha)$ .)

The reflectivity curves obtained exhibit characteristic features: critical edge (A), Kiessig fringes (B), and Bragg peak (C) (Fig. 3). The insets reveal the underlying structure of the samples: an abrupt rise of the Scattering length density (SLD) at the interface, an almost homogeneous film, and a film with four equidistant layers. The film parameters obtained are a very good match to the expected values for PEM [3].

We are indebted to MLZ Garching and HZB Berlin for providing beam time at the NREX and V6 devices, the DFG (project KR 3432/1-1), and the HIT, China for financial support.

- [1] J. Daillant, A. Gibaud (Eds.) X-ray and Neutron Reflectivity: Principles and Application. Springer, Berlin Heidelberg 2009.
- [2] M. Lösche et al., *Macromolecules* 31, 8893 (1998)
- [3] J. Früh et al., *Physica B* 457, 202 (2014).

# PGAA-Actinide: a series of experiments for actinide nuclear data improvement

M. Rossbach<sup>1</sup>, C. Genreith<sup>1</sup>, T. Randriamalala<sup>1</sup>, Z. Revay<sup>2</sup>, P. Kudejova<sup>2</sup>

<sup>1</sup>Institute for Energy and Climate Research, Nuclear Waste Management and Reactor Safety, Forschungszentrum Jülich GmbH, Jülich, Germany

<sup>2</sup>Heinz Maier-Leibnitz Zentrum (MLZ), Technische Universität München, Garching, Germany

The characterization of nuclear waste and residues from the dismantling of nuclear installations is a challenge as large amounts of radioactive materials mixed with heavy metals in various geometries are involved. Long-lived minor actinides produced in the fission process need to be accurately quantified as these radionuclides determine the time scale for safe deposit. An active neutron-generator-based material interrogation technique for the quantification of actinides in heterogeneous matrices requires accurate and reliable nuclear data. PGAA with cold neutrons at the FRM II was used to extract neutron capture cross sections of <sup>237</sup>Np, <sup>242</sup>Pu and <sup>241</sup>Am. A set of well-defined samples was prepared for irradiation to extract partial gamma-ray production and thermal neutron-capture cross sections for these actinides. In addition, for <sup>242</sup>Pu the Monte Carlo code DICEBOX was applied to extract information on the unresolved continuum in the prompt gamma spectrum.

## Sample preparation

Thin Suprasil<sup>®</sup> quartz blades (Heraeus Quarzschmelze, Hanau), 0.2 mm thick and 40 x 40 mm wide were used to encapsulate the actinide samples as Si and O produce little background in PGAA spectra. A 3 mm diam. and 3 μm thick 99.9 % pure gold foil (Alfa Aesar) was placed central to one quartz blade, a drop of the activity solution or an actinide pellet was placed onto the gold and a second quartz blade was subsequently fixed with epoxy on top. This procedure ensured a spot-size sample, giving the possibility of inspecting sample positioning and determining the mass through the measured activity of the actinide [1,2].

## Sample irradiation and spectrum evaluation

Preliminary experiments were carried out at the Budapest Research Reactor of the Centre for Energy Research, **MTA EK** providing a thermal equivalent

cold neutron flux of  $7 \times 10^7 \text{ cm}^{-2}\text{s}^{-1}$ . The Compton suppressed 27 % rel. eff. HPGe detector is 23.5 cm away from the sample irradiation position. At MLZ, the PGAA facility can provide up to  $6 \times 10^{10} \text{ cm}^{-2}\text{s}^{-1}$ , the detector system consists of a 60 % rel. eff. Compton-shielded HPGe crystal and is about 30 cm away from the sample irradiation position.

Hypermet-PC provided by the PGAA group in Budapest [3] was used for the evaluation of the prompt gamma spectra. Corrections for self-absorption of neutrons in the sample and housing as well as attenuation of low energy gammas in the same material were considered.

DICEBOX, a Monte Carlo computer code originally developed at Řež, Czech Republic [4] generates simulated neutron capture decay schemes based on nuclear level density and photon strength function models. The simulated intensities of transitions populating low-lying levels can be normalized to the experimental cross sections, de-exciting those levels in order to determine the unobserved cross section feeding the ground state. Combined with the observed cross section feeding the ground state, the total radiative thermal neutron cross section  $\sigma_0$  were evaluated.

## Neutron capture cross sections

Thermal capture cross sections were calculated after neutron flux determination from a co-irradiated Au foil (0.05 mm thick). Results for <sup>237</sup>Np, <sup>242</sup>Pu and <sup>241</sup>Am compare very well with literature values, as can be seen from Fig. 1-3.

As the uncertainties of the experimentally determined cross section for <sup>242</sup>Pu were relatively large, this nuclide was investigated using DICEBOX at the LBNL, Berkeley. Using this MC code in addition to experimentally determined gamma energies, the decay transitions from the continuum could be evaluated. The result for the capture cross section of <sup>242</sup>Pu (n,γ) <sup>243</sup>Pu obtained from the simulation

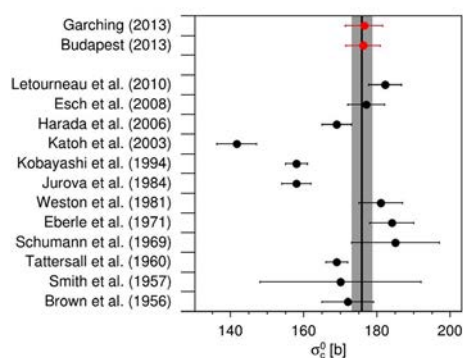


Figure 1: Neutron capture cross section values for  $^{237}\text{Np}$  compared to literature values. Vertical line represents the ENDF value.

is  $21.9 \pm 1.5$  barn, a considerably smaller uncertainty compared to the mean experimental value of  $19.8 \pm 4$  barn. Similar evaluations for  $^{237}\text{Np}$  and  $^{241}\text{Am}$  are in progress.

With respect to the development of PGAA based analysis of actinides, the absolute detection limits for  $^{237}\text{Np}$ ,  $^{241}\text{Am}$  and  $^{242}\text{Pu}$  under FRM II irradiation conditions were found to be (using low-energy gamma lines up to 300 keV) 0.06, 0.02 and 0.2  $\mu\text{g}$  respectively, and 1.4, 0.6 and 10  $\mu\text{g}$  for high-energy gamma rays. These values seem to suffice for the analysis of small samples, such as safeguard swipe samples, and are promising for the further development of methods for actinide analysis in debris from decommissioning or low- and medium-activity nuclear waste forms.

### Energy dependence of $^{241}\text{Am}$ cross section determination

The large scatter of results from  $^{241}\text{Am}$  ( $n,\gamma$ ) cross section determinations, as shown in Fig. 3, provoked a discussion on possible reasons for the discrepancies observed. A low-lying first resonance could have affected the 0.0253 eV capture cross section determination where thermal neutron irradiations are concerned. As our experiments were performed using sub-thermal neutrons, we assume our values to be free from interferences from low energy reso-

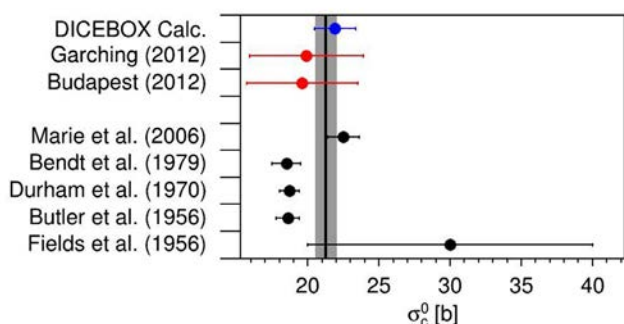


Figure 2: Neutron capture cross section values for  $^{242}\text{Pu}$  compared to literature values. Vertical line represents the ENDF value.

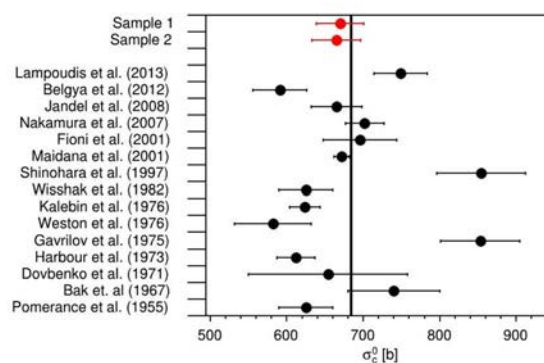


Figure 3: Neutron capture cross section values for  $^{241}\text{Am}$  compared to literature values. Vertical line represents the ENDF value.

nances. Our  $^{241}\text{Am}$  data are related to the 0.0253 eV capture cross section of  $^{197}\text{Au}$  ( $98.65 \text{ b} \pm 0.01 \%$ ) and represent the thermal capture cross section of  $^{241}\text{Am}(n,\gamma)^{242\text{g,m}}\text{Am}$  [6].

### Wrap-up

Sensitive and reliable determination of thermal capture cross section data of actinides is possible by applying PGAA using cold-neutron beams at high-flux research reactors. Our results for  $^{241}\text{Am}(n,\gamma)^{242\text{g,m}}\text{Am}$  neutron capture cross sections of  $711 \pm 35 \text{ b}$  and  $725.4 \pm 34.4 \text{ b}$  compare well with the most recent time-of-flight measurement from IRMM, Geel of  $749 \pm 34 \text{ b}$ . The DICEBOX value of  $^{242}\text{Pu}$  confirmed the most recent experimental result of Marie et al. together with the low uncertainties. Further experiments using the same samples, but with fission neutrons at SR10 (MEDAPP and NECTAR) for irradiation are being planned to lay the grounds for a future analytical method based on neutron generators (DD or TD) for actinide characterization.

### Acknowledgement

We are grateful for financial support from the BMBF under grant **02S9052**. Financial support for irradiation carried out at the Budapest research reactor was generously provided by the EURATOM FP7 ERINDA project (Grant Agreement No. 269499).

- [1] C. Genreith et al., J. Radioanal. Nucl. Chem. 296(2), 699 (2013).
- [2] C. Genreith et al., Proc. of Int. Conf. Nucl. Data Sci. Technol. March 4-8, 2013 New York, USA. Nucl. Data Sheets 119, 69 (2014).
- [3] B. Fazekas et al., J. Trace Microprobe Tech. 14, 167 (1996).
- [4] F. Běčvář, Nucl. Instr. Meth. A 417, 434 (1998).
- [5] C. Genreith, PhD Thesis, Rheinisch Westfälische Technische Hochschule RWTH Aachen (2014).
- [6] M. Rossbach, C. Genreith, CERN, Geneva, Switzerland, 1-3 October 2013, CERN-Proceedings-2014-002 157-163 (CERN, Geneva, 2014).
- [7] M. Rossbach et al., J. Radioanal. Nucl. Chem. published online DOI 10.1007/s10967-015-4001-0

# Versatile module for experiments with focussing neutron guides

T. Adams<sup>1</sup>, G. Brandl<sup>1,2</sup>, A. Chacon<sup>1,2</sup>, J. N. Wagner<sup>1,2</sup>, M. Rahn<sup>1,2</sup>, S. Mühlbauer<sup>1,2</sup>, R. Georgii<sup>1,2</sup>, C. Pfeleiderer<sup>1</sup>, P. Böni<sup>1</sup>

<sup>1</sup>Physik-Department, Technische Universität München, Garching, Germany

<sup>2</sup>Heinz Maier-Leibnitz Zentrum (MLZ), Technische Universität München, Garching, Germany

**W**e report on the development of a versatile module that permits fast and reliable use of focussing neutron guides under varying scattering angles. The change-over between neutron guides with different focussing characteristics requires no readjustments of the experimental setup. Exploiting substantial gain factors, we demonstrate the performance of this versatile neutron scattering module in a study of the effects of uniaxial pressure on the domain populations in the transverse spin density wave phase of single crystal Cr. The development of the module and the experiments with the focussing guides were carried out at the instrument MIRA [1].

## Setting-up the focussing neutron guides

Shown in Fig. 1 (a) are the main components of the module we have developed. A high-precision alignment table (T), providing a circular slide rail, supports two freely-movable base plates (B). Housings (H) containing the focussing guides (G) can be reproducibly installed on these plates (B) using kinematic mounts. While the alignment table (T) and the base plates (B) link the module to the neutron scattering instrument, the neutron guides are aligned and attached to the housings (H) by set-screws. This allows for a highly reproducible alignment and fast turn-around times, because, (i), the combination of the alignment table (T) and base plates (B) provides a rigid and accurate support structure, (ii), the focussing neutron guides need to be aligned only once with respect to the housings (H), and, (iii) the positioning of the housings (H) by virtue of the kinematic mounts is extremely accurate and reproducible (better than 0.01 mm and 0.01°).

Hence, the modul may be set up in a few hours on completely different neutron scattering instruments. To reduce the time for setting up the module, the focussing neutron guides may be pre-aligned with

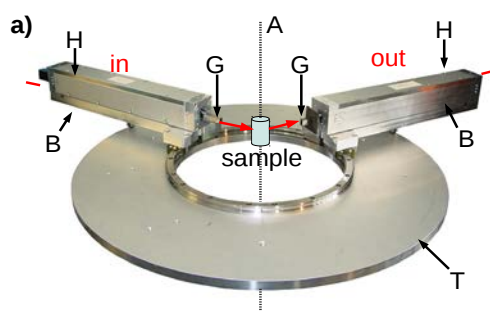


Figure 1: Photograph of the guides-module with the alignment table (T) and the base plates (B), which support the housings (H) with the focussing neutron guides (G) using kinematic mounts. The sample is centered at the axis (A).

respect to the housings by optical methods without the need for neutrons. To this end we designed an optical system comprising of a laser and a set of lenses illuminating the neutron guide (G) uniformly at the back-end of the housing (H). Once the module has been set up, it permits changes between different focussing guides without loss of alignment. This allows the spot size and focal length to be adapted instantly.

## Proof of principle experiment

To demonstrate the improvements in the scattering intensity of the focussing guides module using small samples, we studied the uniaxial pressure dependence of the domain populations in the transverse spin density wave (SDW) state of the single-crystal Cr. At the Néel temperature,  $T_N = 311$  K, Cr undergoes a weak first order transition from paramagnetism to SDW order [2], which is characterised by incommensurate wave vectors  $Q^\pm = (0, 0, 1 \pm \xi)$  with  $\xi \approx 0.046$ . We used a He-activated bellow system [3,4] to apply uniaxial pressure,  $\sigma$ , along the [001] axis of a small cubic sample ( $2 \times 2 \times 2$  mm<sup>3</sup>). Our study was performed at MIRA using a counting tube. Data of the magnetic Bragg peaks were collected in the vicinity of the forbidden (010) nuclear Bragg peak (see Fig. 2 (a)). Higher order scattering was suppressed with a Be filter.

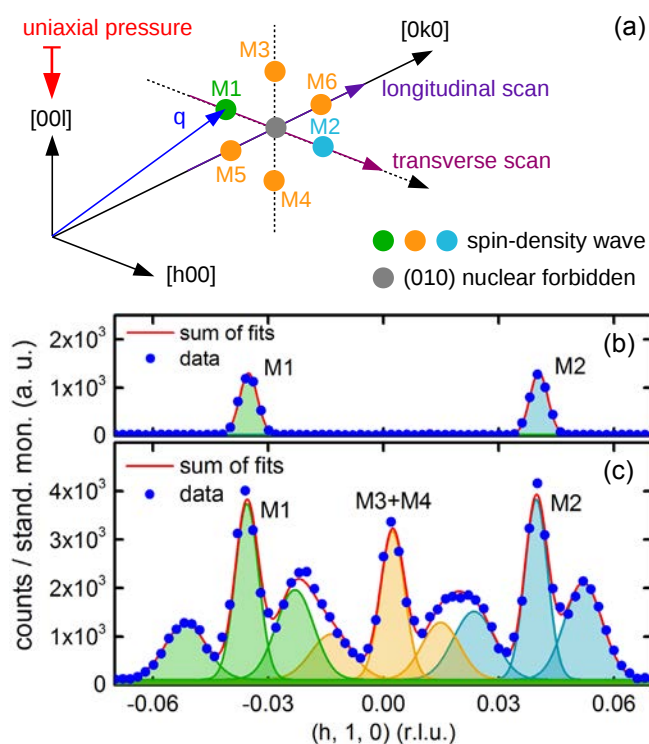


Figure 2: Typical momentum-scans in Cr using focussing neutron guides. (a) Schematic depiction of the magnetic Bragg peaks in the SDW state in the vicinity of the forbidden (010) nuclear Bragg peak. (b) Transverse  $q$ -scan without neutron guides using a counting tube. (c) Transverse  $q$ -scan with two neutron guides using a counting tube. The second neutron guide leads to a main maximum with two side maxima.

### Domain populations depend on uniaxial pressure

Typical transverse scans at ambient temperature are shown in Fig. 2. Without neutron guides (b) the measurement shows the magnetic satellites at M1 and M2. After adding the neutron guides (c) a large increase in intensity is observed. As an important additional feature, each magnetic Bragg peak (M1 and M2) now consists of an intensity maximum and two side peaks, because the second neutron guide captures different parts of the inhomogeneous phase space assumed by the neutron beam at the sample location as the scattering angle changes. The tails of the peaks at M3 plus M4 lead to an additional intensity, because the inhomogeneous phase space distribution at the sample location also yields a larger effective divergence.

To track changes in the domain populations due to uniaxial pressure directly, we performed longitudinal scans at ambient temperature as shown in Fig. 3, where the pairs M3/M4 and M5/M6 reflect the behaviour parallel and perpendicular to the pressure axis, respectively. With increasing pressure,

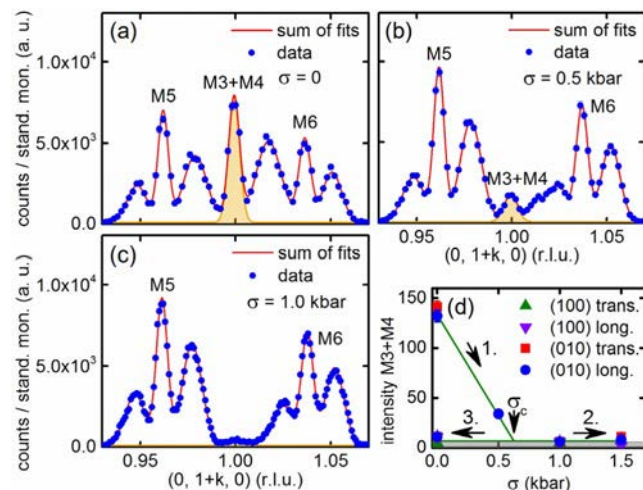


FIG. 3: Effect of uniaxial pressure on the domain distribution in the transverse SDW of Cr as observed in longitudinal  $q$  scans at ambient temperature. With increasing uniaxial pressure the domain population in the direction of the uniaxial stress axis (M3 and M4) is depopulated and vanishes irreversibly above a critical pressure  $\sigma_c \approx 0.6$  kilobars.

the contribution due to M3 and M4 decreases and vanishes above a critical pressure  $\sigma \approx 0.6$  kilobars (Fig. 3 (d)). When again decreasing the pressure to zero at unchanged temperature, the domains M3/M4 remain unpopulated. This is consistent with a uniaxial pressure-induced symmetry breaking, as predicted theoretically.

### Benefit of focussing neutron guides

In our experiments we have readily achieved gains in intensity of a factor of four. The full benefit of using focussing neutron guides will unfold in the presence of large background contributions due to the sample environment. This concerns, for instance, much reduced sample dimensions or high pressure experiments. The biggest benefit of using focussing neutron guides may finally be expected, when the artefacts arising from the combination of inhomogeneous phase space and increased beam divergence at the sample location reported here are not important. A prominent example is inelastic neutron scattering studies, where large beam divergences are favourable. Here, major improvements in the signal to noise ratio exceeding well over an order of magnitude are expected.

[1] T. Adams, *Appl. Phys. Lett.* 105, 123505 (2014).

[2] E. Fawcett, *Rev. Mod. Phys.* 60(1), 209 (1988).

[3] C. Pfleiderer et al., *Rev. Sci. Instrum.* 68, 3120 (1997).

[4] A. Chacon, M.S. thesis, Technische Universität München, 2011.

To ensure the supply of Tc-99m, the construction of an irradiation facility for the production of Mo-99 at the FRM II is underway. The completion and commissioning of the facility is foreseen for 2017.



# Reactor & Industry

# Ten years of reactor operation – A reason to celebrate, but also to work even harder

A. Kastenmüller

Forschungs-Neutronenquelle Heinz Maier-Leibnitz (FRM II), Technische Universität München, Garching, Germany

**F**or the FRM II, the year 2014 was special in two ways: On 2<sup>nd</sup> March, 2014, the FRM II celebrated its 10<sup>th</sup> anniversary since the reactor became critical for the first time on 2<sup>nd</sup> March, 2004 at 14:01 hours. Also, the day of the first criticality was the date when the extensive in-service inspections to be conducted after 10 years of operation became due for the first time, and for which a six-month maintenance break had been scheduled. The check-ups were completed within the planned time frame and after the maintenance break the FRM II started up again right on time. 121 days of operation were announced in the general operation plan and a total of 116 days of beam time at 20 MW were available for our users in 2014. Thus, the operational availability of the FRM II, even in the year of the major 10-year maintenance break, stood at an excellent 96 %.

## Celebrating ten years of safe reactor operation

A small internal celebration on Sunday, 2<sup>nd</sup> March, 2014 at 14:01 hours was followed by an official ceremony on 12<sup>th</sup> March, 2014, at which many prominent personalities from the design and construction phase of the FRM II, as well as from the past 10 years of successful operation, took part. Representatives from the realm of politics as well as users, friends, sponsors, and colleagues came from universities, research centers, the regulatory body and their expert organisation, industry and the press. Particularly pleasing was the attendance of true allies of the FRM II, who had personally contributed in one way or another to the construction and commissioning of the reactor.

## The long maintenance break

Extensive preparations were necessary for the forthcoming inspection of the moderator tank, the

central channel, the beam tubes, the cold and hot source and many other systems and components. So, after removing various blind caps, the moderator tank had to be emptied, dried and filled with light water to make it accessible to a camera inspection. Also, in the experimental hall, the accessibility and visibility of the beam tube end plates had to be prepared by the partial dismantling of the instrument shielding. The pressure check of the moderator tank, the central channel and the beam tubes also required extensive preparation such as the removal of individual components and the manufacturing and installation of special pressure test inserts. Apart from the practical tests and inspections, the material properties also had to be checked, especially of the near-core installations made of AlMg<sub>3</sub>, to verify that they were in an appropriate condition for continued safe operation even under the influence of neutron-induced embrittlement. This was validated for all major components by externally assigned calculations. In these analyzes, the results of an irradiation program in which samples are continuously irradiated during reactor operation were included.



Figure 1: 2<sup>nd</sup> March, 10 years ago: concentration and tension at the same time - the first start of the FRM II in the control room.

On completion of all planned inspections, the moderator tank had to be closed again by reassembly of the blind caps, the light water removed, and the moderator tank dried again and then refilled with heavy water. In addition, a variety of other systems had to be reassembled and brought back into operation step-by-step for the forthcoming start-up of the FRM II.

Through the dedicated efforts of our own staff, the external companies involved and designated experts, all inspections were completed successfully. When the results had been submitted to the regulatory body, the continued operation of the FRM II was approved. Thus, the start-up on 21<sup>st</sup> August corresponded almost perfectly to the proposed start-up date for the 35<sup>th</sup> cycle.

Over the year, 1,932 periodic tests, operability checks, inspections by independent experts from the regulatory body covering 18 different subject areas, as well as maintenance work and around 35 modifications to the facility that had to be referred to the regulatory body, guaranteed that the high safety standard of the FRM II was sustained, and even enhanced. There was one reportable incident in 2014.

#### The fuel cycles of 2014

In 2014, the FRM II was operated safely with cycle no. 30b, 35 and 36a delivering nuclear energy totaling 2320.5 MWd.

For the cycle 30b, a partially burned fuel element was used, which had been used in December 2012 up to a burnup of 650 MWd. This fuel element could only be used up to a burnup of 1174 MWd as on 9<sup>th</sup> February the upper end position of the control rod had already been reached, so that the reactor needed to be shut down before the maximum burnup of 1200 MWd.

The 35<sup>th</sup> cycle had to be interrupted twice: once because of the failure of a motor in a secondary pump and once more due to the failure of a fuse in the control circuit of a power switch of a secondary pump. In both cases, the reactor was shut down as a precaution using the routine shutdown procedure. The cold source remained in operation continuously and a short-term restart after the decay of xenon poisoning was possible. In spite of the two interruptions,



Figure 2: Construction project "Neue Mitte Garching" also poses a challenge to the FRM II.

the target burnup of the fuel assembly was reached, since the last days of operation were attached at the end of the cycle.

Cycle 36, which began on 17<sup>th</sup> November, was interrupted by the automatic shutdown procedure only 7 days later due to large differences in the measured values of the redundant moderator level sensors. According to the reporting criteria of the FRM II, this incident had to be reported to the regulatory body. When the level sensors had been readjusted, cycle 36 was able to be continued until the Christmas break. The latter was then also used for a further clarification of the cause of the measurement differences.

#### Challenges due to construction work

In preparation for the planned construction of a workshop and an office building by the FRM II, as well as a laboratory and an office building by the Forschungszentrum Jülich on the premises of FRM II from 2016 onwards, extensive measures for clearing the construction and building sites had already been put into place in 2014.

Even outside the premises of the FRM II, a big construction project "Neue Mitte Garching" by a private company has started. Due to the close proximity of the construction site and aspects of the security installations of the FRM II, we are also involved in the progress of this work.

Both big on-site, as well as adjacent construction projects, present a permanent additional challenge for the operation of the reactor due to possible impact on the facility that has to be considered and the related administrative procedures.

# Progress in UMo fuel development

H. Breitzkreutz<sup>1</sup>, F. Alder<sup>2</sup>, B. Baumeister<sup>1</sup>, T. Chemnitz<sup>1</sup>, H.-Y. Chiang<sup>1</sup>, A. Egle<sup>1</sup>, L. Fiedler<sup>3</sup>, R. Großmann<sup>1</sup>, T. Hollmer<sup>1</sup>, T. K. Huber<sup>1</sup>, M. Kraut<sup>1</sup>, C. Reiter<sup>1</sup>, R. Schauer<sup>1</sup>, R. Schenk<sup>1</sup>, C. Steyer<sup>1</sup>, A. Wolf<sup>1</sup>, T. Zweifel<sup>1</sup>, A. Röhrmoser<sup>1</sup>, W. Petry<sup>1</sup>

<sup>1</sup>Forschungs-Neutronenquelle Heinz Maier-Leibnitz (FRM II), Technische Universität München, Garching, Germany

<sup>2</sup>Lehrstuhl für Automatisierung und Informationssysteme (AIS), Fakultät für Maschinenwesen, Technische Universität München, Garching, Germany

<sup>3</sup>Fakultät für angewandte Naturwissenschaften und Mechatronik, Hochschule München, München, Germany

The aim of the working group “Hochdichte Brennstoffe” is the development of the new UMo fuel which will serve as a replacement for the current  $U_3Si_2$  HEU fuel. This involves reactor physics calculations to specify fuel conditions during the full reactor cycle in order to guarantee the safety and performance of the reactor, fabrication technology to pave the way for industrialisation, irradiation testing (in-pile and using heavy ions) as well as measurements of physical properties to study fuel behaviour and determine operation parameters.

## Reactor physics

A draft for a fuel element with 25 % enrichment based on monolithic UMo was published at RRFM 2014. This draft utilizes Molybdenum depleted in  $^{95}Mo$  to mitigate the strong parasitic absorption and is similar to the 27 % draft that was presented last year.

To quantify the transient reactor behaviour with a possible new fuel element, calculations that take the full reactor system into account are under development to assess reactor behaviour in these time- dependent processes. First thermal-hydraulic simulations with an ATHLET model of FRM II have been performed and a core model is being adapted for the neutronic code TORT-TD.

## Fuel production

TUM contributes to the development of monolithic as well as dispersion UMo fuel.

## Monolithic fuel

A dedicated chemistry glove box has been constructed and tested in the Uranium lab of the group for the chemical cleaning of UMo foils prior to coating with thin diffusion barriers using PVD. To obtain a thor-

ough understanding of the optimum coating process parameters, a prototypic mini-plate device has been tested and further improved using surrogate material. These surrogate plates will later be tested using the C2TWP process at CERCA to pave the way for the use of uranium in the fabrication process.

Based on experience gained from the mini device, a dedicated glove box and vacuum chamber are currently under construction to house an optimized full-size PVD device. Such a device is necessary to produce coated full-size fuel foils equivalent to the current fuel geometry for future irradiation tests and manufacturing industrialization.

## Dispersion fuel

FRM II and CERCA have succeeded in designing and implementing an industrial prototype U-8Mo fuel-powder production facility. After hot commissioning of the production facility in 2014 and first feasibility tests with uraniferous material, atomizer parameterization tests using depleted U-8Mo were carried out showing results that are consistent with industrial standards including safety, repeatability

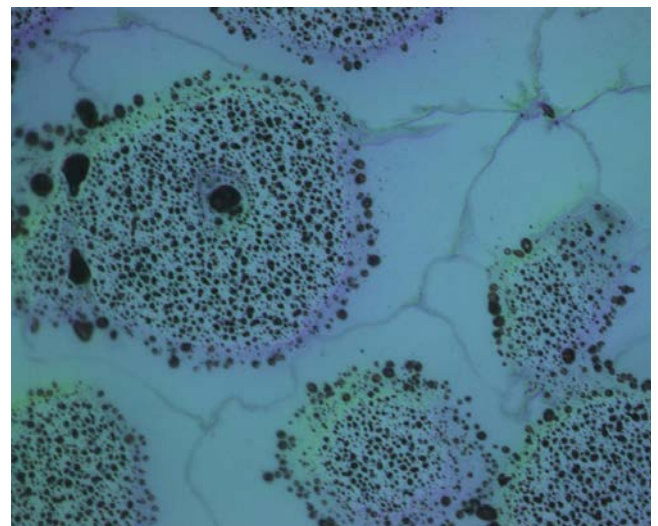


Figure 1: Optical microscopy of an in-pile irradiated dispersion fuel sample from the AFIP-1 experiment.



Figure 2: The new Uranium-lab of the group is licensed according to §9 AtG.

and reliable performance. Notably, powder requirements with respect to particle size, shape, satellites, porosity, voids, surface, homogeneity and oxidation are met.

### Irradiations

The HERACLES group has begun preparations for two in-pile irradiation tests, EMPIRE and SEMPER FIDELIS. Besides fundamental aspects of fuel behaviour such as high burn-up swelling, the irradiation also targets the quantification of the influence of production technology on fuel performance.

Heavy ion irradiation was used to further test transition metal ( $X = \text{Ti, Zr, Nb, Mo}$ ) diffusion barriers to prevent IDL formation. No UMo-Al compounds were found, only slight atomic mixing at the interfaces. All elements formed intermetallic compounds with Al that can act as additional barriers at the X/Al interface. However, Ti and Zr might lead to  $\gamma$ -UMo decomposition by forming orthorhombic U-Ti compounds or segregation of Mo from UMo, respectively. Nb is stable at both interfaces; however the crystallinity of the Nb-Al compound is poor. All in all, Mo is the best performing candidate for diffusion barriers in UMo/X/Al systems in view of its high strength Mo-Al compound to protect the interface.

As a consequent continuation of the Iodine irradiation, Kr was implanted into the irradiated UMo/Al layer system to study inert gas behaviour. SEM and SIMS revealed that Kr accumulates inside the IDL in  $\mu\text{m}$ -sized bubbles with a 1000 times higher quantity than in IDL free regions. This result is in full agreement with in-reactor irradiation experiments, extend-

ing the out-of-reactor irradiation's ability to predict in-pile results.

### Physical properties

Measurements of the thermo-physical properties of spent dispersion UMo fuel were performed at PNNL together with INL (US), using fuel segments from the AFIP-1 irradiation test (atomized U-7 wt.% Mo in an Al/2.1 wt.% Si matrix, max. burn-up  $6.0 \cdot 10^{21}$  f/cc). The specific heat capacity hardly depends neither on temperature nor burn-up. Density decreases by 21 % with burn-up due to fission gas bubbles. The thermal diffusivity increases with temperature but decreases significantly with burn-up. The calculated thermal conductivity therefore increases slightly with temperature, but decreases from originally 50 W/m·K down to 7 W/m·K for the highest burn-up. Parallel measurements of alloyed fresh matrix material have been performed at FRM II to allow for separation effects.

The last missing crystal structure for the  $\alpha''$ -phase of UMo has been determined as P1121/n using X-ray diffraction. Attempts to reproduce the Si-rich layer found around UMo grains during irradiation by out-of-pile alloying showed differences to the crystal structure found in-pile.

### Uranium laboratory

All requirements for the Uranium laboratory associated with §9 AtG license were fulfilled and the laboratory has entered into trial operation. Further licensing processes for additional glove boxes have been initiated.

# Future Mo-99 irradiation facility

C. Müller, H. Gerstenberg, M. Giourges, G. Haas, P. Jüttner, A. Röhrmoser

Forschungs-Neutronenquelle Heinz Maier-Leibnitz Zentrum (FRM II), Technische Universität München, Garching, Germany

The radionuclide molybdenum-99 (Mo-99), whose daughter nuclide technetium-99m (Tc-99m) is the most widely used radioisotope in nuclear medicine, is preferably obtained as a fission product of the irradiation of uranium targets in research reactors. As both Mo-99 and Tc-99m have short half lives, 66 and 6 hours respectively, it is immediately clear that the most widely used radioisotope in medicine, Tc-99m, cannot be stored but needs to be continuously produced. To ensure the supply of this radionuclide, the construction of an irradiation facility for the production of Mo-99 at the FRM II is underway. The Mo-99 irradiation facility is composed of three functionally independent systems that are controlled and monitored by a common control system. The three systems include the Mo-99 cooling system, the Mo-99-changing unit and the Mo-99 thimble with a helium gas protection system. In addition to the construction of the irradiation facility itself, the handling of the uranium targets and transport containers has to be appraised; in addition, various indispensable tools and equipment need to be developed and tested. The completion and commissioning of the facility is foreseen for 2017.



Figure 1: Mock-up on a 1:1 scale of the future Mo-99 irradiation facility made of stainless steel.

## Achievements so far

Following the decision to install a Mo-99 irradiation facility in the moderator tank of the FRM II, in February 2011 the thimble for future Mo-99 production was successfully mounted. The thimble is made of the durable and irradiation-resistant reactor material Zircaloy 4. With a diameter of nine centimeters and a length of five meters, it will in future include 2 independently loadable, identical irradiation channels and enable the simultaneous irradiation of 2 x 8 so-called plate targets. The targets are positioned at a distance of some 45 cm from the fuel element, and thus close to the thermal neutron flux maximum.

The project, with its research and development activities for the optimization of Mo-99 irradiation, is supported by the Federal Ministry of Health. The development of the irradiation facility is divided into four sub-projects which are outlined below, together with a statement of their current status.

## Validation of the thermo-hydraulic design

The waste heat in the targets has to be safely dissipated, regardless of possible accident scenarios. Therefore, an elaborate thermo-hydraulic design has to be considered, and the necessary modeling and calculations performed. Nuclear licensing of the new system inevitably implies that the design for the safe dissipation of the generated heat must be validated/ independently by nuclear engineering computing programs. This independent verification must be carried out by an external expert in the field of nuclear technology.

In summary, for nominal operation at a water flow rate of 5 kg/s, a maximum local temperature of c 122 °C for the cooling water was calculated. This is located in the region of the central targets and is far away from the boiling temperature of 180 °C at 10 bar water pressure. The average temperature of

the cooling water is 60 °C at the outlet of the cooling water channel.

The calculations for irradiation at nominal conditions were completed positively in autumn 2014, and presently the calculations for accident analyses are being processed. The latter essentially include the hot channel conditions and the loss of cooling pumps during irradiation.

### Development and design of a redundant cooling and its integration into the control system

To dissipate the heat generated in the target, the installation of an additional cooling system containing three cooling pumps is planned.

Since the availability of this cooling system is of particular importance for the operation of the reactor and, in particular, its technical safety requirements, the system must be planned and designed procedurally in detail. A concept for adapting and adjusting the reactor cooling and integrating it into the existing control system is in progress. The bidding process for the pumps is set to begin in early 2015.

### Development of a safe system to load and unload the targets during reactor operation

Due to the main use of the FRM II research neutron source, it is mandatory that the planned Mo-99 production run in parallel with the loading and unloading of irradiated targets, which is being carried out continuously during reactor operation.

To implement this concept, the construction of two test stands on a 1:1 scale was realized; a replica of the cooling channel return flow as well as of the complete cooling channel unit with the two irradiation channels. These mock-ups serve to test and to optimize the technical construction, the manufacturability of the irradiation channels, and the handling steps during irradiation. This is of particular importance for the approval and the related evaluation of the concept by the nuclear experts, as the practical feasibility can be demonstrated and proven in advance and outside of the reactor. To ensure a proper operation, the hydraulically actuated clutch is now being optimized and the motor will be replaced.

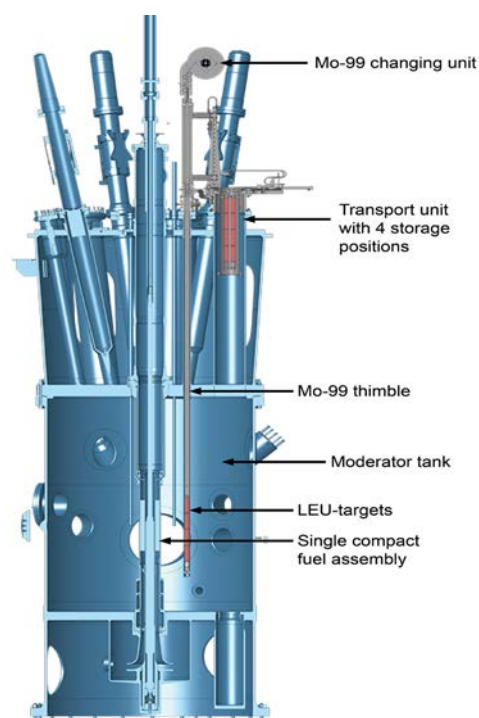


Figure 2: Schematic drawing of the future Mo-99 irradiation facility within the reactor pool. In the thimble, the cooling unit is composed of 2 cooling water supplies and 2 irradiation channels (returning cooling water).

### Dry packaging of the targets after irradiation

A special feature of our concept is the dry packaging of the irradiated targets into the approximately 5 ton heavy shielding container prior to transport to further processors. A dry packaging is possible because of the existing hot cell at the reactor basin of the FRM II. The great advantage of the dry packaging is substantially reduced risk of contamination on the outer surface of the shielding containers. This method also results in a gain in time at the beginning of the Mo-99 supply chain and thus a higher Mo-99 activity during the following processing steps. The handling procedures for this packaging process are being developed, including necessary manipulator operated tools, such as a floor-borne vehicle for the transport of the shielding containers within the FRM II. A 10 tons freight elevator to transport the irradiated targets within the reactor building already been installed in 2013.

Amongst others, the chapter “Facts & Figures” will provide numbers of visitors, staff, budget, publications, as well as submitted proposals.



## Facts & Figures

# Blogging, improving, travelling – The User Office 2014

R. Bucher<sup>1</sup>, F. Carsughi<sup>2</sup>, U. Kurz<sup>1</sup>, I. Lommatzsch<sup>1</sup>, C. Niiranen<sup>1</sup>, B. Tonin<sup>1</sup>

<sup>1</sup>Heinz Maier-Leibnitz Zentrum (MLZ), Technische Universität München, Garching, Germany

<sup>2</sup>Jülich Centre for Neutron Science (JCNS) at MLZ, Forschungszentrum Jülich GmbH, Garching, Germany

Another year with a long maintenance break... But this time the User Office managed to survive six months without users very successfully. Despite having had only one proposal round, we found a lot of other tasks to deal with!

## Always on Fridays...

This year, work at the User Office was punctuated by the long maintenance break that started in early February. But life went on and the users were able to keep up to date via the User Office's blog "Always on Fridays". There, they found an update about the ongoing work, a nice photo, or just a short account of what we were doing at the User Office. During the break, we wrote thirty articles dealing with ducks, frogs and containers as well as construction work on-site, the summer festival, preparations for conference booths, the proposal deadline, and so much more. It was planned to stop blogging after the restart in autumn. However, it became fun and the feedback was really positive, so we decided to carry on.

## Preparations during the break

We used the months without users to improve our procedures and thus make the visits more congenial. One hot topic was safety training. There has been a requirement to watch a one-hour instruction movie on-site once a year. This was very inconvenient as the experiments were thereby delayed and this had to be taken into account when planning the visit. Therefore, any number of users asked: Couldn't this be replaced by an online safety training that could be done at home in advance? Yes, it could – and it was! Our users now have to look at slides and answer some multiple choice questions at the end. The safety training system automatically ensures that each user applying for a visit gets an account and issues a reminder when the training



The MLZ booth at the DPG Spring Meeting in Dresden.

has to be repeated after twelve months. Furthermore, we initiated the Sample Tracker Online Tool. This helps to balance all samples used at the MLZ to the scope of an experiment as requested by the Radiation Protection Ordinance. Each sample has to be logged, then the system checks automatically whether it has to be registered with our radiation protection department. The reasons for this are varied: It is possible that the sample will be activated beyond the limit during the experiment, or has already been activated, or the material is fissionable .... Very convenient: A sample, once logged into the system, can be used again and again. And last but not least, the new information cards have just become available for first users after the break. What are they about? One card deals with the most important places on-site, another with the possibilities for finding something to eat. If you have a smartphone, you can even use the QR-codes to rummage for the menus. Two cards are dedicated to public transport, explaining how to get to the hotels in Garching as well as the airport and main station. QR-codes for the vending machines at the underground stations will help to ensure you always have the right ticket. And the last one... well, in case you need to relax a

little bit – how about learning some Bavarian words? This last one is the most popular and we are running out of it!

### Back to real work and combining forces

On August 22<sup>nd</sup>, user operation started again. Everything ran really smoothly and it was fun to return to business as usual. Even the normally tough period of the famous Oktoberfest hardly affected us. It is always difficult to book hotel rooms during those two weeks, especially if users apply for their stay at short notice. As if by a miracle, this year we found a room for everybody. But who was in charge of this miracle? Hotel bookings are made by the Visitors' Service. The colleagues there organise all guided tours, throughout the whole year for groups as well as for single visitors on the Open Day, about 3000 in total! In addition, they prepare the users' access to the site, checking the applications and compiling the blue folders each user receives when arriving at the MLZ. This is a strong link between the Visitors' Service and the User Office and it is for this reason that we were officially merged in late summer.

### Living out of a suitcase

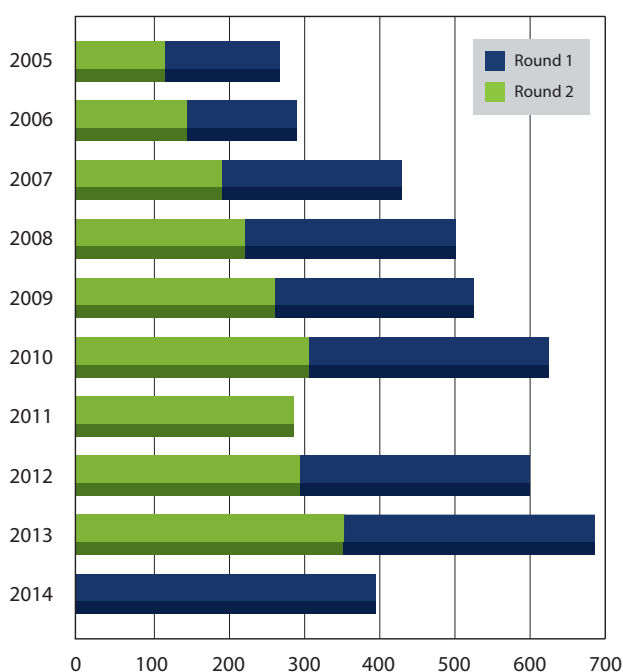
This year, we again participated in the DPG Spring Meeting of the Condensed Matter Section, managing to secure our own conference booth. This time, the host was Dresden and we were able to enjoy the first warm and sunny days there in March. Our booth was located directly at the entrance to the lecture halls – so all participants had to pass us on the way to the next talk. That was a perfect place in order to meet old and new users and inform them about the MLZ! Six months later, we travelled to Bonn for the German Conference for Research with Synchrotron Radiation, Neutrons and Ion Beams at Large Facilities. It took place in the World Conference Center, that uses the Plenary Chamber where the German Bundestag met between 1992 and 1999. This really was a unique experience! The foyer, a space flooded with light and extending over the whole floor was not only used for the booths, but also for the poster sessions, and discussions during the breaks. So, there was a lively atmosphere during the whole conference.



Looking into history at Bonn!

### Only one proposal round

Due to the long maintenance break, only one proposal round took place this year. However, we received the largest number of proposals ever: 399 proposals were submitted to 25 instruments. This was an increase of 13 % compared to the already very successful last round. In total, 2519 beam days were requested. The review panels met in June and allocated the available beam days to 305 proposals.



Proposals submitted since the first round in 2005.

# From science to media: the public relations office

C. Kortenbruck, A. Voit, B. Tonin, C. Niiranen, U. Kurz

Heinz Maier-Leibnitz Zentrum (MLZ), Technische Universität München, Garching, Germany

All in all, 2014 was a highly productive year punctuated by a number of milestones. The most important for the public relations office was the 10<sup>th</sup> anniversary of the FRM II, along with other projects. Since the reactor underwent extensive maintenance work for about 6 months, scientists were not able to carry out experiments, but found the time to publish scientific articles. The press office therefore also had a lot of material for online news and press releases. The last months of the year were dedicated to the planned relaunch of the FRM II web page and preparations for an international ERF workshop in 2015.

## 10<sup>th</sup> Anniversary of the FRM II

Preparations for this important day had already begun many months before, as the celebration was intended to offer the visitors something very special. One idea was a special tour for journalists. But what do you show a group of people who always have the possibility of visiting the facility? The answer: A tour of restricted areas which no regular visitor had ever seen: the Houston-like control room, the cellars, the security measures and so on! Another highlight of the anniversary was a common project with the Werner-Heisenberg Gymnasium in Garching, where pupils painted neutron science in oils. This project was designed to open up a vista besides physics for young people living in the neighborhood of the FRM II and aimed to foster their interest in the research of this facility. They produced about a hundred paintings from which a good dozen were exhibited at the ceremony and for several weeks afterwards in the Garching underground station. Finally, a science slam at the end of the day informed the visitors about three important research projects using neutrons: Tobias Schrader came up with the fairy tale of Prokis and Eukis, who have been fighting each other since time immemorial, but the



Figure 1: The new brochure “Neutronen für Industrie und Medizin” contains many examples of different experiments for and with industrial users.

decisive weapon is destined to be found thanks to research involving neutrons. Sebastian Mühlbauer showed the combed hedgehog and how this special animal can help understand what skyrmions are and what possibilities they offer in daily life. Christoph Hugenschmidt complained that nobody had realised that positrons were also celebrating their 10<sup>th</sup> anniversary at the FRM II. He explained how they prolong their life by finding the right hole and what this means for the surface.

## New Brochures

To mark the anniversary, the press office also produced two new brochures (in German): the Festschrift with some articles about e.g. planning history, operation over the last 10 years, progress in instrumentation, and projects with industrial applications. It concluded with the good wishes of many supportive companions from previous years, beginning with the first planning stages in the late 1970s.

The second fulfilled a long-held wish and need: a new brochure for industrial users that provides some striking examples of common projects. This was composed of statements from industrial users on how neutrons had helped to solve their problems.

### Relocation of the FRM II Web Page

When the MLZ web page had been completed, the former FRM II web page needed to be relaunched and moved to the central server of the Technische Universität München. This meant that the whole content had to be rewritten from scratch and given a new structure. This process took up a lot of the time available in 2014 and is still in progress. The relaunch of the FRM II web page is planned for the first quarter of 2015.

### Media coverage

Not taking into account publications in our own media and press releases, the number amounts to 211 articles in the press, which is well above the average of some 150 articles per year. Television is also represented with six more broadcasts. This relatively high number is due to two part-time employees whose combined working hours well exceed one full-time position. The 10th anniversary attracted a lot of additional press coverage on radio, television and in the newspapers. However, science dominated the topics even in this year: 53 % of all media reports were based on research conducted at the Heinz Maier-Leibnitz Zentrum. A highlight among

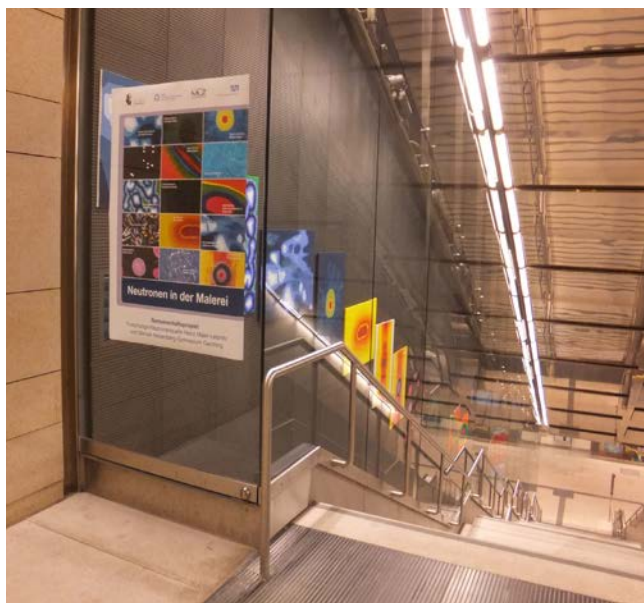


Figure 2: The city of Garching was very proud of its pupils paintings and exhibited the best ones in their underground station.

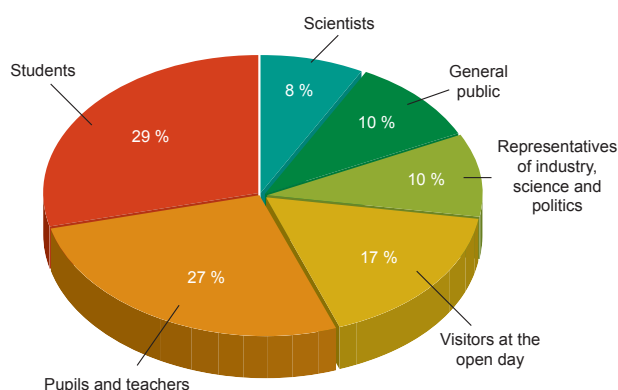


Figure 3: In 2014, a total of 2956 visitors made a guided tour through the FRM II.

the press releases was the publication of the lithium plating that was covered by the national and international press for weeks. A publication in “Science” attracted a great deal of attention even though it dealt with basic research on superconductivity and was surprisingly taken up by the press. This was largely due to a wonderful photo taken by a professional photographer who visited the FRM II last year.

### Own Talks

During the 7<sup>th</sup> Forum Wissenschaftskommunikation organized by “Wissenschaft im Dialog” in Potsdam, the press & public relations office’s abstract on the pupils’ project “Painted Neutrons” was accepted for a talk. Due mainly to the “strange” combination of physics and art, this project aroused exceptional interest among other PR professionals.

### Visitors

In the long run, the 10<sup>th</sup> anniversary attracted many additional visitors from hitherto unknown target groups such as the Green party from Erding or the Munich Chamber of Commerce.

All in all, the number of visitors remained fairly constant at around the 3000 mark. This is only the number the visitors’ service handled and does not include others, e.g. delegations from other countries or other officials. Almost 60 % of the visitors were pupils or students, 505 taking advantage of the open day in October. 82 % opted for a German tour, but 12 % of the visitors preferred an English tour.

# Organisation

## FRM II and MLZ

The Forschungs-Neutronenquelle Heinz Maier-Leibnitz (FRM II) provides neutrons for research, industry and medicine and is operated as a Corporate Research Centre by the Technische Universität München (TUM). The scientific use of the FRM II, with around 1000 user visits per year, is organized within the “Heinz Maier-Leibnitz Zentrum” (MLZ).

The chart below shows the overall network comprising the neutron source FRM II and the MLZ, as well as the funding bodies and the scientific users performing experiments at the MLZ addressing the grand challenges of our today's society.

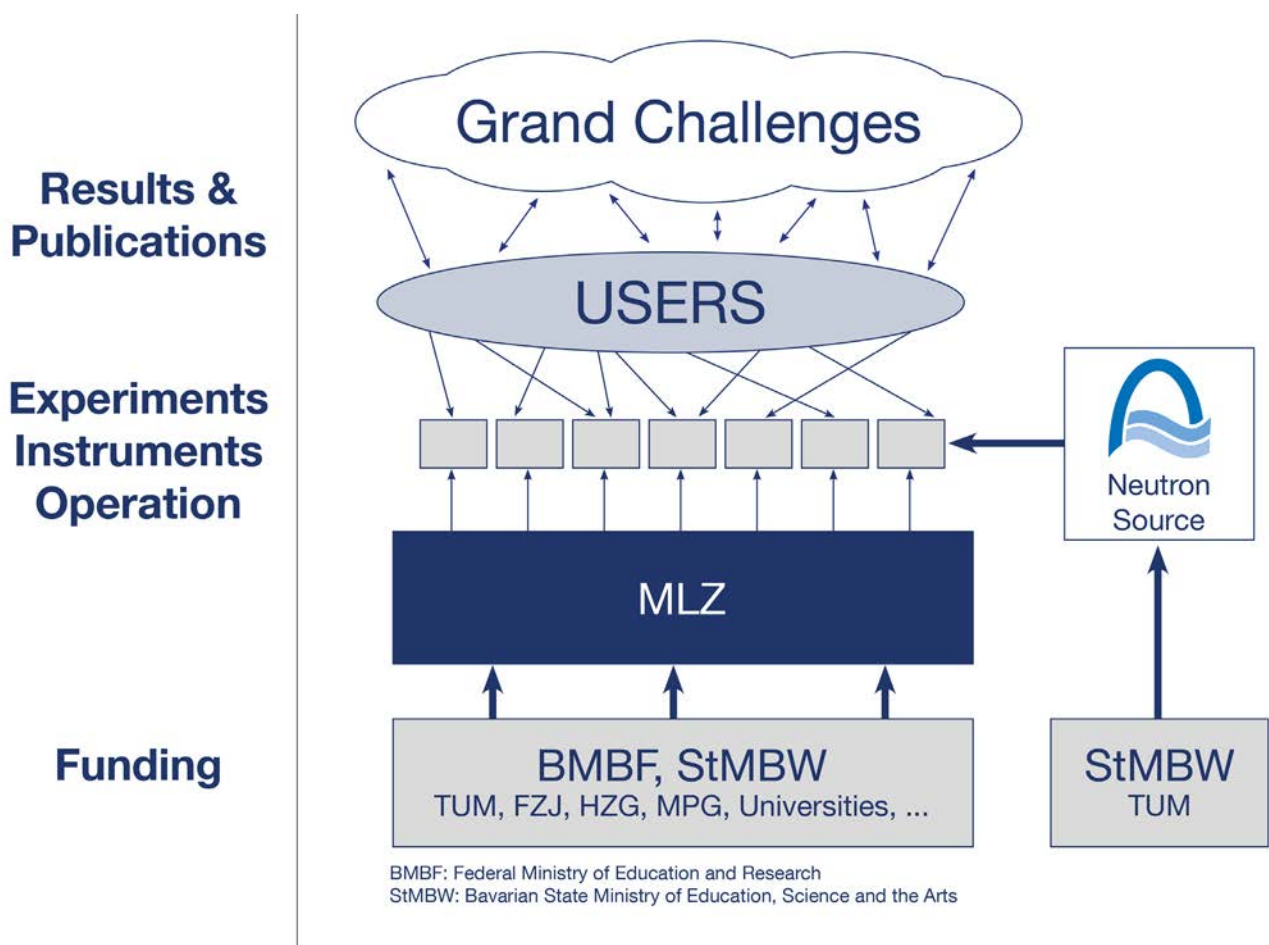


Figure 1: The neutron source FRM II and the user facility MLZ.

### Scientific Director MLZ, FRM II

Prof. Dr. Winfried Petry

### Technical Director FRM II

Dr. Anton Kastenmüller

### Scientific Director MLZ, HGF

Prof. Dr. Dieter Richter

### Administrative Director FRM II

Dr. Klaus Seebach

### Scientific Cooperation at the Heinz Maier-Leibnitz Zentrum (MLZ)

The Heinz Maier-Leibnitz Zentrum with its cooperation partners Technische Universität München (TUM), Forschungszentrum Jülich (FZJ) and Helmholtz-Zentrum Geesthacht (HZG) is embedded in a network of strong partners including the Max Planck Society (MPG) and numerous university groups exploiting the scientific use of the Forschungs-Neutronenquelle Heinz Maier-Leibnitz. The organizational chart of the MLZ is shown below.

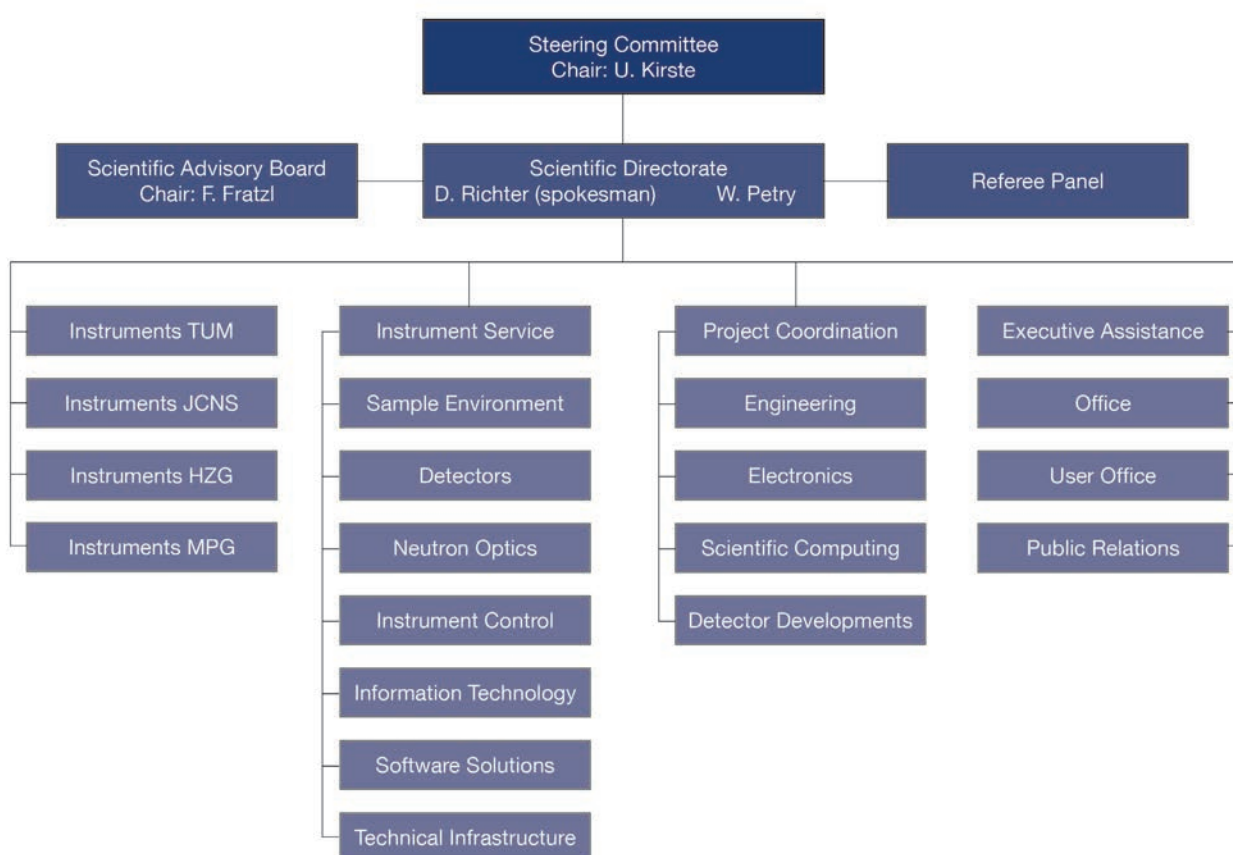


Figure 2: Organisational chart MLZ.

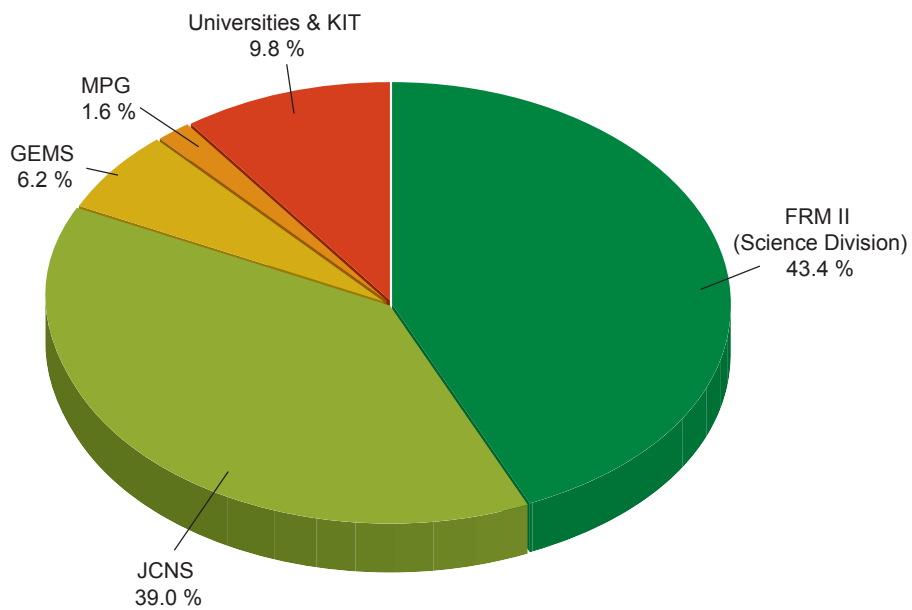
# Staff

## Staff of the MLZ and the FRM II

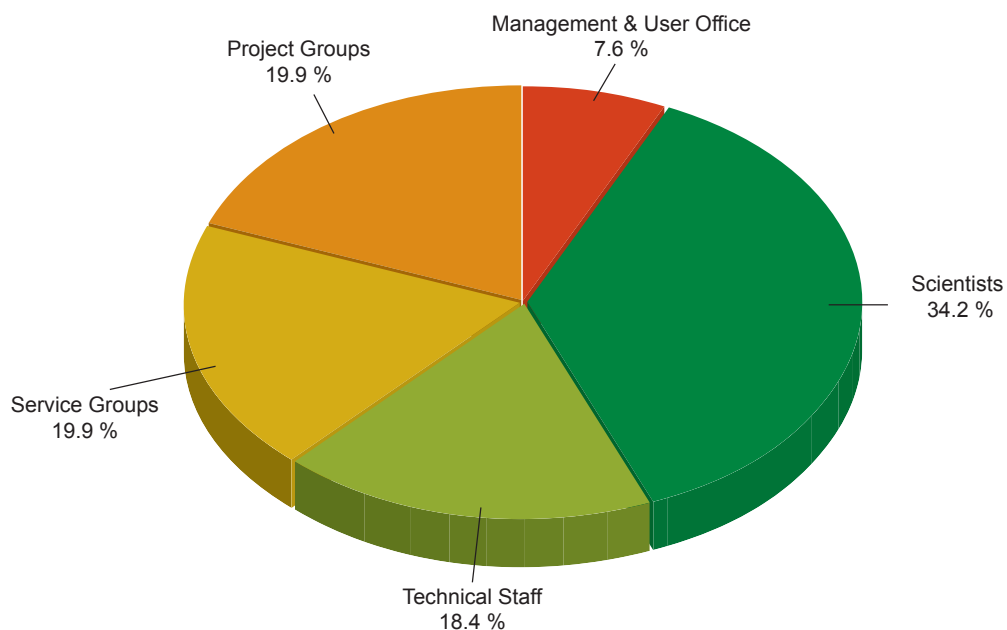
The tables and charts below show the staff of MLZ and FRM II. The staff of MLZ according to its share among the partners with a detailed view according to the function within the MLZ is depicted as well.

MLZ & its Partners	FTE <sup>1</sup>	%
FRM II (Science Division)	105.5	43.4
JCNS	94.8	39.0
GEMS	15.0	6.2
MPG	4.0	1.6
Universities & KIT	24.0	9.8

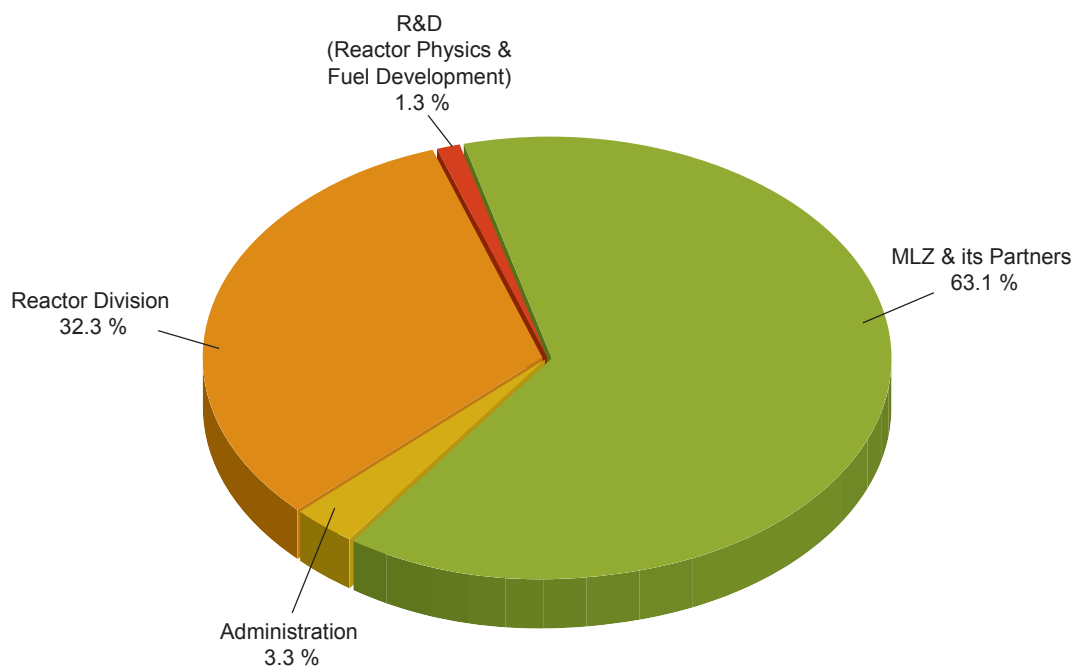
<sup>1</sup>FTE (Full Time Equivalent)



MLZ according to Function	FTE	%
Management & User Office	18.5	7.6
Scientists	83.0	34.2
Technical Staff	44.8	18.4
Service Groups	48.5	19.9
Project Groups	48.5	19.9



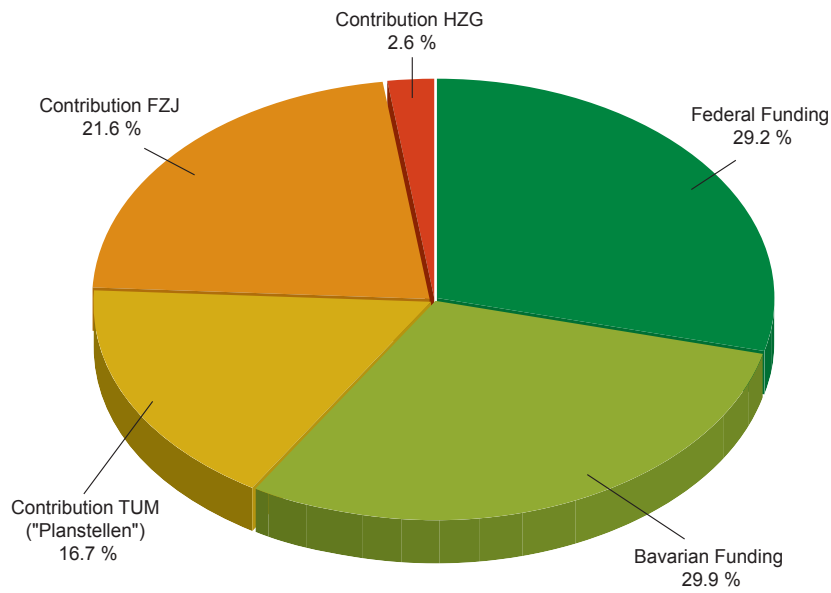
FRM II, MLZ & its Partners	FTE	%
Administration	12.6	3.3
Reactor Division	124.7	32.3
R&D (Reactor Physics & Fuel Development)	5.0	1.3
MLZ & its Partners	243.3	63.1



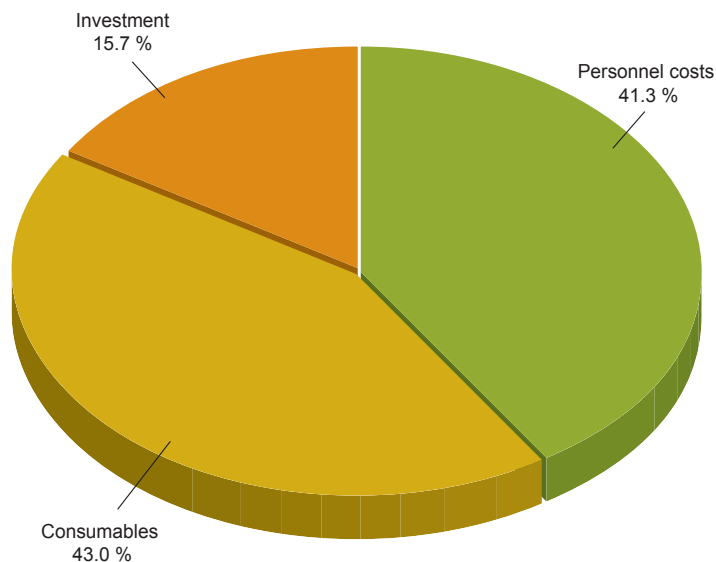
# Budget

The table and charts below show the revenue and expenses in 2014.

Revenue 2014	Total (€)	%
Federal Funding	16.630.000	29.2
Bavarian Funding	17.000.000	29.9
Contribution TUM („Planstellen“)	9.500.000	16.7
Contribution FZJ	12.298.789	21.6
Contribution HZG	1.470.000	2.6
<b>Total</b>	<b>56.898.789</b>	<b>100</b>



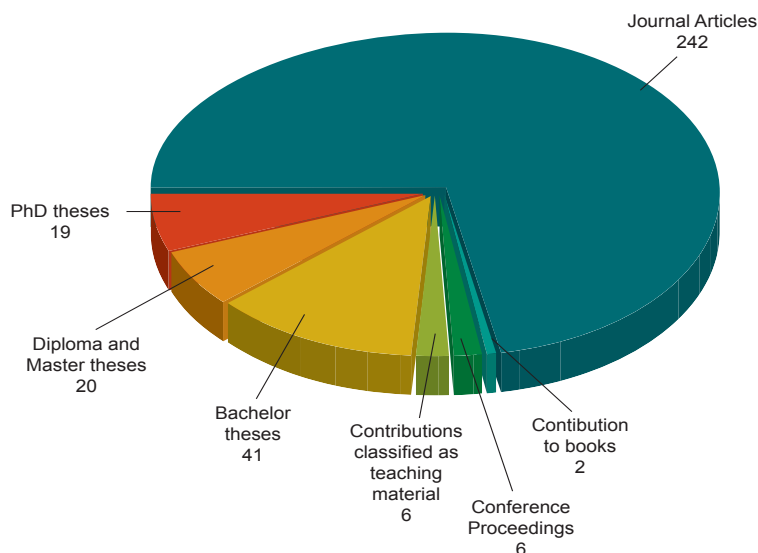
Expenses 2014	TUM (€)	FZJ (€)	HZG (€)	Total (€)	%
Personnel costs	14.300.000	7.678.389	1.490.000	23.468.389	41.3
Consumables	20.000.000	3.919.517	570.000	24.489.517	43.0
Investment	2.960.000	5.890.883	90.000	8.940.883	15.7
<b>Total</b>	<b>37.260.000</b>	<b>17.488.789</b>	<b>2.150.000</b>	<b>56.898.789</b>	<b>100</b>



## Publications & Theses

In 2014, we received notice of a total of 250 scientific publications, including journal articles, contributions to books and conference proceedings, as well as published teaching material (<https://impulse.mlz-garching.de/> and figure below). Furthermore, in total 80 theses supervised by staff of the scientific cooperation partners were completed in 2014.

A user survey conducted for the MLZ Review showed that in 2014 an impressive 200 PhD theses, based on experiments at the MLZ and including external users, were either ongoing or completed. Of these currently ongoing theses, about 100 are under the direct supervision of staff at the MLZ.



The classification of the journal articles by subject is as follows (several tags per journal article are possible):

Scientific Areas	%
Materials Science	20.1
Soft Condensed Matter	17.6
Magnetism	14.5
Instrument and Method Development	11.1
Condensed Matter Physics	9.9
Chemistry	7.4
Biology	5.9
Crystallography	5.3
Industrial Application	3.1
Nuclear & Particle Physics	1.5
Medicine	1.2
Geosciences	1.2
Archaeology, Museums & Arts	0.3
Others	0.9

Grand Challenges	%
Nano Science and Technology	22.2
Soft Matter, Macromolecules, Complex Fluids, Biophysics	21.5
Fundamental Research	15.5
Information Technology and Functional Materials	11.7
Energy	9.4
Life Science and Health	5.7
Earth, Environment and Cultural Heritage	2.3
Others	11.7

# Committees

## Steering Committee

### Chairwoman

MRin Dr. Ulrike Kirste  
Bayerisches Staatsministerium für Bildung  
und Kultus, Wissenschaft und Kunst

### Members

Karsten Beneke  
Vice-Chairman of the Board of Directors of  
Forschungszentrum Jülich GmbH

Albert Berger  
Chancellor  
Technische Universität München

Dr. Ralph Dieter  
Federal Ministry of Education and Research

Thomas Frederking  
Member of the Executive Board of  
Helmholtz-Zentrum Berlin GmbH

Prof. Dr. Dr. h.c. mult. Wolfgang A. Herrmann  
President Technische Universität München

represented by Prof. Dr. Thomas Hofmann,  
Vice-President Technische Universität München

MinR Dr. Ulrich Katenkamp  
Federal Ministry of Education and Research

Prof. Dr. Wolfgang Kaysser  
Member of the Executive Board of  
Helmholtz-Zentrum Geesthacht GmbH

Prof. Dr. Stephan Paul  
Technische Universität München  
Physik-Department E18

### Guests

Prof. Dr. Winfried Petry,  
Scientific Director of the MLZ,  
representing Technische Universität München

Prof. Dr. Dieter Richter,  
Scientific Director of the MLZ,  
representing HGF institutions

RDin Steffi Polwein,  
Head of Central Administration ZA1  
Technische Universität München

Dr. Anton Kastenmüller  
Technical Director ZWE-FRM II,  
Technische Universität München

Dr. Klaus Seebach  
Administrative Director ZWE-FRM II,  
Technische Universität München

Dirk Schlotmann  
Forschungszentrum Jülich GmbH



Figure 1: Steering Committee from left to right: K. Seebach, U. Katenkamp, C. Alba-Simionesco, A. Berger, S. Polwein, T. Frederking, A. Kastenmüller, W. Petry, S. Paul, U. Kirste, W. Schäfer, K. Beneke, D. Schlotmann, D. Richter.



Figure 2: Scientific Advisory Board from left to right: D. Richter, A. Harrison, P. Fratzl, W. Reimers, A. Arbe, W. Petry, C. Alba-Simionesco, J. Rädler, H. Abele, J. Mesot, B. Keimer.

## Scientific Advisory Board

### Chairman

Prof. Dr. Peter Fratzl  
Max-Planck-Institut für Kolloid- und  
Grenzflächenforschung, Potsdam

### Members

Prof. Dr. Hartmut Abele  
Atominstutit der Österreichischen Universitäten  
Technische Universität Wien, Wien

Prof. Christiane Alba-Simionesco  
Laboratoire Léon Brillouin, CEA, Centre de Saclay

Prof. Dr. Arantxa Arbe  
Unidad de Fisica de Materiales  
Facultad de Quimica, San Sebastián

Prof. Dr. Andrew Harrison  
Diamond Light Source, Didcot

Prof. Dr. Dirk Johrendt  
Ludwig-Maximilians-Universität,  
Department Chemie und Biochemie, München

Prof. Dr. Bernhard Keimer  
Max-Planck-Institut für Festkörperforschung,  
Stuttgart

Prof. Dr. Joël Mesot  
Paul Scherrer Institut, Villigen

Prof. Dr. Joachim O. Rädler  
Ludwig-Maximilians-Universität,  
Department für Physik, München

Prof. Dr. Walter Reimers  
Technische Universität Berlin,  
Institut für Werkstoffwissenschaften und  
-technologien, Berlin

Dr. Jens Rieger  
Senior Vice President, Advanced Materials  
& Systems Research, BASF SE, Ludwigshafen

Prof. Dr. Metin Tolan  
Beschleuniger- & Synchrotronlabor  
Technische Universität Dortmund, Dortmund

## Evaluation of Beam Time Proposals: Members of the Review Panels

Dr. Tamás Belgya  
Budapest Neutron Center, Budapest

Dr. Victor Bodnarchuk  
Joint Institute for Nuclear Research  
Frank Laboratory of Neutron Physics, Dubna

Prof. Dr. Jan Bonarski  
Polish Academy of Sciences  
Institute of Metallurgy and  
Materials Science, Kraków

Dr. Laszlo Bottyan  
Hungarian Academy of Sciences  
Institute for Particle and Nuclear Physics, Budapest

Prof. Roberto Brusa  
Università degli Studi di Trento  
Facoltà di Ingegneria, Dipartimento di Fisica, Trento

Prof. Dr. Roberto Caciuffo  
Institute for Transuranium Elements  
Joint Research Center, Karlsruhe

Dr. Monica Ceretti  
Université de Montpellier 2  
Institut Charles Gerhardt, Montpellier

Dr. Niels Bech Christensen  
Technical University of Denmark  
Institute of Physics, Roskilde

Dr. Pascale Deen  
European Spallation Source (ESS AB), Lund

Dr. Sabrina Disch  
University of Cologne,  
Department of Chemistry, Cologne

Prof. Dr. Stefan Egelhaaf  
Heinrich-Heine-Universität Düsseldorf  
Lehrstuhl für Physik der weichen Materie,  
Düsseldorf

Prof. Dr. Helmut Ehrenberg  
Karlsruher Institut für Technologie (KIT)  
Institut für Angewandte Materialien, Karlsruhe

Dr. Tom Fennell  
Paul Scherrer Institute  
Laboratories for Solid State Physics  
Neutron Scattering

Dr. Marie Thérèse Fernandez-Diaz  
Institut Laue-Langevin (ILL), Grenoble

Dr. Peter Fouquet  
Institut Laue-Langevin (ILL), Grenoble

Dr. Victoria Garcia-Sakai  
STFC Rutherford Appleton Laboratory, Didcot

Prof. Giacomo Diego Gatta  
Università degli Studi di Milano  
Dip. Scienze della Terra „Ardito Desio“, Milano

Prof. Dr. Rupert Gebhard  
Archäologische Staatssammlung München,  
Abt. Vorgeschichte, München



Figure 3: Members of the Review Panels from left to right (background): A. Radulecu, J. Neuhaus, O. Stockert, A. Ostermann, T. Nylander, K. Temst, A. Schneidewind, H. Ehrenberg, A. Senyshyn, W. Petry, S. Mattauch, C. Piochacz, A. Magerl, W. Sprengel, P. Schurtenberger. From left to right (foreground): F. Carsughi, P. Staron.

Dr. Jens Gibmeier  
Karlsruher Institut für Technologie (KIT),  
Institut für Angewandte Materialien, Karlsruhe

Dr. Béatrice Gillon  
Laboratoire Léon Brillouin  
CEA, Centre de Saclay

Dr. Arsène Goukassov  
Laboratoire Léon Brillouin  
CEA, Centre de Saclay

Dr. Christian Grünzweig  
Paul Scherrer Institute, Villigen

Prof. Dr. Ian William Hamley  
University of Reading  
Department of Chemistry, Reading

Dr. Thomas Hauss  
Helmholtz-Zentrum Berlin für Materialien  
und Energie GmbH, Berlin

Prof. Dr. Stephen Hayden  
University of Bristol  
HH Wills Physics Laboratory, Bristol

Dr. Arno Hiess  
European Spallation Source (ESS AB),  
Neutron Science Division, Lund

Dr. Klaudia Hradil  
Technische Universität Wien,  
Röntgenzentrum, Wien

Dr. Nikolay Kardjilov  
Helmholtz-Zentrum Berlin für Materialien  
und Energie GmbH, Berlin

Prof. Dr. Michel Kenzelmann  
Paul Scherrer Institute, Laboratories for Solid State  
Physics & Neutron Scattering, Villigen

Prof. Christian Krempaszky  
Technische Universität München,  
Fakultät für Maschinenwesen, München

Dr. Eberhard Lehmann  
Paul Scherrer Institute, Villigen

Prof. Dr. Martin Lerch  
Technische Universität Berlin,  
Institut für Chemie, Berlin

Dr. Dieter Lott  
Helmholtz-Zentrum Geesthacht GmbH,  
Institut für Materialforschung, Geesthacht

Prof. Dr. Andreas Magerl  
Universität Erlangen-Nürnberg,  
Kristallographie und Strukturphysik, Erlangen

Dr. Andreas Michels  
Université de Luxembourg,  
Faculté des Sciences, de la Technologie  
et de la Communication, Luxembourg

Dr. Bert Nickel,  
Ludwig Maximilians-Universität München,  
Fakultät für Physik, München

Prof. Dr. Tommy Nylander  
Lund University, Physical Chemistry, Lund

Prof. Dr. Luigi Paduano  
University of Naples "Federico II",  
Chemistry Department, Naples

Prof. Dr. Catherine Pappas  
Delft University of Technology, Delft

Prof. Dr. Oskar Paris  
Montanuniversität Leoben, Leoben

Prof. Dr. Wolfgang Paul  
Martin-Luther-Universität Halle-Wittenberg,  
Institut für Physik, Halle

Dr. Simon Redfern University of Cambridge,  
Department of Earth Sciences, Cambridge

Prof. Dr. Günther Redhammer Universität Salzburg,  
Materialforschung und Physik, Salzburg

Dr. Matthias Rossbach  
Forschungszentrum Jülich GmbH, Jülich

Dr. Margarita Russina  
Helmholtz-Zentrum Berlin GmbH,  
Institut Weiche Materie und Funktionale Materialien,  
Berlin

Prof. Dr. Michael Sattler  
Technische Universität München,  
Department Chemie, München

Dr. Harald Schmidt  
Technische Universität Clausthal,  
Institut für Metallurgie, Clausthal

Prof. Dr. Andreas Schönhals  
Bundesanstalt für Materialforschung und -prüfung,  
Berlin

Prof. Dr. Peter Schurtenberger University of Lund,  
Physical Chemistry 1, Lund

Dr. Torsten Soldner  
Institut Laue-Langevin (ILL), Grenoble

Prof. Dr. Wolfgang Sprengel  
Technische Universität Graz,  
Institut für Materialphysik, Graz

Dr. Jochen Stahn  
ETH Zürich and Paul Scherrer Institute, Villigen

Dr. Peter Staron  
Helmholtz-Zentrum Geesthacht GmbH  
Institute of Materials Research, Geesthacht

Dr. Paul Steffens  
Institut Laue-Langevin (ILL), Grenoble

Dr. Oliver Stockert  
Max-Planck-Institut für Chemische Physik fester  
Stoffe Dresden, Dresden

Dr. Susana Teixeira  
Institut Laue-Langevin (ILL), Grenoble

Prof. Kristiaan Temst  
Katholieke Universiteit Leuven,  
Nuclear & Radiation Physics Section, Leuven



Figure 4: First discussions among the referees during the welcome buffet for the review.

Prof. Dr. Katharina Theis-Broehl  
Hochschule Bremenhaven, Bremenhaven

Prof. Dr. Thomas Thurn-Albrecht  
Martin-Luther-Universität Halle-Wittenberg,  
Experimentelle Polymerphysik, Halle

Prof. Dr. Tobias Unruh  
Universität Erlangen-Nürnberg,  
Kristallographie und Strukturphysik, Erlangen

Dr. Lambert van Eijck  
Delft University of Technology,  
Department of Radiation, Radionuclides  
and Reactors, Delft

Prof. Dr. Regine von Klitzing  
Technische Universität Berlin,  
Institut für Chemie, Stranski-Laboratorium  
für Physikalische und Theoretische Chemie, Berlin

Dr. Martin Weik  
Institut de Biologie Structurale, Grenoble

Dr. Andrew Wildes  
Institut Laue-Langevin (ILL), Grenoble

Dr. Robert Wimpory  
Helmholtz-Zentrum Berlin für Materialien und  
Energie GmbH, Berlin

## Partner institutions

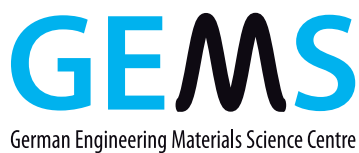


Bayerisches Geoinstitut  
Universität Bayreuth  
[www.bgi.uni-bayreuth.de](http://www.bgi.uni-bayreuth.de)



Georg-August-Universität Göttingen

- Institut für Physikalische Chemie  
[www.uni-pc.gwdg.de/eckold](http://www.uni-pc.gwdg.de/eckold)
- Geowissenschaftliches Zentrum  
[www.uni-goettingen.de/de/125309.html](http://www.uni-goettingen.de/de/125309.html)



German Engineering Materials Science Centre GEMS  
Helmholtz-Zentrum Geesthacht GmbH  
[www.hzg.de/institutes\\_platforms/gems/](http://www.hzg.de/institutes_platforms/gems/)



Jülich Centre for Neutron Science JCNS  
Forschungszentrum Jülich GmbH  
[www.jcns.info](http://www.jcns.info)



Karlsruher Institut für Technologie

- Institut für Angewandte Materialien –  
Energiespeichersysteme (IAM-ESS)  
[www.iam.kit.edu](http://www.iam.kit.edu)



Ludwig-Maximilians-Universität München

- Sektion Kristallographie  
[www.lmu.de/kristallographie](http://www.lmu.de/kristallographie)
- Sektion Physik  
[www.softmatter.physik.uni-muenchen.de](http://www.softmatter.physik.uni-muenchen.de)



MAX-PLANCK-GESELLSCHAFT

Max-Planck-Institut für Festkörperforschung, Stuttgart  
[www.fkf.mpg.de](http://www.fkf.mpg.de)



RWTH Aachen

- Institut für Kristallographie  
[www.xtal.rwth-aachen.de](http://www.xtal.rwth-aachen.de)
- Institut für Anorganische Chemie  
[www.ac.rwth-aachen.de](http://www.ac.rwth-aachen.de)



Technische Universität Clausthal

- Institut für Werkstoffkunde und Werkstofftechnik  
[www.iww.tu-clausthal.de](http://www.iww.tu-clausthal.de)



Technische Universität Dresden

- Institut für Festkörperphysik  
[www.physik.tu-dresden.de/ifp](http://www.physik.tu-dresden.de/ifp)



Technische Universität München

- E13 – Lehrstuhl für Funktionelle Materialien  
[www.e13.physik.tu-muenchen.de](http://www.e13.physik.tu-muenchen.de)



Technische Universität München

- E18 – Lehrstuhl für Experimentalphysik I  
[www.e18.ph.tum.de](http://www.e18.ph.tum.de)



E21  
Arbeitsgebiet stark  
korrelierte Elektronensysteme

Technische Universität München

- E21 – Lehrstuhl für Neutronenstreuung  
[www.e21.ph.tum.de](http://www.e21.ph.tum.de)



Technische Universität München

- Exzellenzcluster „Origin and Structure of the Universe“  
[www.universe-cluster.de](http://www.universe-cluster.de)



Klinikum rechts der Isar

Technische Universität München

- MRI - Klinikum Rechts der Isar  
[www.med.tum.de](http://www.med.tum.de)



RCM  
Radiochemie München

Technische Universität München

- RCM - Radiochemie München  
[www.rcm.tum.de](http://www.rcm.tum.de)



TECHNISCHE  
UNIVERSITÄT  
WIEN  
Vienna University of Technology

Technische Universität Wien

Neutronen- & Quantenphysik  
Forschungsbereich am Atominstitut Wien  
Arbeitsgruppe Abele

[http://ati.tuwien.ac.at/research\\_areas/neutron\\_quantum\\_physics/](http://ati.tuwien.ac.at/research_areas/neutron_quantum_physics/)



Universität der Bundeswehr München

- Institut für Angewandte Physik und Messtechnik  
[www.unibw.de/lrt2](http://www.unibw.de/lrt2)

Universität zu Köln



Universität zu Köln

- Institut für Kernphysik  
[www.ikp.uni-koeln.de](http://www.ikp.uni-koeln.de)
- II. Physikalisches Institut  
[www.ph2.uni-koeln.de](http://www.ph2.uni-koeln.de)

# Imprint

## Publisher

Technische Universität München  
 Forschungs-Neutronenquelle  
 Heinz Maier-Leibnitz (FRM II)  
 Lichtenbergstr. 1  
 85747 Garching  
 Germany

Phone: +49.89.289.14966  
 Fax: +49.89.289.14995  
 Internet: [www.mlz-garching.de](http://www.mlz-garching.de)  
 E-mail: [mlz@mlz-garching.de](mailto:mlz@mlz-garching.de)

## Editors

Henrich Frielinghaus  
 Robert Georgii  
 Connie Hesse  
 Michael Hofmann  
 Olaf Holderer  
 Elisabeth Jörg-Müller  
 Christine Kortenbruck  
 Peter Link  
 Wiebke Lohstroh  
 Andreas Ostermann  
 Björn Pedersen  
 Anatoliy Senyshyn  
 Olaf Soltwedel  
 Yixi Su  
 Andrea Voit

## Photographic credits

Wenzel Schürmann, TUM:  
 Cover front (top right, middle, bottom), 7, 8, 10 (top, bottom), 11 (bottom), 12 (bottom), 13 (bottom), 14 (top, middle), 15 (bottom), 16 (6,7,11), 17 (8, 2), 33 (top), 111, 116 (bottom), 130, 131

Uli Benz, TUM:  
 Cover (top left), 11 (top),

Forschungszentrum Jülich:  
 8 (bottom, 2<sup>nd</sup> from left), 23 (top),

Ralf Engels, Forschungszentrum Jülich:  
 16 (3)

Alexandra Steffens, JCNS:  
 16 (5)

Rainer Bruchhaus, JCNS:  
 17 (10)

Volker Lannert, DAAD:  
 19, 119

Alexander Komarek, MPG:  
 47

Axel Pichlmaier, FRM II:  
 Cover back (right), 12 (top)

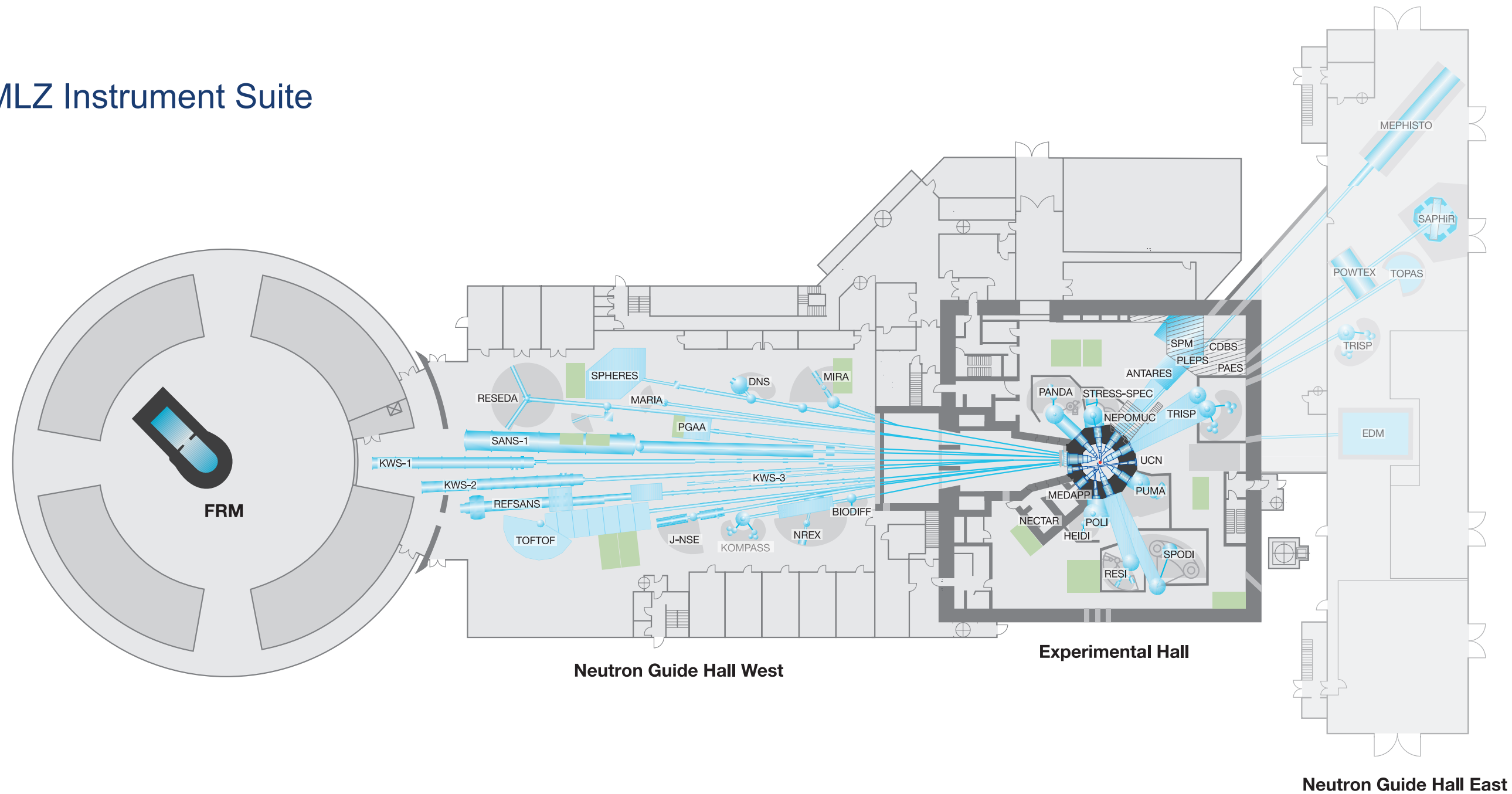
Volker Zill, FRM II:  
 Cover back (left)

Editors and authors:  
 other images

## Design and typesetting

Ramona Bucher  
 Connie Hesse  
 Ina Lommatzsch  
 Adrian Weis

# MLZ Instrument Suite



Instrument	Description	Neutrons	Status	Operated by	Funding
ANTARES	Radiography and tomography	cold	operation	TUM	TUM
BIODIFF	Diffractionmeter for large unit cells	cold	operation	TUM, JCNS	TUM, FZJ
DNS	Diffuse scattering spectrometer	cold	operation	JCNS	FZJ
HEIDI	Single crystal diffractometer	hot	operation	RWTH Aachen	FZJ
J-NSE	Spin-echo spectrometer	cold	operation	JCNS	FZJ
KOMPASS	Three axes spectrometer	cold	construction	Uni Köln, TUM	BMBF
KWS-1	Small angle scattering	cold	operation	JCNS	FZJ
KWS-2	Small angle scattering	cold	operation	JCNS	FZJ
KWS-3	Very small angle scattering	cold	operation	JCNS	FZJ
MARIA	Magnetic reflectometer	cold	operation	JCNS	FZJ
MEPHISTO	Facility for particle physics, PERC	cold	reconstruction	TUM	TUM, DFG
MIRA	Multipurpose instrument	cold	operation	TUM	TUM
MEDAPP	Medical irradiation treatment	fast	operation	TUM	TUM
NECTAR	Radiography and tomography	fast	operation	TUM	TUM
NEPOMUC	Positron source, CDBS, PAES, PLEPS, SPM	-	operation	TUM, UniBw München	TUM, BMBF
NREX	Reflectometer with X-ray option	cold	operation	MPI Stuttgart	MPG
PANDA	Three axes spectrometer	cold	operation	JCNS	FZJ

Instrument	Description	Neutrons	Status	Operated by	Funding
PGAA	Prompt gamma activation analysis	cold	operation	Uni Köln	TUM
PUMA	Three axes spectrometer	thermal	operation	Uni Göttingen, TUM	TUM
POLI	Single-crystal diffractometer polarized neutrons	hot	operation	RWTH Aachen	BMBF, FZJ
POWTEX	Time-of-flight diffractometer	thermal	construction	RWTH Aachen, Uni Göttingen, JCNS	BMBF, FZJ
REFSANS	Reflectometer	cold	operation	GEMS	HZG
RESEDA	Resonance spin-echo spectrometer	cold	operation	TUM	TUM
RESI	Single crystal diffractometer	thermal	operation	LMU	TUM
SANS-1	Small angle scattering	cold	operation	TUM, GEMS	TUM, HZG
SAPHIR	Six anvil press for radiography and diffraction	thermal	construction	BGI	BMBF
SPHERES	Backscattering spectrometer	cold	operation	JCNS	FZJ
SPODI	Powder diffractometer	thermal	operation	KIT	TUM
STRESS-SPEC	Materials science diffractometer	thermal	operation	TUM, TU Clausthal, GEMS	TUM, HZG
TOFTOF	Time-of-flight spectrometer	cold	operation	TUM	TUM
TOPAS	Time-of-flight spectrometer	thermal	construction	JCNS	FZJ
TRISP	Three axes spin-echo spectrometer	thermal	operation	MPI Stuttgart	MPG
UCN	Ultra cold neutron source, EDM	ultra-cold	construction	TUM	TUM, DFG

#### **Front page:**

**Moments from the 10 years' FRM II anniversary celebration (pictures on the left) and impressions of the MLZ review in May 2014 (pictures on the right).**

#### **FRM II 10<sup>th</sup> anniversary celebration (starting top left, continuing downwards)**

From left to right: H. Gabor (mayor of Garching), K. Seebach (administrative director FRM II), H. Zehetmair (former Minister for Science in Bavaria), W. Petry (scientific director FRM II, MLZ), O. Schily (former German Federal Minister for the Interior), A. Kastenmüller (technical director FRM II), M. Solbrig (former mayor of Garching); T. Schrader (JCNS) talking about "Eukis and Prokis" during the 10 years' celebration; Music played by The Occasional Five.

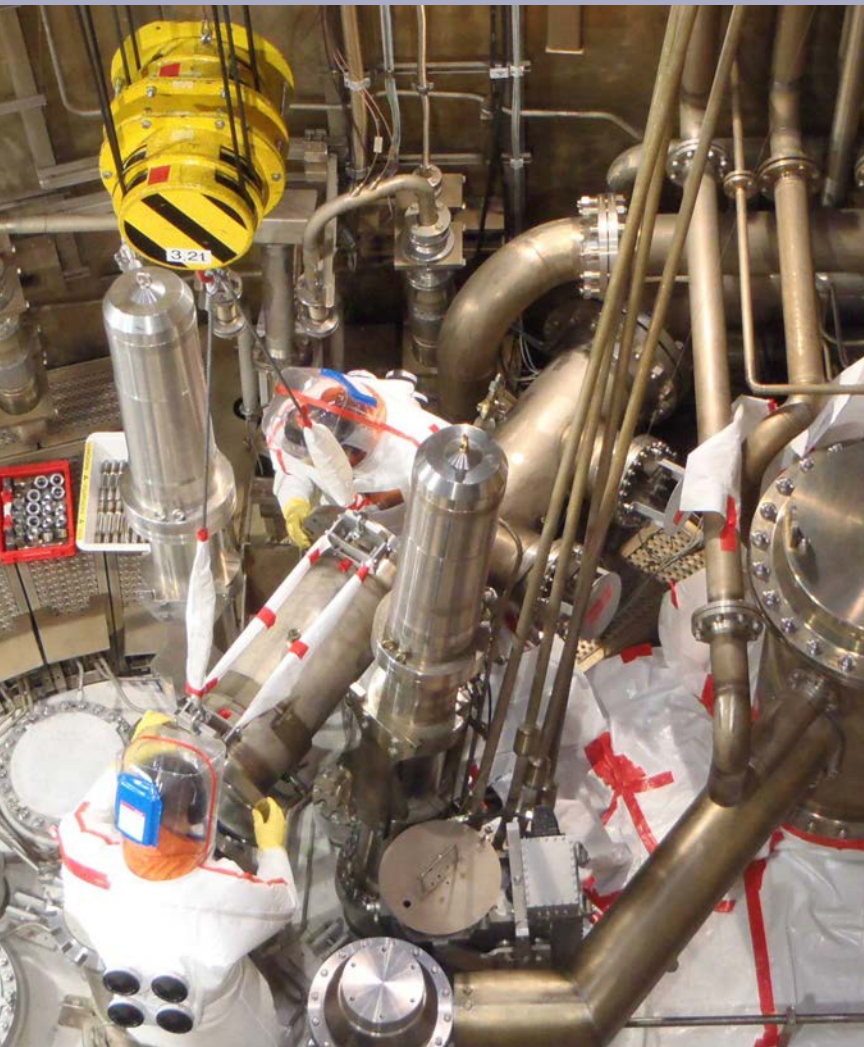
#### **MLZ review (starting top right, continuing downwards)**

From left to right: T. Unruh (FAU Erlangen-Nürnberg), R. von Klitzing (TU Berlin) and J.-F. Moulin (GEMS) at the instrument REFSANS; P. Kudejova (FRM II) and A. Young (North Carolina State University) at the instrument PGAA; A. Schreyer (HZG), A. Young (North Carolina State University), K. Kakurai (JAEA), A. Harrison (Diamond Light Source), C. Alba-Simionesco (LLB), M. Tolian (TU Dortmund), D. Richter (JCNS), W. Petry (FRM II), A. Arbe (CSIC-UPV/EHU), P. Langan (ORNL), R. von Klitzing (TU Berlin), T. Unruh (FAU Erlangen-Nürnberg), A. Ioffe (JCNS), J. Neuhäus (FRM II).

#### **Back page**

#### **Images of the long maintenance break in 2014 (starting top left, continuing clockwise):**

Reassembly of the primary cooling circuit in the reactor pool after the periodic tests of the moderator tank and the central channel had been carried out; view from bottom to top through the cooling tower; inspection of the surface of a flange of a primary cooling circuit.



Heinz Maier-Leibnitz Zentrum (MLZ)

[www.mlz-garching.de](http://www.mlz-garching.de)

DOI: 10.14459/2015md1239870